Performance Analysis of GFDM for 5th Generation Cellular Communication

Submitted in partial fulfilment of the requirements

for the award of the degree of

Doctor of Philosophy

by

Shravan Kumar Bandari

(Roll No: 701356)

Under the supervision of

Dr. V. Venkata Mani

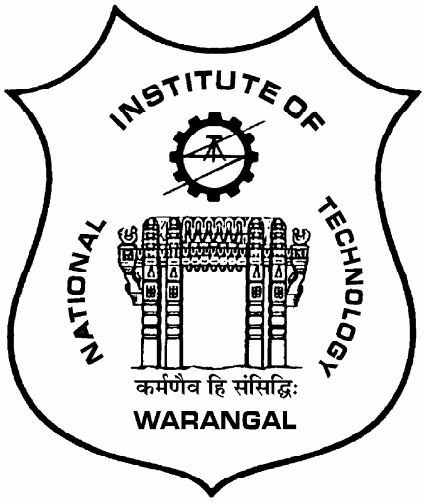

Department of Electronics & Communication Engineering

National Institute of Technology Warangal

Telangana, India - 506004

January-2018

Dedicated

To

My Family,

Teachers & Friends

Approval Sheet

This thesis entitled **Performance Analysis of GFDM for 5^{th} Generation Cellular Communication** by **Shravan Kumar Bandari** is approved for the degree of **Doctor of Philosophy**.

Examiner(s)

Research Supervisor

Dr. V. Venkata Mani
Department of ECE
NIT Warangal, India-506004

Chairman & Head

Prof. N. Bheema Rao
Department of ECE
NIT Warangal, India-506004

Place:

Date:

Declaration

This is to certify that the work presented in this thesis entitled **Performance Analysis of GFDM for 5^{th} Generation Cellular Communication** is a bonafied work done by me under the supervision of **Dr. V. Venkata Mani** and was not submitted elsewhere for the award of any degree.

I declare that this written submission represents my own ideas and even considered others ideas which are adequately cited and further referenced the original sources. I understand that any violation of the above will cause disciplinary action by the institute and can also evoke panel action from the sources or from whom proper permission has not been taken when needed. I also declare that I have adhered to all principles of academic honesty and integrity and have not misrepresented or fabricated or falsified any idea or data or fact or source in my submission.

Place:

Date:

Shravan Kumar Bandari
Research Scholar
Roll No.: 701356

NATIONAL INSTITUTE OF TECHNOLOGY

WARANGAL, INDIA-506004

Department of Electronics & Communication Engineering

CERTIFICATE

This is to certify that the thesis work entitled is a bonafide record of work carried out by **Shravan Kumar Bandari** submitted to the faculty of **Electronics & Communication Engineering** department, in partial fulfilment of the requirements for the award of the degree of **Doctor of Philosophy** in **Electronics and Communication Engineering, National Institute of Technology Warangal, India-506004**. The contributions embodied in this thesis have not been submitted to any other university or institute for the award of any degree.

Dr. V. Venkata Mani
Research Supervisor
Associate Professor
Department of ECE
NIT Warangal,
India-506004.

Place:
Date:

Acknowledgements

First and foremost, I want to thank my research supervisor, Dr. V. Venkata Mani for her continuous guidance, encouragement and constant support throughout my research work. I feel very happy, privilege and pleased to be work with her, who is having lot of knowledge, energy, passion and potential in the area of wireless communication, which helped me to develop fundamental concepts on multicarrier techniques. She is the one whom I look up to as a role model, for inspiration, admiration and seek suggestions at various stages of this duration, at both technical and personal level. She always boosts my confidence, extends my wings in understanding the concepts, foresees my capabilities, spends countless hours and adds every little information to extend my boundary limits. I couldn't imagine a better supervisor than her to complete successfully my PhD work.

My sincere thanks to chairman of the Doctoral Scrutiny Committee (DSC) and Head of the department Prof. N. Bheema Rao for his invaluable advices, motivation and insightful comments at various stages of this work. I would also like to thank the DSC members, Prof. M. Sydulu (Department of Electronics & Electrical Engineering) and Prof. L. Anjaneyulu (Department of Electronics & Communication Engineering) who has always driven me with there constructive suggestions, fruitful discussions and thought provoking words through out my doctoral studies. I extend my thanks to all the faculty members of the Department of ECE and non-teaching staff for their support.

I want to thank Erasmus Mundus - Euphrates programme committee members for selecting and granting me the scholarship to pursue part of my PhD work at TEI of Western Greece, Patras, Greece. My special thanks to Prof. A. Drosopoulos, Electrical Engineering, TEI of Western Greece, Euphrates mentor, for his unparalleled technical assistance, carefully editing the drafts during our collaborative work, crucial discussions, generosity and also making sure that I had a pleasant stay during my visit. It was a nice

working and learning experience with him. I also want to extend my thanks Andreas Theocharis, Teodor Todorov, Diamado Papageorgopoulou, Aashirwad Mahajan, Nupur Kulkarni and Mukesh Kumar, for having fun of cultural discussions and who's company makes me comfortable during my stay in Greece. My sincere thanks to Dr. Sivaprasad Nandyala for being a constant motivator and well wisher. I take this opportunity to thank few people, D. Pavan, Dr. Sulakshana Chilukuri, Dr. Sunny Dayal, N. Suman and other co-scholars of National Institute of Technology Warangal, for supporting me always.

I must thank few of my friends who are always hold a position in my heart. In particular, M. Ranjith Kumar, Ellison Mathe and Kiran Dasari for being with me, sharing personalities, caring during hard times and cherishing moments. I am lucky to have these idiots around me. I have been extremely happy to have some of the incredible people in Wireless Communication Research Laboratory (WCRL), Dr. D. Santhosh Kumar, Dr. Sai Krishna Kondoju, Valluri Sivaprasad, Suseela Vappangi and Kishore Vejandla, whose friendship is truly valuable, always having a healthy technical debates and having enjoyable non-technical aspects as a refreshment. My deep thanks to all the teachers having there blessings and school friends who are constantly in touch with me, wishes me to achieve great heights, giving financial help and supporting all events in my life. I also want to acknowledge anonymous reviewers for taking there valuable time to evaluate this thesis and suggesting improvements.

Whatever I accomplish its only because of my parents everlasting love, blessings, support and care. A simple 'thank you' is not just good enough to show my immense love, gratitude towards them and no words to express my gratefulness to them, I wish them a good healthy life ahead. I want to thank my grandfather Kanakaiah, grandmother Bharatha, sister Sravanthi, brother Praveen, brother-in-law Ganesh, nephew Akhil, niece Harika and other family members for there unwavering support throughout my education, endless love, understanding my goals and for being my side throughout my ups and downs, which kept me to move forward. Further, I want to express my love to my wife Mamatha for her understanding attitude, trust, taking good care of me, having great joy and truly the biggest asset for my life. Finally, thanks to God for giving me an opportunity to meet all this wonderful people and giving me this life with warm memories.

Shravan Kumar Bandari

Abstract

Over a last few decades, there is an enormous increasing interest in the field of wireless communication with continuous emerging demand for new services and applications in day-to-day daily life. Next generation wireless networks should have the capability to connect anything, anytime, anywhere and anypath with several key factors. This includes high data rates ($\geq 10Gbps$), high connection density ($\geq$ one million (1M) connections per km^2), massive security and safety and ultra low latency ($\leq 1ms$). Foreseeing the prerequisites of the future applications/services like Tactile Internet (TI), massive machine type communication (MTC), Internet of Things (IoT) and smart cities, high investments are made for developing the next generation (5G) physical layer multicarrier waveform. This dissertation will focus on several aspects of such a multicarrier scheme which serves the future human needs. Although there are many issues that can be addressed in the context of 5G, it is vital to choose a more reliable modulation scheme. One such multicarrier waveform is Generalized Frequency Division Multiplexing (GFDM) which serves the future wireless goals. Due to the impairments caused by multipath reflections, terrain conditions, scattering from different obstacles and diffraction, the signal that has been transmitted may gets attenuated along with multiple copies of the transmitted signal being received at different time intervals. Hence it is important to study the channel fading effects on the overall system performance. In this thesis we first express the signal processing steps of this pulse shaped flexible GFDM waveform along with performance analysis under various fading channels. Accordingly, the performance of the developed system model is evaluated by deriving analytical expressions for probability of error over different fading environments like Nakagami-m, Rician- K, Nakagami-q (Hoyt), Weibull-v channels and Log-Normal shadowing is included. The effect of each fading parameter (m, K, q, v), filter roll-off factor (α) and modulation order (μ) are examined. Due to inherent

non-orthogonal nature of GFDM, there is a considerable degradation in the system performance. Consequently, investigations are carried to improve the orthogonality of the conventional GFDM system by proposing pulse shaping filter like discrete prolate spheroidal sequences (DPSSs) also known as multi-tapers. In doing so, an additional benefit of lower out of band radiation (OOB) is also achieved. Furthermore, for the proposed system, symbol error rate (SER) is computed over both additive white Gaussian noise (AWGN) and Rayleigh channels. In spite of significant prevalence, the high peak-to-average power ratio (PAPR) which stems out from the superposition of huge number of subcarriers is inevitable in GFDM. Hence, investigations are carried out to reduce the amount of PAPR by incorporating several PAPR reduction schemes like Partial Transmit Sequence (PTS), Selected Mapping (SLM) and Zadoff-Chu sequences highlighting the spectral properties as well as emphasizing the complexity analysis. In addition, we propose a hybrid Walsh-Hadamard precoding with both SLM and PTS PAPR reduction techniques to further reduce the PAPR level at the transmitter side. The Walsh-Hadamard kernel which is a square wave with values $\{\pm 1\}$ helps to reduce the PAPR without introducing distortion, compared to clipping based methods. Using these proposed schemes the results show a superior PAPR reduction improvement when compared to the conventional SLM and PTS techniques. Further improvement in Peak-to-Average-Power Ratio (PAPR) reduction can be done by replacing conventional Fourier transform used in traditional GFDM system by wavelet transforms, which is one of the key contribution of this work. To further improve the SER performance some modifications have been proposed. Of them primarily, exploiting the near orthogonality nature of offset quadrature amplitude multiplexing (OQAM), an improvement in both spectral efficiency and bit error rate performance is obtained upon comparison with the traditional GFDM system. Later, spatial diversity at the transmitter side is proposed under Rayleigh fading channel with the help of derived analytical expressions. At the same time different channel estimation techniques have been discussed using pilot symbols as a reference signal and validated results with the support of the mathematical expressions derived for the channel estimation methods that has been investigated. Lastly, convolution codes are used to decrease the effect of environmental interferences for ensuring a reliable communication. Eventually, the aforementioned modifications enhances the performance of conventional GFDM system.

Contents

List of Figures

List of Tables

List of Abbreviations

AWGN Additive White Gaussian Noise

AMPS Advanced Mobile Phone System

AM Amplitude Modulation

AD Anno Domini

ARPANET Advanced Research Projects Agency Network

BLT Balian's Low Theorem

BC Before Christ

BFDM Bi-orthogonal frequency division multiplexing

BER Bit Error Rate

bps bits per second

CID Caller Identification

CA Carrier Aggregation

CFO Carrier Frequency Offset

CE Channel Estimation

CIR Channel Impulse Response

CSI Channel State Information

CRS Cell-Specific Reference Signals

CDMA Code Division Multiple Access

CMGFDM Coded MGFDM

COFDM Coded OFDM

CCDF Complementary Cumulative Distribution Function

CoMP Coordinated Multi Point

CP Cyclic Prefix

CS Cyclic Suffix

CP-OFDM Cyclic Prefix Orthogonal Frequency Division Multiplexing

D2D Device-to-Device

DAB Digital Audio Broadcasting

DSP Digital Signal Processing

DVB Digital Video Broadcasting

DVB-T DVB-Terrestrial

DFT Discrete Fourier Transform

DGT Discrete Gabor Transform

DPSS Discrete Prolate Spheroidal Sequence

DSL Digital Subscriber Line

ED Energy Detection

EDGE Enhanced Data rates for GSM Evolution

ETRI Electronics and Telecommunications Research Institute

EM Electro-Magnetic

EMPhAtiC Enhanced Multicarrier Technology for Professional Ad-Hoc and Cell-Based Communications

COST European Co-operation in the field of Scientific and Technical research

ETSI European Telecommunications Standards Institute

eNB Evolved NodeB

EPA Extended Pedestrain A

EVA Extended Vehicular A

FEC Forward Error Correction

FFT Fast Fourier Transform

FBMC Filter Bank Multi-Carrier

FP7 Framework Program 7

FDD Frequency Division Duplexing

FDE Frequency Division Equalization

FDM Frequency Division Multiplexing

FDMA Frequency Division Multiple Access

FM Frequency Modulation

FSK Frequency Shift Keying

GPRS General Packet Radio Service

GFDM Generalized Frequency Division Multiplexing

Gbps Giga bps

GHz Giga Hertz

GK GIGA KOREA

GSM Global System for Mobile Communications

HD High Definition

HPF High Pass Filter

HSPA High Speed Packet Access

HSPA+ Evolved High Speed Packet Access

HSDPA High Speed Down-link Packet Access

ICI Inter Carrier Interference

IDFT Inverse Discrete Fourier Transform

IDWT Inverse Discrete Wavelet Transform

IEEE Institute of Electrical and Electronics Engineers

IoT Internet of Things

IP Internet Protocol

IMT International Mobile Telecommunications

ITU International Telecommunication Union

ISI Inter Symbol Interference

IFFT Inverse Fast Fourier Transform

Kbps Kilo bits per second

KHz Kilo Hertz

km kilo meters

LS Least Squares

LOS Line of Sight

LMMSE Linear MMSE

LTE Long term Evolution

LDPC Low-Density Parity-Check

LPF Low-Pass Filter

M2M Machine-to-Machine

MTC Machine Type Communication

MF Matched Filter

MSE Mean Square Error

MAC Media Access Control

Mbps Mega bits per second

MHz Mega Hertz

MMSE Minimum Mean Square Error

mmWave Millimeter Wave

ms milli second

METIS Mobile and wireless communications Enablers for Twenty-twenty (2020) Information Society

MGF Moment Generating Function

MC Multicarrier

MMS Multimedia Messaging Service

MIMO Multiple Input Multiple Output

MGFDM Multi-taper Generalized Frequency Division Multiplexing

NYUW New York University Wireless

NEF Noise Enhancement Factor

NOMA Non Orthogonal Multiple Access

NMT Nordic Mobile Telephone

NTT Nippon Telephone and Telegraph

OQAM Offset Quadrature Amplitude Modulation

OFDM Orthogonal Frequency Division Multiplexing

OFDMA Orthogonal Frequency Division Multiple Access

OSTBC Orthogonal Space Time Block Coded

OOB Out Of Band

PAPR Peak-to-Average-Power Ratio

PTS Partial Transmit Sequence

PSK Phase Shift Keying

PRBs Physical Resource Blocks

PLC Power-Line Communication

PSD Power Spectral Density

PSS Primary Synchronization Signal

PDF Probability Density Function

PSTN Public Switched Telephone Network

PCM Pulse Code Modulation

QAM Quadrature Amplitude Modulation

QPSK Quadrature Phase Shift Keying

QoS Quality of Service

RAN Radio Access Network

RC Raised Cosine

RN Relay Nodes

RRC Root Raised Cosine

SSS Secondary Synchronization Signal

SLM Selected Mapping

SMS Short Message Service

SNR Signal to Noise Ratio

SC Single Carrier

SC-FDMA Single Carrier-Frequency Division Multiple Access

SC-FDE Single Carrier-Frequency Division Equalization

SCM Single Carrier Modulation

SIR Signal-to-interference ratio

SIM Subscriber Identity Module

SIC Successive Interference Cancellation

STBC Space Time Block Code

STC Space Time Code

SUI Stanford University Interim

STO Symbol Time Offset

SER Symbol Error Rate

TI Tactile Internet

TV Television

TDD Time Division Duplexing

TDMA Time Division Multiple Access

TO Timing Offset

TACS Total Access Communications System

UHF Ultra high frequency

UK United Kingdom

UFMC Universal Filtered Multi-Carrier

VDSL Very-high-bit-rate DSL

VoIP Voice over IP

WHT Walsh Hadamard Transform

WM-GFDM Wavelet MGFDM

WCDMA Wide-band Code Division Multiple Access

WLAN Wireless Local Area Network

WRAN Wireless Regional Area Network

WiMAX Worldwide Interoperability for Microwave Access

WWWW Worldwide Wireless Web

ZCT Zad-off Chu Transform

ZF Zero Forcing

ZP Zero Padding

1G First Generation

2G Second Generation

2.5G Second and a half generation

2.75G Second and three-quarters generation

3G Third Generation

3GPP 3rd Generation Partnership Project

3.5G Three and a half generation

3.75G Three and three-quarters generation

4G Fourth Generation

5G Fifth Generation

5G IC 5G Innovation Centre

5GNOW 5th Generation Non-Orthogonal Waveforms

Chapter 1

Introduction

The fundamental theme of communication is the ability to share/transfer information. This exchange of information can be between two individuals having a face-to-face talk (oral/sign language) or a video call over a farther distance. Broadly in engineering terms, communication can be divided into two categories: Wired and Wireless. In wired communication, physical cables (*Copper, Ethernet, optical fibres*) or a guided medium (*Waveguides*) are used to transfer the data between the devices. Wireless communication or a wireless transmission refers to the method of carrying message signals without any electrical conductors or through the air/space. This information can be conveyed between the source and destination through various modes of medium, namely, *Electromagnetic waves, Radio waves or Infrared* signals. In comparison, wired communication is most stable, reliable, having high security, huge speed, less interference effects with better Quality of Service (QoS) over wireless communications. Unlike wired communications, where portability is an issue for any individual to work in a specific location, wireless transmission offers an outstanding flexibility in terms of mobility, more comfort in the deployment, change or upgrading the system. Another important parameter which is more relevant to the present-day scenario is the ability to access internet from anywhere of the globe, any time of the clock, any thing from the web.

The most exciting part in modern days communication system is the capability to receive the information at a rapid pace and with the perspective of electronic media this emanates as the interesting topic for so called *breaking news*. Most of the global activities that are taking place is just within our pocket (hand-hold devices) and this is

due to the tremendous advancements which has taken place in the wireless communication field. Now-a-days smartphones which are integral part of daily routine/body, are not only limited to calls and short message services but also includes more options like processors with high speeds, wider screens, vast storage space and variety of connectivity (*Watsapp, Hike, Skype*), giving users a whole new world of experience.

1.1 Historical Glance

This section elaborates historic review of communications including the early conventional ways of conveying information, discussing analog and digital transmission, basic fundamental blocks in a communication system and various wireless generations that came across so far.

Some of the old fashioned modes of communication used in the early 200 Before Christ (BC) were Smoked signals (brought up by Ploybius-Greece), Light signals for message (Han dynasty in Ancient China), Homing pigeons, flashing mirrors, Drums and Whistles. Interestingly the usage of light and flags remain as key features for wireless communication until the discovery of radio transmission. Related to the present day scenario, it still stays as an obliged requirement for sailors to learn semaphores (flag or arms) just in case of any failure of wireless communication link. In fact, in 1792 Anno Domini (AD) a French engineer Claude Chappe presented the first semaphore system using different arm positions and cross arm posture resulting in 196 combination codes eventually leading to the first telecommunication system. This invention was named as *Telegraphy*, derived from a Greek word meaning *'Tele - at a distance'* and *'graphy - to write'*. In 1837, Samuel Finley Breese Morse invented the first single wire electric telegraph. Later in 1864, the famous scientist James Clerk Maxwell predicts the possibility of Electro-Magnetic (EM) emission and presented the most well known mathematical proofs of *EM waves*. Maxwell manifested that the electric and magnetic fields are travelling at a speed of light through space as waves. The first voice communication over wire happened to be in 1875, after the invention of *Telephone* by the great Scottish born scientist Alexander Graham Bell at his laboratory. From 1886-88, Heinrich Rudolf Hertz experimentally proved the Maxwells's theory of electro-magnetism by transmitting EM waves through air using a

spark transmitter and a receiver comprising of loop antenna with a spark gap.

There were many parallel experiments which were conducted by many scientists from all over the world at the end of 19^{th} century for developing wireless telegraphy. In the early 1890's, a French physicist Edouard Branly exhibited a device named *coherer* inorder to detect the radio waves. Nikola Tesla, a serbian born inventor, in 1891 designed an electrical resonant transformer circuit to create a low-current, high voltage, high frequency alternating current electricity by using what he called a 'Tesla coil', which sets a basis for wireless technologies and demonstrated the wireless lighting in 1892. Motivated by his achievement in wireless power distribution, he extended his idea in developing the wireless tele-communication under the project named Wardenclyffe Tower, unfortunately aborted due to lack of funding. In 1894, Sir Oliver Joseph Lodge desired to know about the potential of employing EM waves as a communication medium. In August, the same year, Lodge used Branly's *'coherer'* as a detector in demonstrating an experiment, in transmitting the Morse code signal using radio waves covering the distance up to 55 meters.

Jagadish Chandra Bose, one of the famous physicist from India, in November 1894 exhibited to public of Calcutta, by transmitting and receiving radio waves without using any set of wires over a distance of 23 metres proving the chance of wireless communication. Unlike many other scientists, J.C. Bose was not concerned regarding patenting his work and hence did not succeed in commercializing his accomplishment properly. Inspite, in recognition to his pioneer work, Institute of Electrical and Electronics Engineers (IEEE) honored him as one among the *'fathers'* in the field of radio science. Another unnoticed physicists, Alexander Stepanovich Popov, from Russia, in early 1895 proposed a modified and better version of coherer detector designed by Oliver Lodge. In 1895, on May 7, Popov demonstrated his experiments to the general public about the wireless transmission of signal through air using Hertzian waves (radio waves) and published his findings in the same year later on in December 15. On this occasion every year May 7 will be celebrated as "Radio Day". Similar to J.C. Bose, Popov didn't realize in applying for patent for his invention, but according to Russians, Popov is considered as the one who invented radio.

Upon inspired by the works carried out by Hertz and Tesla, in 1895, a well renowned physicists Guglielmo Marconi from Italy, suggested the most effective way of receiving

wireless data for communication purpose over a distance of 1.75 miles using Morse code, disproving to many inventors that earths curvature nature is not affecting the wireless transmission. However, innumerable disputes raised over this revolutionary invention of wireless telegraphy. Some of the scientists argued that the Olivers talk in 1895 is basically a physics experiment without showing the telegraphic signalling. However, it was Marconi who is known to be the inventor of radio and in 1909 credited with a Noble Prize for his invaluable contributions towards the growth in the wireless telegraphy.

After the catastrophic disaster of *Titanic* in 1912, the newly invented radio communication took its pace in the development and played a crucial role in world war I for naval and air based operations. In 1918, Edwin Howard Armstrong developed a superheterodyne receiver, which is still a backbone for the modern day radio receivers. Harry Nyquist a Swedish born American, in 1928, formulated the criteria for receiving the transmitted signals without any distortion under random channel conditions. Later on, after the advent of digital era, most of the Nyquist's studies exploited to the digital transmission.

A British engineer named Alec Reeves invented a scheme for digitally encoded voice communication using *Pulse Code Modulation (PCM)* in 1937 and this scheme progressed in world war II for data encryption of the speech signals. Nevertheless the commercial success of PCM had taken place only after the invention of transistor in 1947, reducing the cost for high scale integrated circuits. One of the major breakthrough happened to be in the year 1946 where the interconnection between the mobile user and the Public Switched Telephone Network (PSTN) was established for the first time. A well renowned pioneer in the filed of information theory, Claude Shannon, also known as *"Father of information theory"*, in 1948 published a landmark article *A Mathematical theory of communication* setting the foundation for digitization and cryptography.

Immediately after the invention of transistor in 1947, there is a proliferation in the digital computers with the advancements in the microprocessors and hardware implementation using digital signal processing chips from late 1950s to late 1970s. In 1969, *'Internet'* concept was introduced to the general public by sending out a message over Advanced Research Projects Agency Network (ARPANET). All the organizations of military, academic and government sectors have adopted computers to their working style and have changed the business standards by defining a new set of jobs for data entry.

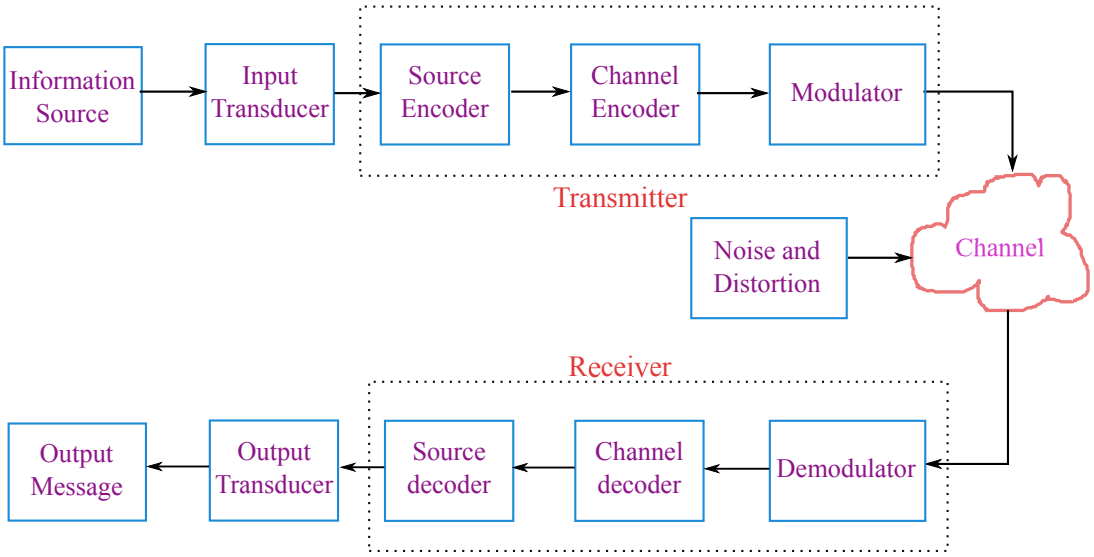

Figure 1.1: Basic elements of a communication system

One of the major invention which paved the path for rapid development of various cellular generations is *microprocessor* in 1971. This powerful discovery, can be embedded in a simple radio unit to carry out various signal processing power based operations.

1.1.1 Brief overview to communication systems

Before going into further details about various generations of cellular communication, we will first introduce the basic elements of a communication system, as shown in Figure 1.1 [1]. The first component of the communication system is the information source block, which generates the message signals such as audio, data, speech or a picture.

The ***input transducer*** is used to convert the non-electrical form of data into a baseband signal. For an efficient mode of transmission, the transmitter block is employed to modify the baseband signal. The transmitter block comprises of several subsystems such as source encoder, channel encoder and a modulator. ***Source Encoder*** in signal processing denotes representation or encoding of information signal with a fewer number of bits, in the form of binary digits (0's or 1's) for an efficient transmission. In order to facilitate resistance to the adverse channel effects, some redundant bits are added in the ***channel encoder*** block for a reliable communication establishment between the source and destination, to avoid vulnerable error rates. This controlled manner of redundancy will be utilized at the receiver side to encounter the interference which might arise during

the signal transmission through the channel. Thus the overall fidelity of the signal obtained at the receiver can be improved. The important functionality associated with the ***Modulator*** is to convert the signal in an appropriate manner for transmission through the ***channel***. The channel behaves like a filter which will attenuate or corrupt the original transmitted signal. Along with the effects of the channel, the signal is distorted (*linear, non-linear*) by random and unwanted signals known as *'Noise'*, which can be both ingress and egress.

The received waveform at the receiver terminal is first fed to the ***demodulation*** block, for estimating the bits that needs to be send to the channel decoder. The demodulator involves several signal processing steps such as equalization algorithms, synchronization of phase and magnitude, channel estimation methods to combat the impairments added by the channel effects. The purpose of the ***channel decoder*** is meant for a faithful reconstruction of the original information sequence and for correcting the errors received from the demodulator block. This can be done by exploiting the knowledge about the redundant bits which is introduced at the channel encoder. The obtained information sequence from the channel decoder is passed through the ***source decoder*** to construct back the approximate original base band signal. The amount of approximation depends on the source encoding and decoding techniques that are used at both transmitter and receiver respectively. The final step required to retrieve the source information is the ***output transducer***. The function of this block is to convert the electrical form of signal to non-electrical and thus the output message can be collected at the destination.

1.1.2 1G to 4G

In this section we will have a concise discussion on evolution of wireless cellular generations with their pros and cons, significance and features. We have witnessed and experienced a phenomenal development in the mobile communications over a period of past few decades. To start with, the 1G wireless telephone has emerged out in 1980s and involves analog signal processing by utilizing Frequency Division Multiple Access (FDMA) technology, controlling signals using Frequency Shift Keying (FSK), supporting basic voice communication covering a distance of up to 40km. The specifications used by different systems of 1G are tabulated in Table 1.1. However, 1G ended up with certain

System	Channel spacing (KHz)	Modulation, Frequency deviation (KHz)	Controlling Signalling Frequency deviation (KHz)	Data Rate (Kbps)
NTT	25 KHz	FM, ±5KHz	FSK,±8KHz	0.3
NMT	25 KHz	FM, ±5KHz	FSK,±3.5KHz	1.2
AMPS	30 KHz	FM, ±12KHz	FSK,±8KHz	10
TACS	25 KHz	FM, ±12KHz	FSK,±6.4KHz	8
C-450	20 KHz	FM, ±4KHz	FSK,±2.5KHz	5.28

Table 1.1: Specifications used by different variants of 1G

limitations like limited capacity, high interferences, poor security, large handset size and limited battery backup. Later on, immense steps were taken to implement wireless data transmission in the form of text messages and images in a reliable and economical manner. In 1991, the Second Generation (2G) cellular networks was commercially launched in Finland using Global System for Mobile Communications (GSM) standard with digital signalling. 2G operates at a carrier frequency range of around 900 MHz or 1800 MHz, 400 MHz or 450 MHz bands and uses Time Division Multiple Access (TDMA) to divide each operator into different time slots for communication. Another significant feature provided by GSM is Subscriber Identity Module (SIM) card, giving the user a flexibility to change over this detachable card to different handsets without losing the information and contacts [2].

GSM utilizes circuit switching routing technique for transfer of information in which the overall circuit is used for an individual user, making it inefficient when the data is carried for a smaller percentage of the total time [3, 4]. To overcome this, packet switching was introduced in Second and a half generation (2.5G) known as General Packet Radio Service (GPRS) technology in 2000. In packet switched domain approach, data is transferred from transmitter to receiver by routing each individual packet, permitting other users to use the same circuitry [5]. Immediately after the advancements in coding techniques, Enhanced Data rates for GSM Evolution (EDGE) technology has emerged out in 2003 with 8-Phase Shift Keying (PSK) encoding and used in Second and three-quarters generation (2.75G) with an agenda of increasing the capacity along with internet connection [4]. In a point, 2G and its family establishes the foundation for digital ser-

vices with crucial features like, Short Message Service (SMS), Caller Identification (CID), Multimedia Messaging Service (MMS) and call forwarding options.

2G mobile telephony after laying its initial track towards wireless internet, its successor Third Generation (3G) took its pace towards wireless *'data'* era. 3G can offer a speed of upto 3.1 Mega bits per second (Mbps) using Wide-band Code Division Multiple Access (WCDMA) technology according to International Mobile Telecommunications (IMT) standards launched by ITU [6, 7]. The frequency bands used for 3G telecommunication system world wide falls in 800 MHz, 900 MHz, 1900 MHz and 2100 MHz. Some of the key features offered by 3G are video calls, high speed internet services and multimedia services with high degree of security. Two of the improved versions of 3G are Three and a half generation (3.5G) and Three and three-quarters generation (3.75G), providing mobile broadband access to hand held devices and modems with a data rate of several 10's of Mbps. In short, 3.5G uses High Speed Down-link Packet Access (HSDPA) protocol with shared channels, adaptive modulation schemes, hybrid scheduling algorithms, thus allowing higher speeds of data rate with an improved latency [8]. Later in 2008, during the second phase of High Speed Packet Access (HSPA), Evolved High Speed Packet Access (HSPA+) was released to further increase the data rates of upto 168 Mbps for downlink and 22 Mbps for uplink by including 64-QAM scheme, beamforming (antenna array technology) and MIMO [7, 9]. Some of the drawbacks of 3G networks are consumption of high powers, high cost for spectrum license, high costly cellular infrastructure and not cost effective.

With the enormous increase in the internet users day-by-day, there is a huge demand for the continuous web connection from all over the parts of the universe. In 2008, ITU issued the requirements/capabailities of the Fourth Generation (4G) in IMT-Advanced to facilitate a secured mobile broadband solution using Internet Protocol (IP) based principle for a variety of applications such as smartphones, online gaming services, ultra mobile broadband (low latency, high bandwidth), streaming high definition videos on mobiles, IP telephony (Voice over IP (VoIP)), smooth handovers and video conferences [10]. The first 4G deployment was done in late 2009 at two of the Scandinavian countries, Sweden and Norway, using Long term Evolution (LTE) standard developed by 3rd Generation Partnership Project (3GPP). LTE supports both Time Division Duplexing (TDD) and

Frequency Division Duplexing (FDD) with adjustable carrier bandwidths varying between 1.4Mega Hertz (MHz) and 20MHz aiding to six different modes of operation (1.4, 3, 5, 10, 15 or 20MHz) with frequency bands ranging from 700MHz to 2600MHz [11]. LTE utilizes a combination of Orthogonal Frequency Division Multiple Access (OFDMA) technique (for downlink) and Single Carrier-Frequency Division Multiple Access (SC-FDMA) (for uplink), with higher modulation orders of up to 64-QAM and spatial multiplexing concepts to achieve high data rates of 75Mbps for uplink and 300Mbps for downlink [12]. With the advancements in Digital Signal Processing (DSP) techniques and introduction of novel modulation methods has paved the way for efficient utilization of available radio frequency spectrum. One of the revolutionary multi-carrier technique which enabled the concept of dividing the high baud rate signals into multiple orthogonal low baud rate signals is OFDM. With this approach a highly spectral efficient and scheduling in both frequency and time can be achieved. Two main important characteristics which attracted industries about OFDM are: firstly, the complex modulators are replaced with simple Fast Fourier Transform (FFT) operations and secondly the Frequency Division Equalization (FDE) is easy to implement thereby reducing the complexity incurred at the receiver. These advantages can be highly appreciated in MIMO environments, where inherently a high complex equalization is required at the receivers. OFDMA suffers from high PAPR forcing to use high cost power amplifiers with linear region operation which poses a problem for mobile handset devices in uplink scenario. Therefore, another multiple access scheme known as SC-FDMA is used in uplink, to eradicate high PAPR generated by OFDMA.

LTE-Advanced evolution focuses on increasing the capacity range and a cost effective way of providing higher bit rates to the end users. To achieve this LTE-Advanced approached with different techniques, *Carrier Aggregation (CA)*, *spatial multiplexing (MIMO)*, *Relay Nodes (RN)* and *Coordinated Multi Point (CoMP)* [13]. In brief, CA is an important feature developed to aggregate/combine different LTE carriers which intelligently fills the spectral gaps. This enables the network operators to provide users with higher mobile data and increase the capacity of the network. CA can be employed for both TDD and FDD modes of operation with a maximum bandwidth of 100MHz with an aggregation of five carriers, each carrier extending up to 20MHz.

One of the crucial changeover occurred with the introduction of spatial multiplexing

into LTE-Advanced standard, where independent encoded data streams are transmitted from multiple antennas, to increase the data rate transfer by exploiting the space dimension more than one time. LTE-Advanced introduced a 8×8 MIMO for uplink scenario and 4×4 MIMO for downlink scenario. The peak download rates of a typical LTE-Advanced that can achieve is 3Giga bps (Gbps) under perfect conditions with 100MHz carrier aggregated bandwidth and 500Mbps for downlink scenario.

In order to improve the coverage and capacity at the cell edges, RN scheme is used to forward the signals from remote areas to the main base station without the necessity of any wired (fibre) connection, also mitigating the effects encountered at cell edge. To ensure optimum performance of the network a viable solution of mixing small and large cell regions has come up in LTE-Advanced naming as heterogeneous network planning.

LTE Release 11 developed a new facility to enhance the capacity performance at the cell edges using CoMP (Joint transmission, Dynamic point selection). In a simple language, CoMP transmission permits to coordinate between neighbouring base stations of various cell sectors by sharing the data and Channel State Information (CSI), allowing to cooperate between base station in downlink for transmission and combinedly process the received signal in uplink [14]. One of the fascinating/exciting advantage of this complex technique is to use the destructive inter-cell interference into a constructive interference nature by selecting an appropriate combining methods.

4G system architecture is simplified by introducing the concept of Evolved NodeB (eNB) by replacing the radio network controller (RNC) and by assigning handover decisions and power management.

1.2 Motivation towards 5G

The shift in the human life paradigm demands a total new set of needs changing from human centric applications to machine-centric applications. Moreover mobile communication has become the default commodity in our daily life as of with water and electricity. First four generation of cellular communication focuses on improving human interaction in voice and data communication. The dream of machine communication

is not yet addressed because of its inability to handle secured short burst transmission which created a good motivation for Fifth Generation (5G) to include applications with Machine-to-Machine (M2M) interaction and Device-to-Device (D2D) communication.

The above discussed multicarrier techniques from 1G to 3G would utilize bank of modulators which would increase hardware complexity and design of channel equalizers for long distance communication which is a difficult task. After the advent of OFDM, a predominant technique, widely accepted in 4G uses simple FFT algorithms for its generation and created a single tap equalization scenario and adds some part of the data packet as Cyclic Prefix (CP) to combat interference resulted from frequency selective channels. This attracted all the researchers over the globe due to which all modern standards (Wireless Local Area Network (WLAN), Digital Subscriber Line (DSL)) accepted OFDM has its physical layer waveform [15]. The advantages of OFDM can be utilized at the expense of maintaining the strict orthogonality between its subcarriers resulting from the utilization of rectangular filters. These created two major problems (Ingress and Egress noises) in its design of receiver. Just for a case, the present LTE standard, is used as a reference to clearly explain these effects.

Firstly, the highest bandwidth mode (20 MHz) operated in LTE uses 2048 point Inverse Fast Fourier Transform (IFFT). According to LTE Release 10, for actual signal transmission, only 1200 subcarriers are used, due to the problem of Out Of Band (OOB) radiation [14]. The left over subcarriers will act as a barrier to compensate the OOB emission. These 1200 subcarrier are divided into 100 Physical Resource Blocks (PRBs), where each PRBs contains 12 subcarriers for imparting a dedicated communication. In lower bandwidth modes of operation (1.4 MHz, 3 MHz), due to bandwidth sharing of this 100 PRBs, ingress noise becomes a crucial hurdle to solve interference problem among users [16–18].

Secondly, for maintaining the orthogonality among subcarriers, various signals like Primary Synchronization Signal (PSS), Cell-Specific Reference Signals (CRS), Secondary Synchronization Signal (SSS) etc., can be employed for Symbol Time Offset (STO), Carrier Frequency Offset (CFO) estimation which results in high bandwidth wastage [17]. To overcome such limitation, it necessitates to employ non-orthogonal waveforms based detection schemes which relaxes the strict orthogonality.

In the perspective of Media Access Control (MAC) layer, 4G replaced code based multi-user detection with orthogonality based detection which in turn increased bandwidth efficacy [18]. This multiple access technique would give better performance only to strong users (having perfect CSI) by utilizing algorithms like water filling for capacity assignment. The future wireless systems demand better data transfer for weak users at the cell edge.

Non-orthogonality multiple schemes like Non Orthogonal Multiple Access (NOMA) offers better performance by assigning higher powers for users with highly distorted channel parameters and creates a better experience with incorporating Successive Interference Cancellation (SIC) in cooperative environment [19].

In order for a multicarrier modulation scheme to be used as a multiple access scheme it needs to be interfaced with existing multiple access techniques like TDMA, FDMA and Code Division Multiple Access (CDMA). Therefore, the well-known combination of OFDM with FDMA has given rise to OFDMA, one of the widely used multiple access technique in mobile cellular communication. In spite of rendering services to multiple roaming user equipments in both uplink and downlink scenarios, the orthogonal nature of OFDM demands for perfect synchronization at the receiver. This leads to complex receiver design. However, in OFDMA different user signals are transmitted at different frequencies. Therefore, an efficient NOMA was proposed to transmit different user signals at same frequencies and at different power levels. It offers better performance by assigning higher powers for users with highly distorted channel parameters and creates a better experience by incorporating SIC in cooperative environment [19]. In addition, NOMA can give better experience for weak users located at cell edges. So, in order to make GFDM flexible to be used as a multiple access scheme it can be combined with NOMA to render better services to end users [20].

Notably, there is an exponential increase in the wireless traffic over the past few years due to the rapid adoption of smart phones which bring the internet paradigm shift from the desktop to handhold devices. Moreover, emerging applications such as self-driving cars, real time gaming, and industrial automation control demand a low latency period of the order of less than 1ms. Even though there is no standard yet for 5G, the industrial and academic research communities are exploring a number of possible implementation

Challenge	Data Rates	Latency	Battery life	Connected Devices	Cost
Expectations	(10-100)× 4G	5 times <4G	(10-100)longer × 4G	(10-100) × 4G	5G $\ll$ 4G

Table 1.2: Expected requirements for 5G

options. With a wide range of envisioned applications like Tactile Internet (TI), M2M communication and Internet of Things (IoT), there is a high demand for one or more new multi-carrier waveform designs in order to serve the never ending wireless needs. Typical services also include virtual reality, ultra-high definition (UHD) video, smart home and internet of vehicles (IoV). Next generation wireless communication systems, 5G, are not only expected to achieve high data rates of Giga byte connectivity, they are also expected to perform well on high energy efficient networks, be reliable, exhibit low latency in applications, support high density users and use efficiently and with high capacity the available spectrum.

1.2.1 5G Requirements

The two reasons for the evolution of the future cellular communication, 5G, is to serve the unexpected traffic volumes posed by the users and the thrust for experiencing new applications. The former involves in enabling the users to experience a seamless wireless exchange of information with high data rates even in crowded areas. Cisco estimated the increase in the global mobile data traffic over the years, resulting an exponential growth [21]. Figure 1.2 depicts the per month mobile data traffic and expected to become seven times in 2021 compared to 2016. The second one involves in evolving new application areas with challenges such as: ultra-low round trip delay, high energy efficient devices, massive number of connected devices, ultra high reliability, smooth and smart handover methods in high mobility scenarios. Table 1.2 just summarizes what are the expected requirements that has to be serve by 5G in comparison to its preceder 4G. One thing that has to be remembered in commercializing any wireless communication designs is, that it's less possible to meet all the design parameters or satisfying all the requirement simultaneously. As an example, for applications of streaming High Definition (HD) video, parameters such as reliability and latency can be given less importance, whereas, in au-

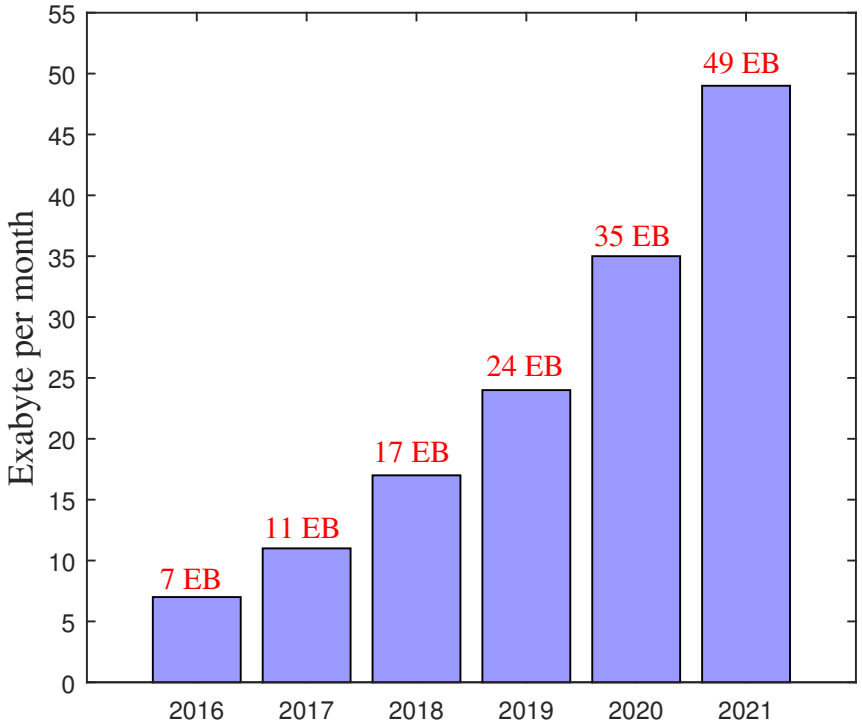

Figure 1.2: Approximate increase in data traffic.

tonomous cars these parameters cannot be ignored. Hence, depending on the application, some factors can be compromised.

High Data Rates: In the present generation (4G), users are offered with a reasonable amount of data rates in public places such as parks, railway stations or movie theatres. With the over connection of smartphone devices over the last couple of years, poses a challenge to provide high data rates in over crowded regions not only breaking the users experience but also constitutes over load on the network. The estimated target of 5G is that it should deliver a 100 times increased data rates even in high crowded and high speed moving vehicles (500 kilo meters (km) per hour) [22].

Capacity: One of the important and challenging objective is to handle the increasing traffic volume day-by-day and expected to increase 1000 times capacity per square kilometer. The current networks LTE-Advanced may not manage such a huge demand and hence 5G efforts has to be made to address this requirement.

Connectivity: 5G wireless systems has to manage a great number of connected devices

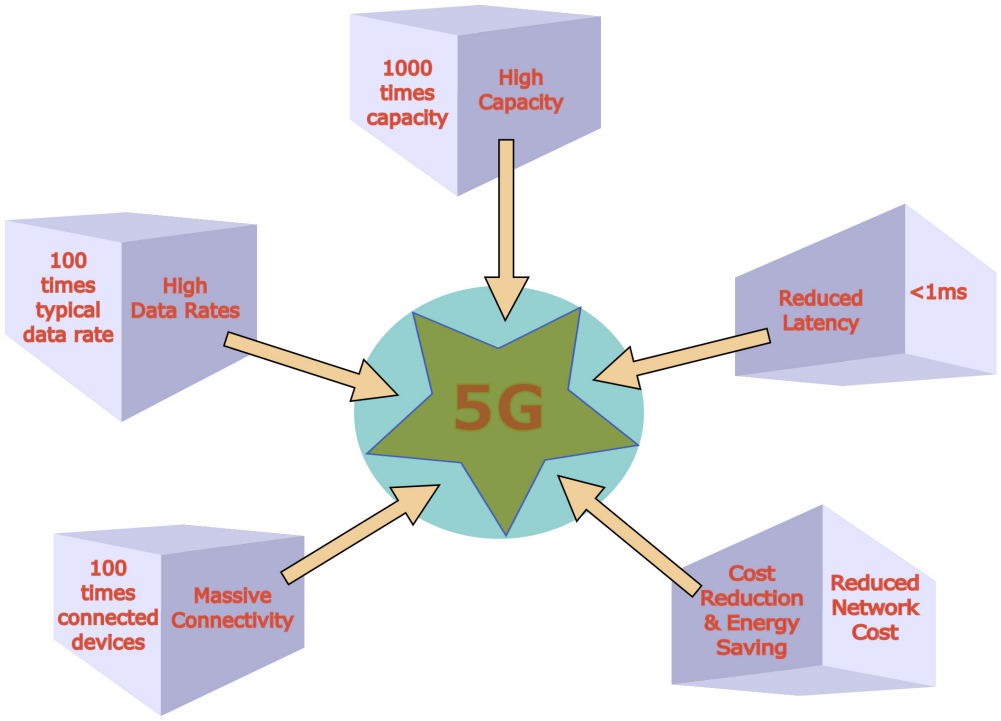

Figure 1.3: 5G Requirements

simultaneously and offer a fair amount of data rates in the premises of open gathering such as stadiums and festivals. With the deployment of multiple sensors for machine type connection, number of connecting devices at the same time for a reliable and low latencies seems to be crucial.

Low Latency: To sense a zero distance between the source and destination, round trip delay of 5G should be < 1 *millisecond*(ms) which is much lesser than the 4G systems with a latency of 5ms. Some of the enabling applications like self-driving cars which requires traffic safety, virtual reality, automated machineries/factories, healthcare, robotics, intelligent transport systems, TI and education in remote areas demands ultra-low latencies.

Cost Effective: The cost of the overall system includes network cost, reduced energy cost for devices and infrastructure at the base station has to withstand the natural calamities. 5G with such ambitious requirements should be able to include these factors in the overall system design.

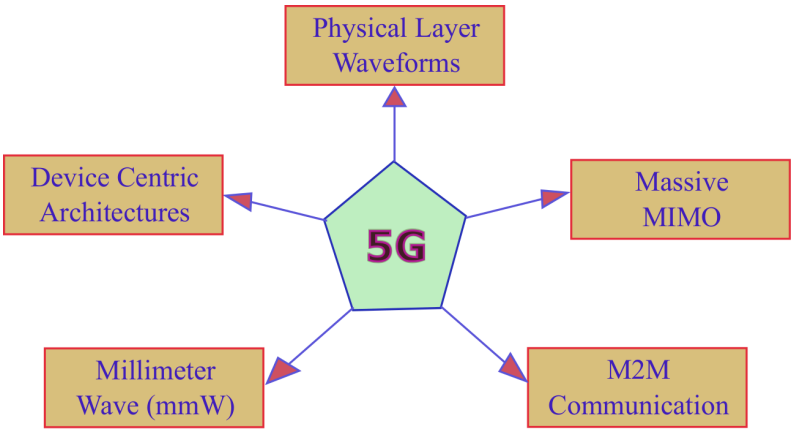

Figure 1.4: Disruptive technoligies for 5G

1.2.2 5G disruptive directions

In this section we will be having a glance at five different technologies directions leading to 5G with focus on architectural changes and evolution of new multicarrier techniques. A pictorial representation of these technologies is given in Figure 1.4.

Device centric architectures

To reduce the strain to the cellular links, a device centric cooperative systems can be utilized to diminish/cut down the overhead information from mobiles to base stations where users requesting information on same data or watching videos. This will enable the cellular networks for better routing the information with the knowledge about control signals, decreasing the effect on base stations, which is requested for data continuously [23]. These well-planned networks will ultimately results in increasing the efficient use of the spectrum, reduces delay to establish the communication link and helps in developing energy efficient base stations. However, for such a clever cellular networks, a careful management of the radio resource has to be done to achieve the gains as discussed. There are some issues that needs to be addressed inorder to develop such a networks: cooperation between the users for a reliable communication and also a tedious job to handle in a crowded environment without any performance loss, the knowledge about CSI to integrate devices, signalling overhead and the computational complexity.

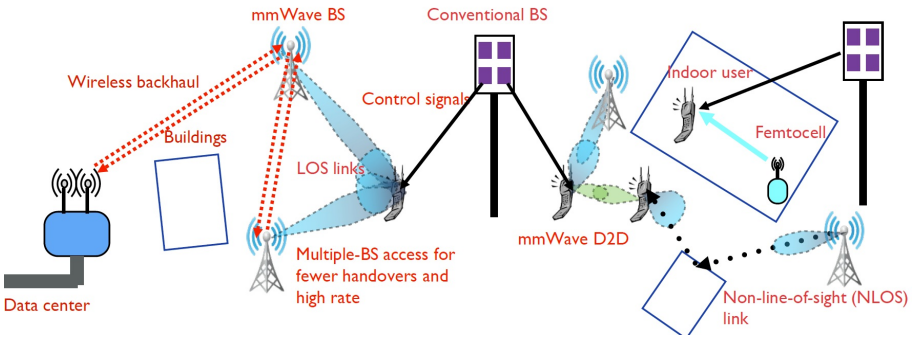

Figure 1.5: Scenarios for mmWave

Millimeter Wave (mmWave)

As spectrum is one of the scarcest and precious entity, efficient use of spectrum is one of the cornerstone in designing any communication generation. Director of New York University Wireless (NYUW), Ted Rappaport, one of the pioneer necessitated to use millimetre wave bands to accommodate more bandwidth ranging from 800 MHz to 2 Giga Hertz (GHz), foreseeing the future [24]. The frequency bands under consideration are: (28-30)GHz to support a bandwidth of 850MHz, (37-40)GHz supports a bandwidth of 3GHz and a bandwidth of 7GHz is supported in the frequency range from (64-71) GHz. One of the major challenging in mmWave frequencies is the propagation through channel with path loss models. A thorough investigations on modelling and analyzing these mmWave has been carried out in [25] and references therein. A simple model for mmWave scenarios is depicted in Figure 1.5. Blockage due to buildings, people, channel constraints and non-line of sight propagation makes vulnerable to transmit a mmWave signal from transmitter to its destination [26]. However, mmWave can offer a large data rates and seems to be potentially technology for 5G applications.

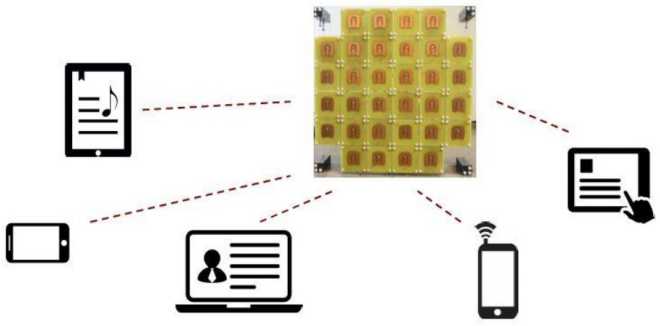

Figure 1.6: Massive MIMO spatially multiplexing several terminals

Massive MIMO

Massive MIMO or Large scale MIMO antenna systems in abstract form is to utilize an array of antennas at the base stations to simultaneously transmit information to several devices [27]. Some of the benefits that massive MIMO can offer are that it provides large throughput gains, can achieve a very good spectral efficiency by exploiting spatial multiplexing and improved energy efficiency with a simple linear processing [28]. Figure 1.6 denotes the spatially multiplexed connected devices to base station using massive MIMO. Unlike in single user MIMO, where the number of antennas are constrained in devices, massive MIMO can employ any number of antennas, allowed Channel Estimation (CE) is performed for uplink scenarios using TDD approach. In basic MIMO systems, in general CSI is crucial to estimate the pilot sequences in uplink and downlink in both TDD, FDD and the complexity proportional to number of antennas used. In particular for massive MIMO, these situation becomes even more challenging, as there is a possibility pilot contamination and these becomes critical in estimating the channel response [28]. Interestingly massive MIMO appears to be attractive at mmWave bands and in combination can lead to a fascinating enabling technology [29].

M2M Communication

Machine-to-machine communication or Machine Type Communication (MTC) is often referred to as exchanging information between machines or at least to one end is a machine for establishing communication link without or minimum intervention of human acts in the process. Figure 1.7 depicts the basic M2M architecture proposed by European Telecommunications Standards Institute (ETSI) [30]. The central theme of M2M devices is to fetch information which includes sensors or meters to record temperature, vehicle speed and its consumption of fuel, autonomous machines, and route this data to nearest hubs employed as roadside units [31]. Some of the applications spanned by M2M includes security (surveillance), tracking (navigation, traffic management), indoor automation and manufacturing with key objectives like low latency or end-to-end delay, *'better'* security, assure availability and for wide coverage, battery life with greater operating time, enhanced throughput and reliable connection to any number of machines in the cell area.

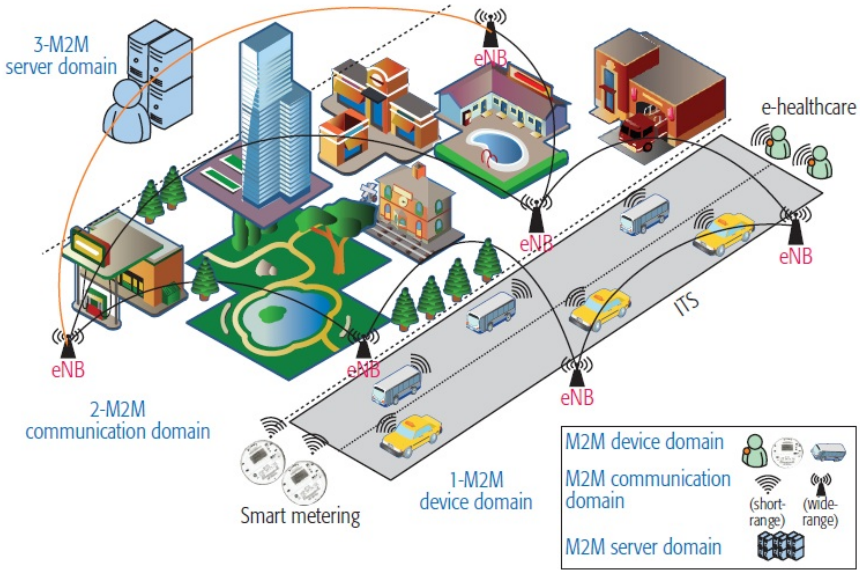

Figure 1.7: M2M communications.

The success/growth of M2M holds within the key challenge of understanding the business models between the vendors and telecom operators, and a good revenue market model for mobile network providers. Apart form these challenges, the issues concerning are identification of these connected devices and appropriate security systems to resist cyber attacks and unauthorized monitoring [30–32].

Physical Layer Waveforms

This section gives the potential multicarrier candidates for 5G. Filter Bank Multi-Carrier (FBMC), a subclass of multi-carrier systems, is a generalization of OFDM where the subcarriers are pulse shaped individually [33]. Typically, the filters are shifted versions of a prototype filter that satisfies the Nyquist criterion and an OQAM implementation can relax OFDM's "all carrier orthogonality" to "neighbour carrier orthogonality" [33,34]. FBMC offers lower OOB than OFDM, which enables us to reduce the guard band, thus increasing the spectral efficiency if the number of transmit symbols are large. Another advantage FBMC offers over OFDM is its low sensitivity to time and frequency offsets which can reduce the synchronization requirements due to the pulse shaping design [34]. See [35, 36] where FBMC is also proposed as one of the 5G candidates. However, FBMC utilizes long filter lengths which sets as a disadvantage for short uplink burst communi-

cations, an important aspect in 5G scenarios. Some additional effort is also required to incorporate MIMO architectures in a diversity context [33, 37].

Other contenders proposed for 5G are Universal Filtered Multi-Carrier (UFMC) [38, 39] and Bi-orthogonal frequency division multiplexing (BFDM) [40]. UFMC, which has a more generalized filtering approach, filtering is applied to a group at the subcarrier level [38]. This block-wise filtering results in filters which are spectrally broader in pass-band and hence shorter in time. This supports short bursts transmissions which is one of the drawbacks in FBMC. The main advantage over OFDM is in terms of improved spectral efficiency and the technique is also robust to time and frequency offsets [41]. Compared to FBMC, UFMC has a lower latency which is due to the shorter filter length and improved support for MTC [42]. Nevertheless, there is a possibility of greater sensitivity to small time misalignments than in CP-OFDM. In BFDM, the transmit and receive pulses are pairwise bi-orthogonal (see [40] and references therein). These well localized bi-orthogonal pulse shapes at transmitter and receiver make the system robust against doppler and multipath effects. BFDM employs OQAM with localized pulses both in frequency and time domains. However, for M2M applications in order to achieve low latency, BFDM needs to handle long pulse tails that reduce the efficiency for short burst transmission. Apart from these approaches, multi-antenna technologies like beamforming and MIMO also play an important role in 5G systems. In the demand for bandwidth, certain issues to be addressed in the context of 5G are spectrum fragmentation and spectrum agility. GFDM which can be seen as a generalization of OFDM, has many attractive properties and covers CP-OFDM, Single Carrier-Frequency Division Equalization (SC-FDE) as special cases [43]. Some additional differences between GFDM and OFDM are:

- GFDM uses a total number of NM data symbols per frame using M time-slots with N subcarriers and a $g(n)$ pulse shape filter whereas in OFDM N subcarriers are transmitted in one time-slot with N subcarriers using a rectangular pulse shape filter.

- Guard band insertion. GFDM uses CP between two frames whereas OFDM uses CP between two time slots. In GFDM, interference between time slots can be taken care by the appropriate choice of pulse shape filter. This effectively reduces spectrum utilization.

We can also deal with synchronization requirements of multi user scenarios in MTC by adding a Cyclic Suffix (CS). Due to flexible block based structure, GFDM can also generate small packets which are suitable for IoT, MTC applications and hence an enthralling choice for low latency applications. In order for GFDM to evolve as a potential candidate for future wireless communications, it is necessary to combat the effects of Inter Carrier Interference (ICI) which arises due to non-orthogonal nature of subcarriers as well as designing low complex receivers is also mandatory. By taking into consideration all the aforementioned aspects, GFDM appears to be one of the most promising multicarrier modulation technique [44, 45].

1.3 Recent activities on 5G

The current shift of focus from human interactions to the human communication with 'things' has propelled many of the industries to characterize the standards for the future wireless communication. This garnered the attraction of different companies to collaborate with several institutions in order to cope up with the pre-requisites anticipated by 5G. In this regard, this section deals with a concise discussion on the projects addressing different aspects of 5G stressing on the requirements as discussed earlier.

1.3.1 Main Projects

Some of the innovative projects working towards the road map of 5G which are under lead from various parts of the world are: Mobile and wireless communications Enablers for Twenty-twenty (2020) Information Society (METIS), 5th Generation Non-Orthogonal Waveforms (5GNOW) from Europe, 5G Innovation Centre (5G IC) from United Kingdom, NYUW from America and GIGA KOREA from Korea. Starting of with couple of European Union projects which laid foundation for 5G are METIS and 5GNOW. In METIS fundamental research were conducted on spectrum usage methods, radio links, network topologies and multi-node scenarios [22, 46]. Immediately after the success of METIS project, attempts were made to develop 5G Radio Access Network (RAN) concepts, design and prepare standardisation bodies in all regions and regulatory under METIS-II project. 5GNOW actively researched non-orthogonal waveforms for 5G with ultra low

latency and high reliability using Gabor signalling. They developed a novel multicarrier technique, GFDM, which relaxes the strict orthogonality requirement that exists in OFDM [47]. This relaxation leads to more degrees of freedom in pulse shaping that can better control the impairments that appear. Some of the other European projects under Framework Program 7 (FP7) can be found at [36, 48, 49] covering various aspects of 5G. The research at NYUW is to integrate communication, computer science and medical fields. Prof. Ted Rappaport and his team conducted several experiments on mmWave path loss propagation models and have introduced efficient use of spectrum at mmWave frequency bands [50]. The work in GIGA KOREA (GK) 5G project from Korea, emphasizes on improving the reliability, hotspot protocols, high capacity and D2D communication. The goal of this project is to build a stand-alone communication system in mmWave bands and to bring its utility at 2018 winter olympics [51, 52]. In United Kingdom (UK) the vision of 5G infrastructure was shared by many leading industries and academics under the project 5G IC [53].

1.4 Scope of the research work

Both the industrial and academic sectors carry enormous research taking into consideration the fast growing trends of the market. Foreseeing the prerequisites of the future applications/services like TI, massive MTC, IoT and smart cities, high investments have been made for developing the next generation physical layer multicarrier waveform. The broad area of topic of this thesis is related to physical layer wireless communication, with special focus imparted on the performance analysis of GFDM, one of the leading and interesting pulse shaped multicarrier waveform to serve the future wireless needs/services. This topic is intended to serve the everlasting needs of the customers who are demanding continuously for high data rate applications with low latencies. The objectives of this thesis focuses on progress in conventional GFDM, making this physical layer modulation waveform more attractive candidate for future generation applications. This thesis also addresses other aspects of GFDM by proposing some improvements/modifications to the conventional GFDM system. One of the objective is to improve the orthogonality of non-orthogonal GFDM transmission. In addition, a deep study on the performance analysis

of GFDM under various fading channels is also the focus of this thesis.

1.5 Thesis Organization and Contributions

These section gives an overview on the thesis outline along with the main contributions of each individual chapter in a box.

Chapter 2: Firstly a deep literature review focusing on the carrier based system modulation schemes is discussed. Subsequently, the most dominant multicarrier technique, OFDM, is presented along with its potentiality highlighting the key features and drawbacks. In addition, critical details about the existing literature that is available explaining a glimpse about the work done so far on GFDM, the point of interest in this thesis. Furthermore, this chapter delineates the shortcomings of this new multi-carrier technique that needs to be addressed.

Chapter 3: This chapter presents the first steps of understanding GFDM under various fading channels by deriving analytical expressions and its validation through Matlab simulations. The frequency selective fading channels includes Nakagami-m, Nakagami-q, Rician-K, Weibull-v fading channels and log-normal shadowing is included. The main motive behind employing different fading channel environments is to emphasize the performance of GFDM over different fading channel environments. Taking into consideration the multipath propagation environment, where the transmitted signal undergoes several reflections, refractions and scattering. Therefore, in addition to line of sight (LOS) path there exists several non-line of sight (NLOS) paths. Moreover, in an indoor room environment, the channel coefficients can be modelled as Nakagami channel. Whereas, when strong LOS component is involved then the channel model suits Rician fading channel. Hoyt channel is used in satellite based cellular communication to characterize more severe fading conditions than those modelled by Rayleigh. While, in case of outdoor the channel environment can be modelled as Weibull. Lognormal shadowing considers a completely different scenario associated with statistics of large-scale path loss variation in slow fading channels.

✠ The research work from this thesis has contributed in deriving the analytical expressions of an GFDM system under different fading channels. Later, the effect of each fading parameter, pulse shaping roll-off factor (α), modulation order (μ) and number of subcarriers (N) is carried out. The simulation results are provided justifying the derived analytical expressions [54, 55].

Chapter 4: This chapter highlights the necessity of searching novel prototype filter using Discrete Prolate Spheroidal Sequence (DPSS) or multi-tapers as a pulse shaping filter in GFDM system for improving the orthogonality. Hence, this modified version of GFDM is named as Multi-taper Generalized Frequency Division Multiplexing (MGFDM) system. In addition, PAPR analysis for the proposed MGFDM system is carried out utilizing some of the standard PAPR reduction techniques namely, Selected Mapping (SLM), Partial Transmit Sequence (PTS) and ZCT. Also, novel hybrid PAPR techniques known as Walsh Hadamard Transform (WHT)-SLM and WHT-PTS are proposed to further reduce the PAPR level. Furthermore, improvement is done by replacing conventional Fourier transform used in traditional GFDM system by wavelet transforms and performance of the wavelet based MGFDM system is analysed in terms of PAPR, SER and power spectral density comparisons.

- For the purpose of improving the performance of GFDM system, it is desired to exploit novel pulse shapes which exhibit orthogonal functionality. In this regard, DPSS also known as multi-tapers are used as pulse shaping filters in conventional GFDM system to improve orthogonality. Furthermore, the performance of the developed system is tested over both AWGN and Rayleigh channel environment. This contribution was reported in our published work [56].

- In any multicarrier system, due to superimposition of huge number of subcarriers, high PAPR is inevitable in MGFDM system. Therefore, this necessitates to impose PAPR reduction techniques like PTS, SLM and ZCT [57]. Even though these are well established techniques, exploring their performance for the MGFDM system model is a necessary step to study the forthcoming hybrid schemes such as WHT-SLM and WHT-PTS. In order to further improve the PAPR performance, Fourier

transform is replaced with Wavelet transform. The performance of the wavelet based MGFDM system is analyzed in terms of PAPR, SER and power spectral density comparisons. This contribution was reported in our published work [58].

- ✠ In [56], we derived mathematical expressions of Multitaper GFDM system under both AWGN and Rayleigh channels.
- ✠ A wavelet based MGFDM system is proposed and a comparative analysis is provided [58].

Chapter 5: This chapter concentrates on what are the possible improvements that can be provided to make GFDM a more suitable structured multicarrier technique. For this, the first part of the chapter explains about utilizing spatial diversity concept and proposing a novel precoded OSTBC for GFDM systems. Second part of this chapter deals with the GFDM/OQAM implementation under various fading channels.

- ✠ To make GFDM more robust in nature to multipath fading effects, spatial diversity at the transmitter side is proposed under Rayleigh fading channels. We investigated a precoded OSTBC Multitaper GFDM system along with conventional GFDM. The SER performance for precoded OSTBC-(M)GFDM systems over a Rayleigh fading channel is examined and a good match between simulation results and analytical expressions is seen to exist [59].
- ✠ GFDM/OQAM performance analysis in various channels namely AWGN channel, Rayleigh fading channel, Nakagami-m, Nakagami-q, Rician-K and Weibull-v fading channels has carried out by deriving analytical expressions of the above mentioned channels [60–62].

Chapter 6: This chapter describes the channel estimation methods for MGFDM system with and without DFT and simulation results are presented using Least Squares (LS) and

Minimum Mean Square Error (MMSE) CE methods. Lastly, convolution codes are used to decrease the effect of environmental interferences and severe channel impairments for ensuring a reliable communication. Also, an analysis on different receivers namely, ZF and MF is studied and the PAPR of the system is evaluated.

- ✠ [63] focuses on estimating the channel impulse response by using a training sequence at the transmitter side. We strengthened our results by proposing analytical expression under LS estimation method for both with and without DFT based channel estimation.
- ✠ [64] presents adapting convolution codes for GFDM system which adds an advantage to the conventional GFDM system.

Chapter 7: This chapter is devoted to a detailed discussion on conclusion of the thesis and the research line in future.

Chapter 2

Review of Literature

2.1 Introduction and Motivation

This chapter gives an overview of different modes of transmission schemes including single and multi-carrier techniques. Later on more insights about OFDM discussing the advantages, standards and disadvantages of it is also provided. Finally, a complete literature on the contender of 5G, GFDM, covering different aspects and related articles will be discussed.

2.2 Single Carrier and Multi Carrier Systems

Single Carrier Modulation (SCM) can be noted as a well known way of transmitting data serially. Yet, it is an important alternative in some of the standards (Worldwide Interoperability for Microwave Access (WiMAX), 3G-LTE) due to the added advantage of having a very low PAPR when compared to multicarrier systems like OFDM. Single carrier transmission in combination with CP was first proposed by [65] in 1994 and implementation of simple FDE, also known as SC-FDE, introduced in [66]. Further, SC-FDE is robust against phase and frequency offsets when compared to OFDM [67, 68].

Over the past two decades there is an enormous development in both wireline and wireless communication applications especially with the usage of MC modulation schemes. Multicarrier modulation systems are the systems that split up a wideband signal at a high

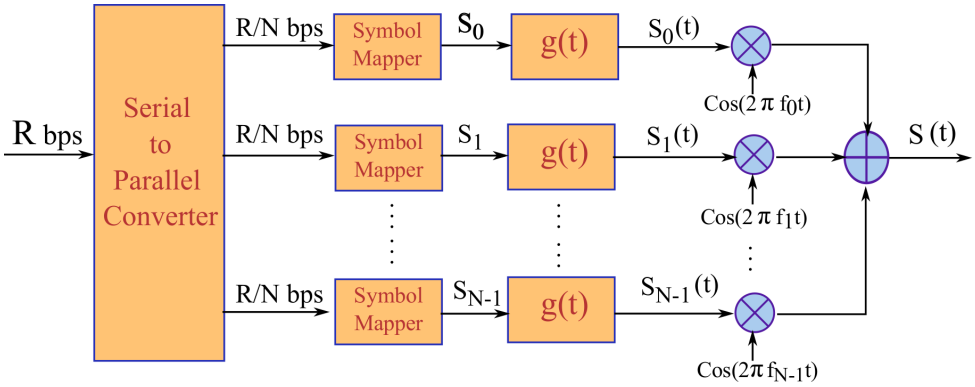

Figure 2.1: Transmitter schematic of general multi-carrier system

symbol rate into a number of lower rate signals through the use of suitable pulse-shaping filters. Each one of the lower rate signals occupies a narrower bandwidth and has its own associated carrier. A multicarrier system splits a total bandwidth into chunks of narrow sub-channels whose bandwidth is much lesser than coherence bandwidth of the channel. This allows the channel to be relatively flat fading and hence immune to Inter Symbol Interference (ISI).

A simple schematic of transmitter and receiver of a general multicarrier system is shown in Figure 2.1 and Figure 2.2. At the transmitter side, the bit stream of data rate R bits per second (bps), is broken into parallel subbands of data rate R/N bps. The transmitted signal after mapping the bits to a specific symbol mapper, pulse shaping waveform and up conversion to each subcarrier frequency is given by,

$$S(t) = \sum_{i=0}^{N-1} s_i g(t) cos(2\pi f_i t + \phi_i) \tag{2.1}$$

where s_i denotes the complex data symbols, ϕ_i indicates the phase offset of the i^{th} subcarrier, f_i is the central frequency of the i^{th} subcarrier, $g(t)$ pulse shaping waveform, R denotes the data rate and N denotes the total number of subcarriers.

At the receiver side, the noisy signal is passed through a Matched Filter (MF), each centred at the frequency of the subcarrier. A coherent demodulation and parallel to serial conversion process is carried out in order to achieve the transmitted bits of data. A special form of multicarrier technique where the subcarriers are orthogonal to each other by using a fourier representation of the symbols is known as OFDM. We will discuss

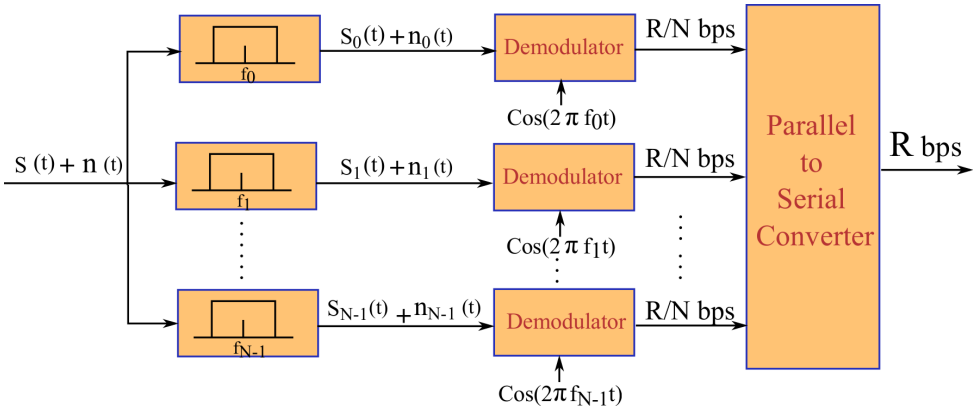

Figure 2.2: Receiver schematic of general multi-carrier system

about this revolutionized MC method which has definitely marked its position in various communication standards in the following section.

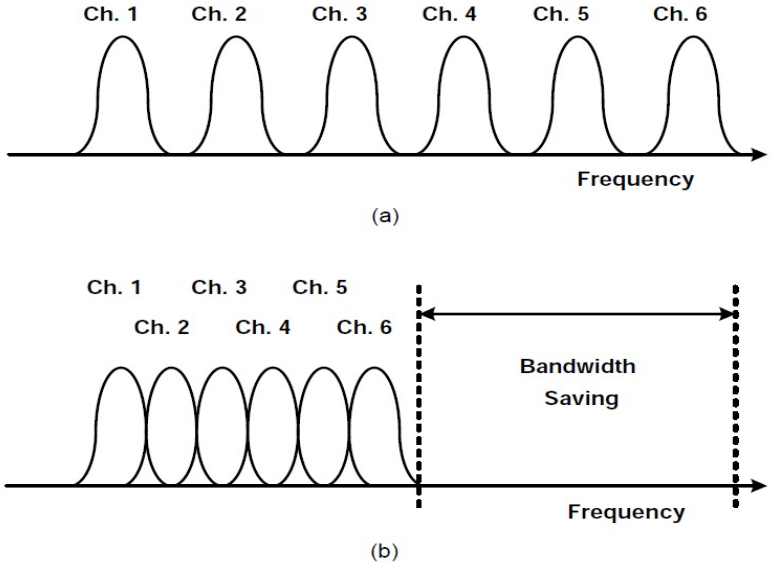

Figure 2.3: (a) General MC technique without overlapping. (b) OFDM technique.

2.3 OFDM

The basic idea behind the multicarrier technique was to divide the total available bandwidth into a number of subbands, allowing the handling of channel effects in an efficient manner. Each generation of mobile communication systems offered many services after which these systems are classified. There are enormous capability advancements in the mobile communications from 1G to the current 4G. A widely adopted air interface

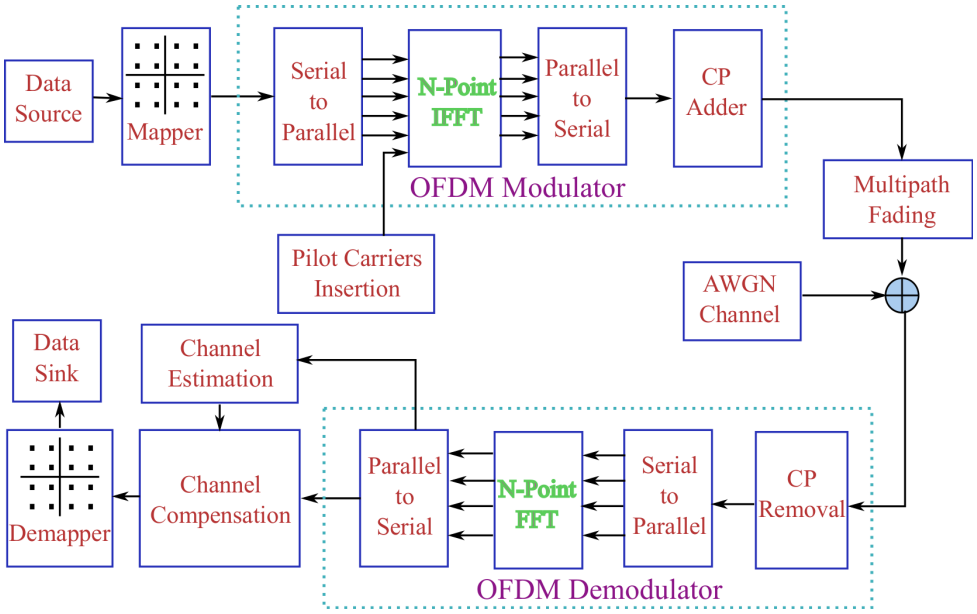

Figure 2.4: Basic block diagram of OFDM

MC technique in many present wireless standards is OFDM, as it offers many advantages [15]. Some of the earlier works on OFDM can be found in [69–71]. The practical way of implementing this MC technique was well discussed in [66, 72–74]. A comparative studies on OFDM technique to that of the single carrier schemes are discussed in [68, 75] and references therein. OFDM utilizes the scarce spectrum resource more efficiently by allowing to overlap the frequency spectrum of every subcarrier of the transmitted signal (see Figure 2.3) [15].

Figure 2.4 is the basic transceiver structure of OFDM. The input bit stream generated from the data source are first mapped to the complex symbols (M-ary PSK, M-ary QAM) and passed through OFDM modulator. In OFDM modulator, first the complex symbols are converted to parallel stream of lower rate, followed by an $N-$point IFFT and finally converted back to serially inorder to generate a basic OFDM waveform. Some of the additional signal processing steps can be involved to combat severe channel fading effects. The foremost is to append CP to serve as a guard interval to diminish the effect of ISI which arrives due to the multipath effect. Next is to insert some pilot carrier information at the transmitter side, for effective channel compensation at the receiver side. Mathematical representation of the transmitted OFDM signal is given by [15],

$$x(n) = \frac{1}{\sqrt{N}} \sum_{k=0}^{N-1} X(k) e^{\frac{j2\pi kn}{N}} \qquad 0 \leq n \leq N-1 \tag{2.2}$$

where N denotes the number of subcarriers, $X(k)$ is the complex data symbol generated from the mapper unit.

Prior to serial to parallel conversion, at the receiver side, the CP is removed. The OFDM demodulator consists of an $N-$point FFT operation to obtain the data that is transmitted on each individual subcarrier. The received parallel $N-$point FFT data is converted to serial for channel estimation block. Finally, a demapper unit is used to decode the originally transmitted binary data.

2.3.1 Summarizing pros of OFDM

1. Eliminates complex oscillators with simple FFT blocks to implement modulation and demodulation.
2. Immune to frequency selective channels.
3. Good protection to interferences using guard intervals.
4. Simpler channel equalization techniques.
5. Efficient use of spectrum.
6. Allows pilot subcarriers for channel estimation
7. Efficient Broadcasting: Multiple base stations can synchronize to combine their transmitted signals enabling higher broadcast data rates.

2.3.2 Standards adopting OFDM technique

An elegant way of executing FFT blocks in order to avoid bank of complex oscillators, a simple equalization process in comparison to single carrier transmission and robustness against frequency selective multipath fading channels are the main properties of OFDM that make it the method of choice in current standards WLAN (IEEE 802.11a/g), Wireless Regional Area Network (WRAN) (IEEE 802.22), WiMAX (IEEE

802.16), LTE, Very-high-bit-rate DSL (VDSL), Power-Line Communication (PLC), Digital Audio Broadcasting (DAB) and DVB-Terrestrial (DVB-T) [76]. More insights about OFDM transceiver design and covering different aspects is readily available in the literature and can be found in [66, 70, 73, 77].

2.3.3 Cons of OFDM

Despite the many advantages offered by OFDM, its capabilities fall short of serving the envisioned future requirements due to some of its defects.

1. PAPR which is caused by the random sum of several in phase subcarriers [78–80],
2. OOB due to the rectangular pulse shape of the filter used in the transmitter [81],
3. ICI which arises from channel frequency dispersion [82],
4. Sensitive to phase noise and frequency offsets,
5. Inclusion of CP for combating ISI results in spectral wastage, and
6. Long round trip delays.

Moreover in any multi carrier system like OFDM, channel dispersion leads to ISI between successive symbols. These effects can be tackled by using a guard interval with length larger than the duration of the channel impulse response. The most commonly used guard interval is a CP of length N_{cp}, where the last N_{cp} samples of each OFDM symbol are added at the front end [69]. The above implementation, known as CP-OFDM, was introduced in the LTE of 3GPP. It is robust to multipath fading and because the signal processing is carried out in the frequency domain the implementation has low complexity [83]. However, due to the addition of a cyclic prefix, CP-OFDM suffers from power efficiency loss. To overcome this problem another possible guard interval solution is to add zeros, also called Zero Padding (ZP) guard interval. [84] investigates the choice of a good guard interval for these implementations. Another problem with CP-OFDM is the spectral efficiency reduction compared to the original OFDM because of CP. The overall overhead is increased and some other drawbacks are introduced like sensitivity to phase

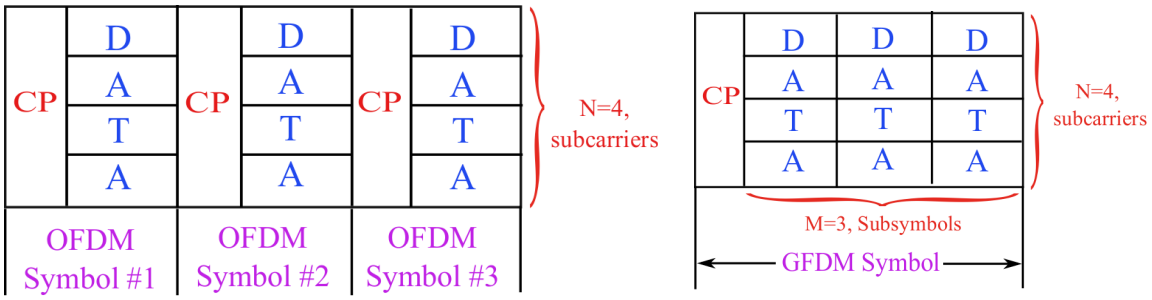

(a) Single OFDM frame consisting of 3 OFDM symbols. (b) Single GFDM frame.

Figure 2.5: Frame structure comparison of OFDM and GFDM.

noise, asynchronous signalling and long round trip delay. It should also be emphasized that TI, one of the core proposed services for 5G, demands a latency of the order of 1 ms in order to provide an acceptable QoS [85]. Many efforts have been made to address these drawbacks [86], but, it is still questionable whether OFDM or modified versions of this multicarrier technique will serve the demands of future applications. Motivated by the above facts, it is of great interest to explore other multicarrier techniques to serve next generation mobile communication systems in the context of 5G applications.

2.4 GFDM

There is a lot of exploration in the research community for the search of an alternate and flexible multicarrier waveform by addressing the shortcomings of OFDM and keeping the advantages in tact. GFDM, a non-orthogonal MC transmission, is one such substitute proposed by Fettweis et al. [43], uses prototype filter with more frequency containment for pulse shaping. Before going into further details, let us first discuss the properties/characteristics of this novel MC technique in comparison to the previously mentioned OFDM method. The pulse shaping filter in GFDM is appropriately chosen in such a manner that, it is having better decaying nature in frequency domain in contrast to OFDM which results in the larger OOB emission due to the usage of rectangular filtering [43]. As stated in the cons of OFDM, inclusion of CP for each symbol in an OFDM frame will lead to spectral inefficiency, whereas, in GFDM single CP is appended for the whole GFDM frame which consists of several symbols. In this context, GFDM reduces the CP overhead and poses to feature a better spectral efficiency and the same

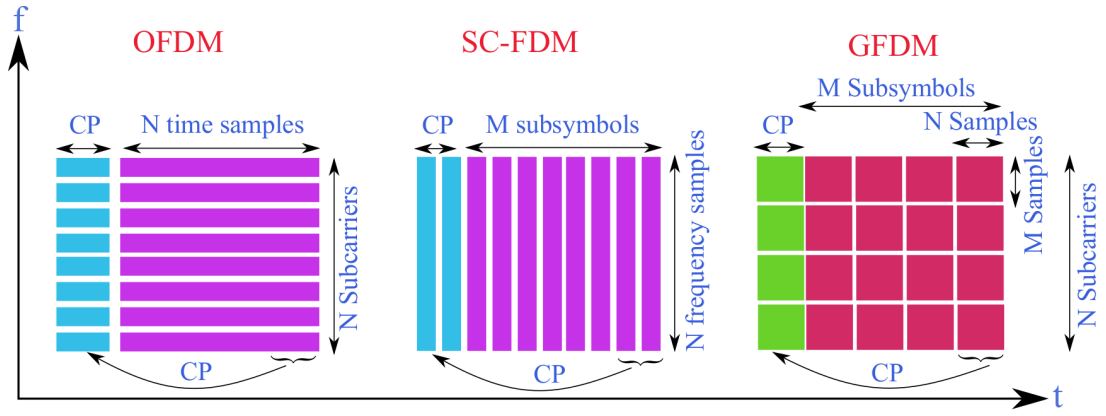

Figure 2.6: Special cases of GFDM

can be verified by using Figure 2.5. OFDM frame adds CP for each symbol consisting of N subcarriers and in GFDM one CP is included for a single frame comprising of M subsymbols.

GFDM is a special block based multicarrier technique covering both OFDM and Single Carrier (SC)-Frequency Division Multiplexing (FDM) as corner cases. As illustrated in Figure 2.6, GFDM reduces to OFDM with $M = 1$ and rectangular pulse shaping, and to SC-FDM with $N = 1$. GFDM is a block based transmission scheme, transmitting M subsymbols in every subcarrier by using circular pulse shaping theme. A complete elaboration on GFDM modulator will be discussed in the following Chapter 3.

2.4.1 Previous Work and Research Gaps

In this section we will cover some of the research articles that are studied as a part of literature review.

In 2009, Fettweis et.al. introduced GFDM concept for spectrum fragmentation, which is one of the challenge for exploiting white space spectrum in Television (TV) Ultra high frequency (UHF) bands [44]. In this paper, the properties of GFDM in comparison to OFDM is explained, in which some of them are ultra low OOB radiation due to filtering giving flexibility in choosing prototype of choice, block based structure using one CP for whole block and efficient utilization of FFT equalization. Comparisons of GFDM and OFDM based secondary system in cognitive radio was explored in [87]. The results analysis depicts that the setup using GFDM secondary system will produce less interference

to the primary system compared to the OFDM secondary system. The prototype filter used for pulse shaping the subcarriers will create a small spread in frequency of operation. Orthogonality loss between the subcarriers leads to inherent self ICI. Double sided serial interference was proposed in [88] to reduce this effect and showed significant improvement in the GFDM bit error rates. The cyclostationary detection of spectrum sensing in cognitive radio using GFDM modulation was presented in [89] and a good comparison of cyclostationary properties of OFDM is also investigated. In addition, spectrum sensing using Energy Detection (ED) is also studied. With the motive of eliminating the ISI and ICI, the authors in [90] proposed Discrete Gabor Transform (DGT) instead of the DFT as used in traditional GFDM system. Furthermore, for the purpose of reducing the complexity caused by the channel equalization, the authors proposed the frequency domain DGT for the received GFDM signal in order to enable its perfect recovery. The authors in [91] analyse the impacts of Timing Offset (TO), CFO and phase noise in OFDM and GFDM systems. Moreover, the different possible scenarios of TO is evaluated analytically and Signal-to-interference ratio (SIR) is computed for each such scenario. In addition, a novel receiver filter that is optimized to maximize SIR in the presence of CFO under AWGN channel is proposed for GFDM system. Upon comparison with OFDM, the simulated result analysis confirms the sensitivity of GFDM to CFO. In [92], authors have proposed discrete Fourier transform spreading based GFDM transmission to reduce the PAPR. Two subcarrier mapping schemes are considered, namely, localised frequency division multiple access and interleaved frequency division multiple access. The observations from [92] are that interleaved frequency division multiple access subcarrier mapping is more effective than localised frequency division multiple access. In addition, bit error rate performance is developed and supported by the analytical expressions. The analytical performance of MMSE receiver along with the proposed precoding techniques is studied in [93]. The precoding techniques proposed in [93] reduces the complexity of the MMSE receiver without compromising the error rate performance. Also, a thorough analysis on the complexity analysis of different transmitters and receivers of both precoded and uncoded GFDM are well presented. Since GFDM requires receivers with high computational complexity, authors in [94] have proposed a novel low-complexity joint MMSE receiver for GFDM by harnessing circulant properties of the matrices involved in the demodulation process.

BER of GFDM system in AWGN and Rayleigh fading channel is performed in

[95]. In this article a linear matrix model is proposed and studies are conducted using three receivers namely ZF, MMSE and MF using simulations. The SER expressions of GFDM under AWGN and Rayleigh fading channels are derived in [43]. The effect of different prototype filters namely Raised Cosine (RC), RRC, Xia and Ramp filters and its implementation aspects are also discussed. Furthermore, the benefit of using space time coded GFDM is also exploit for completeness.

The main motive behind the analysis of the system performance under various fading channel environments is to clearly highlight the impact of mobile radio environment scenarios where the channel coefficients in both indoor and outdoor can be modelled as Rician, Rayleigh, Nakagami, Hoyt and Weibull distribution [96]. The Rician distribution has been associated with fading observed in indoor environments and describes a fading signal with one cluster of multipath waves in which one specular component predominates over scattered waves [97]. This type of channel modelling has proven to gain popularity in wireless channel modelling due to its elegant theoretical significance in the literature. The Rician K factor is the ratio of power of the dominant component and scattered power contribution. The well-known Rayleigh Probability Density Function (PDF) is a special case of Rician and occurs when the Rician factor K is equal to zero. That is, in the received component when there is no dominant component and only scattered components are present then Rician tends to Rayleigh. Nakagami distribution was obtained from extensive field measurements as an approximate curve fitted distribution [98]. A criticism that is often levelled at the Nakagami distribution as a model for fading in radio channel characterization is the lack of a strong theoretical justification. However, this distribution also has Rayleigh as a special case when $m = 1$ and it may also be used to approximate the Rician distribution for $m > 1$. Hoyt distribution is commonly used to describe the short term variation in certain wireless communication system subjected to fading [99]. Specifically, they are used in satellite based cellular communication to characterize more severe fading conditions than those modelled by Rayleigh [96,100]. Lognormal shadowing considers a completely different scenario associated with statistics of large-scale path loss variation in slow fading channels [101]. In a Weibull fading channel, the received signal is obtained as a non linear function of the modulus of the multipath components, where the non linearity is expressed in terms of the power parameter. Weibull distributed envelope may be obtained from two independent zero-mean Gaussian random variables with

identical variance. The Weibull distribution has received some attention as a model for describing the fading obtained in both indoor and outdoor propagation environments [102].

⁕ GFDM system performance is analyzed over frequency selective fading channels like Nakagami-m, Hoyt, Rician-K and Weibull-v. Analytical expressions were derived for the system model under the aforementioned channel conditions and the derived expressions are verified through simulations. This work has been covered in [54, 55].

In [103] David Slepian investigated the extent to which spectrum of the fundamental period concentrated on a subinterval using DPSS. In addition, the mathematical properties of this function and its application to the signal analysis are explained in detail. For a finite data samples, Thomson in [104] have used DPSS to solve spectrum estimation problem based on local eigen expansion. PAPR performance of GFDM is examined in [105]. This work mainly focus on the PAPR properties of the newly proposed physical layer modulation scheme (GFDM) for future cellular systems and presents a unified framework including comparison of OFDM and SC-FDE in an uplink multiple access scenario. R.W. Bauml et.al. in 1996 proposed a new method of reducing the PAPR of any multicarrier scheme, naming the technique as SLM [106]. With moderate complexity a significant reduction in PAPR is observed. In [107], authors have introduced PTS to OFDM system to achieve further reduction in PAPR. The usefulness of zadoff-chu sequence as a precoding matrix is exploited in [108] and the ZCT precoding and postcoding technique will reduce a considerable amount of PAPR. In [109], M.K. Gupta and S. Tiwari explored the wavelet based OFDM system and compared its performance to that of DFT based OFDM system interms of BER and Power Spectral Density (PSD) parameters. Further, the channel estimation techniques using LS and Linear MMSE (LMMSE) techniques are also examined. K. Abdullah and Z.M. Hussain in [110] chooses DVB-T system for evaluating the performance of the wavelet based OFDM system under AWGN and Rayleigh fading channels. In this article, for evaluating the BER performance they have considered wavelets such as Haar and Daubechies. A comparison of this system with that of conventional OFDM system is provided and results shows the benefit of using wavelet transforms.

- ⁕ DPSS are the orthogonal sequences having lower OOB emission to that of conventional RRC filters and hence can be a good choice to investigate its nature towards improving the performance of GFDM and primarily presented in [56].
- ⁕ It is interesting to study the behaviour of some of the standard PAPR reduction schemes in GFDM systems and to explore the hybrid combinations of these techniques.
- ⁕ The potential of wavelet transforms in the context of MGFDM, exploiting the self and mutual orthogonality properties of the wavelet basis functions could be another fascinating area to be researched [58].

For the purpose of facilitating higher data rate communication it is necessary to depend on parallel transmission techniques like MIMO schemes. STBC, proposed by Alamouti [111] and referred to as an open-loop system, is one of the most well-known transmit diversity schemes to achieve full diversity. The basic idea is simply the transmission of a signal over two independently fading channels. Due to its practical importance, STBC is implemented in third generation networks. In addition, a class of STBC known as OSTBC has been proposed by [112]. This achieves full diversity and at the same time exhibits low decoding complexity at the receiver. In particular, [113, 114] deal with OSTBC with partial channel knowledge and a limited feedback system. More recent advancements in precoding techniques have led to precoded OSTBC, which aims to improve overall system performance and maintain full diversity [115, 116]. [117] investigated the application of Alamouti space time coding to mitigate the effects of a multipath environment in such systems.

The analysis and design of OFDM/OQAM using the concept called filterbank theory is presented in [118] where the discrete orthogonality conditions of the system are evaluated and for non-orthogonal systems, analytical expressions of ISI/ICI distortions produced by such imperfect filterbanks are derived. [119] discusses about the zero forcing equalization problem in OFDM/OQAM at the receiver side using three different approaches. There has been a lot of attention in the past about the effect of Nakagami

fading channels on the overall system performance. Briefly these channels can account for both severe and weak fading environments. Nakagami fading channels cover one-sided Gaussian (m=1/2; q=0) and Rayleigh fading (m=1; q=1) as corner cases. Nakagami-m fading model has a simpler analytical expression to evaluate numerically and gained its popularity due to its practical applications in mobile communications. The closed form expressions for secrecy outage performance over Nakagami-m fading channel has been discussed in [120]. Nakagami-q channel model is considered to be crucial for satellite links with strong ionospheric scintillation [96]. The statistics of Nakagami-q fading channel and how they are best suited for real mobile channels is discussed in [121]. The average error performance in Hoyt fading channel for different modulation schemes is reported in [122–124].

- ⋇ Unlike precoded OSTBC in OFDM systems, the application of such technique is still unexplored in GFDM systems [59].
- ⋇ The performance analysis of GFDM/OQAM under fading models is an interesting and important topic that has to be covered [60–62].

Taking into consideration the mobile radio environment, where the transmitted signal undergoes several fluctuations before reaching the receiver. Therefore, this necessitates tracking and estimating the channel. For this, effective channel estimation algorithms such as Least Square (LS) and Minimum Mean Square Error (MMSE) are enforced. Let us brief out the channel estimation algorithms done so far in the literature. OFDM channel estimation is addressed by [125] based on time-domain channel statistics. Channel estimation for various pilot patterns is discussed in [126] and references therein. U. Vilaopornsawai and M. Jia in [127] introduces two scattered pilot based channel estimation methods for GFDM, Pilot Interference Cancellation and Transmitter Interference Cancellation. The article gives an insight into interference cancellation either at the transmitter or the receiver of the communication system. Blind estimation of channel block duration, symbol duration and number of subcarriers is discussed in [128]. Coded OFDM (COFDM) modulation system was developed by P. Shelswell in 1995 for DAB and explains how this system can be used to meet the requirements of the users [129].

- A great amount of research covering channel estimation for OFDM has been done over the years and much of it can be modified and applied to GFDM systems [63].
- Convolution codes improve performance in OFDM multicarrier systems tremendously and investigation of these convolution codes in MGFDM systems has not been reported anywhere [64].

Even though, there are many significant works pertaining to the implementation of GFDM system, we have specified the literature which is closely related to our contributions.

2.5 Problem Statement

This thesis handles different aspects of GFDM, addressing some of the challenging issues as mentioned, in the view of 5G. Mainly this thesis covers the performance analysis of GFDM and its variants under several fading channel environments by giving the analytical expressions to strengthen the simulated results in matlab. In order to improve the orthogonality of the conventional GFDM system, we have proposed novel pulse shape filtering method and its performance is analysed by considering various performance metrics such as SER, PAPR, spectrum information, MSE and constellations diagrams. All the modifications are to make GFDM a more suitable candidate for physical layer waveform to be used in 5G systems.

Chapter 3

Generalized Frequency Division Multiplexing under various fading channels

3.1 Introduction and Motivation

In precise, fading can be described as the variation or attenuation of the signal with various variables like time, geographical position and radio frequency. Due to this effect, multiple copies of the transmitted signal overlaps at the receiver at different time intervals thereby leading to the deterioration in received signal strength. The impairments in mobile communications will attenuate/distort the information signal due to various multiple reflections, scattering from different obstacles, terrain conditions and diffraction. This chapter deals with the effect of such fading channels on the GFDM system performance.

GFDM is a non-orthogonal block based multicarrier transmission technique comprising of a total number of NM symbols in which the term N specifies the number of subcarriers where each subcarrier carries M subsymbols. A number of publications carried out by Fettweis et.al. outlines the system implementation of GFDM. In [130] the bit error rate performance of GFDM based on the linear matrix model was studied. References [43, 44, 105, 131, 132] explore other implementation aspects of the method. Most of the existing literature on this topic examines the performance of GFDM in a Rayleigh fading channel [43] and the performance figures are based on SER expressions. It is worth pursuing to evaluate the GFDM system performance in the presence of other fading channels.

Unlike most fading distributions that model certain conditions, the Nakagami-m fading model is capable of modeling a wide class of fading channel conditions and it fits well the empirical data. The propagation of electromagnetic waves between a transmitter and a receiver through a complex environment is accompanied by typical wave phenomena such as diffraction, scattering, reflection, and absorption. Therefore, the received signal is composed of various components with different delays and amplitudes; these commonly include a direct component and scattered and reflected components. The total received electric field can be interpreted as a vector sum in the complex plane. Due to the existence of a great variety of fading environments, several statistical models are used to describe the probability distribution of the received signal amplitude. Small-scale fading models include Rayleigh, Rician, Nakagami-m, Hoyt-q, and Weibull-v distributions. Making no assumptions on the statistics of the amplitudes and phases of the multiple received versions (i.e., allowing X and Y to have different variances or being correlated) led to the more general Nakagami-m distribution. Larger values of m indicate the existence of a strong (normally, a line-of-sight) component, which represent less-severe fading conditions. Least severe fading is obtained as m approaches infinity. Nakagami-q distribution is used to model the fading channels when it is more severe than the Rayleigh fading. The value of the fading parameter q ranges from 0 to 1. For $q = 0$, the distribution is equivalent to a single-sided Gaussian fading, the highest severity that can be modeled by Hoyt distribution. And for $q = 1$, the distribution is equivalent to Rayleigh fading, representing the lowest severity. It should be noted that Nakagami-q distribution is a special case of the more general Nakagami-m distribution.

Basically, Rayleigh distribution is sufficient to model amplitude in urban areas, Rician distribution suits better in sub-urban areas where LOS components exist, and Hoyt distribution models scintillation effects. The Hoyt or Nakagami-q fading distribution is used to model short-term variations of radio signals resulting from the addition of scattered waves which can be described as a complex Gaussian random variable where the in-phase and quadrature components have zero mean and different variances, or equivalently, where the in-phase and quadrature components are correlated. This distribution is commonly used to model signal fading due to strong ionospheric scintillation in satellite communications or in general those fading conditions more severe than Rayleigh, and it includes both Rayleigh fading and one-sided Gaussian fading as special cases. Further-

more, it was shown in that the second order statistics of Hoyt fading best fit measurement data in mobile satellite channels with heavy shadowing.

The Rician-K Fading Channel is useful for modeling mobile wireless communication systems when the transmitted signal can travel to the receiver along a dominant line-of-sight or direct path. If the signal can travel along a line-of-sight path and also along other fading paths, then you can use this block in parallel with the multipath Rayleigh fading channel block. Fading causes the signal to spread and become diffuse. The K-factor parameter, which is part of the statistical description of the Rician distribution, represents the ratio between direct-path (unspread) power and diffuse power. The ratio is expressed linearly, not in decibels. While the Gain parameter controls the overall gain through the channel, the K-factor parameter controls the gain's partition into direct and diffuse components. K is the ratio between the power in the direct path and the power in the other, scattered, paths. Weibull-v Empirical studies have shown it to be an effective model in both indoor and outdoor environments.

In this chapter, we carry out the performance evaluation of GFDM in other fading channels conditions. The channel models that are simulated in Matlab are Nakagami-m, Rician-K, Nakagami-q (Hoyt), Weibull-v. This fading conditions will affect the transmission process making the transmitted signal random in nature which in turn will degrade the signal strength or quality at the receiver and the results that are established will be able to realize this effects. The key aspect of this chapter is to derive analytical expressions under above mentioned fading channels for GFDM system and the reliability of the GFDM multicarrier is determined in terms of SER. More precisely, a GFDM transceiver is simulated and the results are compared with the analytic expressions. We also verified the results obtained via our simulation model with the results obtained in [43, 95]. Thus we verify our simulation test bed. Further, the impact of the roll-off factor is analyzed under the above mentioned fading channels.

In the following subsections we discuss the system model in detail along with the signal processing steps involved with the help of matrix notation. Building upon, theoretical expressions under various fading channels were provided. Finally results of the GFDM system performance under various fading channel explaining the effect of different parameters are presented.

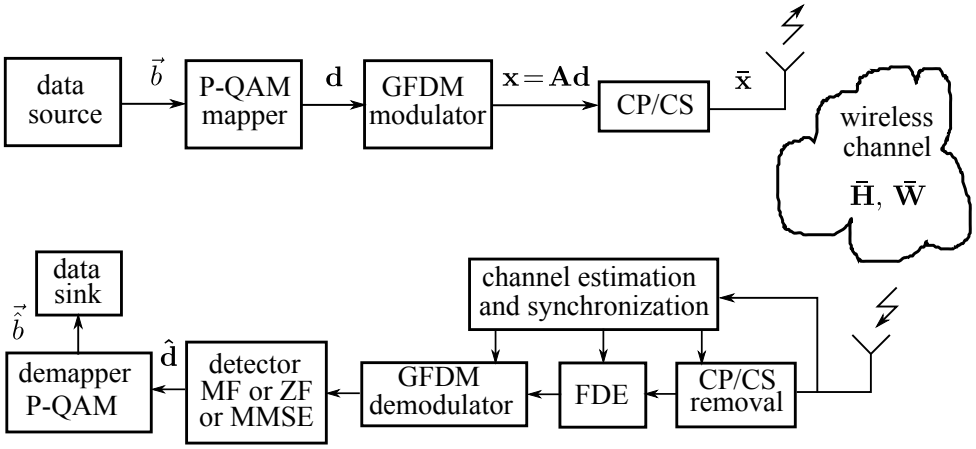

Figure 3.1: Block diagram of GFDM transceiver

3.1.1 Transmitter model

Let us consider a data source which provides the binary data vector $\vec{b}$, as illustrated in Figure 3.1. A mapper, e.g. QAM, maps the bits to symbols from a 2^{μ}-valued complex constellation where μ is the modulation order. The resulting vector $\mathbf{d} = [\mathbf{d_0}^T, \mathbf{d_1}^T, ..., \mathbf{d_{N-1}}^T]^T$ denotes a data block that contains N elements. Each element can be decomposed into M symbols according to $\mathbf{d_i} = [d_i(0), d_i(1), ..., d_i(M-1)]^T$, the data symbols that are to be transmitted on the i^{th} subcarrier. Each $d_i(m)$ corresponds to the data symbol that has to be transmitted on the i^{th} subcarrier in the m^{th} time slot. The details of the GFDM modulator are shown in Figure 3.2 [43]. In GFDM modulation, the data symbols are first upsampled to obtain the following representation as $\tilde{d}_{i,m}(n)$,

$$\tilde{d}_{i,m}(n) = d_i(m)\,\delta(n - mN), n = 0, 1, 2, \cdots MN - 1 \tag{3.1}$$

Further, this upsampled data is pulse shaped where the impulse response of the pulse shaping filter is denoted as $g(n)$, whose length is MN. In general, $g(n)$ represents the prototype filter which can be used for pulse shaping the subcarriers and this can be either RC, RRC, Xia pulse and Dirichlet pulse (more details of these filters can be found in [43]). Therefore, this upsampled data is circularly convolved with $g(n)$ to attain the following expression as [133]:

$$x_{i,m}(n) = \sum_{l=0}^{MN-1} d_i(m)\, g[(n-l)\, mod\ MN]\, \delta(l - mN) \tag{3.2}$$

Upon solving (3.2), the following expression can be obtained as,

$$x_{i,m}(n) = d_i(m)\, g[(n - mN)\, mod\ MN] \tag{3.3}$$

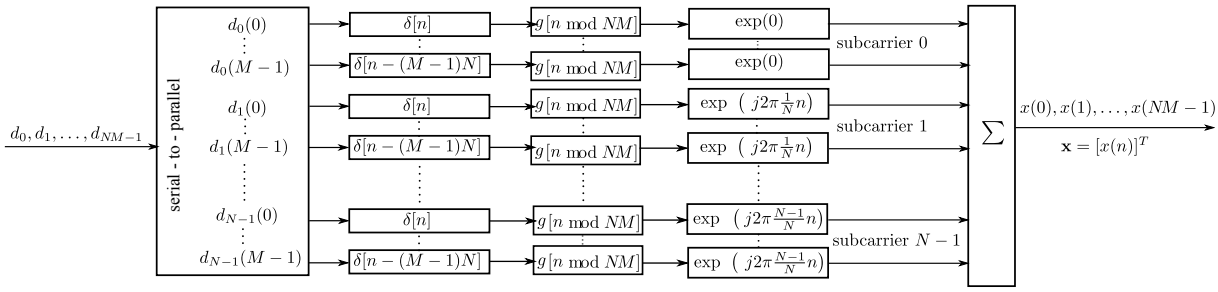

Figure 3.2: Details of GFDM modulator

Now, this is up-converted to the i^{th} subcarrier frequency and is given as [43],

$$x_{i,m}(n) = d_i(m) \underbrace{g\left[(n - mN)\, mod\ MN\right] e^{\frac{j2\pi in}{N}}}_{g_{i,m}(n)} \tag{3.4}$$

where the term under the brace is denoted as $g_{i,m}(n)$ represents the shifted version of the prototype filter $g(n)$ in time and frequency which is given as:

$$g_{i,m}(n) = g[(n - mN) \bmod MN] e^{j2\pi \frac{i}{N} n} \tag{3.5}$$

The modulo operation makes $g_{i,m}(n)$ shift circularly in time and the complex exponential performs the corresponding shifting operation in frequency. Finally, the superposition of all the transmit symbols leads to the GFDM signal $x(n)$ as [43],

$$x(n) = \sum_{i=0}^{N-1} \sum_{m=0}^{M-1} d_i(m) g_{i,m}(n) \tag{3.6}$$

Expressing now all the operations: upsampling, pulse shaping, sub-carrier upconversion and superposition in matrix notation, the GFDM transmitter can be modelled as [43],

$$\mathbf{x} = \mathbf{A}\mathbf{d} \tag{3.7}$$

where $\mathbf{A}$ is an $MN \times MN$ GFDM transmitter modulation matrix which can be further expressed as:

$$\mathbf{A} = \left[\underbrace{\hat{\mathbf{g}}_{0,0}\ \hat{\mathbf{g}}_{1,0}\ \cdots \hat{\mathbf{g}}_{N-1,0}}_{1^{st}\ Time\ Slot} \Big| \underbrace{\hat{\mathbf{g}}_{0,1}\ \hat{\mathbf{g}}_{1,1}\ \cdots \hat{\mathbf{g}}_{N-1,1}}_{2^{nd}\ Time\ Slot} \Big| \cdots \Big| \underbrace{\hat{\mathbf{g}}_{0,M-1}\ \hat{\mathbf{g}}_{1,M-1}\ \cdots \hat{\mathbf{g}}_{N-1,M-1}}_{M^{th}\ Time\ Slot} \right] \tag{3.8}$$

$$\mathbf{A} = \left[\underbrace{\hat{\mathbf{g}}_{0,0}\ \hat{\mathbf{g}}_{0,1}\ \cdots \hat{\mathbf{g}}_{0,M-1}}_{1^{st}\ Subcarrier} \Big| \underbrace{\hat{\mathbf{g}}_{1,0}\ \hat{\mathbf{g}}_{1,1}\ \cdots \hat{\mathbf{g}}_{1,M-1}}_{2^{nd}\ Subcarrier} \Big| \cdots \Big| \underbrace{\hat{\mathbf{g}}_{N-1,0}\ \hat{\mathbf{g}}_{N-1,1}\ \cdots \hat{\mathbf{g}}_{N-1,M-1}}_{N^{th}\ Subcarrier} \right] \tag{3.9}$$

where

$$\hat{\mathbf{g}}_{i,m} = \left[g_{i,m}\left(0\right)\cdots g_{i,m}\left(MN-1\right)\right]^{T} \tag{3.10}$$

A similar low complexity implementation technique for GFDM transmitter model can be found in [134], where $\mathbf{x}$ can be modelled as,

$$\mathbf{x} = \mathbf{\Gamma}^{H}\bar{\mathbf{d}} \tag{3.11}$$

where $\mathbf{\Gamma} = \mathbf{F_b A}$, $\bar{\mathbf{d}} = \mathbf{F_b d}$ and $\mathbf{F_b}$ is the $MN \times MN$ normalized DFT matrix that includes $M \times M$ submatrices denoted by $\mathbf{\Omega}_{ni}$ and can be expressed as:

$$\mathbf{\Omega}_{ni} = \frac{1}{\sqrt{N}} e^{\frac{-j2\pi ni}{N}} \mathbf{I}_M \qquad n, i = 0, 1, 2, 3, \cdots N-1 \tag{3.12}$$

Lastly, on the transmitter side a CP of length N_{CP} samples is appended to the vector $\mathbf{x}$ in order to form a transmit signal vector $\bar{\mathbf{x}}$ of length $MN + N_{CP}$. In order to avoid ISI, which is more predominant in a multipath fading channel it is important to note that the length of the cyclic prefix has to be longer than the maximum excess delay.

3.1.2 Channel model

Let $\mathbf{h} = [h_0, .., h_{Nch-1}]^T$ be the channel impulse response where the maximum delay spread of the channel is represented as N_{ch}. The received signal propagating through the wireless channel after removing CP can be modelled as,

$$\mathbf{r} = \mathbf{H}\mathbf{x} + \mathbf{w} \tag{3.13}$$

where $\mathbf{H} = circ\left\{\tilde{h}\right\}$ and $\tilde{h}$ is the zero padded version of $\mathbf{h}$ of the same length as $\mathbf{x}$. The vector $\mathbf{w} \sim \mathcal{CN}(0, \sigma_w^2 I_{MN})$ denotes the complex AWGN samples with noise variance σ_w^2 and I_{MN} is the identity matrix of order MN. Let $\mathbf{r}$ denote the received signal vector which consists of samples of $r(n)$. Then $r(n) = x(n) * h(n) + w(n)$, where $*$ denotes convolution operation, $h(n)$ specifies the impulse response of the multipath fading channel and $w\left(n\right)$ represents the AWGN. When the channel is AWGN, $h(n) = 1$ or equivalently $\mathbf{H} = \mathbf{I}$.

3.1.3 Receiver Model

In this section we assume perfect time and frequency synchronization as well as perfect channel knowledge. Channel equalization in the frequency domain can be performed

as [132],

$$\mathbf{y} = \text{IDFT}\left\{\frac{\text{DFT}(\mathbf{r})}{\text{DFT}(\mathbf{h})}\right\} \tag{3.14}$$

where DFT(.) is the Discrete Fourier Transform and IDFT(.) is the Inverse Discrete Fast Fourier Transform and $\mathbf{r}$ is the received signal vector after removing cyclic prefix and $\mathbf{h}$ is the realization of multipath channel. The receiver structure for a GFDM signal can be implemented in several ways: MF, ZF and MMSE. In order to obtain estimates of the original transmit data from the received and equalized signal $y(n)$, the exact opposite signal processing operations done on the transmitter have to be performed at the receiver.

$$\hat{\mathbf{d}} = \mathbf{B}\mathbf{y} \tag{3.15}$$

The matrix $\mathbf{B}$ is given as follows [134],

$$\begin{aligned} \text{MF:} \quad & \mathbf{B_{MF}} = {\mathbf{F_b}}^H \mathbf{\Gamma} \\ \text{ZF:} \quad & \mathbf{B_{ZF}} = {\mathbf{F_b}}^H \mathbf{D}^{-1} \mathbf{\Gamma} \\ \text{MMSE:} \quad & \mathbf{B_{MMSE}} = \left({\mathbf{F_b}}^H \mathbf{D} \mathbf{F_b} + \sigma_w^2 \mathbf{I_{MN}}\right)^{-1} \mathbf{A}^H \end{aligned} \tag{3.16}$$

where $\mathbf{D} = \mathbf{F_b}\left(\mathbf{A}^H\mathbf{A}\right){\mathbf{F_b}}^H$ is an $MN \times MN$ block-diagonal matrix and σ_w^2 is the noise variance.

3.2 Performance Analysis

In this section analytical expressions of symbol error rate performance over different fading channels namely Nakagami-q and Weibull-v are derived. The SER performance analysis of GFDM employing ZF receiver will remove the self generated interference but at the cost of increased noise enhancement. This factor is known as Noise Enhancement Factor (NEF) and depends on the pulse shape filter. The NEF ξ determines the SNR reduction when using the ZF receiver and is given by [43],

$$\xi = \sum_{n=0}^{NM-1} \left|[\mathbf{B_{ZF}}]_{i,n}\right|^2 \tag{3.17}$$

The values of ξ are equal for any index i. Derivation of equation (3.17) is provided in Appendix B.

3.2.1 AWGN channel

The GFDM SER expression under AWGN assuming ZF receiver is given by [43]:

$$P_{AWGN}(e) = 2\left(\frac{p-1}{p}\right)\text{erfc}(\sqrt{\gamma}) - \left(\frac{p-1}{p}\right)^2 \text{erfc}^2(\sqrt{\gamma}) \tag{3.18}$$

where

$$\gamma = \frac{3R_T}{2(2^\mu - 1)}\frac{E_s}{\xi N_0} \tag{3.19}$$

and

$$R_T = \frac{NM}{NM + N_{CP} + N_{CS}} \tag{3.20}$$

μ is the number of bits per QAM symbol, $p = \sqrt{2^\mu}$, N_{CP} and N_{CS} are the length of the CP and CS respectively, N and M denote the number of subcarriers and subsymbols respectively, E_s is the average energy per symbol and N_0 is the noise power density. A complete derivation of obtaining equation (3.18) is provided in Appendix D.
The symbol error rate in different fading channels can be derived by averaging the error rates for the AWGN channel over the PDF of the SNR in different fading channels given by [96]:

$$P(e) = \int_0^\infty P_{AWGN}(e)P_\gamma(\gamma)d\gamma \tag{3.21}$$

where the probability densities $P_\gamma(\gamma)$ for various fading channel namely Nakagami-m, Rician-K, Nakagami-q and Weibull-v fading channels are given respectively by (3.29), (3.35), (3.40) and (3.47).

To evaluate the above integral analytically, different methods are available, such as the PDF and Moment Generating Function (MGF) methods. The PDF method involves solving the integral directly, whereas in the MGF method a prior transformation into the frequency domain is carried out, by exploiting the Laplace transform of $P_\gamma(\gamma)$. In our case, we followed PDF method to solve the integrals [135]. It is worth mentioning at this point how we handle some of the integrals used in the derivation. First, let us consider the following integral,

$$A(x) = \int_0^\infty x^{m_1-1}e^{-m_2 x}\text{erfc}^2(\sqrt{x})dx \tag{3.22}$$

Solving integral (3.32) is not trivial. One way to proceed is to use a simple, basic integration by parts method. At first, separate (3.22) into two parts as $\int_a^b udv = [uv]_a^b - \int_a^b vdu$ where $u = \text{erfc}^2(\sqrt{\gamma})$ and $dv = x^{m_1-1}e^{-m_2 x}dx$. In the process the following modified expressions are useful [[135],2.321],

$$\int x^{n-1}e^{-ax}dx = \frac{-(n-1)!}{a^n}e^{-ax}\sum_{j=0}^{n-1}\frac{a^j}{j!}x^j \tag{3.23}$$

$$\frac{d}{dx}\left[\text{erfc}(\sqrt{x})\right] = -\frac{2e^{-x}}{\sqrt{\pi}}$$

The final expression solved for equation (3.22) is given by,

$$A(x) = \frac{(m_1-1)!}{(m_2)^{m_1}}\Big(1 - \frac{4}{\pi}\sum_{j=0}^{m_1-1}\frac{(m_2)^j}{2j+1} \times_2 F_1\big[j+\frac{1}{2}, j+1; j+\frac{3}{2}; -(m_2+1)\big]\Big) \tag{3.24}$$

where ${}_2F_1[.,.;.;]$ is the Gauss hypergeometric function [135].

Using modified formulae of [[135],6.286] we have,

$$\int_0^\infty erfc(\beta\sqrt{y})y^{(v/2)-1}e^{\mu^2 y}dy = \frac{2\Gamma(\frac{v+1}{2})}{\sqrt{\pi}\beta^v v} \times_2 F_1[\frac{v}{2}, \frac{v+1}{2}; \frac{v+2}{2}; -\frac{\mu^2}{\beta^2}] \tag{3.25}$$

In some of the cases where direct integrals are not possible we have calculated the results in terms of the Meijer's G function by using the following relations [136],

$$e^{-g(x)} = G_{01}^{10}\left(g(x)\,\middle|\,\begin{matrix}-\\0\end{matrix}\right) \tag{3.26}$$

$$\text{erfc}(x) = 1 - \frac{1}{\sqrt{\pi}}G_{1,2}^{1,1}\left(x^2\,\middle|\,\begin{matrix}1\\1/2,0\end{matrix}\right) = \frac{1}{\sqrt{\pi}}G_{1,2}^{2,0}\left(x^2\,\middle|\,\begin{matrix}1\\0,1/2\end{matrix}\right) \tag{3.27}$$

$$e^{-\beta x^m} = \sum_{i=0}^{\infty}\frac{(-1)^i\beta^i x^{mi}}{i!} \tag{3.28}$$

where G(.) is the Meijer's G function [135], available in most common mathematical software tools like Mathematica, Maple or Matlab. Definition of Meijer's G function is provided in Appendix C.

3.2.2 Nakagami-m channel fading

Nakagami-m is a generalized distribution which can model different fading environments. It has greater flexibility and accuracy in matching some experimental data than the Rayleigh or Rician distributions. Rayleigh and one-sided Gaussian distribution are special cases of Nakagami-m model. Nakagami-m is applicable to both ionospheric and tropospheric models of propagation.

If the signal amplitude follows a Nakagami distribution, then the PDF of γ follows a gamma PDF given by [96],

$$P_{\gamma}(\gamma) = \left(\frac{m}{\bar{\gamma}}\right)^{m} \frac{\gamma^{m-1}}{\Gamma(m)} \; e^{\frac{-m\gamma}{\bar{\gamma}}} \qquad ; m \geq 1/2 \tag{3.29}$$

where m is the Nakagami parameter and $\bar{\gamma}$ is the average SNR per bit. Substituting Eqs.(3.18) and (3.29) into Eq.(3.21) gives:

$$P_{Nak}(e) = 2\left(\frac{p-1}{p}\right)\left(\frac{m}{\bar{\gamma}_n}\right)^{m} I_1(\bar{\gamma}_n) - \left(\frac{p-1}{p}\right)^{2}\left(\frac{m}{\bar{\gamma}_n}\right)^{m} I_2(\bar{\gamma}_n) \tag{3.30}$$

where

$$I_1(\bar{\gamma}_n) = \frac{1}{\Gamma(m)} \int_0^{\infty} erfc(\sqrt{\gamma})\gamma^{m-1} e^{\frac{-m\gamma}{\bar{\gamma}_n}} d\gamma \tag{3.31}$$

$$I_2(\bar{\gamma}_n) = \frac{1}{\Gamma(m)} \int_0^{\infty} erfc^2(\sqrt{\gamma})\gamma^{m-1} e^{\frac{-m\gamma}{\bar{\gamma}_n}} d\gamma \tag{3.32}$$

where $\bar{\gamma}_n$ is the equivalent SNR under Nakagami fading channel given by $\bar{\gamma}_n = \frac{3R_T\sigma_n^2}{(2^{\mu}-1)}\frac{E_s}{\xi N_0}$ and we have assumed the parameter $\sigma_n^2 = 1/2$ for SER performance.

The first integral (3.31) can be solved by using the modified equation of [[135],6.286] resulting in the following equation:

$$I_1(\bar{\gamma}_n) = \frac{\Gamma(m+1/2)}{\sqrt{\pi}\Gamma(m+1)} \; {}_2F_1[m, m+\frac{1}{2}; m+1; -\frac{m}{\bar{\gamma}_n}] \tag{3.33}$$

where ${}_2F_1[.,.;.;]$ is the Gauss hypergeometric function [135].

Moreover the second integral can be solved using byparts integration method similar to equation (3.24) reducing to,

$$I_2(\bar{\gamma}_n) = \left(\frac{\bar{\gamma}_n}{m}\right)^{m} - \frac{4}{\pi}\left(\frac{\bar{\gamma}_n}{m}\right)^{m} \sum_{j=0}^{\infty} \frac{(m/\bar{\gamma}_n)^j}{(j!)} \frac{\Gamma(j+1)}{(2j+1)} \; \times_2 F_1[j+\frac{1}{2}, j+1; j+\frac{3}{2}; -(\frac{m}{\bar{\gamma}_n}+1)] \tag{3.34}$$

It is to be noted that $m = 1$ reduces to SER expression under Rayleigh fading channel [43].

3.2.3 Rician-K Fading Channel

If the signal strength follows a Rician distribution, the PDF of γ will be given by [96],

$$P_{\gamma}(\gamma) = \left(\frac{1+K}{\bar{\gamma}}\right) e^{\left[-\frac{(1+K)\gamma + K\bar{\gamma}}{\bar{\gamma}}\right]} I_0\left[\sqrt{\frac{4K(1+K)\gamma}{\bar{\gamma}}}\right]; 0 \leq K < \infty \tag{3.35}$$

where K is the Rician parameter and $\bar{\gamma}$ is the average SNR per bit.

Expressing the infinite series representation of the zeroth-order modified Bessel function [137], $I_0(x) = \sum_{s=0}^{\infty} \left(\frac{x^2}{4}\right)^s / (s!)^2$, the PDF of (3.35) can be modified as:

$$P_{\gamma}(\gamma) = \frac{1+K}{\bar{\gamma}_r} e^{-K} \sum_{s=0}^{\infty} \frac{1}{(s!)^2} \left(\frac{K(1+K)}{\bar{\gamma}_r}\right)^s \gamma^s e^{\frac{-\gamma(1+K)}{\bar{\gamma}_r}}; 0 \leq K < \infty \tag{3.36}$$

Substituting equations (3.18), (3.36) in (3.21) we have the final SER expression of the Rician fading channel as:

$$P_{Ric}(\gamma) = \frac{2(p-1)}{p} I_3(\bar{\gamma}_r) - \left(\frac{p-1}{p}\right)^2 I_4(\bar{\gamma}_r) \tag{3.37}$$

where

$$I_3(\bar{\gamma}_r) = \frac{1+K}{\bar{\gamma}_r} e^{-K} \sum_{s=0}^{\infty} \frac{1}{(s!)^2} \left(\frac{K(1+K)}{\bar{\gamma}_r}\right)^s \times \frac{\Gamma(s+3/2)}{\sqrt{\pi}(s+1)} \, {}_2F_1[s+1, s+\frac{3}{2}; s+2; -(\frac{1+K}{\bar{\gamma}_r})] \tag{3.38}$$

$$I_4(\bar{\gamma}_r) = e^{-K} \sum_{s=0}^{\infty} \frac{K^s}{(s!)} (1 - \frac{4}{\pi} \sum_{j=0}^{s} \frac{((1+K)/\bar{\gamma}_r)^j}{2j+1} \times_2 F_1[j+\frac{1}{2}, j+1; j+\frac{3}{2}; -(\frac{1+K}{\bar{\gamma}_r}+1)]) \tag{3.39}$$

and $\bar{\gamma}_r$ is the equivalent SNR under Rician fading channel given by $\bar{\gamma}_r = \frac{3R_T\sigma_r^2}{(2^{\mu}-1)} \frac{E_s}{\xi N_0}$, where we have assumed the parameter $\sigma_r^2 = 1/2$ for SER performance.

To obtain the above results we have followed the same procedure as in (3.33) and (3.34) in evaluating the integrations. As expected when $K = 0$, expression (3.37) reduces to the SER under the Rayleigh fading channel [43].

3.2.4 Hoyt (Nakagami-q) fading channel

Let us assume that the effect of the channel on the propagating signal is best described by Hoyt (Nakagami-q) fading. The PDF of γ is then given by [96] ,

$$P_{\gamma}(\gamma) = \left(\frac{1+q^2}{2q\bar{\gamma}}\right) \exp\left[-\frac{(1+q^2)^2\gamma)}{4q^2\bar{\gamma}}\right] I_0\left[\frac{-(1-q^4)\gamma}{4q^2\bar{\gamma}}\right]; \quad 0 \leq q \leq 1 \tag{3.40}$$

where q is the Hoyt fading parameter, $I_o(.)$ is the zeroth-order modified Bessel function and $\bar{\gamma}$ is the average SNR per bit. Expressing the infinite series representation of the zeroth-order modified Bessel function [137] as $I_0(x) = \sum_{s=0}^{\infty} \left(\frac{x^2}{4}\right)^s / (s!)^2$, the PDF of (3.40) can be written as:

$$P_\gamma(\gamma) = \left(\frac{1+q^2}{2q\bar{\gamma}}\right) e^{-\frac{(1+q^2)^2\gamma}{4q^2\bar{\gamma}}} \sum_{s=0}^{\infty} \frac{1}{(s!)^2} \left(\frac{(1-q^4)\gamma}{8q^2\bar{\gamma}}\right)^{2s} \tag{3.41}$$

The probability of error in this case, $P_{Hoyt}(e)$ can be evaluated by substituting Eqs.(3.18) and (3.40) into Eq.(3.21) giving:

$$P_{Hoyt}(e) = \frac{2(p-1)}{p} I_5(\bar{\gamma}_t) - \left(\frac{p-1}{p}\right)^2 I_6(\bar{\gamma}_t) \tag{3.42}$$

where

$$I_5(\bar{\gamma}_t) = \left(\frac{1+q^2}{2q\bar{\gamma}_t}\right) \sum_{s=0}^{\infty} \frac{1}{(s!)^2} \left(\frac{(1-q^4)}{8q^2\bar{\gamma}_t}\right)^{2s} \int_0^{\infty} erfc(\sqrt{\gamma}) e^{-\frac{(1+q^2)^2\gamma}{4q^2\bar{\gamma}_t}} \gamma^{2s} d\gamma \tag{3.43}$$

$$I_6(\bar{\gamma}_t) = \left(\frac{1+q^2}{2q\bar{\gamma}_t}\right) \sum_{s=0}^{\infty} \frac{1}{(s!)^2} \left(\frac{(1-q^4)}{8q^2\bar{\gamma}_t}\right)^{2s} \int_0^{\infty} erfc^2(\sqrt{\gamma}) e^{-\frac{(1+q^2)^2\gamma}{4q^2\bar{\gamma}_t}} \gamma^{2s} d\gamma \tag{3.44}$$

where $\bar{\gamma}_t$ is the equivalent SNR under the Hoyt fading channel given by,

$$\bar{\gamma}_t = \frac{3R_T\sigma_t^2}{(2^\mu - 1)} \frac{E_s}{\xi N_0}.$$

and we have assumed a Hoyt channel parameter $\sigma_t^2 = 1/2$ for simulation purposes.

The first integral (3.43) can be easily solved by using the modified equation of [[135],6.286] resulting in the following expression:

$$\begin{aligned} I_5(\bar{\gamma}_t) = \frac{1+q^2}{2q\bar{\gamma}_t} \sum_{s=0}^{\infty} \frac{1}{(s!)^2} \left(\frac{(1-q^4)}{8q^2\bar{\gamma}_t}\right)^{2s} \frac{\Gamma((4s+3)/2)}{\sqrt{\pi}(2s+1)} \\ \times {}_2F_1[2s+1, 2s+\frac{3}{2}; 2s+2; -(\frac{(1+q^2)^2}{4q^2\bar{\gamma}_t})] \end{aligned} \tag{3.45}$$

where $\Gamma(.)$ is the gamma function and ${}_2F_1[.,.;.;]$ is the Gauss hypergeometric function [135]. The second integral (3.44) can be solved by using the result obtained in (3.24),

$$I_6(\bar{\gamma}_t) = \begin{cases} \left(\frac{1+q^2}{2q}\right) \sum_{s=0}^{\infty} \frac{1}{(s!)^2} \left(\frac{(1-q^4)}{8q^2}\right)^{2s} 2s! \left(\frac{4q^2}{1+q^2}\right)^{2s+1} \\ \times \left(1 - \frac{4}{\pi} \sum_{j=0}^{2s+1} \frac{(\frac{(1+q^2)^2}{4q^2\bar{\gamma}_t})^j}{2j+1} \times_2 F_1\left[j+\frac{1}{2}, j+1; j+\frac{3}{2}; -(\frac{(1+q^2)^2}{4q^2\bar{\gamma}_t}+1)\right]\right) \end{cases} \tag{3.46}$$

For Hoyt fading parameter $q = 1$, the SER expression will reduce to that of Rayleigh channel [43].

3.2.5 Weibull-v Fading channel

In case of Weibull-v Fading channel, the PDF of γ is given by [138],

$$P_{\gamma}(\gamma) = \left(\frac{v}{2\left(a\bar{\gamma}\right)^{v/2}}\right)\gamma^{\frac{v}{2}-1}\exp\left[-\left(\frac{\gamma}{a\bar{\gamma}}\right)^{v/2}\right] \tag{3.47}$$

where v is the Weibull fading parameter which describes the severity of the fading channel,$\bar{\gamma}$ is the average SNR per bit and $a = 1/\Gamma(1+2/v)$. Substituting this in (3.21) we can obtain a closed form expression for the Weibull fading channel in GFDM. The expression for SER is given by,

$$P_{Wbl}(e) = \frac{2(p-1)}{p}\frac{v/2}{(a\bar{\gamma}_{wb})^{v/2}}I_7(\bar{\gamma}_{wb}) - \left(\frac{p-1}{p}\right)^2\frac{v/2}{(a\bar{\gamma}_{wb})^{v/2}}I_8(\bar{\gamma}_{wb}) \tag{3.48}$$

where

$$I_7(\bar{\gamma}_{wb}) = \int_0^{\infty}\gamma^{\frac{v}{2}-1}e^{-\frac{\gamma^{v/2}}{(a\bar{\gamma}_{wb})^{v/2}}}erfc(\sqrt{\gamma})d\gamma \tag{3.49}$$

$$I_8(\bar{\gamma}_{wb}) = \int_0^{\infty}\gamma^{\frac{v}{2}-1}e^{-\frac{\gamma^{v/2}}{(a\bar{\gamma}_{wb})^{v/2}}}erfc^2(\sqrt{\gamma})d\gamma \tag{3.50}$$

and

$$\bar{\gamma}_{wb} = \frac{3R_T\sigma_{wb}^2}{(2^{\mu}-1)}\frac{E_s}{\xi N_0}$$

where we have assumed a Weibull channel parameter $\sigma_{wb}^2 = 1/2$ for simulation purposes and $\bar{\gamma}_{wb}$ is the equivalent SNR under the Weibull fading channel.

Using eqn. (C.3), $I_7(\bar{\gamma}_{wb})$ can be modified as,

$$I_7(\bar{\gamma}_{wb}) = \int_0^{\infty}\gamma^{\frac{v}{2}-1}e^{-\frac{\gamma^{v/2}}{(a\bar{\gamma}_{wb})^{v/2}}}d\gamma - \frac{1}{\sqrt{\pi}}\int_0^{\infty}\gamma^{\frac{v}{2}-1}e^{-\frac{\gamma^{v/2}}{(a\bar{\gamma}_{wb})^{v/2}}}G_{12}^{11}\left(\gamma\,\middle|\,\begin{matrix}1\\1/2,0\end{matrix}\right)d\gamma \tag{3.51}$$

The first integral has a straight forward solution and in the second integral we substitute eqn. (C.2) and used ([136], eqn.(21)) to obtain the following expression,

$$I_7(\bar{\gamma}_{wb}) = \frac{2(a\bar{\gamma}_{wb})^{v/2}}{v} - \frac{(k/\lambda)^{1/2}\lambda^{v/2}}{\sqrt{\pi}(2\pi)^{\frac{k+\lambda-2}{2}}}G_{2\lambda,k+\lambda}^{k+\lambda,\lambda}\left(\frac{(\lambda)^{\lambda}(k)^{-k}}{(a\bar{\gamma}_{wb})^{vk/2}}\,\middle|\,\begin{matrix}\Delta(\lambda,\frac{1-v}{2}),\Delta(\lambda,1-\frac{v}{2})\\ \Delta(k,0),\Delta(\lambda,-\frac{v}{2})\end{matrix}\right) \tag{3.52}$$

where k and λ are positive integers such that $\lambda/k = v/2$, $\Delta(l_1,l_2) = \frac{l_2}{l_1},\frac{l_2+1}{l_1},...,\frac{l_2+l_1-1}{l_1}$. Depending on the value of v we have to choose the minimum values for k and λ properly.

For example for $v = 5.6$, we need to choose $\lambda = 14$ and $k = 5$. For the special case of v being an integer, $k = 2$ and $\lambda = v$. A similar kind of approach can be found in [139] with integrals of type (3.49). We have derived a novel approach in solving equation (3.50). We have an $\text{erfc}^2(\sqrt{\gamma})$ term to be solved along with other terms in the integral, which is not trivial to solve. The solution now is a two step process. In the first step we make use of the by parts procedure by letting $\int_0^\infty u_2 dv_2$ where $u_2 = \text{erfc}^2(\sqrt{\gamma})$ and $dv_2 = \gamma^{\frac{v}{2}-1} exp\left(-\frac{\gamma^{v/2}}{(a\bar{\gamma}_{wb})^{v/2}}\right) d\gamma$. Also using the formula $\frac{d}{d\gamma}\left[\text{erfc}^2\sqrt{\gamma}\right] = -\frac{e^{-\gamma}}{\sqrt{\pi\gamma}}$, the intermediate step can be written as,

$$I_8(\bar{\gamma}_{wb}) = \frac{2(a\bar{\gamma}_{wb})^{v/2}}{v}\left[1 - \frac{2}{\sqrt{\pi}}\int_0^\infty \frac{1}{\sqrt{\gamma}} e^{-\frac{\gamma^{v/2}}{(a\bar{\gamma}_{wb})^{v/2}}} e^{-\gamma} erfc(\sqrt{\gamma}) d\gamma\right] \tag{3.53}$$

In the second step we use eqns. (C.2), (C.3) and (3.28) in solving the above integral and the solution is written as,

$$I_8(\bar{\gamma}_{wb}) = \frac{2(a\bar{\gamma}_{wb})^{v/2}}{v} \left[1 - \frac{2}{\sqrt{\pi}}\sum_{i=0}^{\infty}\frac{(-1)^i}{i!}\int_0^\infty \gamma^{i-\frac{1}{2}} G_{01}^{10}\left(\frac{\gamma^{v/2}}{(a\bar{\gamma}_{wb})^{v/2}} \;\middle|\; \begin{matrix} - \\ 0 \end{matrix}\right) G_{12}^{20}\left(\gamma \;\middle|\; \begin{matrix} 1 \\ 1/2, 0 \end{matrix}\right) d\gamma\right] \tag{3.54}$$

Finally, using ([136], eqn.(21)), the final expression for $I_8(\bar{\gamma}_{wb})$ can be given as,

$$I_8(\bar{\gamma}_{wb}) = \frac{2(a\bar{\gamma}_{wb})^{v/2}}{v} \left[1 - \frac{2}{\pi}\sum_{i=0}^{\infty}\frac{(-1)^i}{i!}\frac{(k/\lambda)^{1/2}\lambda^{i-1/2}}{\sqrt{\pi}(2\pi)^{\frac{k+\lambda-2}{2}}} G_{2\lambda,k+\lambda}^{k,2\lambda}\left(\frac{(\lambda)^\lambda (k)^{-k}}{(a\bar{\gamma}_{wb})^{vk/2}} \;\middle|\; \begin{matrix} \Delta(\lambda, \frac{1}{2} - i), \Delta(\lambda, -i) \\ \Delta(k, 0), \Delta(\lambda, -i - \frac{1}{2}) \end{matrix}\right)\right] \tag{3.55}$$

Now substituting back eqns.(3.52) and (3.55) to eqn.(3.48) a complete closed form equation under Weibull fading channel can be obtained. As far as the authors are aware this is a novel exact expression of Weibull fading under GFDM without any approximations.

3.2.6 Log-Normal Shadowing Channel

An empirical based path loss measurements study in [140] suggests that the medium-scale variations of the received power, when represented in dB units, follow a normal distribution. Also, another source of attenuation is due to variations of signal strength because of terrain irregularities and obstructions like buildings, which are unavoidable. This kind of model is more realistic that the ones that are commonly used in wireless ad-hoc networks [141]. The linear channel gain may be modeled by a Log-normal random variable e^X, where X is a zero-mean Gaussian random variable with variance σ^2. Log-normal shadowing is usually characterized in terms of its dB-spread, σ_{dB}, which is related to σ by $\sigma = 0.1\ln(10)\sigma_{dB}$ [140].

Table 3.1: Simulation Parameters used for GFDM SER performance

Description	Parameter	Value
Number of Subcarriers	N	64
Number of time slots	M	5
Pulse shape filter	g	RRC
Roll-off factor	α	$\{0.1, 0.9\}$
Length of CP	N_{cp}	8
Channel length	N_{ch}	1
Modulation order	μ	4

3.3 Results and Discussions

In this section we explain the results obtained through simulations and compare them with the analytical expressions under the ZF receiver. Results in [43, 95] prove that the MF receiver outperforms ZF at low SNR values due to the significant influence of noise enhancement and at high SNR values, ZF outperforms MF due to the self-interference created in using MF receiver. The MMSE receiver balances these two effects and simulated results are shown in [95]. Due to the computational complexity of the MMSE receiver, we have chosen to implement the ZF receiver for our analysis to study the effect of NEF.

The system parameters considered for simulations are presented in Table 3.1.

Figure 3.3 compares the theoretical results of equation (3.30) along with simulations for different values of m and $\alpha = 0.1$. Curve (i) e.g., for $m = 1$ is identical to Rayleigh fading conditions and exhibits the same SER performance which matches with previous work [43]. From the figure we can infer that when we increase the value of m from 1 to 3, the SER decreases. For example at 20 dB the error values for $m = 1, 2, 3$ are respectively 0.0566, 0.0150 and 0.0060, i.e. approximately there is a 90% decrease in error from $m = 1$ to $m = 3$.

Figure 3.4 shows the performance of Nakagami fading channel with $\alpha = 0.9$ for different values of m. Similar to the above case, we also observe an error decrease when we increase the m value [curves (i) to (iii)]. For example, in order to obtain an error of 0.01 the values of SNR are 28 dB, 21 dB and 19 dB respectively for $m = 1, 2, 3$.

Figure 3.5 explains the effect of the NEF parameter ξ which plays an important role in GFDM. Comparing curves (i) and (iii) and curves (ii) and (iv) indicates that as the value of the roll-off factor increases from 0.1 to 0.9, there is a significant change in the SER curve due to the fact that as ξ increases there is a wider overlap of the subcarriers which results in an increase in the NEF factor.

Figure 3.6 illustrates the effect of the Rician parameter on the performance of the

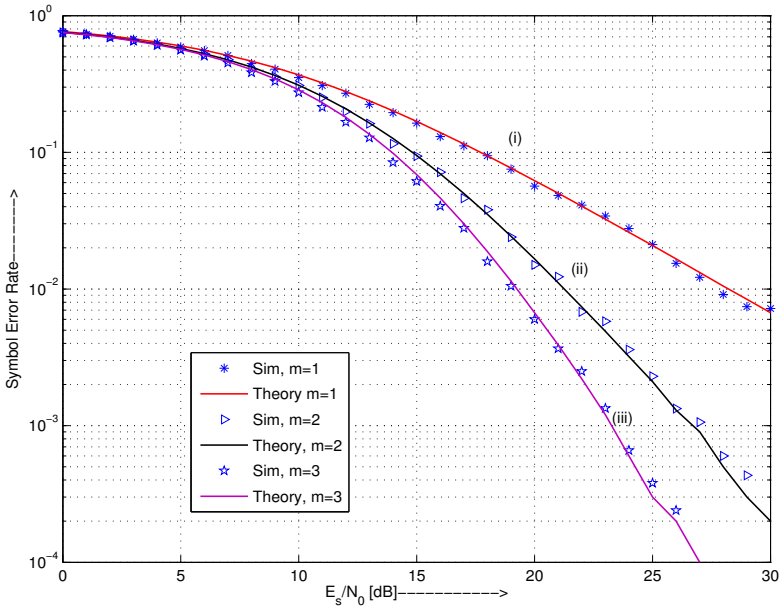

Figure 3.3: GFDM SER performance under Nakagami-m channel with $\alpha = 0.1$

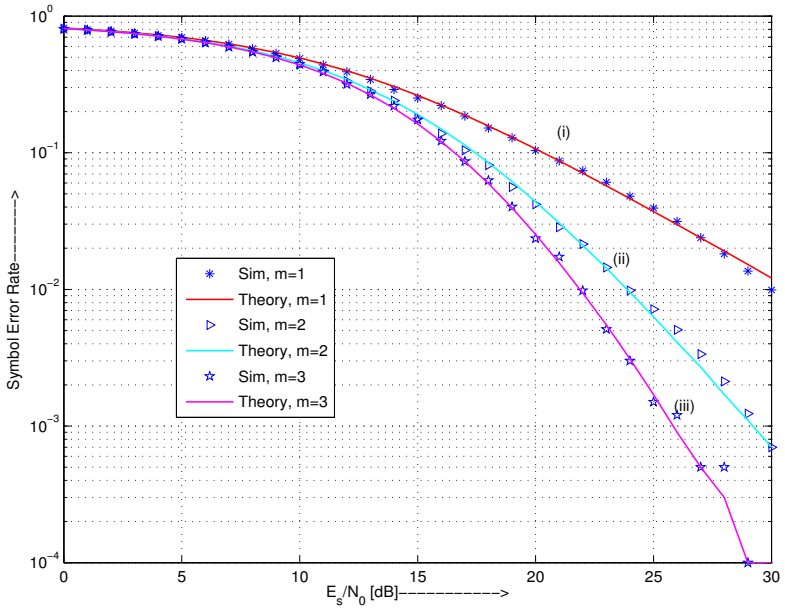

Figure 3.4: GFDM SER performance under Nakagami-m channel with $\alpha = 0.9$

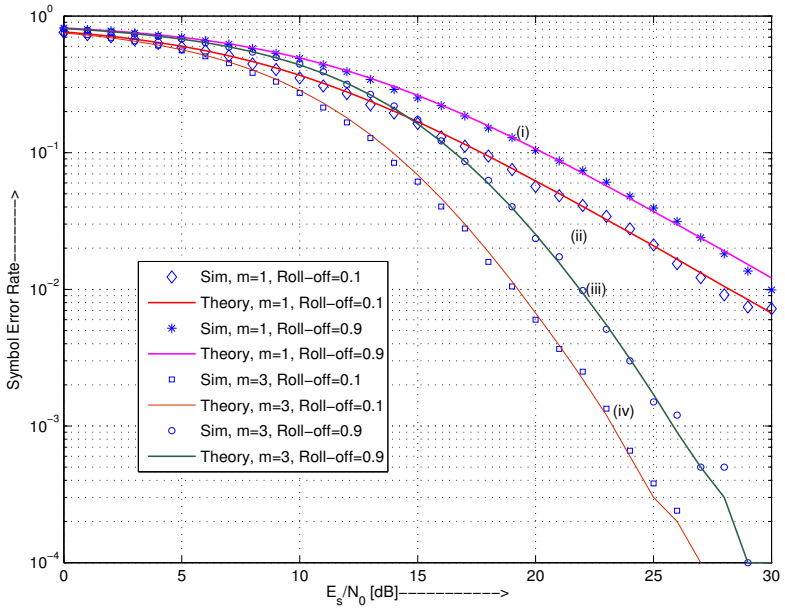

Figure 3.5: Effect of roll-off factor in GFDM performance

system model when $\alpha = 0.1$. Curve (i) indicates that for $K = 0$ (which is equal to the Rayleigh channel) there is a match with the previous results in [43]. As we increase the value of K from 0 to 4, the error decreases [curves (i)-(iv)]. For example, at 25 dB the values of error are 0.0208, 0.0157, 0.0093 and 0.0051 for $K = 0, 1, 2, 3$ respectively. Figure 3.7 shows the performance analysis under the Rician fading channel when $\alpha = 0.9$. Comparing Figure 3.6 and Figure 3.7 the same explanation as in Nakagami-m for the

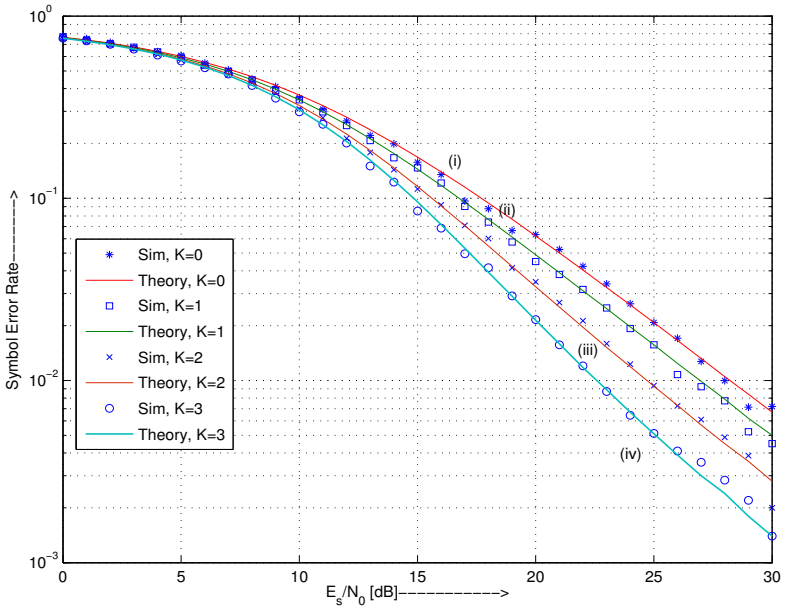

Figure 3.6: GFDM SER performance under Rician-K channel with $\alpha = 0.1$

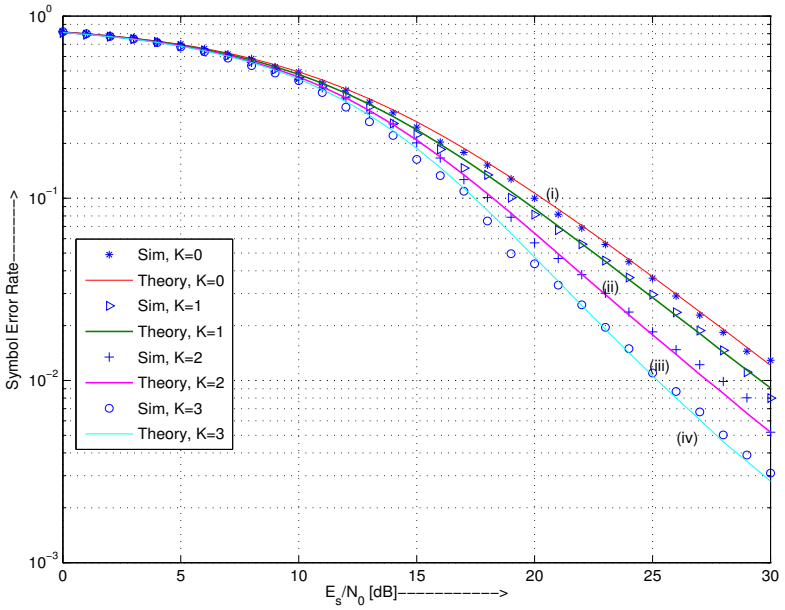

Figure 3.7: GFDM SER performance under Rician-K channel with $\alpha = 0.9$

effect of the roll-off factor holds here as well.

Figure 3.8 compares the theoretical results of equation (3.42) along with simulations for different values of the Hoyt fading parameter q and $\alpha = 0.1$. It is observed that for $q = 1$ which is essentially the Rayleigh fading channel, the result shown in the Figure 3.8 exhibits a match with that of previous work by [43]. Thus we validate the system model developed for the Hoyt fading channel. From the figure, we can infer that as we increase

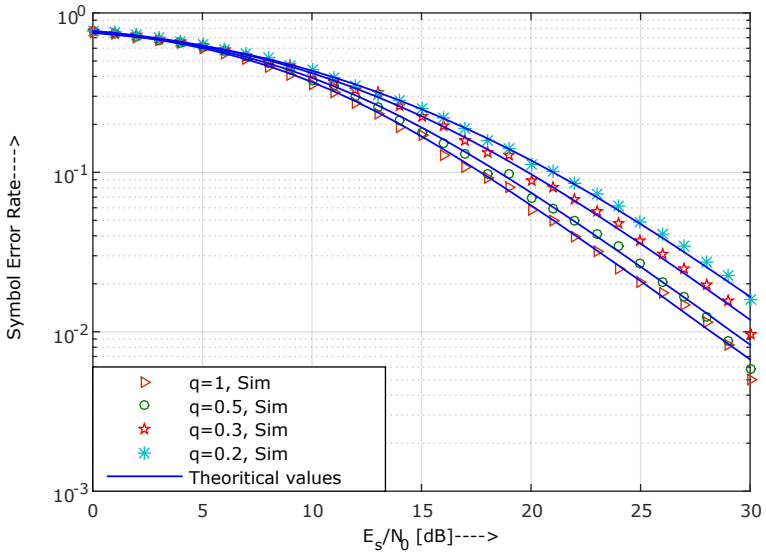

Figure 3.8: GFDM SER performance under Hoyt-q channel with $\alpha = 0.1$

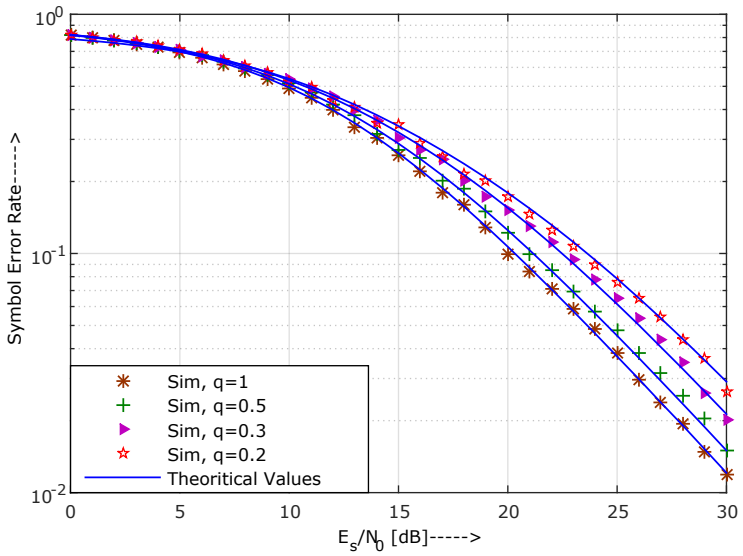

Figure 3.9: GFDM SER performance under Hoyt-q channel with $\alpha = 0.9$

the value of q the SER decreases. Hoyt distribution is commonly used to model signal fading due to strong ionospheric scintillation in satellite communications or in general those fading conditions more severe than Rayleigh. The simulated result analysis as depicted from figure emphasizes that upon decreasing the value of q from $1, 0.5, \cdots 0.2$, the SER performance deteriorates.

Figure 3.9 shows the performance analysis of the Hoyt fading channel with $\alpha = 0.9$ and for different values of Hoyt fading parameter q. We notice that as we decrease the

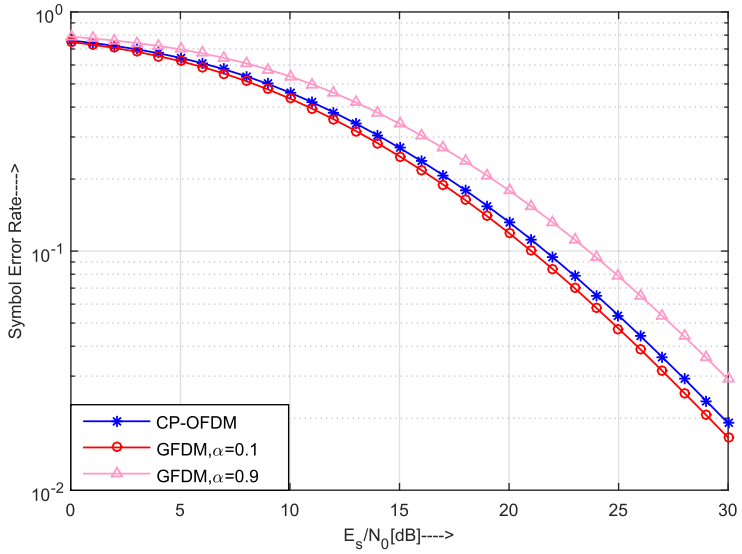

Figure 3.10: Effect of Roll-off factor and comparison to CP-OFDM with Hoyt factor $q = 0.2$

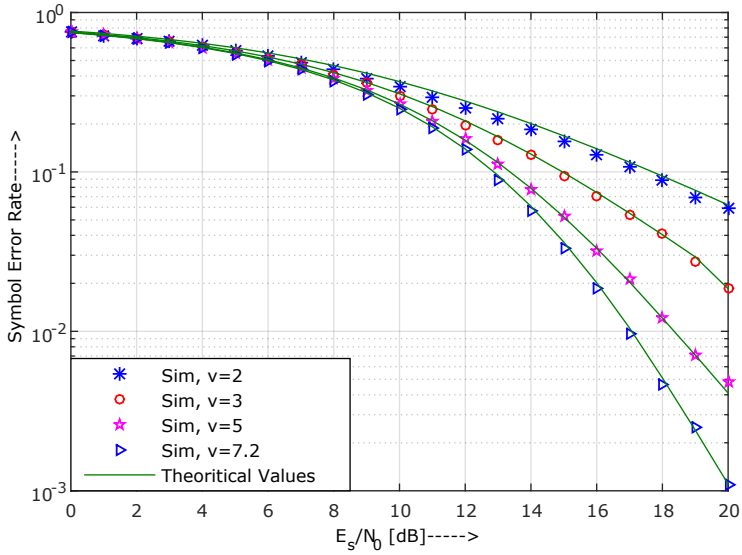

Figure 3.11: GFDM SER performance under Weibull-v channel with $\alpha = 0.1$

value of q, the SER increases. For example at 20dB, the values of SER are 0.0991, 0.1222, 0.1510, 0.1728 for q=1, 0.5, 0.3, 0.2 respectively.Comparing Figure 3.8 with Figure 3.9 illustrates the effect of the NEF ξ parameter which plays an important role in GFDM SER performance. As the roll off factor increases from 0.1 to 0.9 there is a considerable increase in the SER which is due to the wider overlap increase between the subcarriers which in turn increases the NEF ξ. So the prototype pulse shape must be properly chosen

to avoid degradation in system performance.

Figure 3.10 is an important figure which shows the comparison of the GFDM system to that of the conventional CP-OFDM model. SER performance is compared between GFDM and CP-OFDM under the Hoyt fading channel with fading parameter q =0.2. From the figure we observe that pulse shape and NEF play an important role in GFDM system performance as explained earlier. We observe that with $\alpha = 0.1$ the GFDM and OFDM SER curves almost match. On the other hand as we increase the roll-off factor to $\alpha = 0.9$ there is a considerable degradation in system performance. Irrespective of any fading channel, the effect of roll-factor follows the same trend (i.e., as we increase the roll-off factor the probability of error increases).

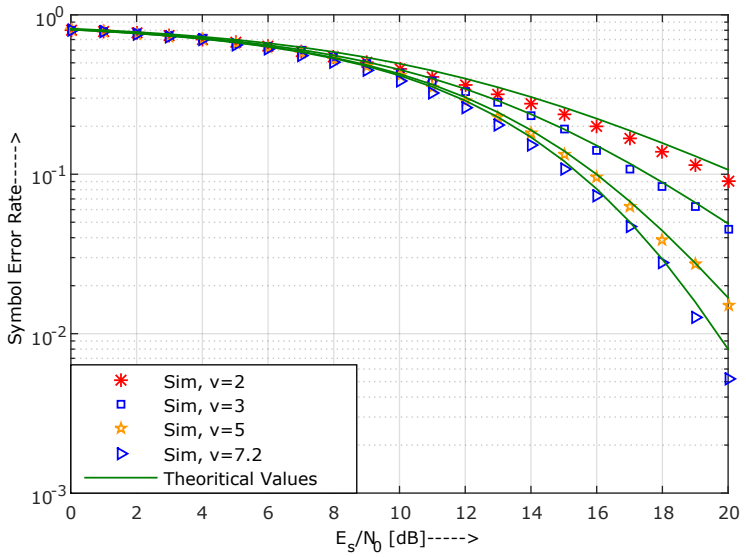

Figure 3.12: GFDM SER performance under Weibull-v channel with $\alpha = 0.9$

Figure 3.11 shows the performance of the Weibull fading channel with $\alpha = 0.1$ for various values of fading parameter v. It is observed that for Weibull fading parameter $v = 2$, the SER curve matches that of the Rayleigh fading channel and exhibits the same SER performance as in [43]. From the figure we can observe that as we increase the fading parameter the SER decreases. For example at 15dB the values of SER for $v = 2, 3, 5, 7.2$ are 0.1525, 0.0937,0.0525,0.335 respectively.

Figure 3.12 illustrates the effect of varying the Weibull fading parameter v for a fixed value of $\alpha = 0.9$. Similar to the above case, we observe that when we increase the fading parameter the error rate decreases.

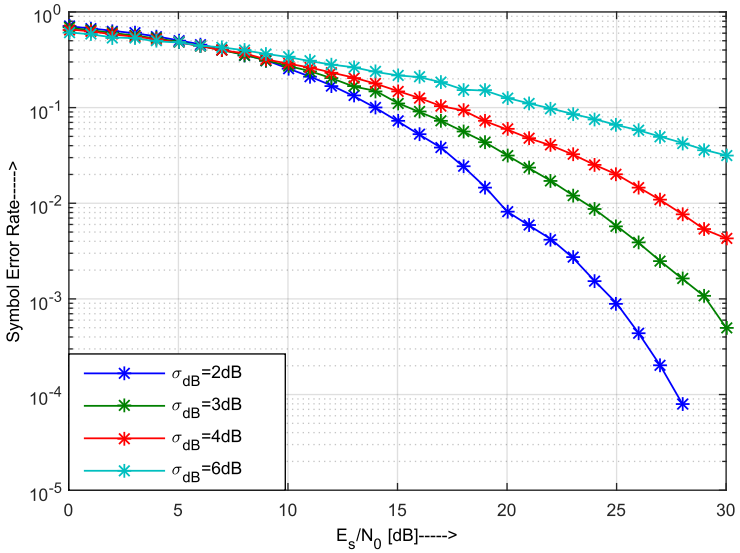

Figure 3.13: GFDM SER performance under Log-Normal Shadowing with $\alpha = 0.1$

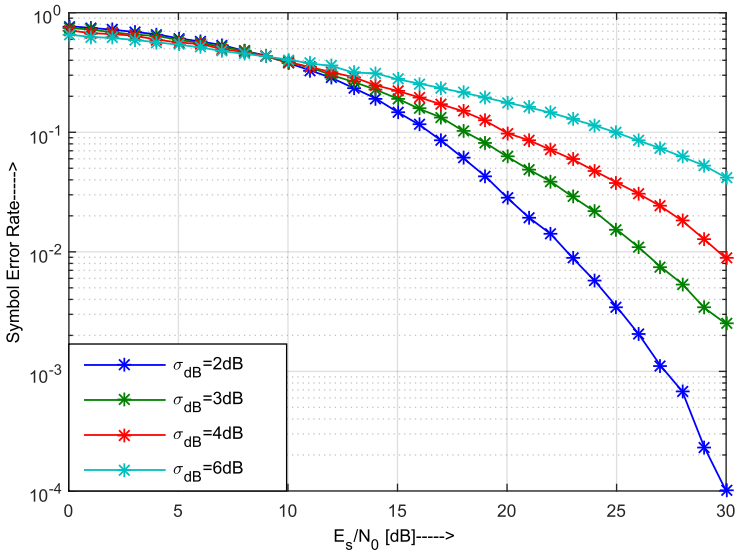

Figure 3.14: GFDM SER performance under Log-Normal Shadowing with $\alpha = 0.9$

Figure 3.13 elucidates the simulation results of Log-Normal shadowing with $\alpha = 0.1$. When the standard deviation of shadowing, σdB, increases from 2dB to 6dB, SER increases as shown in the figure. For example, at $E_s/N_0 = 25$dB, the values of SER are 0.0107, 0.0353, 0.0642, 0.1279 for $\sigma dB = 2, 3, 4, 6$ respectively.

Figure 3.14 shows the simulation results of Log-Normal shadowing with $\alpha = 0.9$. When standard deviation of shadowing, σdB, increases from 2dB to 6dB, SER increases as shown in the figure. For example, at 25dB the values of SER are 0.0336, 0.0688, 0.1119,

0.1682 for $\sigma dB = 2, 3, 4, 6$ respectively. One can observe that there is an error increase when α is increased from 0.1 to 0.9 as expected.

3.4 Chapter Summary

In this chapter a detailed analysis of GFDM performance under different channel environments is performed. The channels investigated are Nakagami-m, Rician-K, Hoyt-q, Weibull-v and Log-Normal Shadowing.

In summary, for Nakagami-m fading, for fixed pulse shaping filter parameter α, we observed a significant SER decrease as the Nakagami fading parameter m increased from the value 1 to 3. This implies that GFDM has better error performance for strong fading conditions. The noise enhancement factor, NEF parameter ξ also showed an error increase as ξ increased for fixed fading parameter m. This is explained by observing that increased ξ means an increased overlap between adjacent subcarriers. Similar effects are observed for Rician fading. When the Rician parameter K is increased we observe a SER decrease for fixed filter parameter α. Similarly, we observe an error increase as the NEF factor ξ increases for fixed fading conditions.

For Hoyt-q fading and fixed pulse shaping filter parameter α, we observed a significant SER decrease as the Hoyt fading parameter q increased from the value 0.2 to 1. Likewise, as the Weibull fading parameter v is increased, there is a significant decrease in the SER for a fixed value of α. This implies that GFDM exhibits better error performance for strong fading conditions than conventional OFDM. For Log-Normal Shadowing and a fixed prototype pulse shape, we observe that as the standard deviation of shadowing, σ_{dB}, increases from 2 dB to 6 dB, the error rate increases.

Another important observation to be noted is that the NEF ξ also shows an error increase as ξ is increased for a fixed fading parameter for any channel. This is explained by observing that an increase in ξ means an increased overlap between adjacent subcarriers.

Finally, an important inference can be drawn from the evaluation of GFDM system performance over various fading channel environments like Nakagami-m, Rician-K, Hoyt-q and Weibull-v. Considering the case of Nakagami-m fading, where the value of m varies

between $m = [\frac{1}{2}, \infty)$. Upon increasing the value of m, the effect of fading reduces and hence a better probability of error floor can be attained. While with Hoyt-q fading channel, when the value of $q = 1$, it is similar to that of Rayleigh fading. But, when the value of q decreases, the amount of fading severity increases and hence the SER performance deteriorates. In case of Rician-K, where the value of K implies the ratio of the power in the direct path to the power in the scattered path. When $K = 0$, the channel tends to follow Rayleigh fading. But as the value of K increases then the power in the direct path increases therefore, an improved error floor can be achieved. Finally, in case of Weibull-v, as the value of v increase the PDF spread decreases which signifies the decrease in channel fluctuations and hence a better performance in SER can be observed.

Chapter 4

Pulse Shaping and PAPR reduction techniques to GFDM

4.1 Introduction and Motivation

In this chapter firstly we analyze the slepian sequences and the usefulness of generating such pulse shaping waveforms to GFDM. In general, the design of such time frequency localized functions are effective in the perspective of communication engineering and is very relevant to GFDM in the context of 5G, where filters with low OOB emission is desired. DPSS has fascinating properties, one such property to our point of interest is the orthogonality between the sequences. Therefore, we make use of this specific characteristic of DPSS to convert the non-orthogonal nature of conventional GFDM system to be orthogonal in nature. Approach of this kind will definitely improve the system performance and will be discussed in the later sections.

High PAPR which is one of the problems in any multicarrier system, also exists with MGFDM and hence understanding the behaviour of PAPR is crucial. Many PAPR reduction techniques are proposed in the literature and three of the most popular ones used in multicarrier systems, such as, OFDM [142] and CDMA [143], are SLM [106], PTS [107] and ZCT [57, 108]. The exploitation of these schemes in GFDM systems is however unexplored. Therefore, in order to reduce the detrimental aspects of PAPR, we have enforced the aforementioned PAPR reduction schemes to the system model.

Going into the details of such PAPR reduction techniques like SLM, where one

GFDM signal with the lowest PAPR is selected for transmission from a set of sufficiently different candidate signals, which all represent the same data sequence. Each candidate signal is actually the result of multiplication of the modulation matrix with a specific phase rotation vector. While in case of PTS technique the transmitter partitions the original data sequence into a number of disjoint sub blocks and then optimally combines the sub blocks obtained after multiplication with modulation matrix to generate a GFDM signal with lowest PAPR for transmission.

In addition to the above standard approaches, we proposed a novel hybrid PAPR reduction technique for MGFDM systems. By combining with the WHT with SLM we exploit the advantages of both methods to reduce the probability of high PAPR values in an MGFDM system. In addition, we apply WHT [144] to the PTS scheme and show that this combination also reduces further the PAPR compared to conventional PTS. The proposed schemes reduce the occurrence of high peaks compared to the conventional SLM and PTS methods. In brief, WHT is a widely used transform technique due to its efficient orthogonal implementation compared to other transforms such as the Discrete Cosine Transform or the Discrete Fourier Transform.WHT only consists of ± 1 and hence is computationally efficient since no multiplications are required. The basic idea in combining these techniques is to reduce PAPR by reducing the autocorrelation of the input sequences.

Multicarrier techniques like GFDM or MGFDM, typically employ IFFT to multiplex transmitted data. We propose a Wavelet based approach which uses an Inverse Discrete Wavelet Transform (IDWT) block for the same purpose. This kind of approach supports a more robust data transmission implementation. The use of wavelets and its potential in the context of OFDM has been studied in [109,110,145]. Wavelet MGFDM (WM-GFDM) exploits the self and mutual orthogonality properties of the wavelet basis functions and increases spectral efficiency due to the exclusion of the CP. For PAPR analysis we have used the Haar, Daubechies, Symlets, Coiflets, Biorthogonal, Reverse Biorthogonal and Discrete Meyer wavelets.

In this chapter first we start with the multi-tapers and how this orthogonal windows are relevant to modify GFDM. We then carry out our analysis in performing PAPR reduction techniques to MGFDM system. Further investigations held on proposing hybrid

methods to reduce PAPR. Finally we deal with the wavelet based MGFDM system and comparison to the existing OFDM, GFDM and IFFT based MGFDM systems in terms of PAPR, SER and power spectral density is examined.

4.2 Slepian Basis

The problem of accurately estimating the frequency representation of a bandlimited signal from a finite sample of available data is a well-established and familiar method. Under the assumption that the data $\{x(n)\}$, $n = 0, 1, \ldots, Q-1$, are Q observations from a stationary, complex, ergodic, zero-mean, Gaussian process with orthogonal increment $dZ(f)$, the frequency representation $\tilde{x}(f)$ can be written as a convolution of the Dirichlet kernel:

$$\tilde{x}(f) = \int_{-1/2}^{1/2} \mathsf{D}_Q(d-\nu) dZ(\nu)$$

where

$$\mathsf{D}_Q(f) = \sum_{n=0}^{Q-1} e^{-j2\pi fn} = \exp[-j\pi f(Q-1)] \frac{\sin Q\pi f}{\sin \pi f}$$

In order to get the optimum frequency representation estimate $\tilde{x}(f)$ within a specified frequency window W we first need to perform an eigen decomposition of the Dirichlet kernel.

Slepian [103] has already done this and for the discrete data case all that is needed is to perform the eigen decomposition of the following Toeplitz system (see Appendix E for more details),

$$\sum_{m=0}^{Q-1} \frac{\sin 2\pi W(n-m)}{\pi(n-m)} v_m^{(l)}(Q,W) = \lambda_l(Q,W) v_n^{(l)}(Q,W) \tag{4.1}$$

In matrix form, the above eigenvalue equation is written as

$$\mathbf{T}(Q,W)\mathbf{v}_{(l)}(Q,W) = \lambda_l(Q,W)\mathbf{v}_{(l)}(Q,W) \tag{4.2}$$

where

$$T(Q,W) = \begin{cases} \frac{sin[2\pi W(m-n)]}{\pi[m-n]} & ; for\ m,n = 0,1,2,\cdots Q-1 \quad m \neq n \\ 2W & ; for\ m = n \end{cases} \tag{4.3}$$

The eigenvectors $v_n^{(l)}(Q,W)$ are the DPSSs or Slepian sequences in honour of David Slepian who first studied their properties. They form an orthonormal expansion basis within W, the analysis window (in normalized units $0 < W < 0.5$) related to the time-bandwidth product QW of the process $\{x(n)\}$. The eigenvalues $\lambda_l(Q,W)$ are a measure of how much signal energy is concentrated in W. Only the first $L \approx 2QW$ Slepian sequences, which all have $\lambda_l(Q,W) \approx 1$ need be used with suitable averaging to obtain the best possible signal energy concentration within the specified finite frequency band W. Thomson [104] has already used them to solve the spectrum estimation problem for a finite data sample.

Both Thomson [104] and Slepian [146], [147], [103], [148] give asymptotic expressions for the computation of the Slepian sequences. From [103] it is noted that the DPSS's satisfy a Sturm-Liouville differential equation leading to

$$\mathbf{S}(Q,W)\mathbf{v}_{(l)}(Q,W) = \theta_l(Q,W)\mathbf{v}_{(l)}(Q,W)$$

where

$$\mathbf{S}(Q,W)_{ij} = \begin{cases} \frac{1}{2}i(Q-i) & ;\, j = i-1 \\ (\frac{Q-1}{2}-i)^2\cos 2\pi W & ;\, j = i \\ \frac{1}{2}(i+1)(Q-1-i) & ;\, j = i+1 \\ 0 & ;\, \text{otherwise} \end{cases}$$

is a tridiagonal matrix with the same eigenvectors as $\mathbf{T}(Q,W)$. One can use LAPACK routines for their direct computation in FORTRAN or C/C++, or the `dpss()` routine for development in MATLAB.

Essentially the DPSS's can be used in a similar manner to other windows (rectangular, Hanning, etc.) in e.g. filtering the incoming data in an GFDM system. For comparison, the first DPSS and the PHYDYAS prototype filter are shown in Figure 4.1 where they are scaled so that

$$\int_0^T g(t)dt = 1 \qquad \text{for } 0 \le t \le T$$

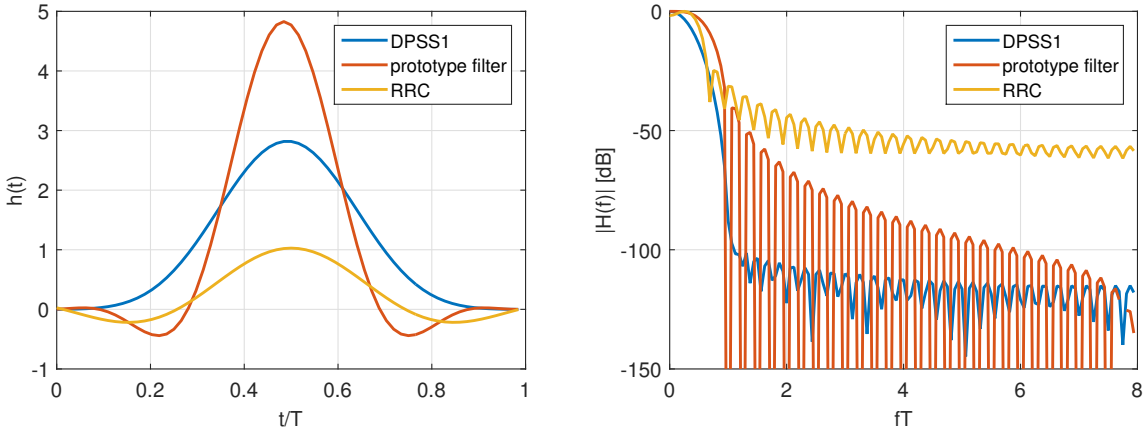

Figure 4.1: Time and frequency domain plots of RRC, DPSS1 and the PHYDYAS prototype filter.

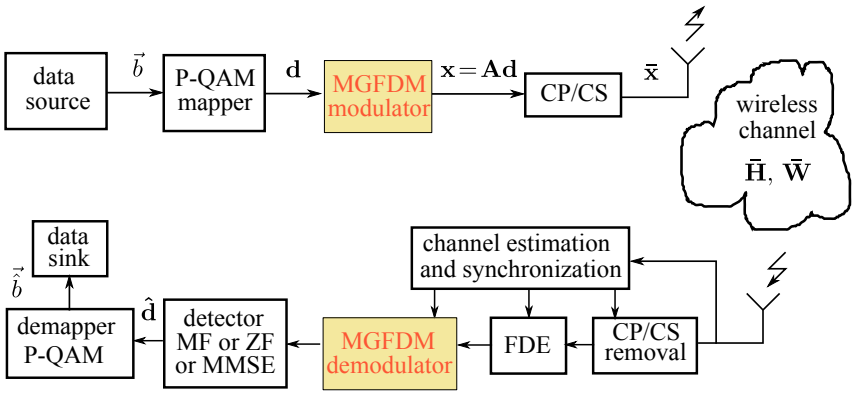

Figure 4.2: Block diagram of MGFDM transceiver

and zero otherwise. Note the deeper sidelobes of the DPSS1, which leads to better overall performance.

4.3 MGFDM system model

GFDM is a non-orthogonal block based multi-carrier transmission model with a total number of N subcarriers that include M subsymbols in each block. The total number of symbols is given by NM. In the following subsections we discuss the system model of MGFDM in detail.

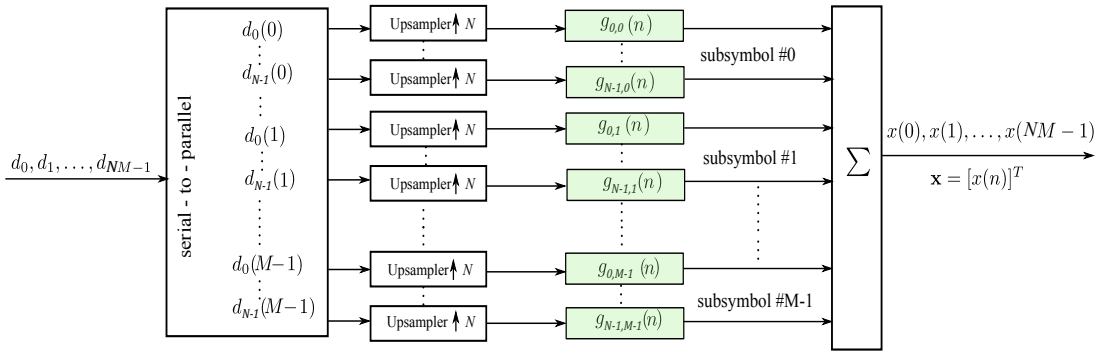

Figure 4.3: Details of MGFDM modulator

4.3.1 Transmitter Model

A block diagram of an MGFDM transceiver system is shown in Figure 4.2. A binary data vector $\vec{b}$, is mapped to constellation points resulting in a data block given by,

$$\mathbf{d} = [d_0(0), ..., d_{N-1}(0), ..., d_0(M-1), ..., d_{N-1}(M-1)]$$

The data block which contains NM elements is divided into M subsymbols $\overrightarrow{d_m} = [d_0(m), d_1(m), ..., d_{N-1}(m)]$ carrying data in the mth subsymbol. Each $d_i(m)$ corresponds to the data symbol that has to be transmitted on the i^{th} subcarrier in the m^{th} time slot. The details of the MGFDM modulator are shown in Figure 4.3.

In MGFDM modulation, the data symbols are first upsampled, passed through the mth taper and are then upconverted to the corresponding subcarrier frequency. Finally, the superposition of all the transmit symbols leads to the MGFDM signal $x(n)$ as,

$$x(n) = \sum_{i=0}^{N-1} \sum_{m=0}^{M-1} d_i(m) g_{i,m}(n) \quad n = 0, 1, .., NM-1 \tag{4.4}$$

where $g_{i,m}(n)$ is given by,

$$g_{i,m}(n) = g_m(n) e^{\frac{j2\pi in}{N}} \tag{4.5}$$

with $g_m(l)$ being the l^{th} coefficient of the m^{th} taper and j specifies the imaginary value $j = \sqrt{-1}$. Both Slepian [103, 146] and Thomson [104] gives asymptotic expressions for the computation of the Slepian DPSS sequences. One can use MATLAB's *dpss*() routine (based on [149]) for development in MATLAB. A recent survey [150] on filters for multicarrier communications also points to current alternative implementation aspects for

DPSS sequences (e.g. [151]). Essentially the DPSSs can be used in a similar manner to other windows (rectangular, Hanning, etc.) in e.g. filtering incoming data. Expressing now all operations: upsampling, pulse shaping, sub-carrier upconversion and superposition in matrix notation, the MGFDM transmitter output samples $\mathbf{x}$ of length $NM \times 1$ can be modelled as [43],

$$\mathbf{x} = \mathbf{A}\mathbf{d} \tag{4.6}$$

where $\mathbf{A}$ is known as the transmitter modulation matrix defined as [134],

$$\mathbf{A} = [\mathbf{G} \;\; \mathbf{E_1 G} ... \mathbf{E_{N-1} G}]$$

where $\mathbf{E_i} = diag\left\{[\mathbf{e_i}^T, ..., \mathbf{e_i}^T]^T\right\}$ is a $NM \times NM$ diagonal matrix whose diagonal elements are comprised of M concatenated copies of the vector $\mathbf{e_i} = [1, e^{j\frac{2\pi i}{N}}, ... \; .., e^{j\frac{2\pi i}{N}(N-1)}]^T$. And matrix $\mathbf{G}$ of size $NM \times M$ is constructed with a slight difference as compared to conventional GFDM in [95]. In MGFDM the columns of matrix $\mathbf{G}$ are the first M tapers from the DPSSs $\mathbf{g} = [g_0, ..., g_{NM-1}]^T$ each of length NM. It is observed that $\mathbf{G}^T\mathbf{G} = \mathbf{I}$, which implies that the tapers are orthogonal to each other reducing the GFDM transmission to be an improved orthogonal system.

We further elaborate the aforesaid explanation with a simple example: where we consider the number of subcarriers N to be 2, and the number of subsymbols M to be 2. Therefore, the size of matrix $\mathbf{A}$ is 4×4 and $\mathbf{G}$ is of 4×2. Hence, the matrix $\mathbf{A}$ can be expressed as

$$\mathbf{A} = [\mathbf{G} \;\; \mathbf{E_1 G} \;\; \mathbf{E_2 G} \;\; \cdots \;\; \mathbf{E_{N-1} G}] \tag{4.7}$$

Since, we have assumed the number of subcarriers and subsymbols to be 2, (4.7) can be reduced to

$$\mathbf{A} = [\mathbf{G} \;\; \mathbf{E_1 G}]_{4\times 4} \tag{4.8}$$

The matrix $\mathbf{G}$ pertaining to GFDM and MGFDM can be expressed as

$$\mathbf{G}_{GFDM} = \begin{bmatrix} g_0 & g_2 \\ g_1 & g_3 \\ g_2 & g_0 \\ g_3 & g_1 \end{bmatrix} \tag{4.9}$$

$$\mathbf{G}_{MGFDM} = \begin{bmatrix} g_0(0) & g_1(0) \\ g_0(1) & g_1(1) \\ g_0(2) & g_1(2) \\ g_0(3) & g_1(3) \end{bmatrix} \tag{4.10}$$

$$e_1 = \begin{bmatrix} 1, & e^{j\frac{2\pi}{2}} \end{bmatrix}^T = \begin{bmatrix} 1, & e^{j\pi} \end{bmatrix}^T = [1, \quad -1]^T \tag{4.11}$$

Therefore, E_1 can be expressed as

$$\mathbf{E}_1 = \begin{bmatrix} 1 & 0 & 0 & 0 \\ 0 & -1 & 0 & 0 \\ 0 & 0 & 1 & 0 \\ 0 & 0 & 0 & -1 \end{bmatrix} \tag{4.12}$$

Lastly, on the transmitter side a CP of length N_{CP} samples is appended to the vector $\mathbf{x}$ in order to form a transmit signal vector $\bar{\mathbf{x}}$ of length $NM + N_{CP}$. The overhead in the case of MGFDM is one CP for all subsymbols while conventional OFDM requires one CP for every symbol, i.e. MGFDM exhibits improved spectral efficiency compared to OFDM. It is important to note that the length of the cyclic prefix has to be longer than the channel delay spread.

4.3.2 Receiver Model

Let $\mathbf{h} = [h_0, .., h_{N_{ch}-1}]^T$ be the channel impulse response of length N_{ch}. The received signal propagating through the wireless channel after removing CP can be modelled as,

$$\mathbf{r} = \mathbf{H}\mathbf{x} + \mathbf{w} \tag{4.13}$$

where $\mathbf{H} = circ\left\{\tilde{h}\right\}$ and $\tilde{h}$ is the zero padded version of $\mathbf{h}$ of the same length as $\mathbf{x}$. The vector $\mathbf{w} \sim \mathcal{CN}(0, \sigma_w^2 I_{NM})$ denotes the complex AWGN samples with noise variance σ_w^2 and I_{NM} is the identity matrix of order NM. Let $\mathbf{r}$ denote a vector which consists of time samples of $r(n)$. Then $r(n) = x(n) * h(n) + w(n)$, where $*$ denotes convolution and $h(n)$ denotes the impulse response of the multipath fading channel. When the channel is AWGN, $\mathbf{H} = \mathbf{I}$.

We have used FDE to handle channel impairments. Channel equalization in the frequency domain can be performed as,

$$\mathbf{y} = \text{IDFT}\left\{\frac{\text{DFT}(\mathbf{r})}{\text{DFT}(\mathbf{h})}\right\} \tag{4.14}$$

The receiver structure for a MGFDM signal can be implemented in several ways: MF, ZF and MMSE. The estimated data symbols of the original transmit data from the received signal $y(n)$ are given by.

$$\hat{\mathbf{d}} = \mathbf{B}\mathbf{y} \tag{4.15}$$

The matrix $\mathbf{B}$ is given as follows [95],

$$\begin{aligned} \text{MF:} \quad & \mathbf{B_{MF}} = \mathbf{A}^H \\ \text{ZF:} \quad & \mathbf{B_{ZF}} = \left(\mathbf{A^H A}\right)^{-1}\mathbf{A^H} \\ \text{MMSE:} \quad & \mathbf{B_{MMSE}} = \left(\frac{\sigma_w^2}{\sigma_d^2}\mathbf{I} + \mathbf{A^H A}\right)^{-1}\mathbf{A^H} \end{aligned} \tag{4.16}$$

where σ_w^2 is the noise variance and σ_d^2 is the data symbols variance. In [95], a good comparison of the three receivers is provided and there are some tradeoffs in choosing the receiver type. For our analysis with multi-tapers, we have chosen ZF and compared the results with that of the derived analytical expressions.

4.4 Performance Analysis

In this section we analyze performance in terms of symbol error rate performance versus E_s/N_0 assuming a ZF receiver with AWGN and Rayleigh fading channel. The SER expression under conventional GFDM and our proposed GFDM model differs by the NEF i.e., equivalent SNR. Under AWGN this is given by:

$$P_{AWGN}(e) = 2\left(\frac{p-1}{p}\right)\text{erfc}(\sqrt{\gamma}) - \left(\frac{p-1}{p}\right)^2 \text{erfc}^2(\sqrt{\gamma}) \tag{4.17}$$

where

$$\gamma = \frac{3R_T}{2(2^\mu - 1)}\frac{E_s}{\xi N_0} \tag{4.18}$$

and

$$R_T = \frac{NM}{NM + N_{CP} + N_{CS}} \tag{4.19}$$

μ is the number of bits per QAM symbol, $p = \sqrt{2^{\mu}}$, N_{CP} and N_{CS} are the length of the cyclic prefix and cyclic suffix respectively, N and M denotes the number of subcarriers and subsymbols respectively, E_s is the average energy per symbol and N_0 is the noise power density. The NEF ξ is given by,

$$\xi = min \left\{ \sum_{n=0}^{NM-1} \left| [\mathbf{B_{ZF}}]_{i,n} \right|^2 \right\} = 1 \qquad ; i = 1, 2, ...N \tag{4.20}$$

ξ in case of GFDM is equal for all subcarriers [43] and plays a crucial role in determining the error performance. More precisely, as the roll-factor of RRC is increased, there will be an overlap between subcarriers which in turn increases the NEF. With the use of DPSSs such an effect can be avoided leading to an overall system performance improvement. Precisely, ξ is 1 (for MGFDM system), selecting the minimum value from the list of summation values generated for each subcarrier.

Similarly, the SER of MGFDM for the Rayleigh fading channel is given by [43],

$$P_{Ray}(e) = 2\left(\frac{p-1}{p}\right)\left(1 - \sqrt{\frac{\gamma_r}{1+\gamma_r}}\right) - \left(\frac{p-1}{p}\right)^2 \left[1 - \frac{4}{\pi}\sqrt{\frac{\gamma_r}{1+\gamma_r}}\text{atan}\left(\sqrt{\frac{1+\gamma_r}{\gamma_r}}\right)\right] \tag{4.21}$$

where γ_r is the equivalent SNR under Rayleigh fading channel given by,

$$\gamma_r = \frac{3R_T\sigma_{ray}^2}{(2^{\mu}-1)}\frac{E_s}{\xi N_0}$$

and

$$\sigma_{ray}^2 = \sigma_r^2 \sum_{j=0}^{N_{ch}-1} |\mathbf{h_j}|^2$$

where $\mathbf{h}$ is the channel impulse response with length N_{ch} and $\sigma_r^2 = 1/2$ the parameter of Rayleigh distributed taps is considered for SER performance.

4.5 PAPR Analysis

One of the drawbacks of any multi-carrier technique is high PAPR. In this section we discuss some of the well known PAPR reduction techniques applied to the MGFDM system model. PAPR is the ratio of peak power to average power of the same MGFDM

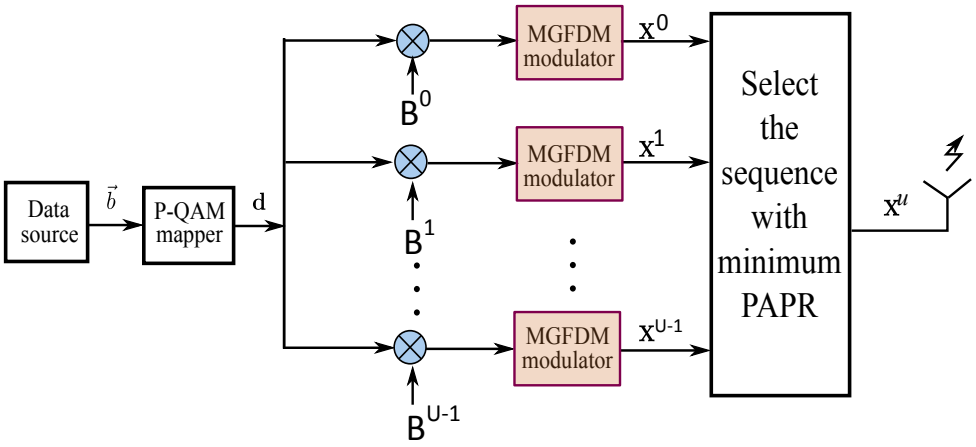

Figure 4.4: Block diagram of SLM Technique

symbol. Mathematically it can be written as,

$$PAPR = \frac{max\left\{|\mathbf{x}|^2\right\}}{E\left\{|\mathbf{x}|^2\right\}} \tag{4.22}$$

where $E\{.\}$ indicates the ensemble average calculated over the MGFDM symbol. The performance of the proposed technique is measured by means of the complementary CCDF of the PAPR, which denotes the probability that the PAPR of a data block exceeds a given threshold ($PAPR_0$) and is expressed as follows,

$$CCDF(PAPR_0) = Pr\left\{PAPR > PAPR_0\right\}) \tag{4.23}$$

Simulations were conducted to verify the performance of the proposed PAPR reduction scheme using the SLM, PTS, and Zadoff-Chu sequence Techniques as is commonly done in such investigations.

4.5.1 Selected Mapping (SLM)

In the SLM technique, a set of sufficiently different candidates of data blocks are generated by multiplying each data block with statistically independent phase sequences and finally selecting the sequence with minimum or lowest PAPR. The amount of PAPR reduction depends on two factors. The number of the phase sequence U and the design of the phase sequence. In this article we have used $\{0, \pi\}$, a binary random sequence. The transmitted symbols of the MGFDM model can be given by equation (4.6).

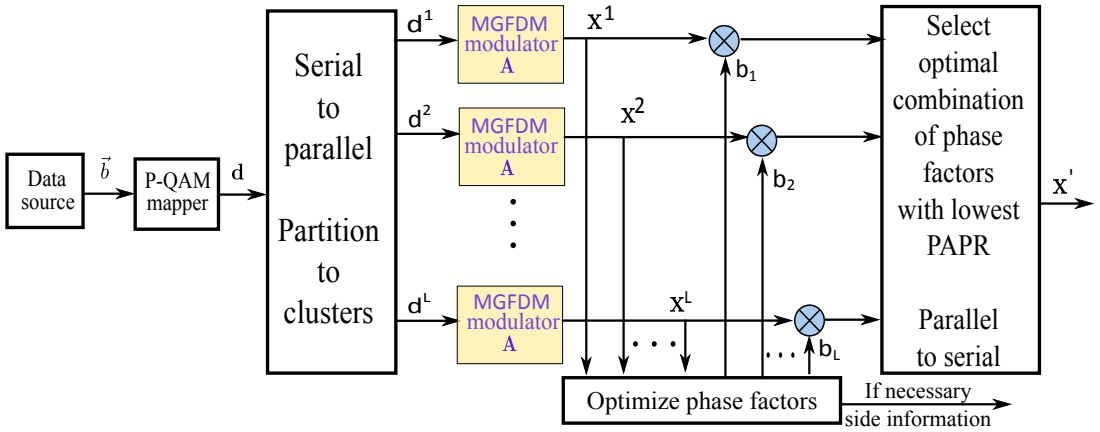

Figure 4.5: Block diagram of PTS Technique

Let $B^u = \{b_u(n)\} \ \forall \ \ u = 0, 1, ..., U-1$ be a vector with NM complex numbers defined such that $|b_u(n)| = 1$, where $|.|$ denotes the modulus operator. The idea of SLM is to multiply the data vector $\mathbf{d}$, element by element with B^u and the resulting vectors passed through MGFDM blocks as shown in Figure 4.4. These produce the corresponding vectors $\mathbf{x}^u$ composed of NM elements given by,

$$x^u(n) = \sum_{i=0}^{N-1} \sum_{m=0}^{M-1} b_u(n) d_i(m) g_{i,m}(n) \tag{4.24}$$

Among these U vectors, the one with the lowest PAPR is selected for transmission. The PAPR can be calculated using (4.22).

4.5.2 Partial Transmit Sequence (PTS)

A typical block diagram of the PTS technique applied to an MGFDM system in order to reduce PAPR is shown in Figure 4.5. In PTS [107], the data block $\mathbf{d}$ is first partitioned into L disjoint subblocks or clusters $\mathbf{d^l}$, $l = 1, 2, ..., L$ such that,

$$\mathbf{d} = \left[\mathbf{d^1}, \mathbf{d^2}, \mathbf{d^3}, \cdots \mathbf{d^L}\right]^T \tag{4.25}$$

Here, it is assumed that each cluster consists of a set of the total number of subcarriers of equal size. Next, the partitioned clusters are passed through the MGFDM blocks. Then, these sequences are combined with the complex phase factors $\mathbf{b} = [b_1, b_2, ..., b_L]$ to minimize PAPR, where $b_l = e^{j\phi_l}$, $\phi_l \ \epsilon \ [0, 2\pi)$. One issue with the PTS approach is

the computational complexity for searching for the optimal phase factors. To reduce this issue, we only considered binary phase factors *i.e.*, $\{\pm 1\}$. The objective of using PTS is to optimally combine these L clusters in a way to minimize PAPR. After selecting the optimal phase factors, the final equation is given by,

$$\mathbf{x}' = \sum_{l=1}^{L} b_l \mathbf{A}\mathbf{d}^{\mathbf{l}} \tag{4.26}$$

The PAPR of this technique can be calculated using (4.22).

4.5.3 Zadoff-Chu sequence

Zadoff-Chu sequences are a class of polyphase sequences having optimum correlation properties such as ideal periodic autocorrelation and constant magnitude [57]. The Zadoff-Chu sequence of length L_c can be defined as,

$$z_v = \begin{cases} \exp\left[j\dfrac{2\pi r}{L_c}\left(\dfrac{v^2}{2} + qv\right)\right] & \text{for } L_c \text{ even} \\ \exp\left[j\dfrac{2\pi r}{L_c}\Big(v(v+1) + qv\Big)\right] & \text{for } L_c \text{ odd} \end{cases} \tag{4.27}$$

where $n = 0, 1, ..., L_c - 1$, q is any integer, r is any integer relative prime to L_c.

The proposed MGFDM system PAPR can be reduced by introducing a precoder matrix $\mathbf{R}$ of size $S \times S$, $S = NM$ given by [108],

$$\mathbf{R} = \begin{bmatrix} r_{0,0} & r_{0,1} & \cdots & r_{0,N-1} \\ r_{1,0} & r_{1,1} & \cdots & r_{1,N-1} \\ \vdots & \vdots & \ddots & \vdots \\ r_{S-1,0} & r_{S-1,1} & \cdots & r_{S-1,S-1} \end{bmatrix} \tag{4.28}$$

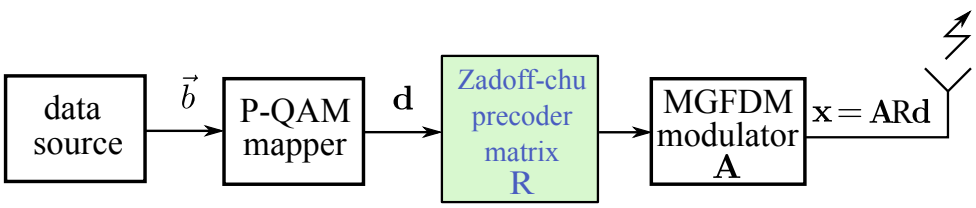

Figure 4.6: Block diagram of ZCT Technique

where $r_{i,j}$ is the i^{th} row and j^{th} column of the precoder matrix. We have used $q = 0$ and $r = 1$ for constructing the matrix R with reordering $v = iS + j$ and filling the row-wise precoding matrix of size $L_c = S \times S$. For even L_c, ZCT can be written as $r_v = \exp[j\pi v^2/L_c^2]$.

These precoder matrices are applied to the complex data vector $\mathbf{d}$ as shown in Figure 4.6. Accordingly, the transmitted data with ZCT precoding can be written as,

$$\mathbf{x} = \mathbf{ARd} \tag{4.29}$$

The PAPR of (4.29) can be calculated using (4.22).

4.6 Proposed Schemes

In this section we discuss the proposed hybrid PAPR reduction technique which combines both conventional SLM and PTS with the Walsh Hadamard precoding technique to reduce the PAPR of GFDM and MGFDM systems. The WHT is a linear orthogonal transform which can be implemented by a butterfly structure. WHT can be conveniently defined by a simple square matrix with elements that have values ± 1. For example, the WHT matrix of second order can be expressed as,

$$W_2 = \frac{1}{\sqrt{2}} \begin{bmatrix} 1 & 1 \\ 1 & -1 \end{bmatrix}$$

4.6.1 Walsh-SLM Technique

The two methods, WHT and SLM, which are used individually to reduce the PAPR of any multicarrier system are combined together with the goal to achieve further PAPR reduction. The combined technique based on the two appropriate methods is shown in Figure 4.7. At the transmitter side, the binary data stream is first mapped to a $P-$QAM mapper unit and is individually multiplied by independent phase sequences followed by the MGFDM modulator. Later on, the kernels of WHT which act as a precoding matrix, are applied to each individual MGFDM block. Finally the sequence with minimum PAPR

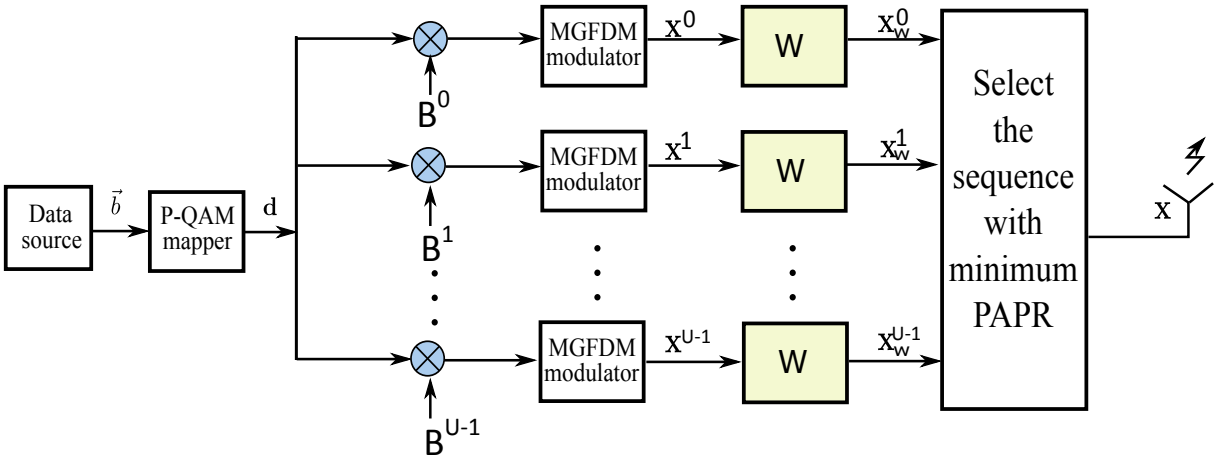

Figure 4.7: Block diagram of Walsh-SLM Technique

is selected and transmitted. The time domain equation of a MGFDM system with the usage of the WHT-SLM technique is given by,

$$x_w^u(n) = \sum_{i=0}^{N-1} \sum_{m=0}^{M-1} \sum_{j=0}^{N-1} w_{j,i} b_u(i,m) d_i(m) g_{i,m}(n) \tag{4.30}$$

where $w_{j,i}$ are the elements of the Walsh-Hadamard matrix,

$$W_i = \frac{1}{\sqrt{N}} \begin{bmatrix} W_{i/2} & W_{i/2} \\ W_{i/2} & -W_{i/2} \end{bmatrix}$$

with $W_1 = [1]$.

In this scheme each data block is multiplied by U different phase vectors, each of length KM. Thus the u^{th} sequence after multiplication with the corresponding data block is given by,

$\mathbf{D}^u = \{d_i(m)b_u(i,m)\}\ \forall\ k = 0,..,K-1; m = 0,..,M-1; u = 0,..,U-1$, a vector of length NM.

In matrix notation Equation (4.30) can be written as,

$$\mathbf{X}_w^u = \mathbf{WAD}^u = \mathbf{Wx^u} \tag{4.31}$$

where $\mathbf{W} = \frac{1}{\sqrt{N}}\mathbf{I_M} \otimes \mathbf{W_i}$, $\otimes$ is the matrix Kronecker product. Note that $\mathbf{x^u}$ is the matrix

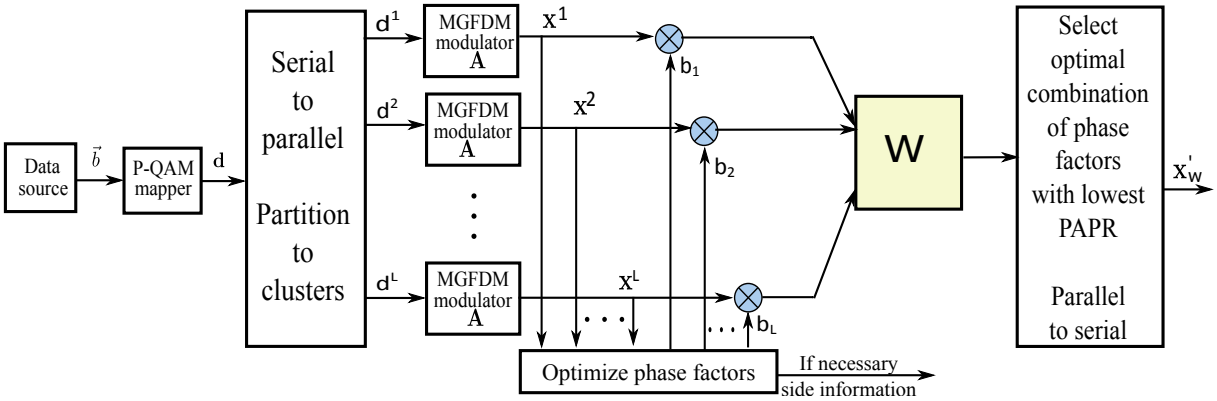

Figure 4.8: Schematic of Walsh-PTS precoding Technique

notation of Equation (4.24).

4.6.2 Walsh-PTS Technique

The schematic of the WHT-PTS precoding technique is shown in Figure 4.8. This method consists mainly of four major parts. Initially the data is partitioned into a number of clusters and passed through the MGFDM modulator blocks. Secondly, each sub block is multiplied by a phase factor as explained in the PTS section. Thirdly, all the sub blocks are added and precoded with the WHT matrix as depicted in Figure 4.8. Finally, the best phase factor with minimum PAPR is selected and transmitted through the wireless channel. The transmitted signal after passing through the Walsh-Hadamard block is given by,

$$\mathbf{x}'_{\mathbf{w}} = \mathbf{W} \sum_{l=1}^{L} b_l \mathbf{A} \mathbf{d}^{\mathbf{l}} = \mathbf{W} \mathbf{x}' \tag{4.32}$$

4.7 WM-GFDM Model

A simple transmitter block diagram of WM-GFDM is shown in Figure 4.9 [152]. In WM-GFDM the complex exponentials of conventional GFDM are replaced by wavelets at different scales j and time location i. These wavelet functions are generated by the translation and dilation of a unique function known as the Mother Wavelet denoted as

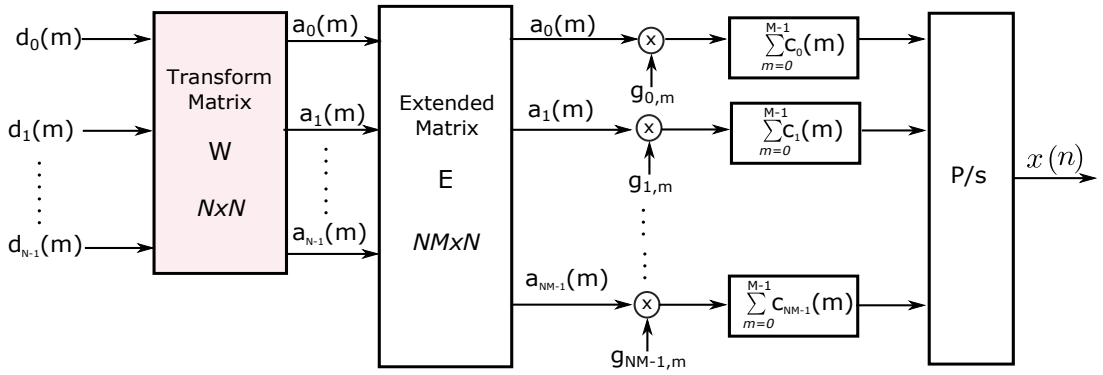

Figure 4.9: Transmitter Block Diagram for Wavelet Multitaper GFDM

[153],

$$\psi_{J,N}(n) = S_0^{-j/2}\psi(S_0^{-j/2}n - i\tau_0) \tag{4.33}$$

and the members of the wavelet family are orthonormal

$$\langle \psi_{p,q}(n), \psi_{r,s}(n) \rangle = \begin{cases} 1 & \text{if } \; p = r, q = s \\ 0 & \text{otherwise} \end{cases} \tag{4.34}$$

A widely used choice of S_0 and τ_0 are $S_0 = 2$ and $\tau_0 = 1$.

The transmit signal $x(n)$ of one WM-GFDM block can then be given by,

$$x(n) = \sum_{m=0}^{M-1} \underbrace{\sum_{i=0}^{N-1} \sum_{j=0}^{\infty} d_i(m)\psi_{J,N}(n)}_{a_i(m)} g_{i,m}(n) \tag{4.35}$$

where $g_{i,m}(n)$ is given by equation (6.26). Expressing all operations in matrix notation following [152], the transmitted signal of block size NM can be written as,

$$\mathbf{x} = diag\left\{ \mathbf{G_{Tx}} \left(\mathbf{EWD} \right)^{\mathbf{T}} \right\} \tag{4.36}$$

where $(.)^T$ indicates the matrix transpose operation and $diag(.)$ indicates the extraction of the diagonal elements of a matrix. Next, the data block $\mathbf{d}$ is reshaped by a serial to parallel conversion to the matrix $\mathbf{D}$ given by, $\mathbf{D} = \{d_i(m)\}_{N \times M}$. $\mathbf{W}$ is the IDWT matrix of size $N \times N$ expressed by different wavelets as discussed in section 4.7.1,

Note that for the conventional GFDM model using the IFFT block, $\mathbf{W}$ can be

expressed as $\mathbf{W} = \left\{ e^{j2\pi \frac{i}{N} n} \right\}_{N \times N}$ with indices $(i, n) \in [0, N-1]$. The extended matrix $\mathbf{E}$ of size $NM \times M$ is given by an M times repetition of the identity matrix $I_{N \times N}$,

$$\mathbf{E} = [I_{N \times N}, ..., I_{N \times N}]^T \tag{4.37}$$

The prototype filter matrix is given by, $\mathbf{G_{Tx}} = \{g_m(n)\}_{NM \times M}$ with $g_m(n)$ the m^{th} taper of length NM for MGFDM and $g_m(n) = g[(n - mN) \bmod NM]$ for conventional GFDM.

Expression (4.36) can also be expressed in a more convenient form as,

$$\mathbf{x} = \mathbf{Ad} \tag{4.38}$$

where $\mathbf{A}$ is a $NM \times NM$ transmitter modulation matrix encompassing all signal processing steps involved in the modulation [134]. Let us denote $\mathbf{W_{Tx}} = \mathbf{WE^T}$. Since only the diagonal elements of the matrix product are transmitted, the n^{th} element of $x(n)$ depends only on the n^{th} row of $\mathbf{G_{Tx}}$, denoted by $\mathbf{g_{Tx,n}}$, the data matrix $\mathbf{D}$ and the n^{th} column of $\mathbf{W_{Tx}}$ given as $\mathbf{w_{Tx,n}}$. Consequently, $\mathbf{x}$ can be written as,

$$x(n) = \mathbf{g_{Tx,n}} \mathbf{D} \mathbf{w_{Tx,n}}$$

or, equivalently

$$x(n) = ((\mathbf{w_{Tx,n}})^T \otimes \mathbf{g_{Tx,n}}) \mathrm{vec}(\mathbf{D}) \tag{4.39}$$

where $\otimes$ denotes the Kronecker product and vec($\mathbf{D}$) indicates the operation of stacking all columns of $\mathbf{D}$ into a vector.

4.7.1 Construction of Wavelets

Wavelet theory offers many orthogonal filters with good time-frequency properties [154, pp. 115]. We investigated various wavelets namely Haar, Daubechies (dBN_v, with vanishing moments of order N_v), Symlet, Coiflets, Biorthogonal, Reverse Biorthogonal and Discrete Meyer wavelets for PAPR analysis. The construction of wavelet matrix $\mathbf{W}$, for these wavelets can be found in [154]. For example the wavelet transform matrix for both Haar and Daubechies (dB2)is given by [155],

$$\mathbf{W_{Haar}} = \begin{bmatrix} W_{N/2\times N/2} \otimes [1,1] \\ I_{N/2\times N/2} \otimes [1,-1] \end{bmatrix}$$

where $\otimes$ indicates the Kronecker product and

$$W_{2\times 2} = \frac{1}{\sqrt{2}} \begin{bmatrix} 1 & 1 \\ 1 & -1 \end{bmatrix}$$

$$\mathbf{W_{db2}} = \begin{bmatrix} h_0 & h_1 & h_2 & h_3 & 0 & 0 & \cdots & 0 & 0 \\ 0 & 0 & h_0 & h_1 & h_2 & h_3 & \cdots & 0 & 0 \\ \vdots & \vdots & \vdots & \vdots & \vdots & \vdots & \cdots & \vdots & \vdots \\ h_2 & h_3 & 0 & 0 & 0 & 0 & \cdots & h_0 & h_1 \\ e_0 & e_1 & e_2 & e_3 & 0 & 0 & \cdots & 0 & 0 \\ 0 & 0 & e_0 & e_1 & e_2 & e_3 & \cdots & 0 & 0 \\ \vdots & \vdots & \vdots & \vdots & \vdots & \vdots & \cdots & \vdots & \vdots \\ e_2 & e_3 & 0 & 0 & 0 & 0 & \cdots & e_0 & e_1 \end{bmatrix} \tag{4.40}$$

where,

$$\{h_0, h_1, h_2, h_3\} = \left\{ \frac{1+\sqrt{3}}{4\sqrt{2}}, \frac{3+\sqrt{3}}{4\sqrt{2}}, \frac{3-\sqrt{3}}{4\sqrt{2}}, \frac{1-\sqrt{3}}{4\sqrt{2}} \right\}$$

are the Low-Pass Filter (LPF) coefficients (h_v) of length four. The corresponding High Pass Filter (HPF) coefficients e_n are obtained by,

$$e_v = (-1)^v h_{N_v+1-v} \tag{4.41}$$

where v is the index coefficient, N_v is the vanishing moments (i.e., 2 for dB2). The choice of wavelet functions depends on the applications. The simplest, basic and oldest orthonormal wavelet is the Haar wavelet. It conserves the energy of the signal and is also a memory efficient wavelet. Daubechies dBN_v wavelets are of shorter duration and smoother than the Haar ones. Improved versions of the Daubechies wavelets, the Symlets, denoted by $symN_v$, with increased symmetry have been developed [156]. Coiflets, which are derived from the Daubechies are a bit more complex and follow the same structure as the Haar and Daubechies. Biorthogonal wavelets are the generalization of orthogonal wavelet systems which are more flexible and easy to design. A comparison between the orthogonal and biorthogonal wavelets is given in [157].

Table 4.1: Channel delay profile used for simulations

jth sample	0	1	2	3	4	5	6	7
Delay (s)	$0\times t_s$	$1\times t_s$	$7\times t_s$	$18\times t_s$	$35\times t_s$	$54\times t_s$	$86\times t_s$	$125\times t_s$
h_j[dB]	0	-1.5	-1.4	-0.6	-9.1	-7	-12	-16.9

4.8 Results and Discussions

In this section we would be presenting the results and significance in modifying the conventional GFDM through simulations. Firstly we demonstrate the results obtained for MGFDM under AWGN and Rayleigh fading channels through simulations and compare them with the analytical results for the ZF receiver. The channel delay profile based on the Extended Vehicular A (EVA) [83] has been considered to evaluate SER performance and is given in Table 4.1. The sampling frequency and the sampling period are respectively given by $f_s = 180MHz$ and $t_s = \frac{1}{f_s}$ [158]. The system parameters used in the simulations for evaluating the MGFDM system performance under Rayleigh fading channel are presented in Table 4.2.

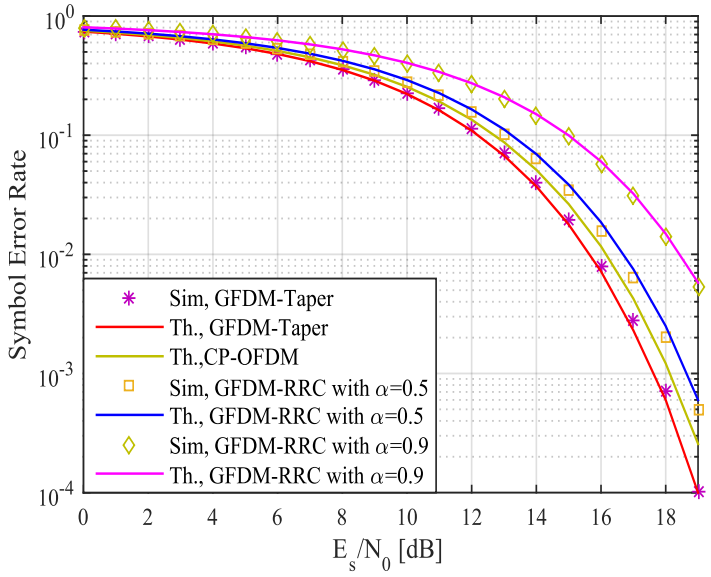

Figure 4.10: MGFDM performance comparision with AWGN channel

Figure 4.10 shows the SER performance comparison under AWGN channel for the proposed method and the existing literature. From the figure we can infer that GFDM using prolate spheroidal windows outperforms both CP-OFDM and conventional GFDM.

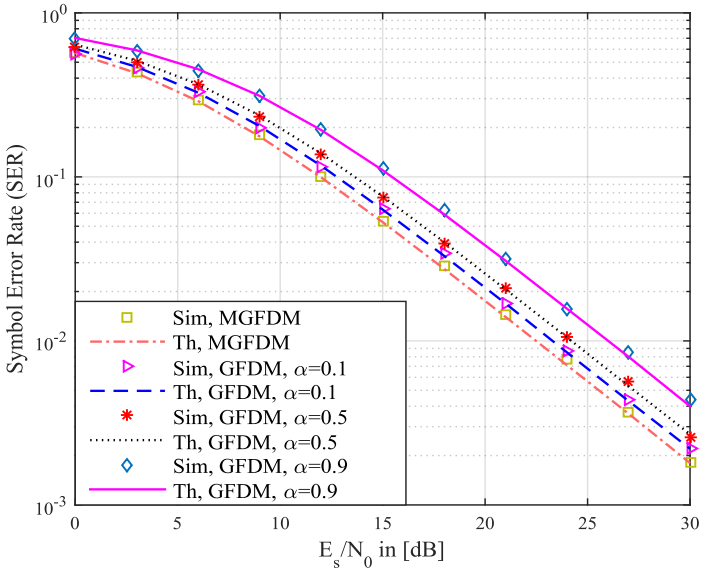

Figure 4.11: MGFDM performance comparision in Rayleigh fading channel

Table 4.2: Simulation parameters generated for evaluating MGFDM SER performance

Description	GFDM/OFDM	GFDM-DPSS
Number of Subcarriers, N	64	64
Number of time slots, M	5/1	5
Pulse shape filter, g	RRC/Rectangular	DPSS
Roll-off factor, α	$\{0.1, 0.5, 0.9\}$ /-	-
Length of CP, N_{cp}	8	8
Modulation order, μ	4	4

Also the theoretical analysis exactly matches with the simulated SER for different values of E_s/N_0. In conventional GFDM there is a trade-off to select the RRC filter roll-off factor for better ISI and ICI effects [95]. With the use of the prolate windows this is not relevant anymore. Also evident from the figure is the effect of the NEF in the case of conventional GFDM. As we increase the RRC roll-off factor from 0.5 to 0.9 the SER increases considerably.

The behaviour of SER against E_s/N_0 for different models under Rayleigh fading channel conditions is shown in Figure 4.11. Clearly, the derived analytical expressions match with the simulated values. Similar to the AWGN channel, GFDM using prolate windows outperforms conventional GFDM. Due to the non-orthogonal nature of the con-

ventional GFDM model there is a decrease in performance when compared to MGFDM, but with the use of prolate spheroidal windows we can reduce this effect (Figure 4.11). For example, an SER of 0.01 is achieved at 22.5dB, 23.2dB, 24.1dB and 26dB for MGFDM, GFDM with $\alpha = 0.1, 0.5, 0.9$ respectively. The results observed are promising despite the hardware implementation complexity of multi-tapers and the fact that as originally computed they are not Nyquist filters. The work by Nigam et.al. [151] corrects the non-Nyquist aspect and improvements in technology are expected to do the same for the implementation complexity.

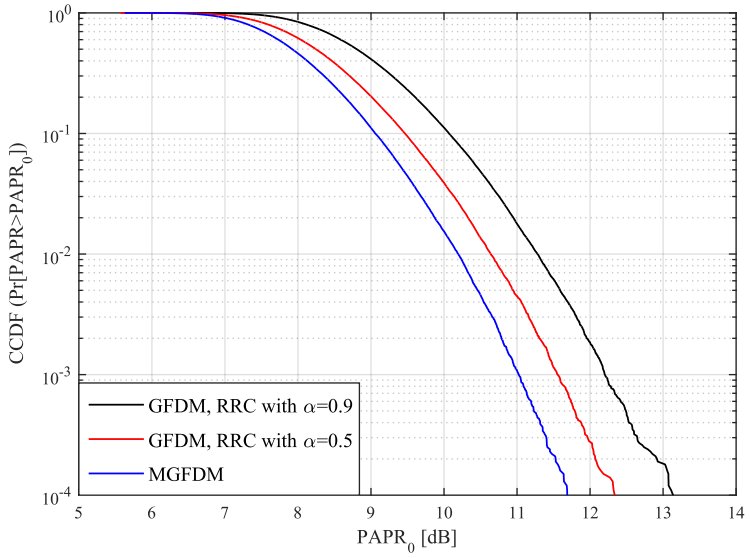

Figure 4.12: PAPR comparison for conventional GFDM and MGFDM with N=64, M=5, 16-QAM.

Simulations were conducted to verify the performance of the proposed PAPR reduction schemes. The simulation parameters used for IFFT based GFDM, MGFDM and

Table 4.3: Parameters used for PAPR reduction schemes

Description	Value
Number of subcarriers, N	32, 64, 128, 256
Number of subsymbols, M	5
Pulse shape filter, g	DPSS, RRC $\{\alpha = 0.1, 0.5, 0.9\}$
Modulation order, μ	2, 4, 5, 6

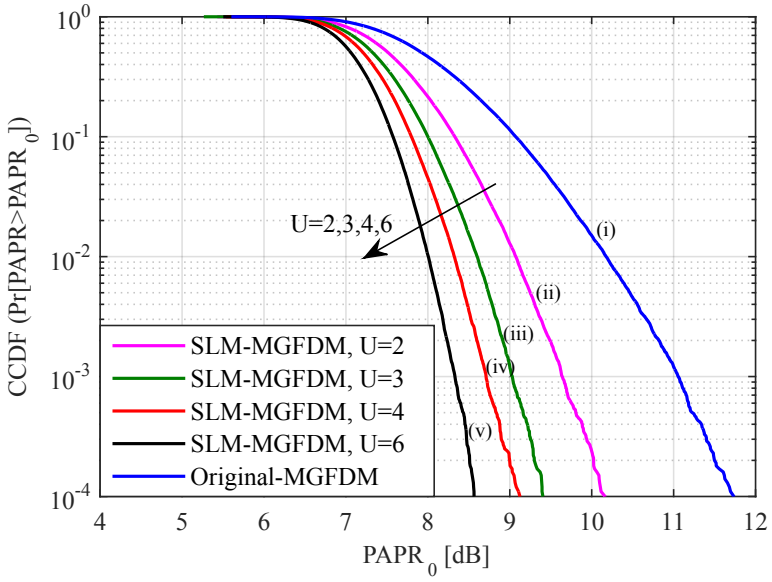

Figure 4.13: PAPR performance of SLM-MGFDM with $U \epsilon \{2, 3, 4, 6\}$ for N=64, M=5, 16-QAM.

WM-GFDM are documented in Table 4.3. We can also do a comparison of conventional GFDM using the RRC with roll-off factor $\alpha = 0.5$ and $\alpha = 0.9$, with the proposed WM-GFDM. 10^5 transmitted blocks of symbols were used.

Figure 4.12 compares the 16-QAM PAPR for both MGFDM and conventional GFDM, where GFDM uses RRC with roll-off factors $\alpha = 0.5$ and $\alpha = 0.9$. Clearly MGFDM outperforms conventional GFDM for both roll-off factor values used. Due to the orthogonal nature of the multi-tapers in MGFDM a superior PAPR performance compared to conventional GFDM is observed. It is also of interest to note that as the roll-off factor is increased from 0.5 to 0.9, the PAPR performance becomes worse. For comparison, consider the PAPR value that exceeds the threshold value with probability 0.01% i.e., $Pr\{PAPR > PAPR_0\}) = 10^{-4}$. MGFDM reduces PAPR by an additional 1.4 dB and 0.6 dB compared to conventional GFDM with $\alpha = 0.9$ and $\alpha = 0.5$ respectively.

Figure 4.13 shows the CCDF of the MGFDM system using SLM. We have used a binary random sequence for improving PAPR performance. From the figure we can see that as the value of U increases the PAPR decreases (curves *(ii)-(v)*). In other words, due to an increase in U the occurrence probability of low PAPR is higher. However, the complexity increases with the increase of U. So there is a trade off between performance and

computational complexity. Curve *(i)* shows the original MGFDM system, for comparison.

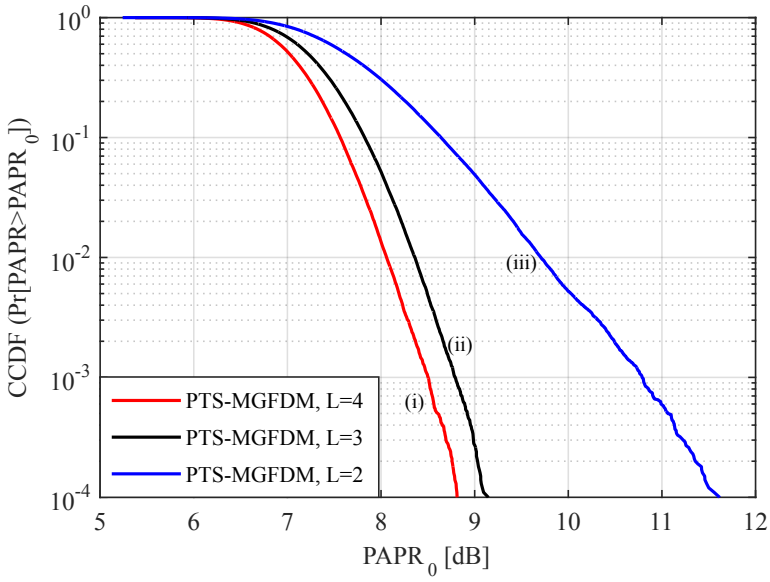

Figure 4.14: PAPR performance of PTS-MGFDM with $L \epsilon \{2, 3, 4\}$ for N=64, M=5, 16-QAM.

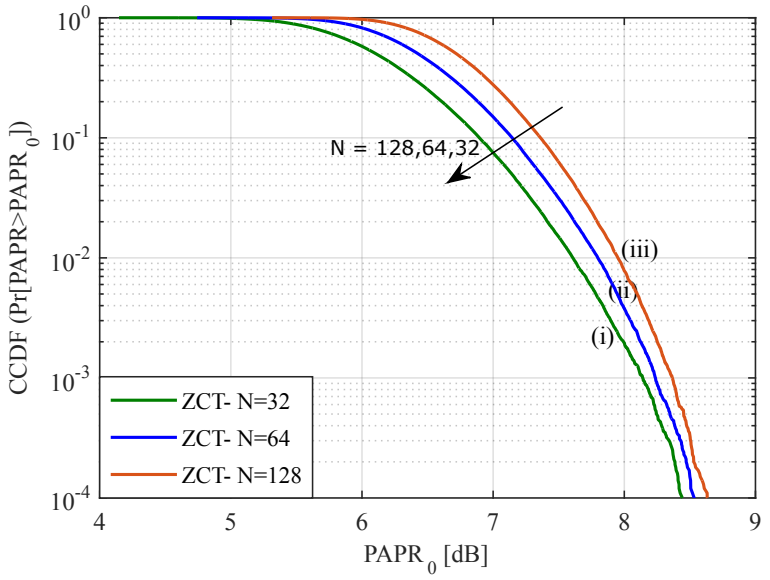

Figure 4.15: PAPR performance of 16-QAM, ZCT-MGFDM for varying N=32,64,128 and M=5.

Figure 4.14 shows the CCDF for the PTS technique in MGFDM systems for different values of L, where L denotes the number of clusters. It is evident that as we

increase the number of clusters, the PAPR values decrease (curves *(i)-(iii)*). For comparison, consider the PAPR value that exceeds the threshold value with probability 0.01% i.e., $Pr\{PAPR > PAPR_0\}) = 10^{-4}$. MGFDM-PTS with $L = 4$ reduces PAPR by an additional 0.3 dB and 2.7 dB compared to MGFDM-PTS with $L = 3$ and $L = 2$ respectively. Here also, the gain in the PAPR performance is at the cost of computational complexity and is proportional to the number of clusters L. The effect of number of subcarriers N (curves *(i)-(iii)*) on the PAPR performance under ZCT is shown in Figure 4.15. PAPR decreases as we decrease the N value from 128 (curve *(i)*) to 32 (curve *(iii)*). At CCDF of 10^{-2} the values of PAPR are 7.95dB, 7.80dB and 7.61dB for N=128, 64 and 32 respectively.

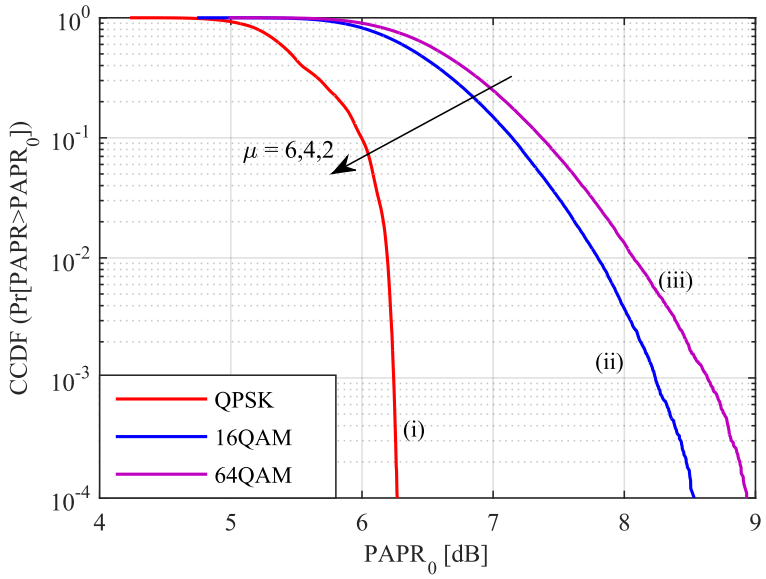

Figure 4.16: PAPR performance of ZCT-MGFDM for varying $\mu \in \{2, 4, 6\}$ and N=64, M=5.

Figure 4.16 shows the PAPR plot for ZCT-MGFDM systems for different modulation order $\mu = 2, 4, 6$ with $N = 64$ and $M = 5$. As we decrease the value of μ the PAPR values decrease as shown in the figure. Typical values at CCDF = 10^{-4} are 6.25 dB, 8.52 dB and 8.92 dB for Quadrature Phase Shift Keying (QPSK), 16-QAM and 64-QAM respectively.

The CCDF of the PAPR for the three techniques used for MGFDM systems is shown in Figure 4.17. From the figure we can observe that the three techniques (curves *(i)-(iii)*) improve considerably PAPR reduction performance compared to the original MGFDM system (curve *(iv)*). For example at CCDF of 10^{-4}, the PAPR gain of 3.3 dB, 3 dB

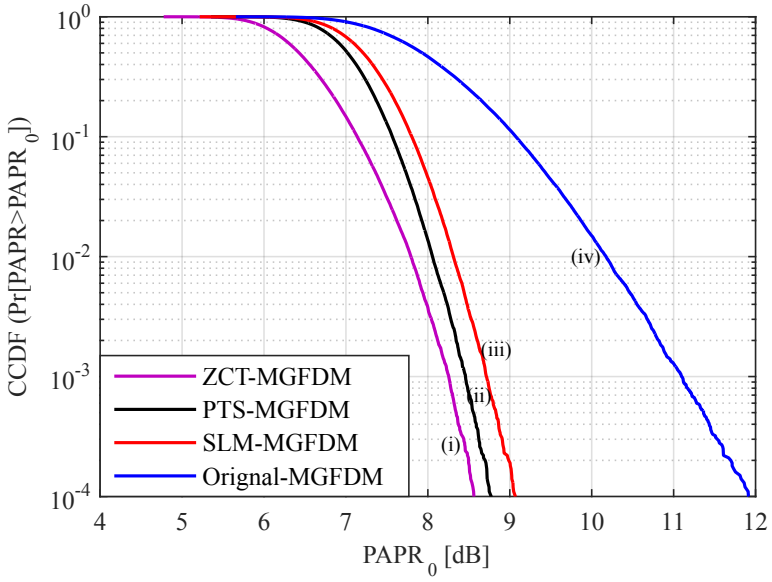

Figure 4.17: PAPR comparison with SLM (U=4), PTS (L=4), ZCT for MGFDM with N=64, M=5, 16-QAM.

and 2.7 dB is achieved by using ZCT, PTS (L=4) and SLM (U=4) respectively when compared to the original MGFDM system.

The simulation results of the CCDF and PAPR of the original MGFDM system and the proposed hybrid WHT- SLM are depicted in Figure 4.18. We have chosen the phase sequence of order U=6, 16-QAM, K=64, M=5 for simulation purpose. The results reveal the benefit of using WHT as a precoding technique in combination with the SLM technique. More specifically, there is a 0.2dB decrease in the hybrid technique when compared to SLM- MGFDM and a 3.2dB decrease to the original MGFDM at a CCDF value of 10^{-4}. Moreover, it can be shown that there is a significant decrease in the PAPR of WHT- SLM by increasing the phase sequence order to $U = 2, 3, 4$. This is similar to Figure 4.13, where, the PAPR of WHT- SLM will decrease as the value of U increases from 2 to 4. Also, the variation of PAPR for different μ values of the modulation order, can be easily plotted. For comparative analysis, we have investigated the performance of WHT- PTS PAPR reduction technique based on the system model as illustrated in Figure 4.8. We have considered the parameters $L = 3$ sub-blocks, $\mu = 4$, 64 subcarriers and 5 subsymbols for PAPR analysis. In addition, we show the corresponding analysis for a conventional GFDM system with the PTS technique, which uses RRC as a prototype filter with roll-off factors $\alpha = 0.9$ and 0.5. It is obvious from the Figure 4.19 that there

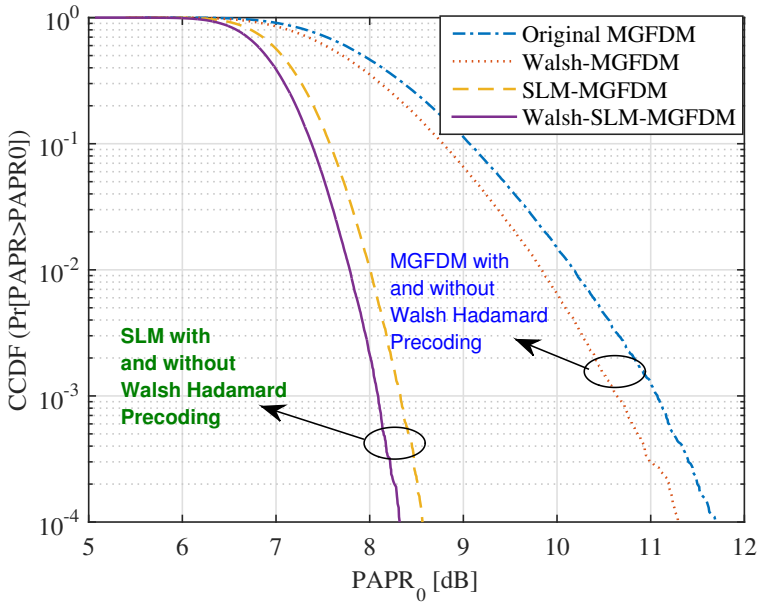

Figure 4.18: PAPR performance of SLM method for various techniques with 16-QAM, U=6, K=64, M=5.

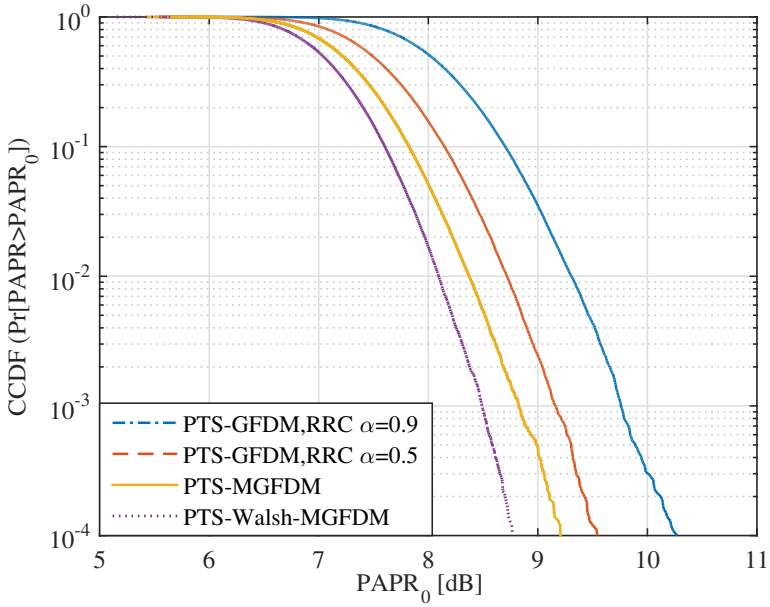

Figure 4.19: PAPR performance of PTS technique for various techniques with 16-QAM, L=3, K=64, M=5.

is a significant reduction in PAPR by applying the Walsh precoding method to the PTS technique. For example, at a CCDF of 10^{-4}, the PAPR of the PTS scheme with GFDM

($\alpha = 0.9, 0.5$), MGFDM and Walsh-MGFDM is achieved at 10.2dB, 9.5dB, 9.1dB and 8.8dB respectively.

Table 4.4: Wavelet Parameters

Name	Vanishing order	Order
Haar, *haar*	1	1
Daubechies, dBN_v	N_v	2, 3, 8, 10, 20
Symlets, $symN_v$	N_v	4, 10, 20
Coiflet, $coifN_v$	N_v	1, 2, 5
Biorthogonal, *bior*	-	1.3, 2.2, 2.8, 3.3
Reverse Biorthogonal, *rbior*	-	1.5, 2.8, 4.4
Discrete Meyer, *dmey*	-	-

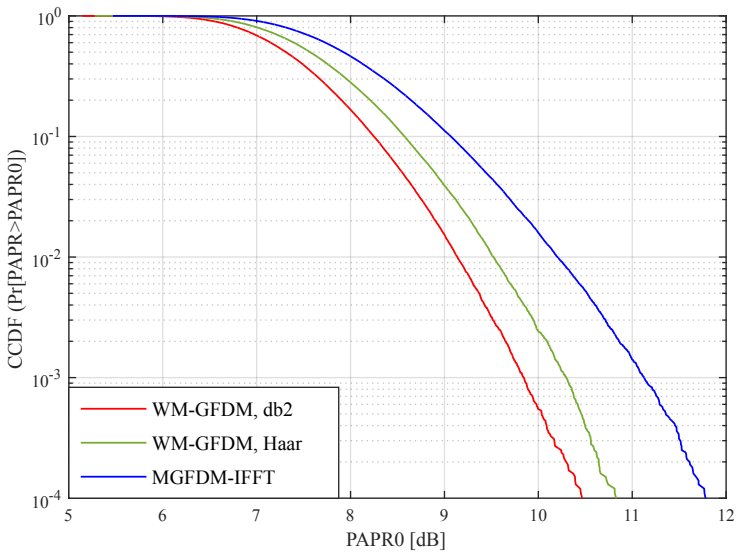

Figure 4.20: Fourier and Wavelet based MGFDM comparison with N=64, M=5, 16-QAM.

The CCDF of the PAPR for the proposed Haar, db2 wavelet based WM-GFDM is shown in Figure 4.20. The wavelet parameters used for simulations are given in Table 4.4. From the figure we can infer that there is a significant improvement in PAPR reduction when we used the proposed wavelets. At a CCDF of 10^{-4}, WM-GFDM further reduces PAPR by 1.3 dB and 0.9 dB compared to MGFDM with both db2 and Haar wavelets

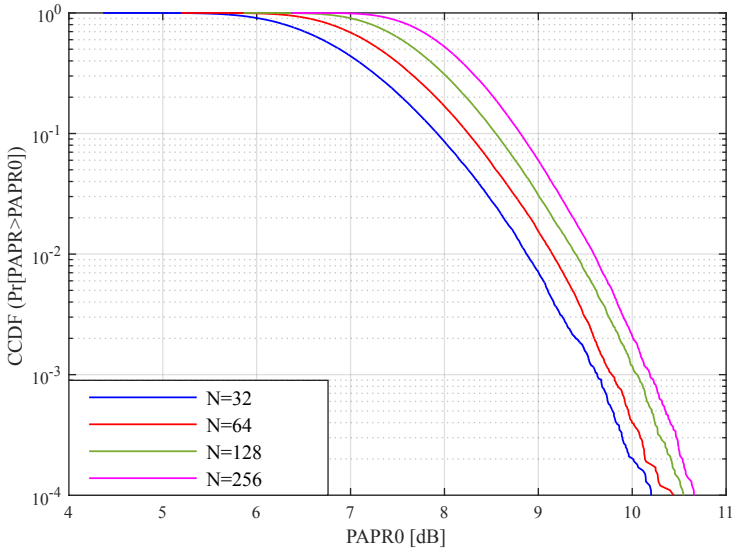

Figure 4.21: PAPR analysis of WM-GFDM with db2 wavelet under different subcarriers with M=5, 16-QAM.

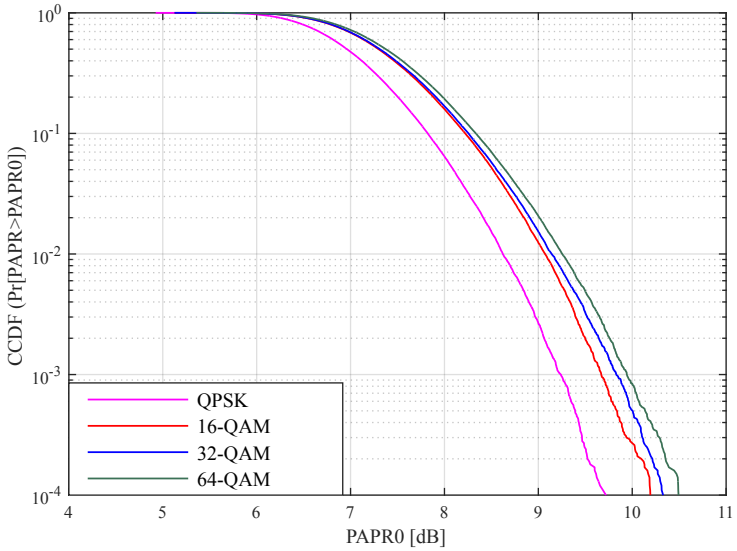

Figure 4.22: CCDF curves for N=64, M=5, 16-QAM with Daubechies db2 wavelet varying the modulation order μ.

respectively. Comparing Figure 4.12 and Figure 4.20 the role of wavelets in reducing PAPR can be analyzed.

Figure 4.21 shows the PAPR for different number of subcarriers N with M=5, 16-QAM modulated WM-GFDM and db2 wavelet. We can observe that PAPR grows as we increase N. In Figure 4.22 for 64 subcarriers and M=5, the CCDF plots of the proposed

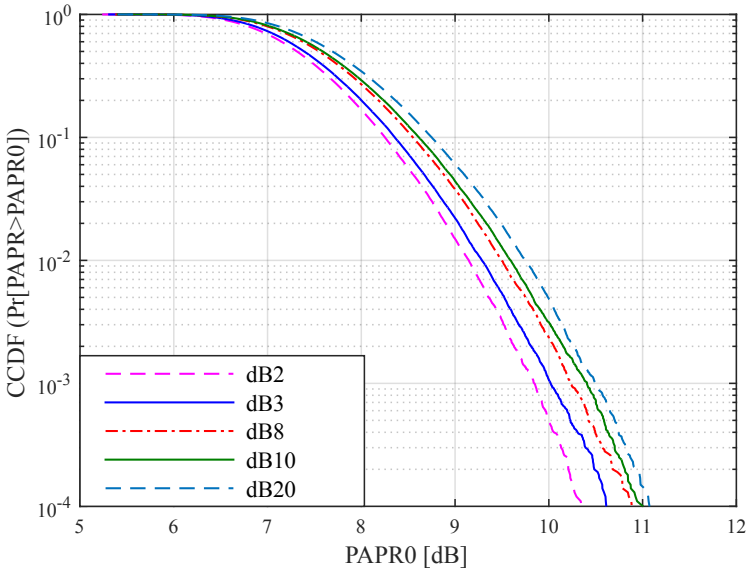

Figure 4.23: PAPR plot for different Daubechies Wavelet vanishing moments.

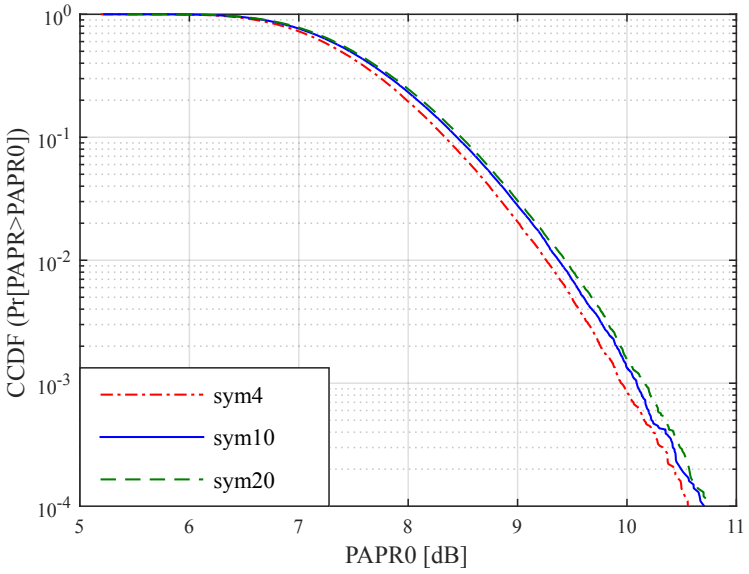

Figure 4.24: PAPR plot for different Symlet Wavelets.

db2 wavelet for different modulation orders $\mu = 2, 4, 5, 6$ are shown. This figure shows that QPSK offers the best PAPR under the same conditions compared with 16-QAM, 32-QAM and 64-QAM.

Figures 4.23, 4.24, 4.25, 4.26, 4.27 individually show the variation in PAPR with different orders under Daubechies, Symlets, Coiflet, Biorthogonal, Reverse Biorthogonal and Discrete Meyer Wavelets with N=64, M=5, 16-QAM. The orders considered for each

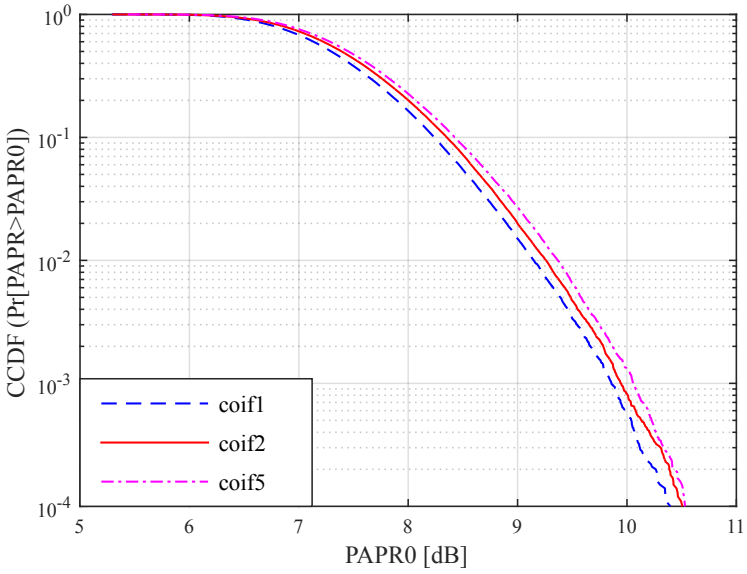

Figure 4.25: PAPR plot for different Coiflet Wavelets.

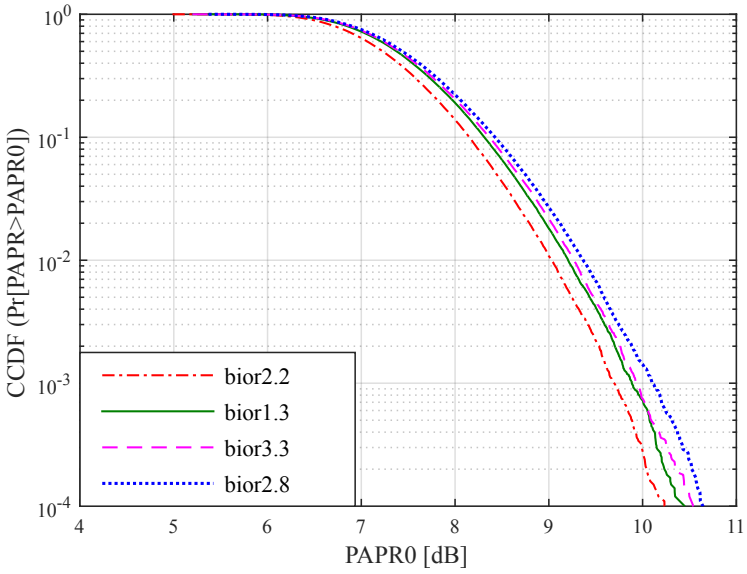

Figure 4.26: PAPR plot for different Biorthogonal Wavelets.

wavelet method is shown in the figure. Out of all the wavelets, the Biorthogonal Wavelet with bior2.2 has the lowest PAPR of 10.23dB at a CCDF of 10^{-4} (Figure 4.26) which is better than the MGFDM with IFFT (11.70dB, Figure 4.12).

The SER for WM-GFDM, MGFDM, GFDM and OFDM are shown in Figure 4.28. The simulation parameters that are considered, are shown in Table 4.5. From the figure we can infer that the SER of WM-GFDM is the same as that of MGFDM. An improvement is

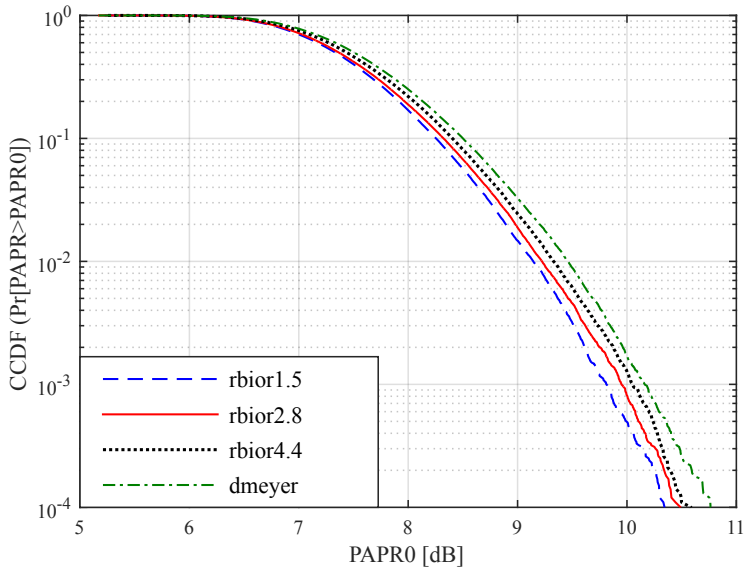

Figure 4.27: PAPR plot for different Reverse Biorthogonal and Discrete Mayer Wavelets.

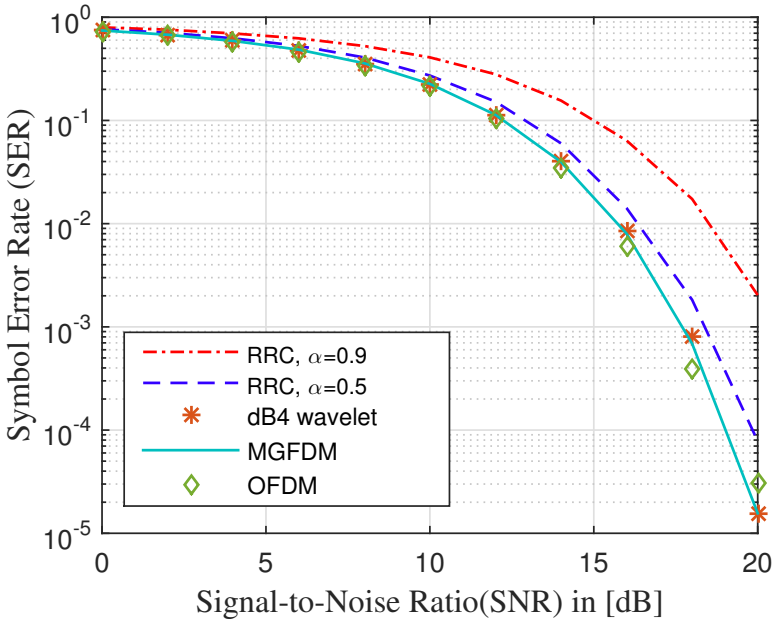

Figure 4.28: Symbol Error Rate performance under AWGN for various MC techniques.

also observed compared to a conventional GFDM system with RRC filters of roll-off factors $\alpha = 0.5, 0.9$. The SER for an OFDM system is also provided for comparison purposes. As mentioned before, OFDM is a special case of GFDM with number of subsymbols $M = 1$ and a rectangular filter as a prototype filter. GFDM is a non-orthogonal multicarrier technique producing inherent ISI/ICI which will affect the SER performance as compared to an OFDM system and is depicted in the figure. In GFDM a single CP is inserted for

Table 4.5: Simulation Parameters for SER analysis

Description	WM-GFDM/MGFDM	GFDM/OFDM
Number of Subcarriers, N	64	64
Number of time slots, M	5	5/1
Pulse shape filter, g	DPSS	RRC ($\alpha = 0.5, 0.9$) / Rectangular
Transform	IDWT (dB4)/IFFT	IFFT
Length of CP,N_{cp}	0/8	8
Modulation order, μ	4	4

Table 4.6: Parameters for transmit spectrum

Description	Values
Number of Subcarriers, K	64
Number of Subsymbols. M	5, 1(OFDM)
Cyclic Prefix length	16
Pulse Shaping	Rectangular (OFDM), RRC (GFDM), DPSS (MGFDM, WM-GFDM)
Modulation order, μ	4 (16-QAM)
Spectral Estimation Method	pwelch

the entire block, consisting of a number of subcarriers and multiple subsymbols, whereas a CP for OFDM is inserted for each transmitted symbol. This will increase the spectral efficiency of the system. Moreover, in WM-GFDM, no CP is required, which in addition will further increase spectral efficiency.

Finally, we can compare PSD for the various multicarrier techniques discussed in this paper and displayed in Figure 4.29. The simulations are carried out in Matlab and the parameters that are used are given in Table 4.6 with a sampling frequency of 20MHz. From the figures we can observe that the PSD of GFDM has a better spectral efficiency property compared to an OFDM system, as GFDM uses separate filters to pulse shape each subcarrier utilizing the tail-baiting concept.

The spectra of MGFDM and WM-GFDM are also shown in Figure 4.30. MGFDM

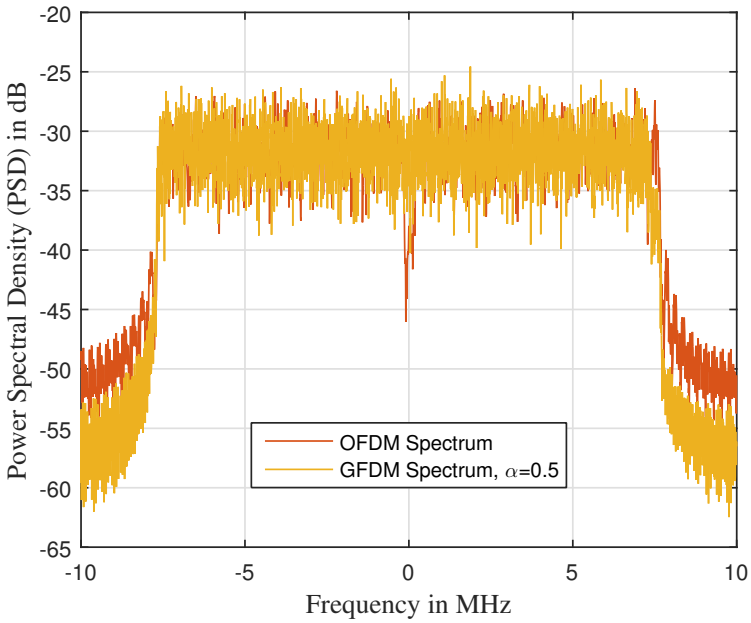

Figure 4.29: Spectrum comparison of OFDM and Conventional GFDM with root raised cosine filter of roll-off factor 0.5.

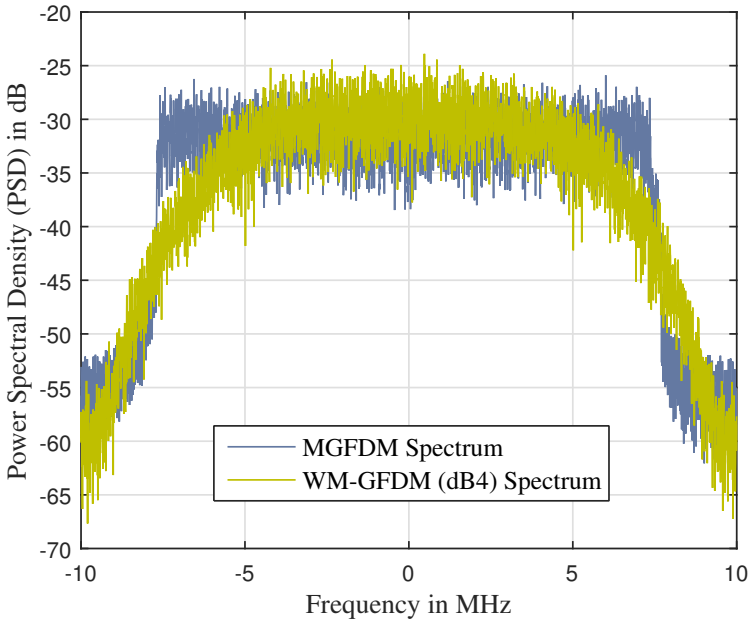

Figure 4.30: Spectrum comparison of MGFDM and WM-GFDM

has almost the same spectrum shape as the GFDM system. Therefore, retaining the same spectral property, we can achieve a better PAPR performance for an MGFDM system compared to the conventional GFDM. It is interesting to note that the spectrum of the WM-GFDM system with Daubechies (dB4) wavelets is bell-shaped and has a much

deeper fall-off compared to the MGFDM system.

4.9 Chapter Summary

This chapter presents a novel alternative approach for the implementation of conventional GFDM inorder to improve the orthogonality of the originally proposed GFDM system. This can be achieved by using multi-tapers (prolate spheroidal windows) as pulse shaping filters. We have investigated SER performance for the current standard conventional GFDM and CP-OFDM systems and compared it with our multi-taper GFDM for the cases of AWGN channels as well as Rayleigh fading channels. Analytical expressions where for the above channels were derived and it is shown through computer simulations there is a good match with the mathematical equations. A considerable amount of improvement in the SER plots using prolate windows compared to CP-OFDM and conventional GFDM systems.

This chapter also gives an overview of the implementation of the most popular PAPR reduction techniques, SLM, PTS and ZCT MGFDM systems and the results show an improvement in PAPR reduction when compared to MGFDM at the expense of additional complexity. A comparative analysis among the three schemes is also carried out. Based on the simulation results, ZCT is seen to be the most effective in reducing PAPR when compared to the SLM and PTS schemes. Despite of PAPR reduction compared to conventional GFDM, still complexity poses a challenging issue with this techniques. Variation in the subcarriers and the modulation order leads to its own effects. Similarly to any other MC technique there is an increase in PAPR as the value of μ is increased. In addition, novel hybrid PAPR reduction schemes are proposed to reduce the PAPR of an MGFDM system. Simulation results shows that the Walsh Hadamard precoding matrix can be exploited to further reduce the PAPR of the SLM and PTS methods. These schemes effectively decrease the PAPR of the MGFDM system. Furthermore, a comparative analysis with the SLM and PTS techniques applied to a conventional GFDM system is also carried out. Furthermore, the results suggest that the Walsh Hadamard precoding matrix can be exploited to further reduce the PAPR of the SLM and PTS methods. These schemes effectively decrease the PAPR of the MGFDM system.

A preliminary examination of implementing wavelet transforms in the context of MGFDM is carried out by using the Haar, Daubechies, Symlets, Coiflets, Biorthogonal, Reverse Biorthogonal and Discrete Meyer wavelets. A comparative study between conventional GFDM, MGFDM and WM-GFDM is also presented. The main goal is to reduce PAPR in conventional GFDM systems and to make GFDM more attractive as a 5G contender. Results show that there is an improvement in PAPR in both WM-GFDM and MGFDM as compared to conventional GFDM. More precisely, WM-GFDM with the Daubechies dB2 and Biorthogonal bior2.2 wavelets performs better than the other approaches. Furthermore, a comparison is provided for the effect on PAPR by varying the number of subcarriers K and the modulation order μ. The SER performance of a WM-GFDM system with db4 wavelets as well as with MGFDM, GFDM and OFDM modulation techniques is provided. Analysis shows that WM-GFDM can achieve the same SER as MGFDM and OFDM, an improvement is observed compared to the conventional GFDM system. A good spectral comparison among the proposed technique and the other multicarrier techniques is also carried out where, the simulation results show that the spectrum of the proposed system follows the steps of OFDM and MGFDM.

The overall conclusion from the above analysis is that the modified GFDM design model is a trustworthy candidate for future wireless needs.

Chapter 5

Improvements in GFDM

5.1 Introduction and Motivation

The primary concern which is associated in the design of 5G mobile communication is to assure seamless exchange of information for the purpose of interconnecting the entire world. Assuring a secure and reliable communication emerges as the most vital challenge of 5G communication. In this regard, it is crucial to guarantee reliable high data rate communication over the wireless channel. It is apparent that, the wireless channel suffers from time-varying impairments like multi-path fading, interference and noise. Therefore, the previous chapters emphasizes on the investigations carried to analyze the SER performance over different fading channel environments. Furthermore, in order to improve the performance of conventional GFDM system we have employed the DPSS also called as multi-tapers and analyzed the developed system performance under such channel conditions.

In this chapter, two kinds of improvements have been made to conventional GFDM system. Motivated by the fact that, to improve the reliability, one can think of utilizing the available resources in the spatial domain, time domain or frequency domain. In order to mitigate the effects of fading, spatial diversity is one of the effective ways to improve the performance of wireless communication systems. This can be achieved by employing multiple antennas at either the transmitter side (transmit diversity) and/or the receiver side (receive diversity) [159]. While dealing with the cellular communication it is advisable to exploit transmitter diversity schemes rather than the receiver diversity

techniques pertaining to downlink scenarios i.e., when the data is transmitted form the base station to the mobile station. This is due to the fact that it is very difficult to deploy more than one receive antennas in a small-sized portable mobile unit. Furthermore, it is more advantageous to consider transmit diversity in the downlink scenarios because it is easy to install multiple transmit antennas in the base station and provide extra power for multiple transmissions. In addition, transmit diversity decreases the required processing power of the receiver, resulting in a simpler system structure, lower power consumption and lower cost. Transmitter diversity can obtain diversity gain even without channel information at the transmitter. But, in this work we have considered transmitter diversity with feedback.

GFDM, a physical layer proposal for 5G wireless network is expected to be compatible with MIMO scheme. In recent years, efforts have been made to exploit the spatial diversity [117, 160–164]. The application of Space Time Code (STC) to GFDM has been investigated in [43,117]. In this work, it has been shown that GFDM and the STC scheme proposed by S. Alamouti can be easily integrated and a full diversity gain is achieved with a very small computational overhead. However, the space-time combiner does not fully mitigate the ISI between the data sent in each GFDM. A multi user resource sharing of time reversal STC GFDM in the up-link scenario is proposed in [160]. To minimize the effect of ISI introduced by the multipath channel to the STC GFDM, the application of widely linear estimation was introduced in [161]. In [162], authors described about MIMO GFDM test bed taking into consideration STC for achieving diversity gain. In addition, preamble based synchronization and channel estimation for the developed system was detailed. Analysis of sphere decoded aided successive interference cancellation demapper at the receiver side for a coded MIMO GFDM is carried out in [163]. A system level performance of MIMO-GFDM is proposed in [164], evaluating the performance with spatial multiplexing explaining the effect of spatial correlation between the antennas. Even though some of the existing literature covers the analysis of STC codes with GFDM, to increase the reliability of the wireless network, a precoded based multi-taper GFDM with feedback in the presence of Alamouti coding scheme can offer a better performance. So, we carried out precoded OSTBC MGFDM system with Alamouti space time coding in Rayleigh fading channel. Also, we provide in this chapter a non-trivial analytical expressions for both conventional GFDM and MGFDM precoded based OSTBC technique.

GFDM is a block based multi carrier technique in which each subcarrier is shaped with a non-rectangular pulse shape filter to improve frequency localisation of pulses. However, according to Balian's Low Theorem (BLT), it is not possible to get a well localized prototype filter both in the time-frequency domain and maintain the orthogonality principle at the same time [165]. Good time-frequency localization is needed to deal the asynchronous nature (created by the adverse channel effects) and to allow a low OOB emission. These in turn leads to fulfill the applications involving spectrum efficiency and carrier aggregation. [73] proposed one possible way to circumvent the BLT is by transmitting the real valued symbols at twice the Nyquist rate and gives rise to OQAM. Hence, it is worth exploring the near orthogonality properties of OQAM.

Due to the non-orthogonal nature of the GFDM modulation technique, inherent ISI and ICI is expected to occur. By exploiting the benefits of OQAM these effects can be mitigated [118]. In order to achieve better spectral efficiency and concurrently reduce the combined ICI and ISI, another GFDM scheme using offset QAM is introduced. Contrary to conventional GFDM, also called GFDM/QAM, which modulates each subcarrier block with a complex-valued symbol, GFDM/OQAM modulates carriers with a real-valued symbol in each sub-carrier block, keeping the advantages of a non-rectangular pulse shape in GFDM. It is mentioned in the literature that OFDM/OQAM is more suitable for high data rate applications [166]. Since GFDM is one such multicarrier technique similar explanation holds good for GFDM/OQAM system.

In this chapter we investigate the performance analysis of GFDM with OQAM. To be precise, we have evaluated the system performance in terms of SER under AWGN, Rayleigh, Racian-K and Nakagami fading channels. The simulated results are compared with the derived analytical expressions. The effect of the roll-off factor (α) is also studied under fading channels.

Firstly, this chapter, provides the analysis on precoded transmit diversity scheme for MGFDM system under Rayleigh fading channel and compared the results to that of GFDM system. Next part of the chapter focuses on challenges in designing a near orthogonality of the conventional GFDM system and with the combination of GFDM/OQAM, the analysis under various channels has been reported.

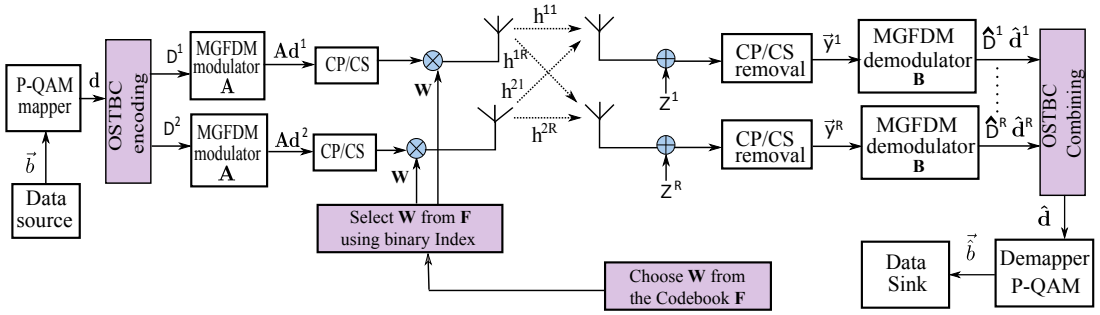

Figure 5.1: Block diagram of feedback precoded OSTBC MIMO-MGFDM system with Alamouti space time coding.

5.2 Precoded OSTBC MGFDM system with Alamouti space time coding

Consider a wireless communication system with N_t transmit antennas and N_r receive antennas whose CSI is assumed to be available at the transmitter. Figure 5.1 depicts the proposed block diagram of a feedback precoded OSTBC MIMO-MGFDM system with the Alamouti space coding scheme. In this model, the data vector is given by $\mathbf{d} = [d_0(0), .., d_{N-1}(0), ..., d_0(M-1), .., d_{N-1}(M-1)]$. These can also be represented in block structure form according to [117],

$$\mathbf{D} = \begin{pmatrix} d_0(0) & \cdots & d_0(M-1) \\ \vdots & \ddots & \\ d_{N-1}(0) & \cdots & d_{N-1}(M-1) \end{pmatrix} \tag{5.1}$$

$\mathbf{d}$ is passed through a space time encoding block to generate the data blocks $\mathbf{D}^1$, $\mathbf{D}^2$ given by (5.2), (5.3) according to [117].

$$\mathbf{D}^1 = \mathbf{D} \tag{5.2}$$

$$\mathbf{D}^2 = \left(\begin{array}{cc|c|cc} -d_0^*(1) & d_0^*(0) & \cdots & -d_0^*(M-1) & d_0^*(M-2) \\ \vdots & \vdots & \cdots & \vdots & \vdots \\ -d_{N-1}^*(1) & d_{N-1}^*(0) & \cdots & -d_{N-1}^*(M-1) & d_{N-1}^*(M-2) \end{array}\right) \tag{5.3}$$

Each data block is passed through MGFDM modulator block in which superposition of all

operations namely upsampling, circular convolution and frequency upconversion is carried out. All this mathematical analysis can be represented in matrix form $\mathbf{A}$ which is the transmitter modulation matrix given by [134],

$$\mathbf{A} = [\mathbf{G} \;\; \mathbf{E_1 G} \cdots \mathbf{E_{N-1} G}] \tag{5.4}$$

where $\mathbf{E_i} = diag\left\{[\mathbf{e_i}^T, ..., \mathbf{e_i}^T]^T\right\}$ is a $NM \times NM$ diagonal matrix whose diagonal elements are comprised of M concatenated copies of the vector $\mathbf{e_i} = [1, e^{j\frac{2\pi i}{N}}, ..., e^{j\frac{2\pi i}{N}(N-1)}]^T$. Matrix $\mathbf{G}$ of size $NM \times M$ is constructed with circular shift of $[g_0, ..., g_{NM-1}]^T$ each of length NM. A CP is added to both the signals individually as shown in Figure 5.1. Note that the length of CP must be larger than the Channel Impulse Response (CIR).

In a precoded OSTBC-MGFDM system, the signal vectors are multiplied by a precoded matrix $\mathbf{W} \; \epsilon \; \mathbb{C}^{N_t \times M_c}$, which is selected from the codebook $\mathbf{F} = \{\mathbf{W_1}, \mathbf{W_2}, ..., \mathbf{W_{L_c}}\}$, where M_c, L_c corresponds to codeword length and codebook size respectively. The objective is to choose an optimum codeword which improves the overall system performance in terms of channel capacity or error performance. The criterion for choosing the optimal precoding matrix from the codebook was investigated in [167]. In brief, the problem for selecting the optimal codeword is directly related to the Grassmannian subspace packing problem in the Grassmann manifold and proves full diversity order in the Rayleigh fading channel. Considering the pair-wise probability of error and using the upper bound by the Chernoff [168–171], the optimal codeword can be chosen from the following equation [170],

$$\mathbf{W_{opt}} = \underset{\mathbf{W} \epsilon \mathbf{F}}{arg} \;\; max \, \|\mathbf{hW}\|_F^2 \tag{5.5}$$

where $\mathbf{h}$ of size $N_r \times N_t$ represents the channel response from transmit antenna N_t to receive antenna N_r and $\mathbf{W_{opt}}$ is the optimal code word chosen from the codebook $\mathbf{F}$.

The design method of code book using Grassmannian packing problem is a time consuming process [172]. Instead, [171] proposed a method to design $\mathbf{F}$ using DFT matrices and given as,

$$\mathbf{F} = \left\{\mathbf{W_{DFT}}, \; \theta \mathbf{W_{DFT}}, \cdots, \theta^{\mathbf{Lc-1}} \mathbf{W_{DFT}}\right\} \tag{5.6}$$

where $\mathbf{W_{DFT}}$, the first codeword can be determined by selecting the M_c columns from the DFT matrix of order $N_t \times N_t$, given by the (p', q') element as $e^{j2\pi(p'-1)(q'-1)}/\sqrt{N_t}$,

$p', q' = 1, 2, .., N_t$. θ can be given by the diagonal matrix as,

$$\theta = diag\left(\left[e^{j2\pi u_i/\sqrt{N_t}}\right]\right) \quad i = 1, \cdots, N_t \tag{5.7}$$

where $\{u_i\}_{i=1}^{N_t}$ is the free variable that can be determined such that minimal chordal distance is maximized,

$$\mathbf{u} = \underset{\{u_1,..u_{N_t}\}}{argmax} \quad \underset{l=1..L_c-1}{min} d\left(\mathbf{W_{DFT}}, \theta^l \mathbf{W_{DFT}}\right) \tag{5.8}$$

Given the first codeword $\mathbf{W_{DFT}}$ and θ, the code book $\mathbf{F}$ can be constructed using (5.6).

The received signal after the removal of CP can be written as [43],

$$y^r = \mathbf{h^{1r}Ad^1} + \mathbf{h^{2r}Ad^2} \tag{5.9}$$

where $\mathbf{h^{tr}} = circ\{\mathbf{h_w^{tr}}\}$ is the circulant channel matrix and $\mathbf{h_w^{tr}}$ is the multipath CIR from transmit antenna t to receive antenna r given by (5.10) and $\mathbf{h_w^{tr}}$ is zero padded to the length of the transmit signal. $\mathbf{d^t} = vec(\mathbf{D^t})$, where the columns of $\mathbf{D^t}$ are stacked on top of each other [117].

$$\mathbf{h_w^{tr}} = \mathbf{hW_{opt}} \tag{5.10}$$

Above equation (5.10) can be seen as the effective channel with feedback. The signal on each receiver can be demodulated as [43, 117],

$$\mathbf{d^r} = \mathbf{By^r} \tag{5.11}$$

The matrix $\mathbf{B} = \mathbf{A}^\dagger$ is the zero forcing receiver matrix. The STC combining is carried according to the following rule [117]:

$$\begin{aligned} \hat{d}_{im} &= \frac{\sum_{r=1}^{R}(H_i^{1r})^* d_{i,m}^r + H_i^{2r}(d_{i,m+1}^r)^*}{\sum_{r=1}^{R}|H_i^{1r}|^2 + |H_i^{2r}|^2} \quad m\ even \\ \hat{d}_{im} &= \frac{\sum_{r=1}^{R}(H_i^{1r})^* d_{i,m}^r - H_i^{2r}(d_{i,m-1}^r)^*}{\sum_{r=1}^{R}|H_i^{1r}|^2 + |H_i^{2r}|^2} \quad m\ odd \end{aligned} \tag{5.12}$$

where H_i^{tr} denotes the ith point DFT of the CIR $\mathbf{h_w^{tr}}$.

5.2.1 Performance Analysis of Precoded OSTBC MGFDM under Rayleigh Fading Channel

In this section we provide the SER theoretical expressions for the precoded OSTBC GFDM system under consideration by using the upper bound probability for the maximum ratio combiner [15]. Note that the effect of the NEF and the precoding matrix is taken into account and the approximate expression is given by,

$$P_e = 4\eta \sum_{j=0}^{N_t N_r - 1} \binom{N_t N_r - 1 + j}{j} \left(\frac{1+\lambda}{2}\right)^j \tag{5.13}$$

where

$$\eta = \left(\frac{\sqrt{P}-1}{\sqrt{P}}\right)\left(\frac{1-\lambda}{2}\right)^{N_t N_r}$$

$$\lambda = \sqrt{\frac{\frac{3\|\mathbf{h^{tr}}\|_F^2}{2(P-1)}\frac{E_s}{N_0 R_s N_t \xi_0}}{1+\frac{3\|\mathbf{h^{tr}}\|_F^2}{2(P-1)}\frac{E_s}{N_0 R_s N_t \xi_0}}}$$

$$\xi_{0,GFDM} = \xi\frac{NM + N_{cp} + N_{cs}}{NM}$$

R_s, the symbol rate of the OSTBC is given by $R_s = \frac{Q}{T}$ where T time periods are used to transmit Q symbols. NEF ξ under a GFDM system with zero forcing receiver is given by [43],

$$\xi = \sum_{n=0}^{NM-1} \left|[\mathbf{B}]_{i,n}\right|^2 \qquad \forall i = 1, 2, ..., N \tag{5.14}$$

The values of ξ are equal for any index i. Under an MGFDM system, NEF is given by [56],

$$\xi = min\left\{\sum_{n=0}^{NM-1} \left|[\mathbf{B}]_{i,n}\right|^2\right\} = 1 \tag{5.15}$$

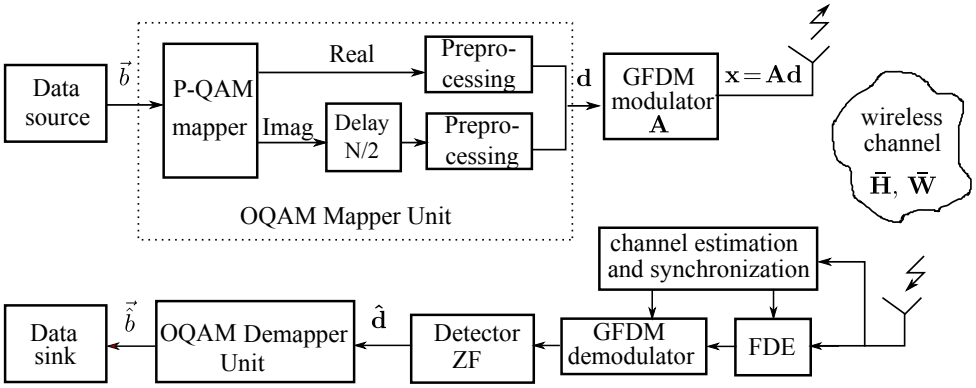

Figure 5.2: Block diagram of GFDM/OQAM transceiver

5.3 GFDM/OQAM Signal Model

GFDM/OQAM modulation uses the same components as GFDM with two main differences. Firstly, it uses QAM mapping, followed by the application of a $N/2$ samples offset in the time domain between the in-phase and quadrature component of the complex QAM data. The resulting OQAM mapper enables an efficient reduction of ICI/ISI when a properly designed filter is applied [118]. Secondly, pulse-shape orthogonality can be achieved without the need for a cyclic prefix which in turn increases spectral efficiency, is one of the requirement for 5G. Figure 5.2 depicts the proposed block diagram of the GFDM-OQAM scheme.

5.3.1 Principle of GFDM/OQAM

Instead of using complex baseband symbols in the GFDM/QAM scheme, real valued symbols modulated by offset QAM are transmitted on each sub-carrier with the synthesis basis functions obtained by the time-frequency translated version of this prototype function in the following way [118, 119]:

$$g_{i,m}(n) = g[(n - \frac{mN}{2}) \bmod NM] e^{\frac{j2\pi i}{N}\left[n - \frac{L_p - 1}{2}\right]} \tag{5.16}$$

where $n = 0, 1, ...NM-1$, $g_{i,m}(n)$ is the shifted version of the prototype filter $g(n)$ in time and frequency. The shift in time is carried out by the an offset of $N/2$ samples and the modulo operation describes the circular shift in time of $g_{i,m}(n)$. The complex exponen-

tial term explains the upconversion to the i^{th} subcarrier and also the phase component introduced by the delay of the filter. L_p is the length of the prototype filter. Finally, the superposition of all the transmitted symbols leads to the discrete time baseband GFDM/OQAM modulator output written as follows:

$$x(n) = \sum_{i=0}^{N-1} \sum_{m=0}^{M-1} a_i(m) g_{i,m}(n) e^{j\phi_{m,i}} \qquad , where \;\; n = 0, 1, ...NM-1 \tag{5.17}$$

$a_i(m)$ is the real data obtained from the real and imaginary parts of the QAM constellation and $\phi_{m,i} = \frac{(i+m)\pi}{2}$, $e^{j\phi_{m,i}}$ ensures a $\pi/2$ phase difference in time and frequency between the real data $a_i(m)$ [166]. The real valued symbols $a_i(m)$ together with the phase term $e^{j\phi_{m,i}}$ constitutes the OQAM symbols. $N/2$ is the discrete time offset and the *mod* operator does the circular shift.

Expressing all operations in matrix form, $\mathbf{x} = \mathbf{Ad}$, where $\mathbf{A}$ is a $NM \times NM$ transmitter modulation matrix containing all the signal processing steps involved in the modulation. $\mathbf{A}$ is given by equation (5.4) and $\mathbf{d}$, a data vector of size $NM \times 1$, is the stack of all elements from the OQAM mapping unit.

5.3.2 Channel Model

Let $\mathbf{h} = [h_0, .., h_{N_{ch}-1}]^T$ be the channel impulse response of length N_{ch}. The received signal after propagation through the wireless channel can be modelled as,

$$\mathbf{r} = \mathbf{Hx} + \mathbf{w} \tag{5.18}$$

where $\mathbf{H} = circ\left\{\tilde{h}\right\}$ is a circulant channel convolution matrix and $\tilde{h}$ is the zero padded version of $\mathbf{h}$ of the same length as $\mathbf{x}$. The vector $\mathbf{w} \sim \mathcal{CN}(0, \sigma_w^2 I_{NM})$ denotes the complex AWGN samples with noise variance σ_w^2 and I_{NM} is the identity matrix of order NM. The individual elements $r(n)$ of $\mathbf{r}$ are $r(n) = x(n) * h(n) + w(n)$, where $*$ denotes convolution and $h(n)$ denotes the impulse response of the multipath fading channel. When the channel noise is AWGN, $h(n) = 1$ or equivalently $\mathbf{H} = \mathbf{I}$. The fading channels under investigation are Rayleigh, Rician, Nakagami-m, and Nakagami-q (Hoyt).

5.3.3 Receiver Model

Channel equalization in the frequency domain can be performed as [43],

$$\mathbf{y} = \text{IDFT}\left\{\frac{\text{DFT}(\mathbf{r})}{\text{DFT}(\mathbf{h})}\right\} \tag{5.19}$$

The estimated data vector $\hat{\mathbf{d}}$, from the received and equalized signal can be written as,

$$\hat{\mathbf{d}} = \mathbf{B}\mathbf{y} \tag{5.20}$$

The matrix $\mathbf{B}$ is given as follows [95],

$$\begin{aligned} \text{MF:} \quad & \mathbf{B_{MF}} = \mathbf{A}^H \\ \text{ZF:} \quad & \mathbf{B_{ZF}} = \left(\mathbf{A^H A}\right)^{-1}\mathbf{A^H} \\ \text{MMSE:} \quad & \mathbf{B_{MMSE}} = \left(\frac{\sigma_w^2}{\sigma_d^2}\mathbf{I} + \mathbf{A^H A}\right)^{-1}\mathbf{A^H} \end{aligned} \tag{5.21}$$

where σ_w^2 is the noise variance and σ_d^2 is the data symbols variance.

5.3.4 Performance Analysis of GFDM/OQAM under several channels

In this section we present the analytical expressions for GFDM/OQAM under AWGN, Rayleigh, Rician-K, Nakagami-m and Nakagami-q fading channels.

AWGN channel

The NEF ξ determines the SNR reduction when using the ZF receiver and is given by [43],

$$\xi = \sum_{n=0}^{NM-1} \left|[\mathbf{B_{ZF}}]_{i,n}\right|^2 \tag{5.22}$$

The values of ξ are equal for any index i. Both NEF and the number of OQAM samples per symbol N_s, adjust the equivalent SNR for GFDM/OQAM at the receiver

side. Consequently, GFDM and GFDM/OQAM SER performance under AWGN differs in the equivalent SNR. The GFDM/OQAM SER expression under AWGN channel is given by,

$$P_{AWGN}(e) = 2\left(\frac{p-1}{p}\right)\text{erfc}(\sqrt{\gamma}) - \left(\frac{p-1}{p}\right)^2 \text{erfc}^2(\sqrt{\gamma}) \tag{5.23}$$

where

$$\gamma = \frac{3R_T}{2(2^\mu - 1)}\frac{N_s E_s}{\xi N_0} \tag{5.24}$$

and

$$R_T = \frac{NM}{NM + N_{CP} + N_{CS}} \tag{5.25}$$

μ is the number of bits per QAM symbol, $p = \sqrt{2^\mu}$, N_{CP} and N_{CS} are the length of the cyclic prefix and cyclic suffix respectively, N and M denote the number of subcarriers and subsymbols respectively, E_s is the average energy per symbol and N_0 is the noise power density. The factor N_s has the value 2 for OQAM and 1 for QAM.

Rayleigh fading channel

The SER of GFDM/OQAM under any fading channel can be derived by using [96],

$$P_{Fad}(e) = \int_0^\infty P_{AWGN}(e) P_\gamma(\gamma) d\gamma \tag{5.26}$$

where $P_\gamma(\gamma)$ is the probability density function under various fading channels. $P_\gamma(\gamma)$ under Rayleigh fading channel is given by,

$$P_\gamma(\gamma) = \frac{1}{\bar{\gamma_r}} exp\left(\frac{-\gamma}{\bar{\gamma_r}}\right) \tag{5.27}$$

where $\bar{\gamma_r}$ is given in equation (5.29). Now substituting equations (5.23), (5.27) in (5.26) and using [135] the following expression can be obtained,

$$P_{Ray}(e) = 2\left(\frac{p-1}{p}\right)\left(1-\sqrt{\frac{\bar{\gamma_r}}{1+\bar{\gamma_r}}}\right) - \left(\frac{p-1}{p}\right)^2\left[1-\frac{4}{\pi}\sqrt{\frac{\bar{\gamma_r}}{1+\bar{\gamma_r}}}\arctan\left(\sqrt{\frac{1+\bar{\gamma_r}}{\bar{\gamma_r}}}\right)\right] \tag{5.28}$$

where $\bar{\gamma_r}$ is the equivalent SNR under Rayleigh fading channel given by,

$$\bar{\gamma_r} = \frac{3R_T\sigma_r^2}{(2^\mu-1)}\frac{N_sE_s}{\xi N_0} \tag{5.29}$$

$$\sigma_{ray}^2 = \sigma_r^2\sum_{j=0}^{N_{ch}-1}|\mathbf{h_j}|^2$$

where $\mathbf{h}$ is the channel impulse response with length N_{ch} and $\sigma_r^2 = 1/2$ the parameter of Rayleigh distributed taps is considered for SER performance.

Rician-K channel

The probability density function under the Rician-K fading channel is given by [96],

$$P_\gamma(\gamma) = \left(\frac{1+K}{\bar{\gamma}}\right)\exp\left[-\frac{(1+K)\gamma+K\bar{\gamma}}{\bar{\gamma}}\right]I_0\left[\sqrt{\frac{4K(1+K)\gamma}{\bar{\gamma}}}\right];0\le K<\infty \tag{5.30}$$

where K is the Rician parameter and $\bar{\gamma}$ is the average SNR per bit.

Expressing the infinite series representation of the zeroth-order modified Bessel function [137], $I_0(x) = \sum_{q=0}^{\infty}\left(\frac{x^2}{4}\right)^q/(q!)^2$, the PDF of (5.30) can be modified as:

$$P_\gamma(\gamma) = \frac{1+K}{\bar{\gamma_r}}e^{-K}\sum_{q=0}^{\infty}\frac{1}{(q!)^2}\left(\frac{K(1+K)}{\bar{\gamma_r}}\right)^q\gamma^q\exp\left(-\frac{\gamma(1+K)}{\bar{\gamma_r}}\right);0\le K<\infty \tag{5.31}$$

Substituting equations (5.23) and (5.31) in (5.26) we have the final SER expression for the Rician fading channel as:

$$P_{Ric}(\gamma) = \frac{2(p-1)}{p}I_1(\bar{\gamma_r}) - \left(\frac{p-1}{p}\right)^2 I_2(\bar{\gamma_r}) \tag{5.32}$$

where

$$I_1(\bar{\gamma}_r) = \frac{1+K}{\bar{\gamma}_r} e^{-K} \sum_{q=0}^{\infty} \frac{1}{(q!)^2} \left(\frac{K(1+K)}{\bar{\gamma}_r} \right)^q \times \frac{\Gamma(q+3/2)}{\sqrt{\pi}(q+1)} \, {}_2F_1[q+1, q+\frac{3}{2}; q+2; -(\frac{1+K}{\bar{\gamma}_r})] \tag{5.33}$$

$$I_2(\bar{\gamma}_r) = e^{-K} \sum_{q=0}^{\infty} \frac{K^q}{(q!)} \Big(1 - \frac{4}{\pi} \sum_{j=0}^{q} \frac{((1+K)/\bar{\gamma}_r)^j}{2j+1} \times_2 F_1\big[j+\frac{1}{2}, j+1; j+\frac{3}{2}; -(\frac{1+K}{\bar{\gamma}_r}+1) \big] \Big) \tag{5.34}$$

and $\bar{\gamma}_r$ is the equivalent SNR under Rician fading channel given by

$$\bar{\gamma}_r = \frac{3R_T\sigma_r^2}{(2^\mu - 1)} \frac{N_s E_s}{\xi N_0}$$

where we have assumed a Rician channel with parameter $\sigma_r^2 = 1/2$ for SER performance and ${}_2F_1[.,.;.;]$ is the Gauss hypergeometric function [135]. A similar kind of derivation of equation (5.32) is attempted in Chapter 2 and more insights about the derivation can be found there. As mentioned earlier, the number of OQAM samples per symbol N_s will make a difference in the SER performance.

Nakagami-m fading channel

If the signal amplitude follows a Nakagami-m distribution, then the PDF of γ follows a gamma PDF given by [96],

$$P_\gamma(\gamma) = \left(\frac{m}{\bar{\gamma}} \right)^m \frac{\gamma^{m-1}}{\Gamma(m)} \; e^{\frac{-m\gamma}{\bar{\gamma}}} \qquad ; m \geq 1/2 \tag{5.35}$$

where m is the Nakagami parameter and $\bar{\gamma}$ is the average SNR per bit.

By substituting equations (5.23), (5.35), in (5.26) and using [[135],2.321.2,6.286] to solve the integrations, the following expression can be obtained as,

$$P_{Nak}(e) = 2 \left(\frac{p-1}{p} \right) \left(\frac{m}{\bar{\gamma}_n} \right)^m I_3(\bar{\gamma}_n) - \left(\frac{p-1}{p} \right)^2 \left(\frac{m}{\bar{\gamma}_n} \right)^m I_4(\bar{\gamma}_n) \tag{5.36}$$

where

$$I_3(\bar{\gamma}_n) = \frac{1}{\Gamma(m)} \int_0^\infty \text{erfc}(\sqrt{\gamma}) \gamma^{m-1} \exp\left(-\frac{m\gamma}{\bar{\gamma}_n}\right) d\gamma \tag{5.37}$$

$$I_4(\bar{\gamma}_n) = \frac{1}{\Gamma(m)} \int_0^\infty \text{erfc}^2(\sqrt{\gamma}) \gamma^{m-1} \exp\left(-\frac{m\gamma}{\bar{\gamma}_n}\right) d\gamma \tag{5.38}$$

$\bar{\gamma_n}$ is the equivalent SNR under the Nakagami-m fading channel, given by,

$$\bar{\gamma}_n = \frac{3R_T\sigma_n^2}{(2^\mu - 1)} \frac{N_s E_s}{\xi N_0} \tag{5.39}$$

where we have assumed the parameter $\sigma_n^2 = 1/2$ to evaluate SER performance.

Integral (5.37) can be solved by using expressions provided in [[135],6.286] and is given by,

$$I_3(\bar{\gamma}_n) = \frac{\Gamma(m+1/2)}{\sqrt{\pi}\Gamma(m+1)} \ {}_2F_1[m, m+\frac{1}{2}; m+1; -\frac{m}{\bar{\gamma}_n}] \tag{5.40}$$

Another way of solving the above expression is given in Appendix A.

Solving integral (5.38) is not trivial. One way to proceed is to use a simple, basic integration by parts method. At first, separate (5.38) into two parts as $\int_a^b udv = [uv]_a^b - \int_a^b vdu$ where $u = \text{erfc}^2(\sqrt{\gamma})$ and $dv = \gamma^{m-1} e^{\frac{-m\gamma}{\bar{\gamma}_n}} d\gamma$. In the process the following modified expressions are useful [[135],2.321],

$$\int x^{n-1} e^{-ax} dx = \frac{-(n-1)!}{a^n} e^{-ax} \sum_{j=0}^{n-1} \frac{a^j}{j!} x^j \tag{5.41}$$

$$\frac{d}{d\gamma}\left[\text{erfc}(\sqrt{\gamma})\right] = -\frac{2e^{-\gamma}}{\sqrt{\pi}}$$

Utilizing this approach, the following intermediate expression will be obtained,

$$I_4(\bar{\gamma}_n) = \begin{cases} \Gamma(m)\left(\frac{\bar{\gamma}_n}{m}\right)^m - \frac{2}{\sqrt{\pi}}\Gamma(m)\left(\frac{\bar{\gamma}_n}{m}\right)^m \sum_{j=0}^{m-1} \frac{(m/\gamma_n)^j}{j!} \\ \int_0^\infty \text{erfc}(\sqrt{\gamma}) \gamma^{j-\frac{1}{2}} \exp\left(-(\frac{m}{\bar{\gamma}_n}+1)\gamma\right) d\gamma \end{cases} \tag{5.42}$$

Now the integral part of the above equation (5.42) is similar to the one solved in (5.37). Proceeding with the same approach, the final expression of $I_4(\bar{\gamma}_n)$ can be obtained as,

$$I_4(\bar{\gamma}_n) = \begin{cases} \left(\frac{\bar{\gamma}_n}{m}\right)^m - \frac{4}{\pi}\left(\frac{\bar{\gamma}_n}{m}\right)^m \sum_{j=0}^{\infty} \frac{(m/\bar{\gamma}_n)^j}{(j!)} \frac{\Gamma(j+1)}{(2j+1)} \\ \times {}_2F_1[j+\frac{1}{2}, j+1; j+\frac{3}{2}; -(\frac{m}{\bar{\gamma}_n}+1)] \end{cases} \tag{5.43}$$

where ${}_2F_1[.,.;.;]$ is the Gauss hypergeometric function [135]. Lastly, substitute (5.40) and (5.43) in (5.36) to obtain the final expression. It is to be noted that for $m = 1$, expression (5.36) matches with the GFDM/OQAM under Rayleigh fading channel [60] and the same is verified by using matlab simulations.

Hoyt-q fading channel

Let us assume that the effect of the channel on the propagating signal is best described by Hoyt (Nakagami-q) fading. The PDF of γ is then given by [96],

$$P_\gamma(\gamma) = \left(\frac{1+q^2}{2q\bar{\gamma}}\right) \exp\left[-\frac{(1+q^2)^2\gamma)}{4q^2\bar{\gamma}}\right] I_0\left[\frac{-(1-q^4)\gamma}{4q^2\bar{\gamma}}\right]; \quad 0 \leq q \leq 1 \tag{5.44}$$

where q is the Hoyt fading parameter, $I_o(.)$ is the zeroth-order modified Bessel function and $\bar{\gamma}$ is the average SNR per bit. The infinite series representation of the zeroth-order modified Bessel function can be expressed as [137], $I_0(x) = \sum_{i=0}^{\infty}\left(\frac{x^2}{4}\right)^i/(i!)^2$, the PDF of (5.44) can be written as:

$$P_\gamma(\gamma) = \left(\frac{1+q^2}{2q\bar{\gamma}}\right) e^{-\frac{(1+q^2)^2\gamma}{4q^2\bar{\gamma}}} \sum_{i=0}^{\infty} \frac{1}{(i!)^2}\left(\frac{(1-q^4)\gamma}{8q^2\bar{\gamma}}\right)^{2i} \tag{5.45}$$

By substituting equations (5.23), (5.45) in (5.26), the final SER expression under the Hoyt fading channel can be expressed as,

$$P_{Hoyt}(e) = \frac{2(p-1)}{p} I_5(\bar{\gamma}_t) - \left(\frac{p-1}{p}\right)^2 I_6(\bar{\gamma}_t) \tag{5.46}$$

where $\bar{\gamma}_t$ is the equivalent SNR under the Hoyt fading channel given by,

$$\bar{\gamma}_t = \frac{3R_T\sigma_t^2}{(2^\mu - 1)} \frac{N_s E_s}{\xi N_0} \tag{5.47}$$

and we have assumed a Hoyt channel parameter $\sigma_t^2 = 1/2$ for simulation purposes.

$I_5(\bar{\gamma}_t)$ and $I_6(\bar{\gamma}_t)$ are the integrals that have to be solved given by,

$$I_5(\bar{\gamma}_t) = \left(\frac{1+q^2}{2q\bar{\gamma}_t}\right) \sum_{n=0}^{\infty} \frac{1}{(n!)^2} \left(\frac{(1-q^4)}{8q^2\bar{\gamma}_t}\right)^{2n} \int_0^{\infty} erfc(\sqrt{\gamma}) e^{-\frac{(1+q^2)^2\gamma}{4q^2\bar{\gamma}_t}} \gamma^{2n} d\gamma \tag{5.48}$$

$$I_6(\bar{\gamma}_t) = \left(\frac{1+q^2}{2q\bar{\gamma}_t}\right) \sum_{n=0}^{\infty} \frac{1}{(n!)^2} \left(\frac{(1-q^4)}{8q^2\bar{\gamma}_t}\right)^{2n} \int_0^{\infty} erfc^2(\sqrt{\gamma}) e^{-\frac{(1+q^2)^2\gamma}{4q^2\bar{\gamma}_t}} \gamma^{2n} d\gamma \tag{5.49}$$

$I_5(\bar{\gamma}_t)$ is similar to the equation presented in (5.37) and following the same method the final expression can be given by,

$$I_5(\bar{\gamma}_t) = \begin{cases} \left(\frac{1+q^2}{2q\bar{\gamma}_t}\right) \sum_{j=0}^{\infty} \frac{1}{(j!)^2} \left(\frac{(1-q^4)}{8q^2\bar{\gamma}_t}\right)^{2j} \frac{\Gamma((4j+3)/2)}{\sqrt{\pi}(2j+1)} \\ \times {}_2F_1[2j+1, 2j+\frac{3}{2}; 2j+2; -\frac{(1+q^2)^2}{4q^2\bar{\gamma}_t}] \end{cases} \tag{5.50}$$

where $\Gamma(.)$ is the gamma function and ${}_2F_1[.,.;.;]$ is the Gauss hypergeometric function [135].

$I_6(\bar{\gamma}_t)$ can be evaluated by using integration by parts, analogously to (5.38) and is given by,

$$I_6(\bar{\gamma}_t) = \begin{cases} \left(\frac{1+q^2}{2q}\right) \sum_{i=0}^{\infty} \frac{1}{(i!)^2} \left(\frac{(1-q^4)}{8q^2}\right)^{2i} 2i! \left(\frac{4q^2}{1+q^2}\right)^{2i+1} \\ \times \Big(1 - \frac{4}{\pi} \sum_{j=0}^{2i+1} \frac{(\frac{(1+q^2)^2}{4q^2\bar{\gamma}_t})^j}{2j+1} \times_2 F_1\big[j+\frac{1}{2}, j+1; j+\frac{3}{2}; -(\frac{(1+q^2)^2}{4q^2\bar{\gamma}_t}+1)\big]\Big) \end{cases} \tag{5.51}$$

For a Hoyt fading parameter $q = 1$, the SER expression is reduced to that of the Rayleigh channel [60].

5.4 Results and Discussions

In order to demonstrate the performance of the above mentioned improvements to GFDM system, in this section we provide a detailed analysis of the results obtained.

Table 5.1: Simulation Parameters used for precoded OSTBC MGFDM

Description	GFDM	GFDM-DPSS
Number of Subcarriers, K	64	64
Number of time slots, M	8	8
Pulse shape filter, g	RRC	DPSS
Roll-off factor, α	{0.1}	-
Length of CP, N_{cp}	10	10
Modulation order, μ	2,4,5,6	4
(N_t, N_r)	(2,1)	(2,1)

Table 5.2: Codebook design parameters for OSTBC in IEEE 802.16e

N_t	Codeword length, M_c	Codebook size, L_c	Rotation Vector , $\mathbf{u}$
2	1	8	[1,0]
3	1	32	[1,26,28]
4	2	32	[1,26,28]
4	1	64	[1,8,61,45]
4	2	64	[1,7,52,56]
4	3	64	[1,8,61,45]

5.4.1 SER assessment for precoded OSTBC GFDM systems

In this section we present the simulation results to illustrate and verify the SER of STBC-MGFDM, precoded OSTBC MGFDM and precoded OSTBC-GFDM under the Rayleigh fading channel. The simulation parameters under consideration are mentioned in Table 5.1. Furthermore, the code book generation for a different number of antennas are mentioned in Table 5.2. Throughout the simulation we have considered 16-QAM, $N_t = 2$ and $N_r = 1$.

Figure 5.3 illustrates the SER performance comparison for both STBC-MGFDM and precoded OSTBC MGFDM systems. The solid or dashed lines correspond to the theoretical expressions (5.26) and (5.15) while the labels correspond to simulations. It can be observed that there is an improvement in performance with precoded OSTBC (curves $(i) - (ii)$). For example at an SER of 10^{-4} there is an additional $2dB$ required for STBC-MGFDM compared to the precoded OSTBC-MGFDM.

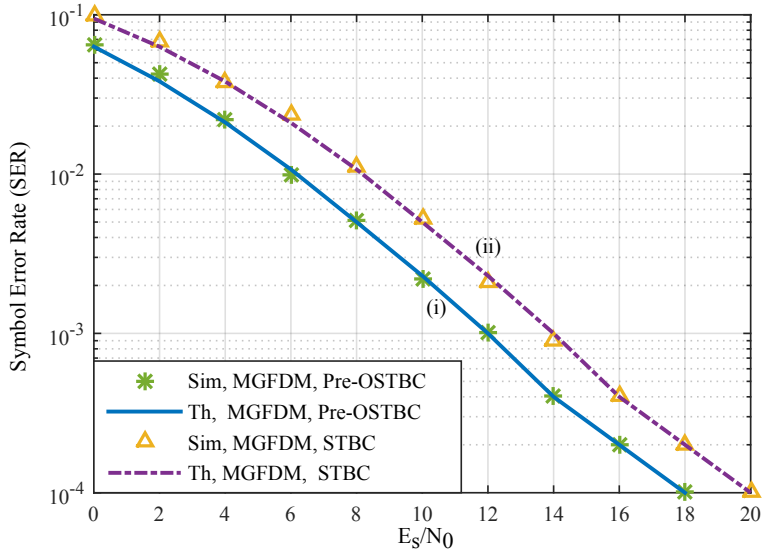

Figure 5.3: Comparison plot for precoded OSTBC MGFDM and STBC MGFDM systems with 16-QAM, Rayleigh fading channel.

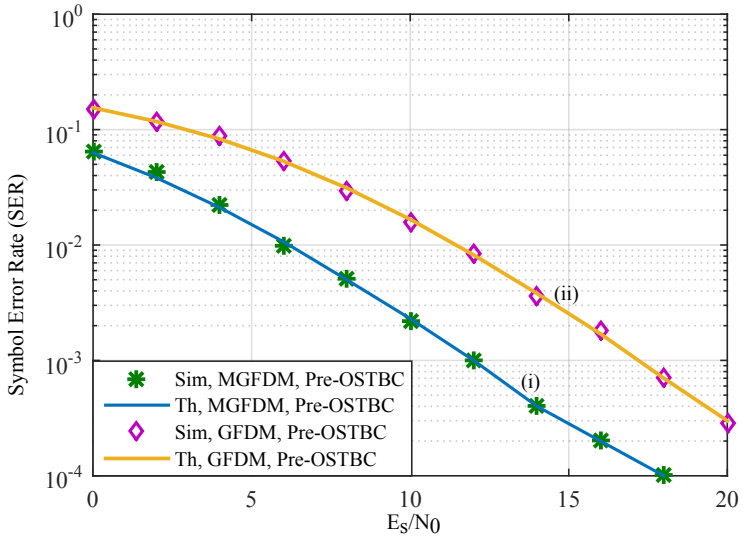

Figure 5.4: Comparison plot under precoded OSTBC technique for both MGFDM and conventional GFDM systems with 16-QAM.

Figure 5.4 demonstrates the SER performance for precoded OSTBC under both MGFDM and conventional GFDM with roll-off factor $\alpha = 0.1$ using 16-QAM over a flat Rayleigh fading channel. With the use of prolate windows we can compensate the orthogonality loss in conventional GFDM systems and as is evident from the figure, the same holds with the application of precoded OSTBC. There is a good match between the derived analytical expressions and the simulated results. An SER of 10^{-3} is achieved at

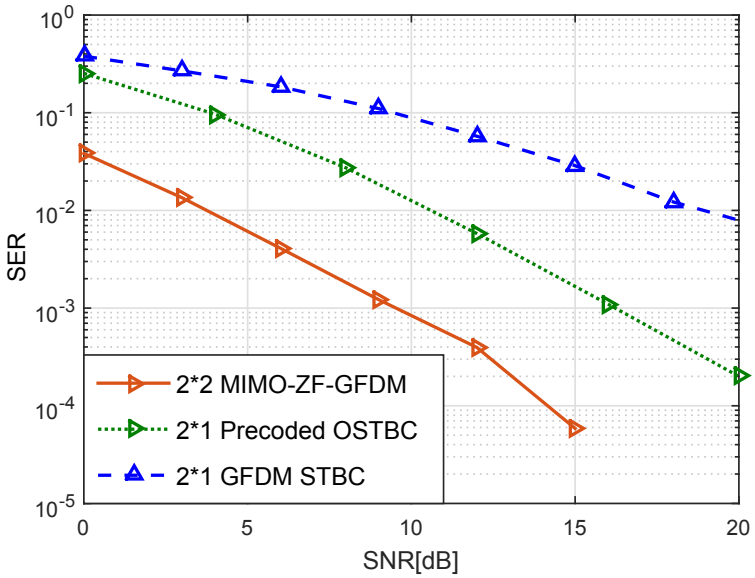

Figure 5.5: Comparison plot under precoded MIMO (2*2), precoded OSTBC technique and STBC for GFDM system with 16-QAM.

an E_s/N_0 of approximately $12dB$ for the precoded OSTBC-MGFDM system ((curve (i)) and $17dB$ in the case of the precoded OSTBC-GFDM system (curve $((ii)$).

A comparison plot for GFDM using ZF precoded MIMO (2*2) technique, precoded OSTBC and STBC methods for GFDM system is shown in Figure 5.5. Interestingly MIMO precoding gains an advantage over the precoded OSTBC. For example, at an SNR of $15dB$ the corresponding BER values for STBC, precoded OSTBC and ZF precoded MIMO techniques are respectively 0.85, 0.09 and 0.0005 This can be well explained by the fact that, using MIMO (2*2) the spatial diversity is increased and hence the throughput is doubled compared to the single antenna configuration. In addition the precoding matrix further helps to decrease the error rates.

5.4.2 Evaluation of GFDM/OQAM under various channels

In this section we present the simulation results along with the theoretical expressions obtained under the ZF receiver, 16-QAM. The system parameters considered for simulations are presented in Table 5.3. Table 5.4 presents the channel delay profile based on Extended Pedestrain A (EPA) model [83] that has been considered to evaluate SER performance under the Rayleigh fading channel.

Table 5.3: Simulation Parameters used for evaluation of GFDM/OQAM

Description	Parameter	Value
Number of Subcarriers	N	64
Number of time slots	M	5
Pulse shape filter	g	RRC
Roll-off factor	α	$\{0.1, 0.5, 0.9\}$
Length of CP	N_{CP}	0
Modulation order	μ	2,4,5,6,7
Rician fading parameter	K	0,1,2,3
Nakagami fading parameter	m	1,2,3
Hoyt fading parameter	q	1,0.4,0.3,0.2

Table 5.4: Channel delay profile

jth sample	0	1	2	3	4	5	6
h_j[dB]	0	-1	-2	-3	-8	-17.2	-20.8

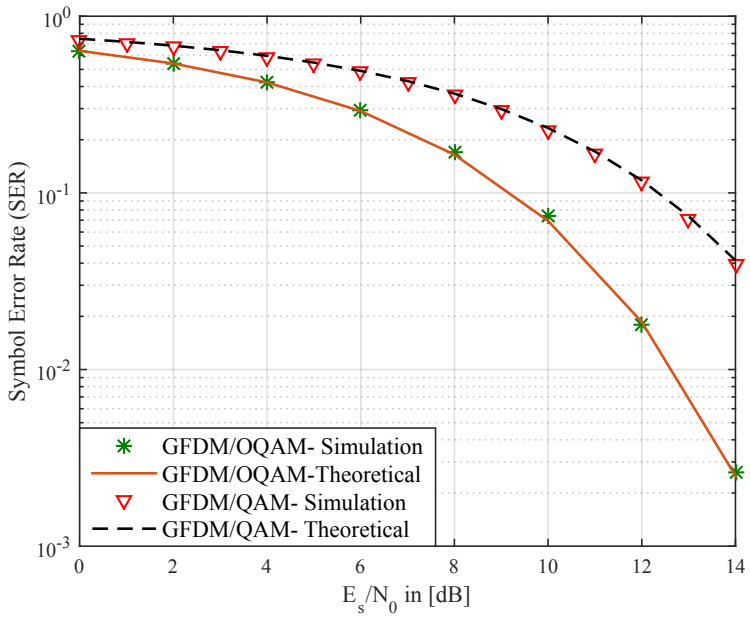

Figure 5.6: SER performance under AWGN channel with $\alpha = 0.1$, 16-QAM

Figure 5.6 shows the plot between SER versus E_s/N_0 in AWGN channel. We have used Table 5.3 parameters for simulations in GFDM and no CP for GFDM/OQAM. The SER obtained from the analytical expression and that of the simulation match quite well. Conventional GFDM is also provided for comparison purpose. From the figure we can

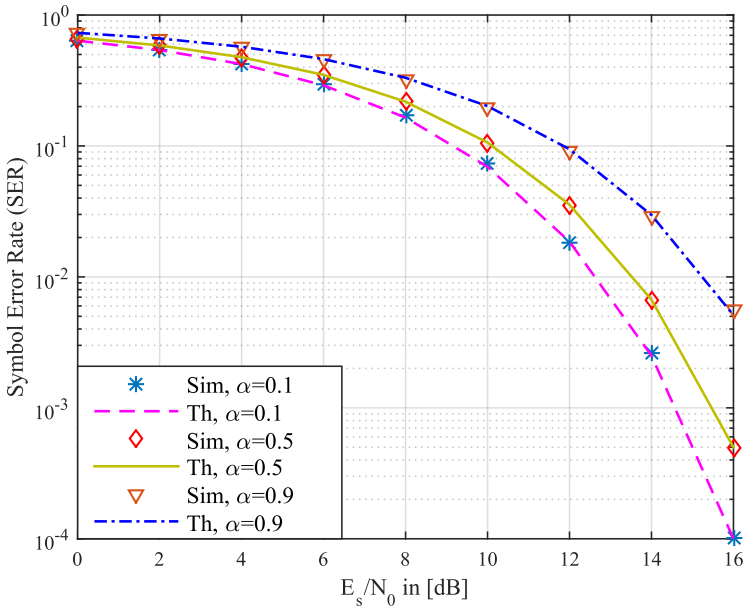

Figure 5.7: Effect of roll-off factor with $\alpha = 0.1, 0.5, 0.9$ under AWGN channel

infer that GFDM/OQAM outperforms the conventional GFDM model. For example, a SER of 0.16 is achieved at $9dB$ for GFDM/OQAM and $12dB$ for GFDM. Hence there is a $3dB$ difference for the same SER. Moreover there is no need of CP as in the case of GFDM-OQAM, which in turn increases the spectral efficiency.

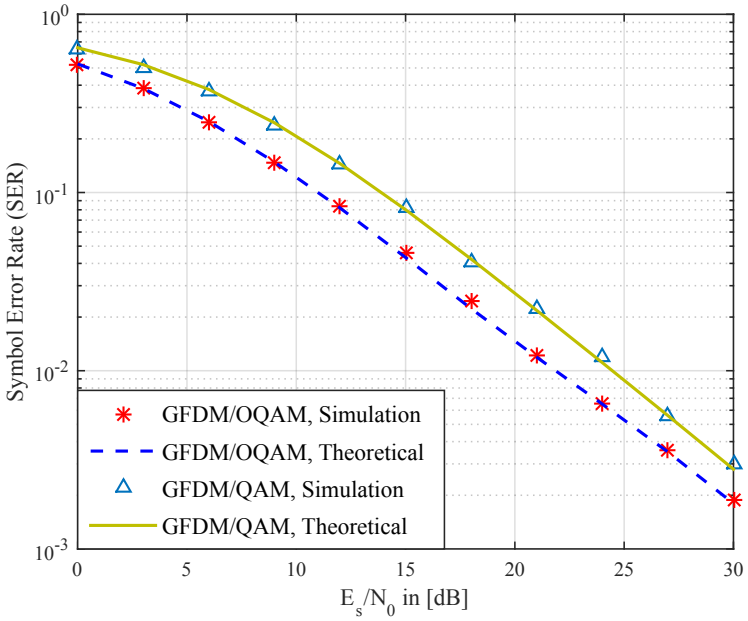

Figure 5.8: SER performance under Rayleigh channel with $\alpha = 0.5$

The effect of the roll-off factor on the system performance is shown in Figure 5.7.

As we increase the roll-off factor from 0.1 to 0.9, the SER increases in GFDM/OQAM system. This is due to the fact that as we increase the roll-off factor, there is a wider overlap between the subcarriers which in turn increases the NEF ξ factor.

Figure 5.8 illustrates the theoretical results of equation (5.28) along with simulations under Rayleigh fading channel with channel delay profile coefficients as mentioned in Table 5.4, with a roll-off factor of 0.5. The theoretical result matches quite well with the simulation values. GFDM/QAM is provided for comparison. Similar to the AWGN case, we can see that there is an improvement in the system when we follow OQAM in comparison to that of conventional GFDM/QAM system. For instance at $15dB$ SNR, the SER for GFDM with OQAM and QAM are respectively 0.0454 and 0.0823. In GFDM/OQAM, allowing the orthogonality condition to the real field of the QAM symbols with good time-frequency localized pulse shaping provides a better performance when compared to GFDM/QAM. In detail, GFDM using QAM modulation, the BLT prohibits orthogonality completely (allowing only good time-frequency localized pulse shaping), which effects the performance of SER when using ZF detectors. Hence, even under the assumption of perfect synchronization, GFDM/QAM SER performance deteriorates compared to GFDM/OQAM. In addition, the exclusion of CP not only increases the spectral efficiency but also saves the power consumed by adding the CP.

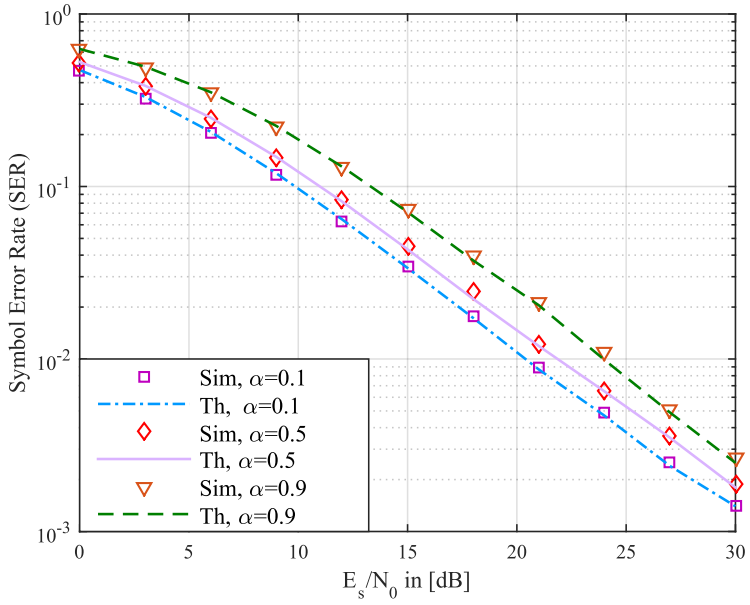

Figure 5.9: SER performance under Rayleigh channel with $\alpha = 0.1, 0.5, 0.9$

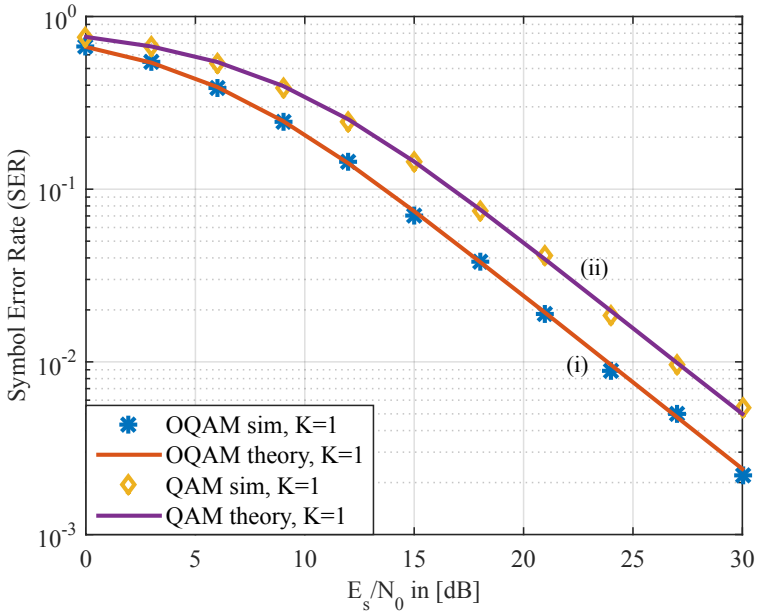

Figure 5.10: Comparing GFDM SER with OQAM and QAM under Rician-K fading channel with $K = 1$, $\alpha = 0.1$

Figure 5.9 is the plot between SER and E_s/N_0 under a Rayleigh fading channel for different α values. From the figure we can infer that as we increase the roll-off factor the error rates increase. The same explanation we gave for the AWGN channel holds here as well. Typical values at $15dB$ are 0.0343, 0.0454 and 0.0736 for roll-off factors of 0.1, 0.5 and 0.9 respectively.

In Figure 5.10 we see the simulation results and analytical computations of GFDM using the QAM and OQAM techniques. The parameters under consideration are: Rician fading factor $K = 1$, roll-off factor $\alpha = 0.1$ and modulation order $\mu = 4$. Curve (i) shows the GFDM-OQAM system performance whereas curve (ii) depicts the corresponding GFDM-QAM system performance under the same channel conditions.

Clearly there is an improvement in terms of SER when using GFDM-OQAM compared to GFDM-QAM. For example, an error rate of 0.0096 can be achieved by GFDM-OQAM at an SNR of $24dB$ while the same error rate is achieved by GFDM-QAM at $27dB$. Hence, for the same error rate GFDM-OQAM can transmit symbols with half the power when compared to GFDM-QAM. This improvement can be explained by the use of the near orthogonality concept of OQAM.

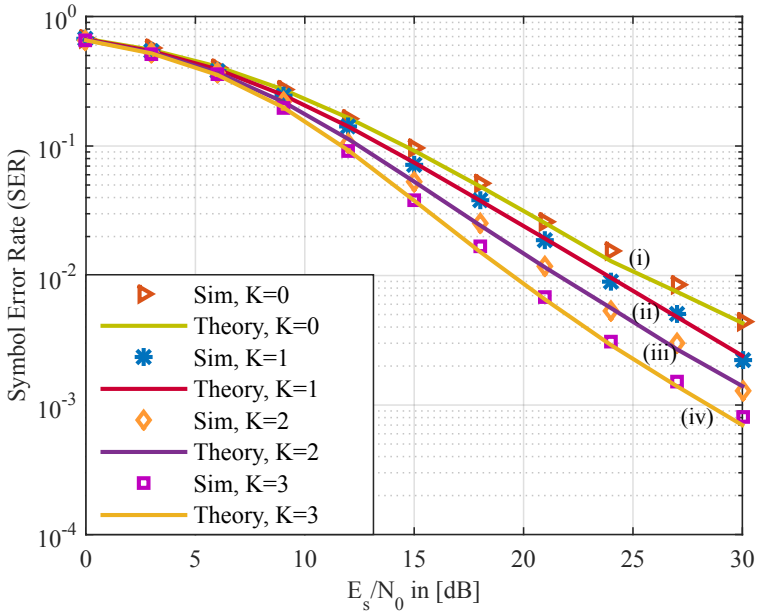

Figure 5.11: SER performance of GFDM-OQAM under Rician channel with $\alpha = 0.1$, $\mu = 4$

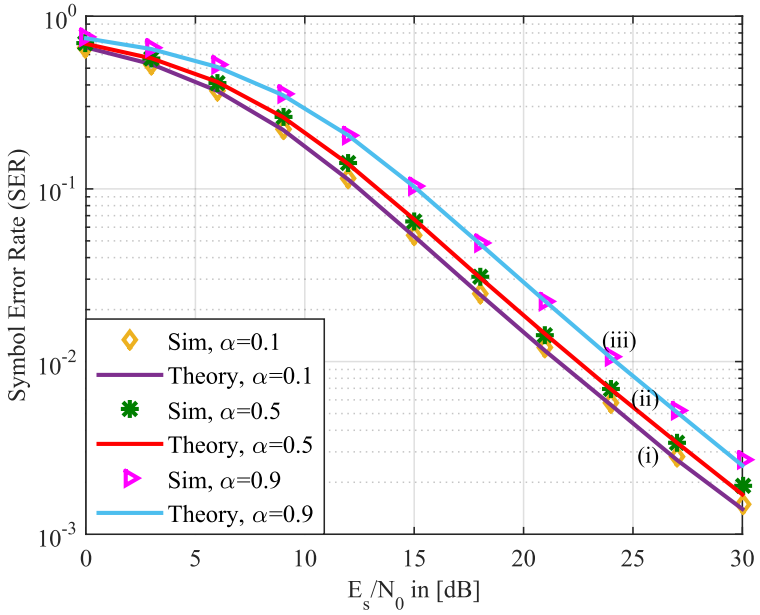

Figure 5.12: Effect of roll-off factor with $\alpha = 0.1, 0.5, 0.9$ under Rician fading channel parameter $K = 2$, $\mu = 4$

Figure 5.11 shows the influence of the Rician fading parameter K on system performance. The parameters considered are roll-off factor, $\alpha = 0.1$ and a 16-QAM modulation scheme. From the figure we can infer that as we increase the K value from 0 to 3, there

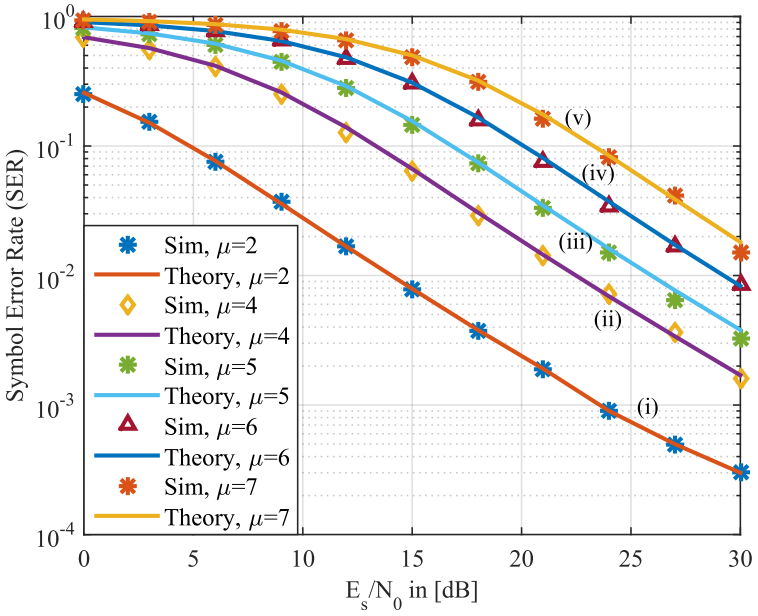

Figure 5.13: SER performance under Rician channel with $K = 2$, $\alpha = 0.5$ for various μ

is a decrease in the SER values (curve (i) to curve (iv)). Typical values at an SNR of $21dB$ for $K = 0, 1, 2, 3$ are respectively given by 0.0260, 0.0189, 0.0117 and 0.0068.

Figure 5.12 explains the effect of the NEF factor ξ with Rician fading parameter $K = 2$. As we increase the roll-off factor α from 0.1 to 0.9, there will be a wider overlap between the subcarriers leading to an increase in NEF. Hence, there is a decrease in system performance as we increase the NEF factor.

In Figure 5.13 we show the effect of modulation order μ with Rician fading parameter $K = 2$ and $\alpha = 0.5$. It is observed that as we increase the modulation order μ from 2 to 7, the SER increases as depicted in the figure.

Figure 5.14 shows the plot between SER versus E_s/N_0 in the Nakagami-m fading channel with fading parameter $m = 3$. There is a good match between the simulation results and the SER analytical expression under the Nakagami-m fading channel. Conventional GFDM with QAM (curve (i)) implementation is also provided for comparison purposes. There is a marked improvement in terms of SER in the GFDM/OQAM implementation when compared to that of conventional GFDM. For example, a SER of 10^{-4} is achieved at approximately $24dB$ for GFDM/OQAM and $27dB$ for GFDM, a $3dB$ difference in order to achieve the same SER.

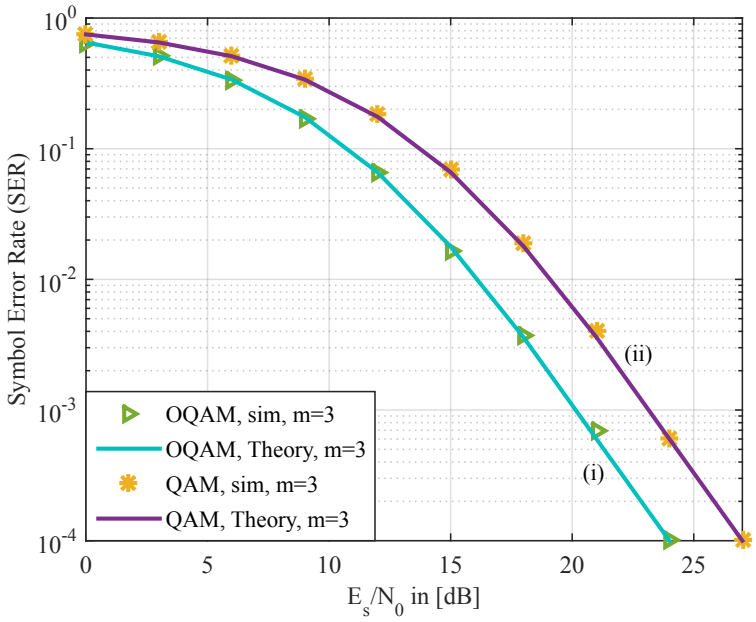

Figure 5.14: SER comparison of GFDM with OQAM and QAM under Nakagami-m fading channel with $m = 3$, $\alpha = 0.1$

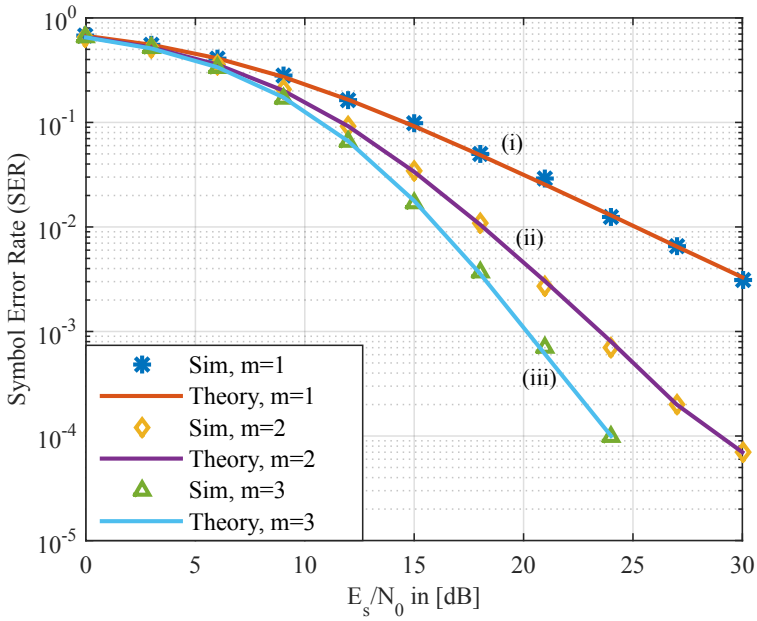

Figure 5.15: SER performance of GFDM-OQAM under Nakagami-m Fading channel with $\alpha = 0.1$, $\mu = 4$

The effect of the Nakagami fading parameter m on system performance is shown in Figure 5.15. The parameters considered are a roll-off factor, $\alpha = 0.1$ and a 16-QAM modulation scheme. From the figure, we can infer that, as we increase the m value from

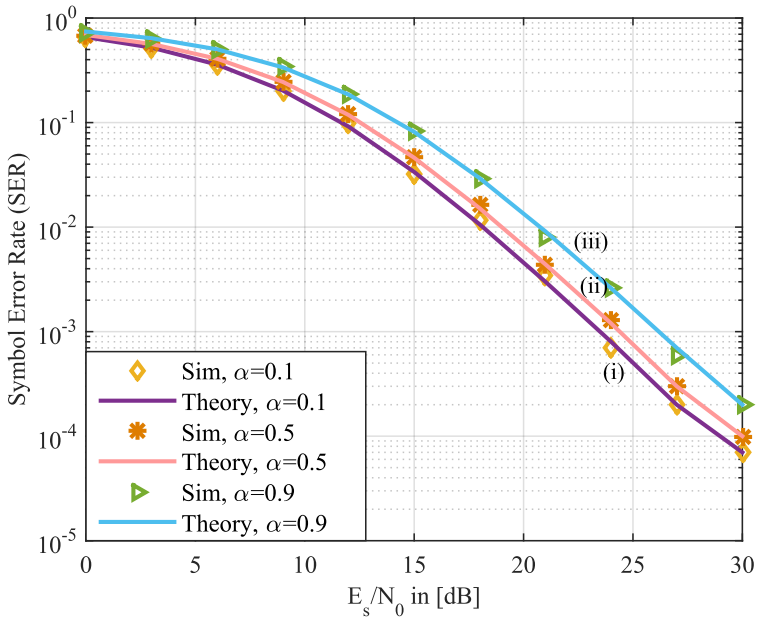

Figure 5.16: Effect of roll-off factor $\alpha = 0.1, 0.5, 0.9$ under Nakagami fading channel with $m = 2$, $\mu = 4$

1 to 3, there is a decrease in the SER values (curve (i) to curve (iii)). It should be noted that the curve (i) is identical to Rayleigh fading conditions and matches with our previous work [60]. Typical values at an SNR of $20dB$ for $m = 1, 2, 3$ are given respectively by 0.0210, 0.0030 and 0.001.

Figure 5.16 displays the effect of the NEF factor ξ with a Nakagami fading parameter of $m = 2$. As we increase the roll-off factor α from 0.1 to 0.9, there will be a wider overlap between the subcarriers, which leads to an increase in NEF.

In Figure 5.17, we show the effect of the modulation order μ for the case of a Nakagami fading parameter $m = 2$ and $\alpha = 0.5$. It is observed that, as we increase the modulation order μ from 2 to 7, the SER increases, as depicted in the figure.

Figure 5.18 depicts the SER performance comparison of the proposed GFDM/OQAM to that of conventional GFDM with Hoyt fading parameters $q = 0.3$ and $\alpha = 0.1$. Due to the near orthogonality nature of OQAM, the symbol error rate in GFDM/OQAM decreases considerably when compared to conventional GFDM. For example, an SER of 10^{-2} can be achieved at an SNR of $27dB$ for GFDM/OQAM and at $30dB$ by conventional GFDM. Hence, just as in the case of the Nakagami-m fading channel, there is also

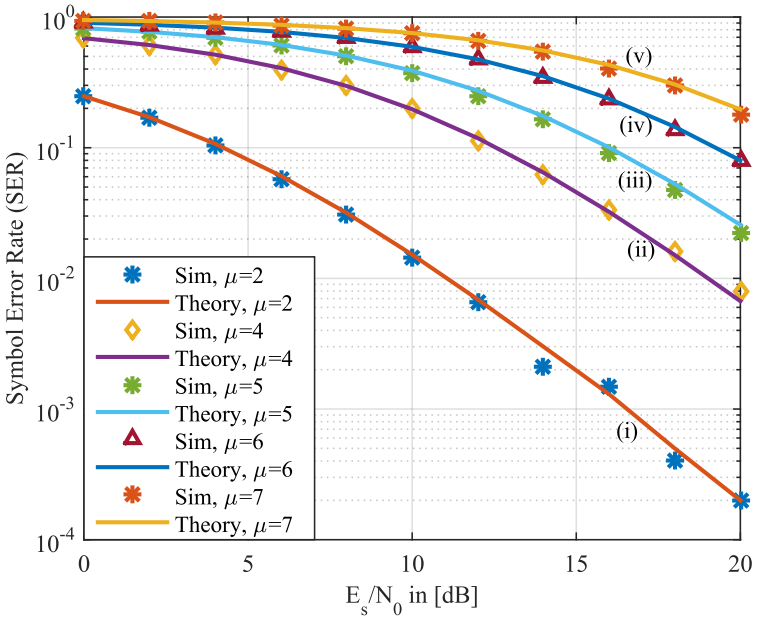

Figure 5.17: SER performance under Nakagami fading channel with $m = 2$, $\alpha = 0.5$ for various μ

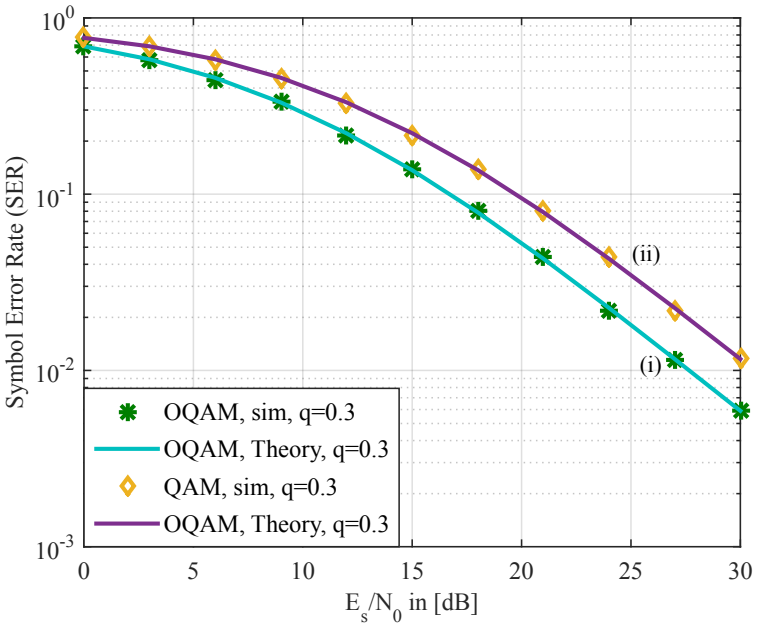

Figure 5.18: SER comparison of GFDM with OQAM and QAM under Hoyt-q fading channel with $q = 0.3$, $\alpha = 0.1$

a $3dB$ improvement in the proposed scheme here. A good match between the analytical expressions and the simulation results is observed as well.

Figure 5.19 illustrates the effect of the Hoyt fading parameter q on the GFDM/OQAM

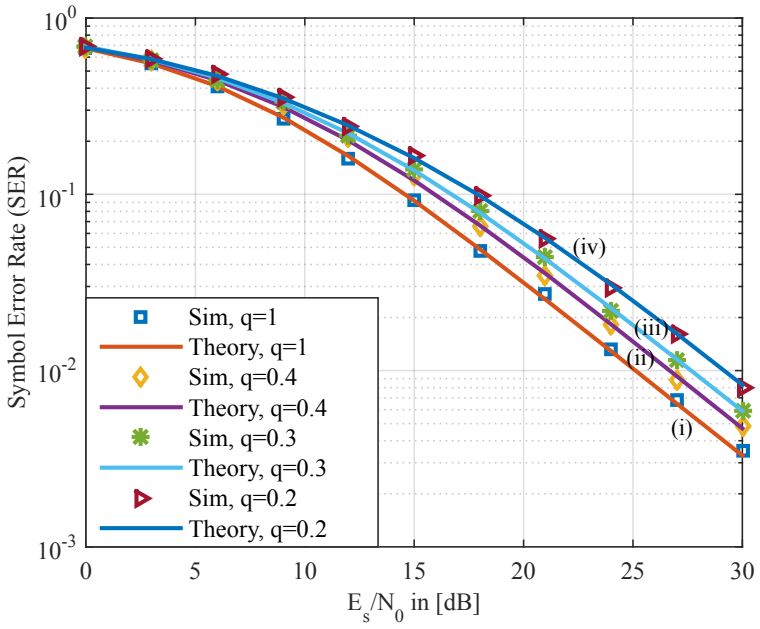

Figure 5.19: SER performance of GFDM-OQAM under Hoyt fading channel with $\alpha = 0.1, \mu = 4$

system performance with a roll-off factor of $\alpha = 0.1, \mu = 4$. From the figure, it is obvious that, as we decrease the value of the Hoyt fading parameter q from 1 (curves (iv)) to 0.2 (curves (i)), the SER decreases. Typical values at an SNR of $27dB$ for $q = 1, 0.4, 0.3, 0.2$ are 0.0068,0.0089,0.0114 and 0.0163 respectively.

The effect on SER performance with Hoyt fading parameter $q = 0.3$, $\mu = 4$ and for various values of roll-off factor α is shown in Figure 5.20. Similar to Nakagami-m case as we increase the α value from 0.1 (curve (i)) to 0.9 curve (iii), the SER increases as depicted in Figure 5.20. As an example, an SER of 10^{-2} is achieved approximately at an SNR of $27dB$, $28.5dB$ and $30dB$ for $\alpha = 0.1, 0.5, 0.9$ respectively.

Figure 5.21 compares the performance of the GFDM/OQAM system under a Hoyt fading channel with $q = 0.3$, $\alpha = 0.5$ and for various values of modulation order $\mu = 2, 4, 5, 6, 7$. The results show a good match between simulation and analytical values. The SER decreases as we decrease the modulation order μ (curves (v) to (i)).

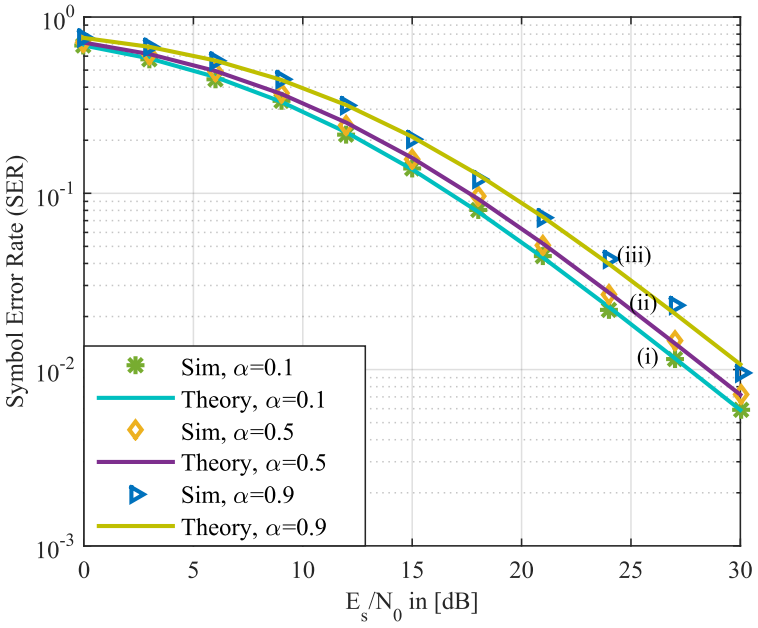

Figure 5.20: Effect of roll-off factor $\alpha = 0.1, 0.5, 0.9$ under Hoyt fading channel with $q = 0.3$

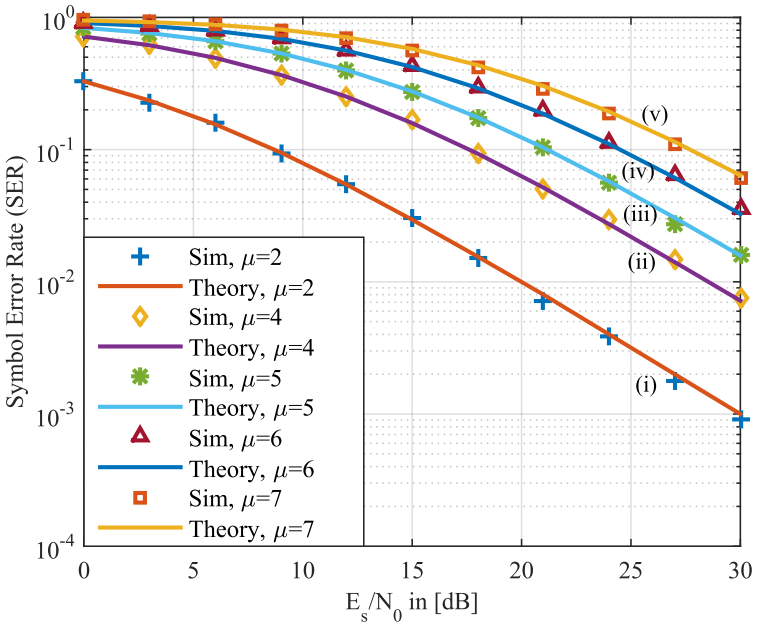

Figure 5.21: SER performance under Hoyt fading channel with $q = 0.3$, $\alpha = 0.5$ for various μ

5.5 Chapter Summary

In this chapter an overview of the improvements that has been made to the conventional GFDM system is provided.

Initially, we investigated the performance of conventional GFDM and MGFDM systems combining the Alamouti scheme and precoded OSTBC over a Rayleigh fading channel. More explicitly, we derived analytical SER expressions of precoded OSTBC-MGFDM and conventional GFDM systems. The derived analytical results are then validated through simulations. Our analysis proves that there is an improvement in SER performance when comparing STBC-GFDM systems to conventional GFDM as well as a higher diversity advantage. In fact, with the further use of multi-tapers as prototype filters we observe a still additional improvement in an OSTBC-GFDM system.

Next we presented a preliminary performance analysis of the novel GFDM/OQAM modulation scheme in AWGN, Rayleigh, Rician-K, Nakagami-m and Nakagami-q channels. The SER result obtained from simulations is supported by that obtained using the analytical expression developed in this chapter. A comparision between conventional GFDM with that of the proposed GFDM/OQAM in the presence of above mentioned channels is studied. The near orthogonality concept of OQAM provides a GFDM system with more robustness in a fading environment. Due to the non-orthogonal pulse shape prototype filters in conventional GFDM, there is a performance degradation not only in terms of the SER but also in using a CP. It is shown here that with the use of the near orthogonal OQAM approach, performance can be significantly improved. Furthermore, the effect of the roll-off factor on the system performance is studied and it is observed that as we increase the roll-factor, the SER increases. Moreover, the influence of the modulation orders μ on system performance was also demonstrated. Even though there is an additional complexity in designing the GFDM/OQAM system, we can gain advantage in achieving better spectral efficiency and better error rate performance.

In summary, the investigations provide us with an important understanding of the behaviour of modifications that are applied to non-orthogonal conventional GFDM systems.

Chapter 6

Channel Estimation and Coding techniques for GFDM

6.1 Introduction and Motivation

Unlike the OFDM based systems, GFDM waveform is a non-orthogonal multicarrier technique with inherent inter-carrier and inter-symbol interferences. This poses challenges in designing the receiver along with the adverse effects of the channel environment. Thus channel estimation is one of the crucial part at the receiver for an essential reliable communication [173]. Hence by utilizing the reference signals (also known as pilots), one can minimize the degradation of system performance [174].

For any mobile communication system, since the channel is very random and time variant in nature it is crucial to know about the channel behaviour (also referred as CSI). This chapter initially handles the channel estimation of MGFDM system. Generally, the two major categories of estimating the channel are blind (non-data aided) and non-blind (data aided) methods, with a major difference in exploiting the information from the signal. Typically, behaviour of the received signal statistics are utilized for blind channel estimation, while the training sequence or pilot tones are exploited by the receiver for non-blind aided channel estimation. Pilot symbols are multiplexed along with the information data symbols and this type of arrangement is known as *comb-type* pilot insertion, where pilot tones are inserted in each MGFDM symbol on some of the subcarriers at specific locations. These pilot symbols are known to both transmitter and receiver and a variety

of interpolation techniques can be employed to estimate the channel response. Since the channel environment is highly dispersive in nature, sensing and tracking of this channel is essential for the purpose of ensuring perfect reception of the transmitted data. In particular, wireless channel estimation can be performed by employing a specific pilot arrangement based channel estimation. However, due to block based structure of GFDM system incorporating these techniques is not straightforward. In brief, LS and MMSE channel estimation techniques are used for estimating the channel at pilot frequencies followed by interpolating the channel. Consequently, once the channel information at the pilot carriers is estimated, then the channel state at the data subcarriers can be estimated by employing various interpolation techniques like linear and spline based interpolation. The channel estimation methods like LS and MMSE are exploited to estimate the channel response along with the support of theoretical expressions.

Finally, the performance of the convolution coded MGFDM system along with conventional GFDM is investigated. With the primary aim to assure a reliable and high-speed wireless data service for mobile and portable cellular subscribers, one way is to combine multicarrier modulation technique with coding schemes. For the provision of facilitating reliable transmission over a noisy channel, Forward Error Correction (FEC) plays a vital role in modern digital wireless communication systems. In particular, a certain amount of redundancy must be added to the transmitted data. Even though these additional bits do not convey any information, they provide a means for the channel decoder to detect and correct the information bearing bits. Furthermore, error correction and detection reduces the overall probability of error. In IEEE 802.11a/g transmitters, convolution codes are used for FEC at the physical layer. A number of wireless communication standards use convolutional coding for FEC with detection being carried out by Viterbi decoding. The convolutional code uses a Trellis structure and it is to be noted that the industry standard for the Trellis is (7, [171, 133])-i.e., a constraint length of 7 with generator polynomials 171_8 and 133_8. During data transmission, random bit errors may occur due to environmental interference and physical defects. For reliable communications, FEC codes are most commonly used in order to overcome the adverse effects of the AWGN channel. The analysis of such CMGFDM complex system is a challenging job and this kind of structure will result in an effective way to combat the effects of channel fading environment.

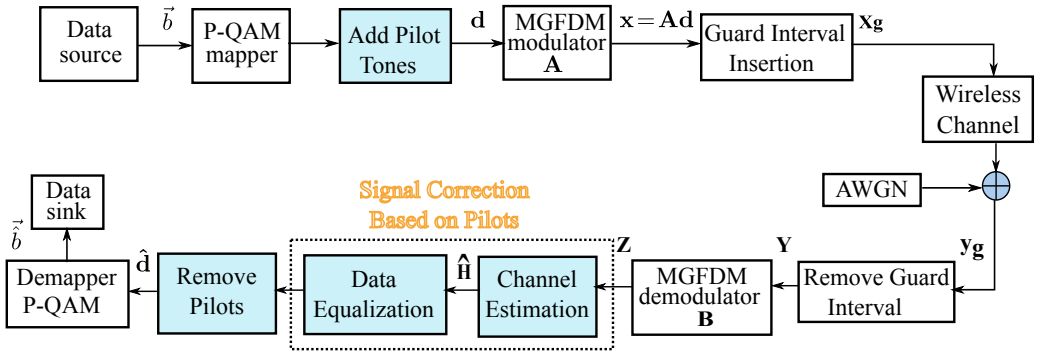

Figure 6.1: Baseband model for pilot based MGFDM system

In brief this chapter evaluates the performance of CMGFDM system by incorporating various channel estimation techniques using training symbols. Furthermore, the main aspects of convolution coded MGFDM is also highlighted.

6.2 Training Based Channel Estimation for MGFDM System

This approach is applicable in general, to any multi-carrier technique. Pilot symbols are multiplexed along with the information data symbols. These pilot symbols are known to both transmitter and receiver and a variety of interpolation techniques can be employed to estimate the channel response. As is widely done for CE when training symbols are available, the techniques used are LS and MMSE. Figure 6.1 shows the system model for training based channel estimation for the MGFDM system.

6.2.1 Signal model Design for pilot based MGFDM system

The binary data generated from the source are grouped together to form P-QAM modulated data, where $P = 2^{\mu}$ and μ is the modulation index. The training symbols or pilot information bits are inserted at an equal spacing between data symbols. The time domain signal after passing through the MGFDM modulator is given by [56],

$$x(n) = \sum_{i=0}^{N-1} \sum_{m=0}^{M-1} d_i(m) g_{i,m}(n) \quad n = 0, 1, .., NM-1 \tag{6.1}$$

The matrix notation of equation (6.1) is described earlier in Chapter 5.

$$\mathbf{x} = \mathbf{Ad} \tag{6.2}$$

where $\mathbf{A}$ is the transmitter modulation matrix as described earlier in Chapter 5, equation (5.4), while $\mathbf{d}$ is a vector containing the data symbols $d_i(m)$ along with the pilot symbols which are generated randomly and uniformly inserted $\mathbf{X_p} = [X_p(0)\ X_p(1) \cdots X_p(N_p - 1)]$.

Guard interval bits are added at the front side of the symbol in order to prevent ISI that may possible affect the MGFDM system. The signal is then transmitted through the frequency selective multi-path fading channel $h(n)$. The signal received can be represented as [127],

$$y_g[n] = x_g[n] * h[n] + w[n] \tag{6.3}$$

where $*$ denotes linear convolution, $h[n]$ represents the channel impulse response and $w[n]$ is AWGN.

The guard interval bits are removed from the corrupted signal with AWGN i.e., $y_g[n]$ and are sent to the MGFDM demodulator block. There are several receivers found in the literature to demodulated the data [43]. Here we have used the ZF receiver as described earlier in Chapter 5. The demodulated output is written as,

$$\mathbf{Z} = \mathbf{BY} \tag{6.4}$$

where $\mathbf{Y}$ is the received data after removal of guard interval. It should be noted that the length of the guard interval is required to be greater than the length of the channel impulse response in order to avoid ISI. The demodulated output is passed through the signal correction block which is done based on the pilot symbols that are added at the transmitter side. The steps involved in this block are elaborated in Figure 6.2. In this block, the channel estimation of the pilot tones is first carried out, followed by channel interpolation (linear/spline). Finally, the demodulated data are equalized with the estimated channel coefficients.

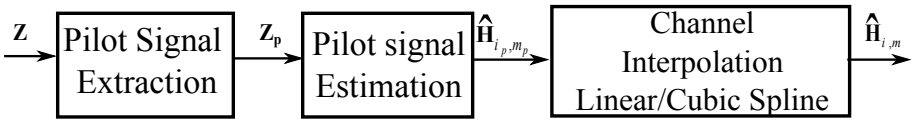

Figure 6.2: Steps involved in Channel Estimation

6.2.2 Channel Estimator

In this section we will briefly discuss the most popularly used channel estimation techniques, LS and MMSE, applicable to any multicarrier technique. This work was inspired by [175] which was originally proposed for OFDM systems. As MGFDM is the generalization of FDM systems, we carried out the same approach to estimate the channel response.

LS

Let $\mathbf{H_p}$ be the channel response of the pilot symbols and $\mathbf{Z_p}$ be the vector of received signal at pilot locations.

$$\mathbf{H_p} = [H_p(0)\ H_p(1) \cdots H_p(N_p - 1)]^T \tag{6.5}$$

$$\mathbf{Z_p} = [Z_p(0)\ Z_p(1) \cdots Z_p(N_p - 1)]^T \tag{6.6}$$

Based on the LS approach [175], the channel estimates of the pilot signals are given by,

$$\begin{aligned} \hat{\mathbf{H}}_{p,LS} &= \mathbf{X_p^{-1}} \mathbf{Z_p} \\ &= \left[\frac{Z_p(0)}{X_p(0)}, \frac{Z_p(1)}{X_p(1)}, \cdots, \frac{Z_p(N_p-1)}{X_p(N_p-1)} \right] \end{aligned} \tag{6.7}$$

where N_p is the number of the pilot symbols used, $\mathbf{X_p}$ and $\mathbf{Z_p}$ are the pilot symbols data at the transmitted side and the pilot information obtained at the receiver side after demodulation respectively. Let us state that the FFT of equation (6.2) is given by,

$$X[i, m] = FFT(\mathbf{x}) \tag{6.8}$$

Then the MSE of the i^{th} subcarrier and m^{th} subsymbol is given by,

$$MSE_{LS}[i, m] = \frac{\beta}{SNR} \tag{6.9}$$

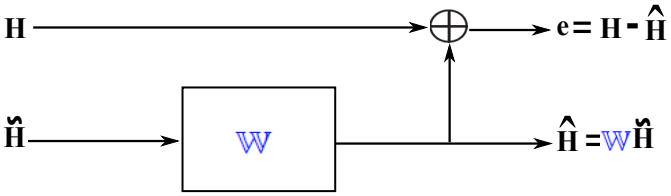

Figure 6.3: MMSE channel estimation

where the factor β [176, 177], is given by $\beta = E\left[|X[i,m]|^2\right] E\left[|X[i,m]|^{-2}\right]$ and is a constant depending on the constellation. For example, β for 16-QAM is 17/9 and $\beta = 1$ for BPSK [177]. $SNR = E\left[|X[i,m]|^2\right]/\sigma_w^2$ is the average SNR.

MMSE

We begin by considering the LS solution obtained in the above approach, $\hat{\mathbf{H}}_{LS} = \mathbf{X_p}^{-1}\mathbf{Z_p} \triangleq \tilde{\mathbf{H}}$. Let us consider the weight matrix $\mathbb{W}$, and define $\hat{\mathbf{H}} \triangleq \mathbb{W}\tilde{\mathbf{H}}$, corresponding to the MMSE estimate. A simple diagram of MMSE channel estimation is given in Figure 6.3. The MSE of $\hat{\mathbf{H}}$ can be obtained by the follwing cost function,

$$C\left(\hat{\mathbf{H}}\right) = \mathbb{E}\left\{\|\mathbf{e}\|^2\right\} = \mathbb{E}\left\{\left\|\mathbf{H} - \hat{\mathbf{H}}\right\|^2\right\} \tag{6.10}$$

From the principle of orthogonality, the error vector $\mathbf{e}$ is orthogonal to $\tilde{\mathbf{H}}$, such that

$$\begin{aligned} \mathbb{E}\left\{\mathbf{e}\tilde{\mathbf{H}}^H\right\} &= \mathbb{E}\left\{\left(\mathbf{H} - \hat{\mathbf{H}}\right)\tilde{\mathbf{H}}^H\right\} \\ &= \mathbb{E}\left\{\left(\mathbf{H} - \mathbb{W}\tilde{\mathbf{H}}\right)\tilde{\mathbf{H}}^H\right\} \\ &= \mathbb{E}\left\{\mathbf{H}\tilde{\mathbf{H}}^H\right\} - \mathbb{W}\mathbb{E}\left\{\tilde{\mathbf{H}}\tilde{\mathbf{H}}^H\right\} \\ &= \mathbf{R}_{\mathbf{H}\tilde{\mathbf{H}}} - \mathbb{W}\mathbf{R}_{\tilde{\mathbf{H}}\tilde{\mathbf{H}}} = 0 \end{aligned} \tag{6.11}$$

Equation (6.11) can be easily solved yielding to,

$$\mathbb{W} = \mathbf{R}_{\mathbf{H}\tilde{\mathbf{H}}}\mathbf{R}_{\tilde{\mathbf{H}}\tilde{\mathbf{H}}}^{-1} \tag{6.12}$$

where $\mathbf{R}_{\tilde{\mathbf{H}}\tilde{\mathbf{H}}}$ is the auto-correlation matrix of the LS estimate. The MMSE estimate of the channel is given by [126],

$$\hat{\mathbf{H}}_{mmse} = \mathbf{R}_{\mathbf{H_pH_{p,LS}}}\left(\mathbf{R}_{\mathbf{H_pH_p}} + \sigma_w^2(\mathbf{X_pX_p^H})^{-1}\right)^{-1}\hat{\mathbf{H}}_{LS} \tag{6.13}$$

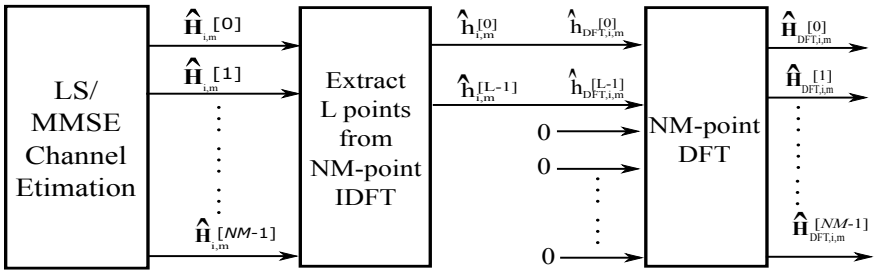

Figure 6.4: Block diagram of DFT based channel estimation.

where $\mathbf{R_{H_pH_{p,LS}}} = E[\mathbf{H_p}\mathbf{H}^{\mathbf{H}}_{\mathbf{p,LS}}]$ is the cross correlation matrix between $\mathbf{H_p}$ and $\mathbf{H_{p,LS}}$. $(.)^{\mathbf{H}}$ is the hermitian of a matrix, $\hat{\mathbf{H}}_{LS}$ is the least square channel estimation and σ_w^2 is the variance of the noise.

6.2.3 Channel Interpolation

To estimate the complete response of the channel, we make use of the interpolation concept. In this, the samples of the channel response are interpolated according to the estimated channel response of the pilot tones. This kind of work was considered for OFDM systems [175] and is shown to be efficient. In order to increase the overall system performance of such an advanced multi-carrier technique (MGFDM), the complete channel state/coefficients should be estimated more accurately. Hence, information about the channel at both pilot and non-pilot locations is essentially what is required to enhance performance. The interpolation method is an efficient way to estimate the non-pilot (data location) channel characteristics by making use of the channel coefficients at the pilots. In this article we examined two interpolation techniques, namely piecewise linear interpolation and cubic spline interpolation. More details on these techniques can be found in [175].

6.2.4 DFT based channel estimation

In order to improve the performance of LS and MMSE, a DFT based channel estimation is considered. The performance of such DFT based channel estimators are analyzed for OFDM systems and [177,178] provides more insights about the method. The scope of this work is to investigate such estimators for MGFDM system using MSE as a measuring

parameter. A simple block diagram of DFT based CE is shown in Figure 6.4. In this, application of DFT on LS and MMSE will improve the performance of the estimators by eliminating the noise outside the channel delay. It transforms the frequency channel estimation to time channel estimation using Inverse Discrete Fourier Transform (IDFT) and considers the part which is larger than channel delay L as noise, treats that part as zero in order to eliminate the impact of noise. Let $\hat{\mathbf{H}}_{\mathbf{i,m}}$ denote the estimation of the channel response at the ith subcarrier and mth subsymbol, calculated either by using the LS or the MMSE method. This is a two step process. First, we take the IDFT of the $\hat{\mathbf{H}}_{\mathbf{i,m}}$ and ignore the coefficients outside the maximum channel delay. Next, the obtained time domain channel estimation coefficients are converted back to frequency domain by taking an NM point DFT. This can be mathematically represented as follows,

$$IDFT[\hat{\mathbf{H}}_{\mathbf{i,m}}[\mathbf{n}]] = \hat{h}_{i,m}[n] = \hat{h}_{DFT,i,m}[n] \tag{6.14}$$

$$\hat{\mathbf{H}}_{\mathbf{DFT,i,m}}[\mathbf{n}] = DFT[\hat{h}_{DFT,i,m}[n]] \tag{6.15}$$

where $n = 0, 1...., NM - 1$.

The individual MSE of the DFT based channel estimation is given by,

$$MSE_{DFT}[i, m] = \frac{L}{N_c}\frac{\beta}{SNR} \tag{6.16}$$

where N_c is a constant and L depends on the channel environment. According to [179], $L/N_c = T_G/T_s$ in IEEE 802.11, IEEE 802.16 standards is selected from $\{1/32,\ 1/16,\ 1/8,\ 1/4\}$.

The simulated MSE is given by the average of the error matrix,

$$MSE = \frac{1}{NM}E\left\{\left(\hat{\mathbf{H}} - \mathbf{H}\right)\left(\hat{\mathbf{H}} - \mathbf{H}\right)^T\right\} \tag{6.17}$$

where $E.$ is the expectation operator, $(.)^T$ is the transpose of the matrix and $\hat{\mathbf{H}}$ is the channel estimate.

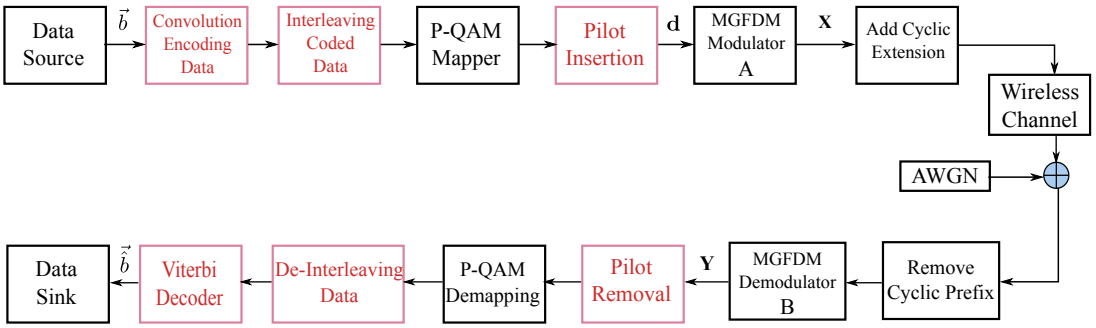

Figure 6.5: Transceiver schematic of Coded MGFDM system

6.3 Convolution Codes for GFDM Systems

In this section, we consider an MGFDM communication system with a convolution code at the transmitter side for efficient data transmission. At the receiver side, the detection scheme is carried out by using Viterbi decoding [180] and a fair amount of channel errors can be corrected by exploiting the redundant data that are transmitted. These CMGFDM systems can effectively tolerate more interference and noise effects. The baseband transceiver structure of CMGFDM is shown in Figure 6.5.

6.3.1 CMGFDM Transmitter

The data source generates a binary vector $\vec{b}$ that is supplied to the convolution encoder as shown in Figure 6.5. Convolutional codes which are widely used as channel codes for error correction are incorporated in this system model. In essence, convolution coding is performed by appropriately combining the fixed number of input bits. These bits are stored in the fixed length shift registers and are combined with the help of modulo-2 adders [181]. This operation is equivalent to binary convolution and hence is called convolution coding. In order to have an idea of the encoding process we start with the simple block diagram of a convolutional encoder with code rate 1/2. Figure 6.6 illustrates that the information bits are fed in small groups of p_g-bits at a time to a shift register. The output encoded bits are obtained by modulo-2 addition (EXCLUSIVE-OR operation) of the input information bits and the contents of the shift registers which contain a few previous information bits. In brief, the encoder generates a group of q_g encoded bits per group of p_g information bits, where the code rate R_c has the following representation,

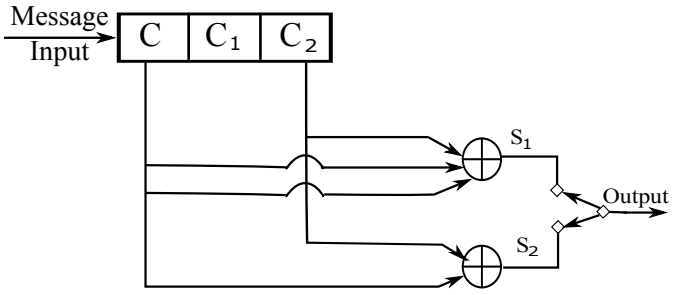

Figure 6.6: Convolutional encoder with shift registers

$$R_c = \frac{p_g}{q_g} \tag{6.18}$$

where $p_g < q_g$. Generally, q_g and p_g are significant in determining the dimension of the code. Here, the dimension of the code is denoted by (p_g, q_g) where, q_g represents the encoded output bits for p_g number of message bits. A widely used decoding algorithm for convolutional codes is the Viterbi algorithm.

Before starting with the Viterbi decoding algorithm explanation, a simple mathematical analysis has been developed starting with the states of the encoder. Referring to Figure 6.6 the previous two successive message bits c_1 and c_2 represent the state of the encoder. The input message bit c effects the 'state' of the encoder as well as the outputs s_1 and s_2 during that state. Whenever a new message bit is shifted to c, the contents of c_1 and c_2 define the new state. Also, the outputs s_1 and s_2 are changed according to the new state c_1, c_2 and message bit c. Here, for $p_g = 1$ the number of encoded bits for one message bit is $q_g = 2$. Also the outputs are expressed as,

$$s_1 = c \oplus c_1 \oplus c_2 \tag{6.19}$$

$$s_2 = c \oplus c_2 \tag{6.20}$$

The Trellis diagram of the convolutional code is obtained from its state diagram. All state transitions at each time step are explicitly shown in Figure 6.7. Usually, supporting descriptions on state transitions, corresponding input and output bits etc., are labeled in the Trellis diagram. It is interesting to note that the Trellis diagram, which describes the operation of the encoder, is very convenient for also describing the behavior of the corresponding 'Viterbi Algorithm' decoder.

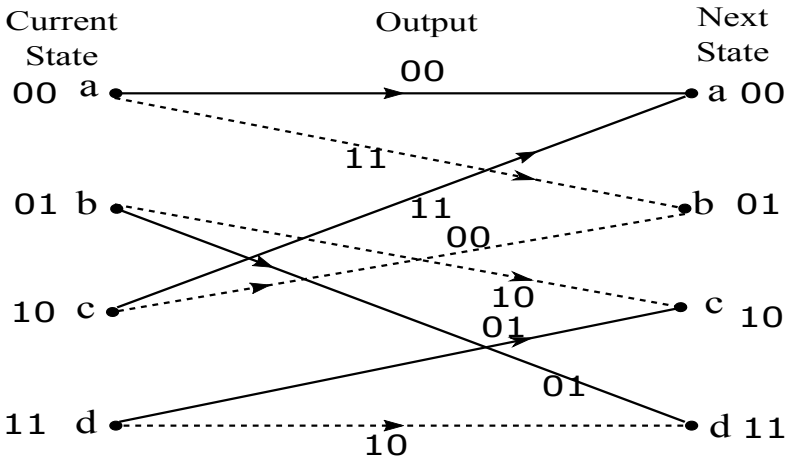

Figure 6.7: Trellis Diagram

Table 6.1: State Table

C_1	C_2	State of the encoder
0	0	a
0	1	b
1	0	c
1	1	d

The output of the encoded data is interleaved. The interleaved data is passed through the $P-$QAM mapper to map groups of μ bits, where μ denotes the modulation order representing the number of bits per symbol of a chosen modulation scheme. Pilot symbols are later inserted at precise locations that are known at the receiver side. The resultant data block $\mathbf{d}$ is given by, $\mathbf{d} = \{d_i(m)\}\ \forall\ \ i\ \epsilon\ (0, N-1)$ and $m\ \epsilon\ (0, M-1)$. It is to be noted that each data symbol $d_i(m)$ corresponds to the information transmitted on the i^{th} subcarrier and m^{th} subsymbol. The data vector of length NM generated from the mapper unit along with the pilot symbols are passed through the MGFDM modulator. In a later part, a cyclic extension is transmitted along with the output of the MGFDM modulator for better protection against channel distortions. The transmitted signal $x(n)$ of each MGFDM block is given by [56],

$$x(n) = \sum_{i=0}^{N-1} \sum_{m=0}^{M-1} d_i(m) g_{i,m}(n) \quad n = 0, 1, .., NM-1 \tag{6.21}$$

where

$$\begin{aligned} \text{MGFDM:} \quad & g_{i,m}(n) = g_m(n)e^{\frac{j2\pi in}{N}} \\ \text{GFDM:} \quad & g_{i,m}(n) = g[(n - mN) \bmod NM]e^{\frac{j2\pi in}{N}} \end{aligned} \tag{6.22}$$

with $g_m(l)$ being the l^{th} coefficient of the mth taper. Observe that the modulo operation to the filter coefficients corresponds to the circular convolution which leads to tail biting process [44]. An alternate matrix representation is written as,

$$\mathbf{x} = \mathbf{Ad} \tag{6.23}$$

where $\mathbf{A}$ denotes the modulation matrix incorporating all the signal processing steps of upconversion, pulse shaping and frequency shifting and can be given in matrix notation as [134],

$$\mathbf{A} = [\mathbf{G} \;\; \mathbf{E_1 G} ... \mathbf{E_{N-1} G}]$$

with $\mathbf{G}$ a $NM \times M$ transmitter filter matrix containing the first M tapers each of length NM for MGFDM system and $\mathbf{G}$ is a $NM \times M$ filter matrix where the first column of the matrix consists of the NM samples of the prototype filter and the subsequent columns of the matrix are the K times shifted versions of the previous columns.

$\mathbf{E_i} = diag\left\{[\mathbf{e_i}^T, ..., \mathbf{e_i}^T]^T\right\}$ is a $NM \times NM$ diagonal matrix whose diagonal elements are comprised of M concatenated copies of the vector $\mathbf{e_i} = [1, e^{j\frac{2\pi i}{N}}, ..., e^{j\frac{2\pi i}{N}(N-1)}]^T$. Lastly, a cyclic extension is performed in order to combat channel effects.

6.3.2 CMGFDM Receiver Structure

The received signal after adding AWGN is given by,

$$\mathbf{R} = \mathbf{x} + \mathbf{W} \tag{6.24}$$

where $\mathbf{R}$ is the noise affected signal, $\mathbf{W} \sim \mathcal{CN}(0, \sigma_w^2 I_{NM})$ are the complex additive white Gaussian noise samples with noise variance σ_w^2 and I_{NM} is the identity matrix of order

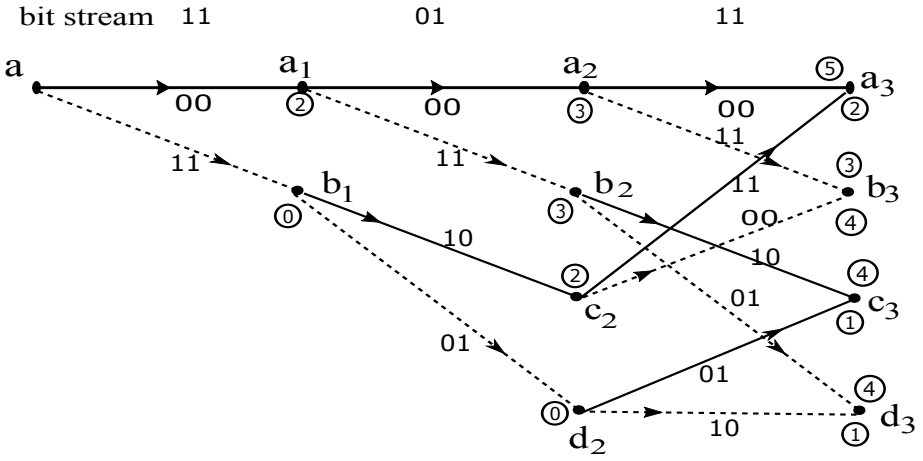

Figure 6.8: Viterbi Decoding

NM.

At the receiver side, the initial cyclic prefix is removed form the corrupted signal. Then, in the MGFDM demodulator, the signal will undergo a series of operations that are opposite to that of the MGFDM modulator at the transmitter side. The demodulated output can be expressed as,

$$\mathbf{Y} = \mathbf{BR} \tag{6.25}$$

where $\mathbf{B}$ under Zero Forcing (ZF) and Matched Filter (MF) receivers are given by,

$$\begin{aligned} \text{ZF:} \quad & \mathbf{B_{ZF}} = \left(\mathbf{A^H A}\right)^{-1} \mathbf{A^H} \\ \text{MF:} \quad & \mathbf{B_{MF}} = \mathbf{A^H} \end{aligned} \tag{6.26}$$

Later, pilot synchronization is performed, followed by symbol demapping to bits. The data is de-interleaved and passed to the Viterbi decoder where the convolutional encoded data is decoded.

We perform maximum likelihood or Viterbi decoding to regenerate the sequence of data bits that are actually the convolution encoder input used for encoding the message or information bits. The input to the Viterbi decoder is the received bit stream and now the main purpose of the Viterbi decoder is to decode the received stream of bits [181].

Here, the Viterbi algorithm utilizes the Trellis diagram to compute the path metrics.

The decoding operation starts from state '00′, i.e. with the assumption that the initial state of the encoder is '00′. With the receipt of one noisy codeword, the decoding operation progresses by one step deeper into the Trellis diagram. The branches, associated with a state of the Trellis tell us about the corresponding codewords that the encoder may generate starting from this state. Hence, upon receipt of a codeword, it is possible to note the 'branch metric' of each branch by determining the Hamming distance of the received codeword from the valid codeword associated with that branch. Path metrics of all branches, associated with all the states are calculated similarly. And now, at each level of the Trellis, each state also carries some 'accumulated path metric', which is the addition of all the metrics of all branches that construct the 'most likely path' to that state. At any depth of the Trellis, each state can be reached through two paths, one from the previous stage and one from the Viterbi Algorithm. The path with lower accumulated path metric is chosen. Finally, the decoded binary bits are collected at the data sink as shown in Figure 6.5.

6.4 Results and Discussions

6.4.1 Channel Estimation analysis

In this section, we will discuss the performance of the channel estimation methods that are investigated in previous sections for the MGFDM system. We have considered a 2-tap random channel model. In Matlab we use the `interp1()` command for interpolation, as this command is based on piecewise linear and cubic interpolation. The simulation parameters that are considered are as shown in Table 6.2. We have used a total of $N * M$ samples in which N_p number of pilots are inserted in between the data points with a pilot spacing of 8.

Figure 6.9 shows the channel estimates obtained by using various types of channel estimation methods and are compared with the true channel. We have assumed that the guard interval is greater than the channel delay L. From the figure it is clear that the MMSE estimation shows an improvement compared to that of the LS approach. In the LS estimate we have used linear interpolation and cubic spline interpolation methods to

Table 6.2: Simulation Parameters used for channel estimation

Description	Value
Number of Subcarriers N, Subsymbols M	32, 4
Total number of samples $(N * M)$	128
Length of CP, N_{cp}	8
Modulation order, μ	4
Length of pilot symbols,N_p	16
Length of the channel, N_{ch}	2

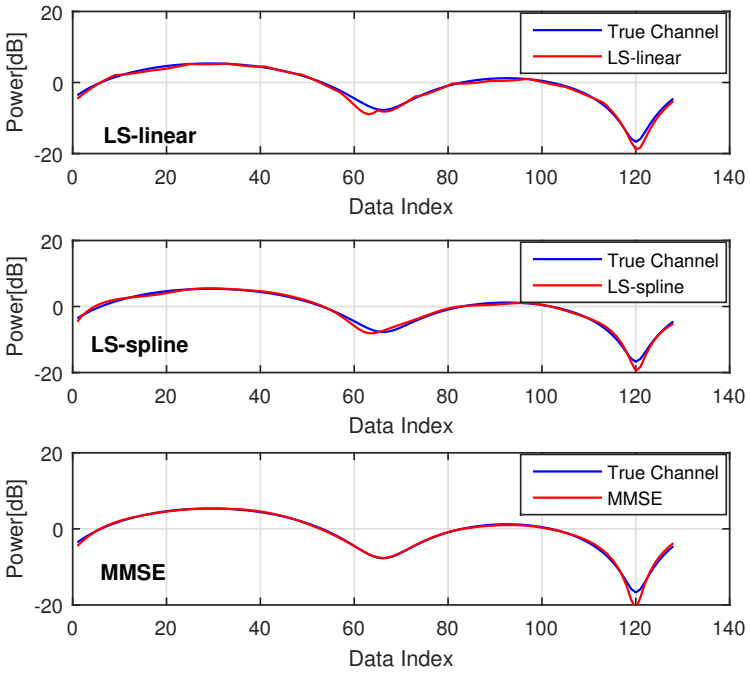

Figure 6.9: Channel Estimation without DFT

estimate the complete channel response.

A DFT based channel estimation method using LS and MMSE is shown in Figure 6.10. A good match between the true channel and the estimated channel response is observed. Comparing Figure 6.9 and Figure 6.10, an improvement is observed in estimating the channel using DFT based channel estimation.

Figure 6.11 illustrates the MGFDM system performance in terms of MSE for different SNR values. The MSE of the proposed three techniques with and without the use of DFT based channel estimation is provided. To strengthen the simulated results,

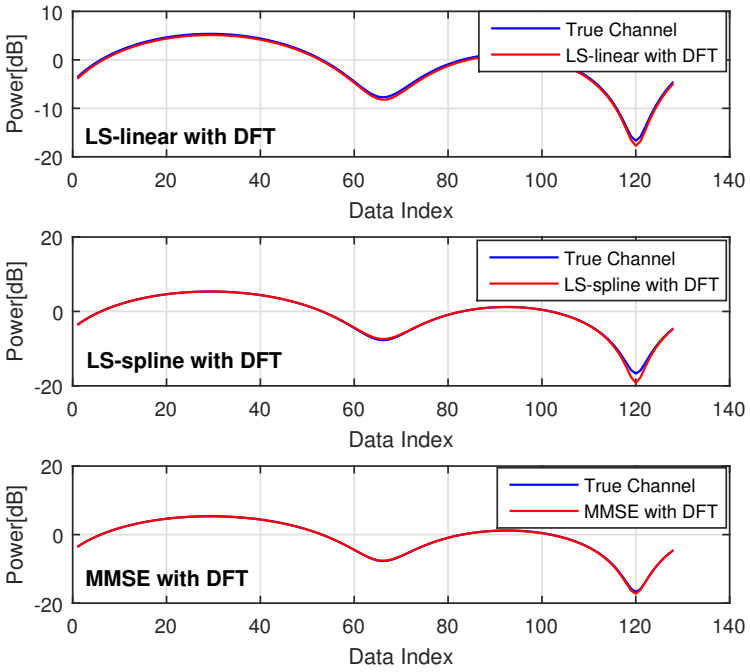

Figure 6.10: DFT based Channel Estimation

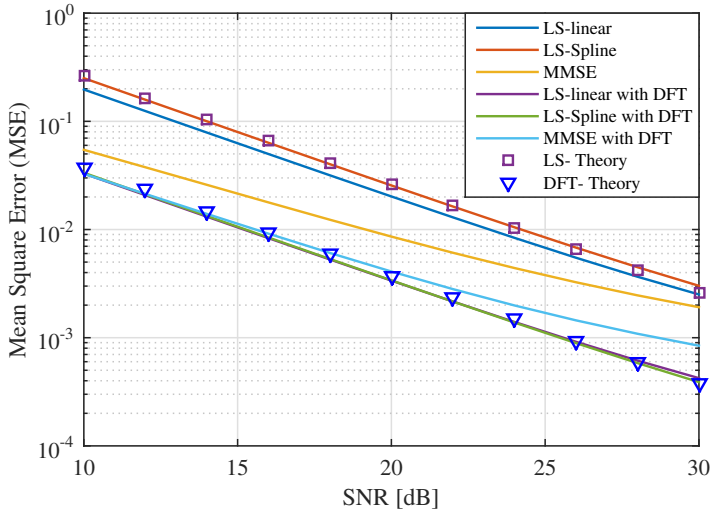

Figure 6.11: Performance evaluation of MGFDM with different channel estimation techniques

theoretical plots for the expressions provided in the above sections under LS and DFT based channel estimation methods are also given. It should be noted that both simulated and theoretical values are in good agreement and matches almost at every SNR. MMSE results in a better performance when compared to the LS approach, without DFT estimation. To enhance the performance, DFT based CE is proposed in this article and from

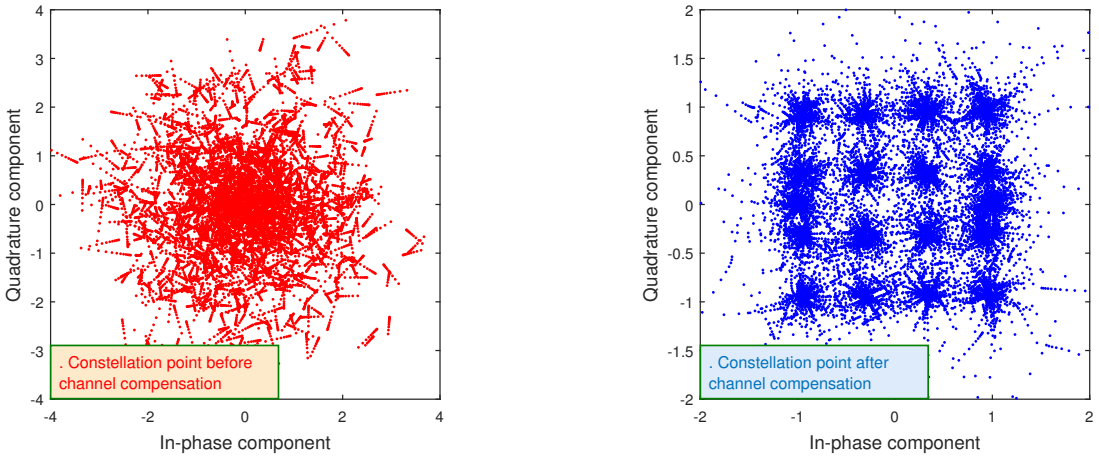

Figure 6.12: Received signal constellation before and after channel compensation using 16-QAM modulation scheme.

the figure we can infer that there is a reduction in MSE significantly. The results suggests the benefit of using DFT based CE methods but this comes at a cost of additional computational complexity.

The received signal constellation of a GFDM system with 16-QAM before and after channel compensation is shown in Figure 6.12. We can infer from the figure that the data symbols are properly mapped after channel compensation using MMSE channel estimation with DFT technique. From these results it is obvious that DFT based channel estimation methods reduces the MSE at a faster rate.

To complete the analysis, let us consider the well established channel models such as EPA [182], European Co-operation in the field of Scientific and Technical research (COST) [158], ITU [183] and SUI [184]. For ITU path loss model, we have considered a low delay spread (channel A) for both indoor office and vehicular test environment [183]. SUI channel model is a set of 6 channel models (SUI-1,2 (Terrain type C), SUI-3,4 (Terrain type B), SUI-5,6 (Terrain type A)), for representing three types of terrain. In this thesis, we have considered, three types namely SUI-1 Terrain Type C, SUI-2 Terrain Type B and SUI-3 Terrain Type A. The power delay profiles values for these channels are listed in Table 6.3, Table 6.4, Table 6.5 and Table 6.6. The corresponding results for each of these channel is plotted in Figure 6.13, Figure 6.14 and Figure 6.15. One can easily observe that depending on the power delay profile of the channel the corresponding effect on the MSE varies.

Table 6.3: Path Loss for 3GPP Pedestrain A Model

Tap Index	For EPA Model	
	Delay (ns)	Power [dB]
1	0	0
2	30	-1
3	70	-2
4	90	-3
5	110	-8
6	190	-17.2
7	410	-20.8

Table 6.4: Power delay profile for COST 207 Model

Tap Index	Typical Urban	
	Delay (μs)	Average Power
1	0	0.189
2	0.2	0.379
3	0.5	0.239
4	1.6	0.095
5	2.3	0.061
6	5.0	0.037

Table 6.5: Channel Models for ITU Channel-A

Tap Index	For Indoor Office		For Vehicular Test Environment	
	Delay (ns)	Power [dB]	Delay (ns)	Power [dB]
1	0	0	0	0
2	50	-3	310	-1
3	110	-10	710	-9
4	170	-18	1090	-10
5	290	-26	1730	-15
6	310	-32	2510	-20

Table 6.6: Channel Models for SUI

Tap Index	SUI-1, Type C		SUI-3, Type B		SUI-6, Type A	
	Delay (μs)	Power [dB]	Delay (μs)	Power [dB]	Delay (μs)	Power [dB]
1	0	0	0	0	0	0
2	0.4	-15	0.4	-5	14	-10
3	0.9	-20	0.9	-10	20	-14

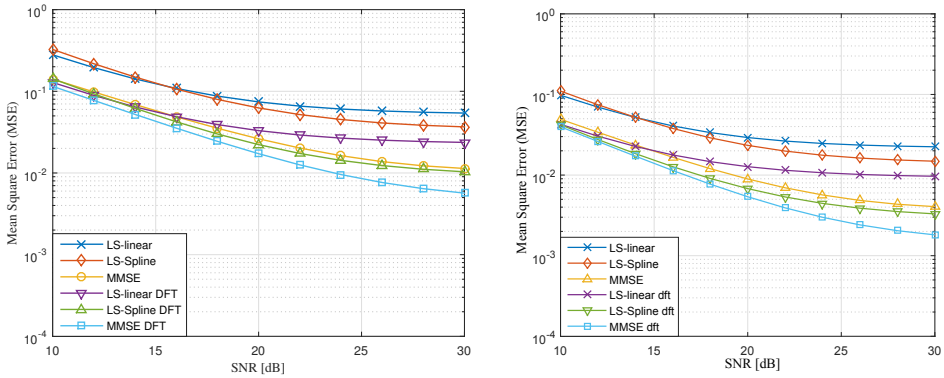

(a) EPA channel model (b) COST 207 Typical Urban model

Figure 6.13: MSE Vs SNR for various channel models.

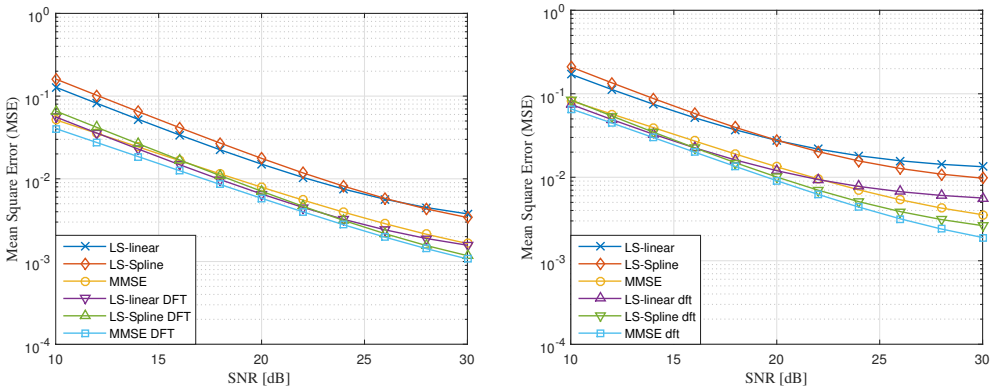

(a) For Indoor Office (b) For Vehicular Test Environment

Figure 6.14: MSE Vs SNR for ITU channel models under different environments.

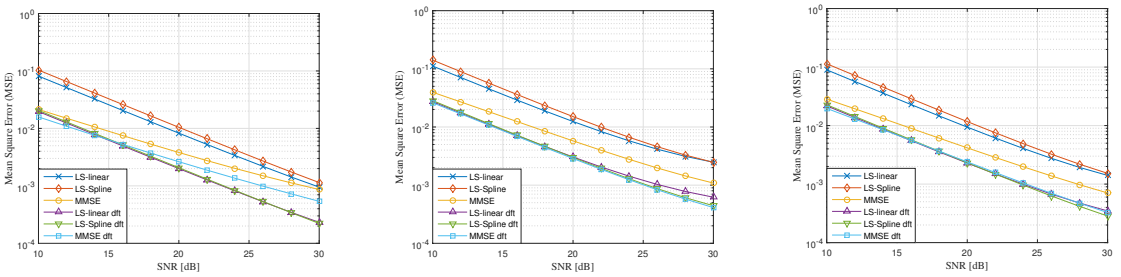

(a) SUI-1, Terrain Type C (b) SUI-3, Terrain Type B (c) SUI-6, Terrain Type A

Figure 6.15: MSE Vs SNR for SUI channel models.

Table 6.7: Parameters used for CMGFDM

Description	Parameter	Value
Number of Subcarriers	N	32
Number of time slots	M	2
Pulse shape filter	g	DPSS, RRC
Roll-off factor	α	$\{0.1, 0.9\}$
Length of CP	N_{cp}	16
Number of pilots	N_p	4
Modulation order	μ	4

6.4.2 Findings from coded GFDM systems

The simulation results in terms of BER and PAPR, which compare the coded MGFDM system to that of the conventional GFDM and MGFDM systems are reported in this section. The simulation parameters that are used for investigation are displayed in Table 6.7 with pilot locations at $1, 14, 27, 40$. The channel is assumed to be AWGN. At the receiver, we have used ZF and MF receiver structures in the (M)GFDM demodulator to retrieve the data.

Figure 6.16 compares the proposed coded MGFDM system with an uncoded MGFDM system using the ZF receiver. As an example, for comparison purposes, we have utilized an RRC pulse shaping filter, with a roll-off factor $\alpha = 0.5$ for uncoded GFDM. From the results, we can observe the benefit of using a convolution code to an MGFDM system as the BER performance is much improved compared to the corresponding uncoded

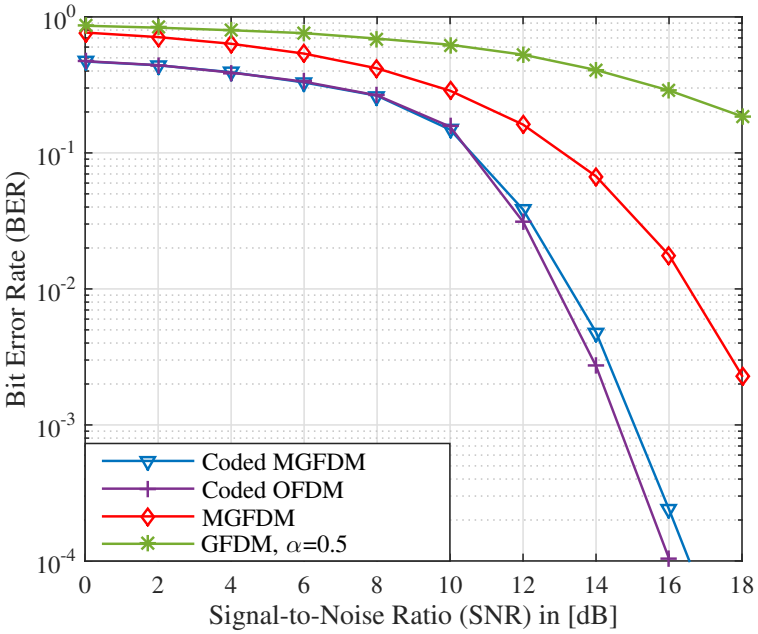

Figure 6.16: BER comparison under AWGN channel with N=32, M=2, $\mu = 4$ using ZF receiver

MGFDM and conventional GFDM systems. For instance, at an SNR of $14dB$, the BER for CMGFDM, MGFDM and conventional GFDM is given by 0.006, 0.06 and 0.6 respectively. This improvement in system performance comes at a cost of adding redundant bits to the original MGFDM system and hence there is a trade off involved. Lastly, for comparison purposes, we have plotted the corresponding performance curves for an OFDM structure with 64 subcarriers using convolution code as a reference. As can be observed from the figure, coded OFDM and CMGFDM have similar performance but it is to be noted that CMGFDM adds one cyclic prefix for a whole block consisting of M subsymbols, whereas in coded OFDM the cyclic extension is added to every symbol. Lower OOB radiation in CMGFDM using DPSSs is also observed, increasing the spectral efficiency compared to the high OOB emission in OFDM.

For evaluating PAPR performance, we have considered 10^5 symbols and the PAPR CCDF is shown in Figure 6.17. In this figure we compare the PAPR of the proposed CMGFDM system to that of an MGFDM and a conventional GFDM system with $\alpha = 0.5, 0.9$. Interestingly, the CMGFDM PAPR is increased when compared to the MGFDM system, which may be due to the effect of adding the redundant bits for encoding the data. The PAPR of an MGFDM system is decreased in comparison to a conventional

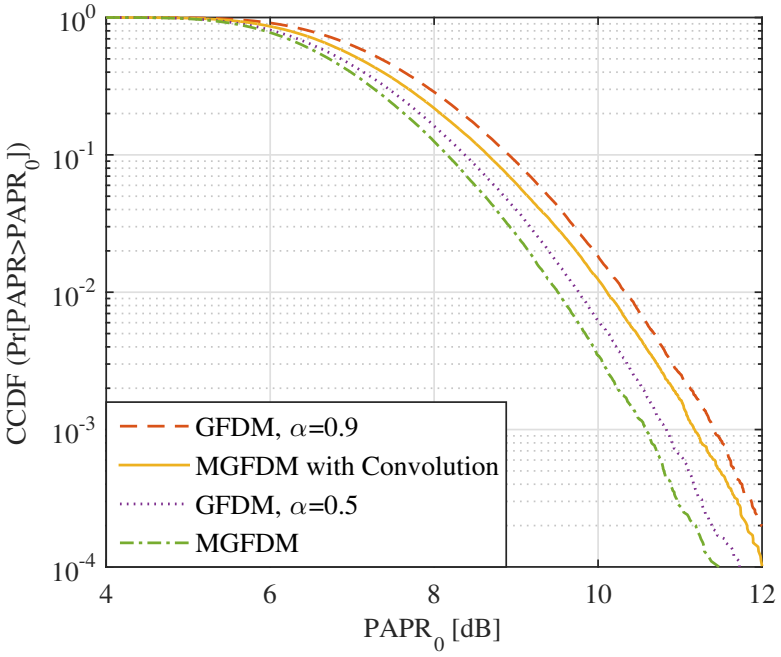

Figure 6.17: Comparison plot of PAPR analysis

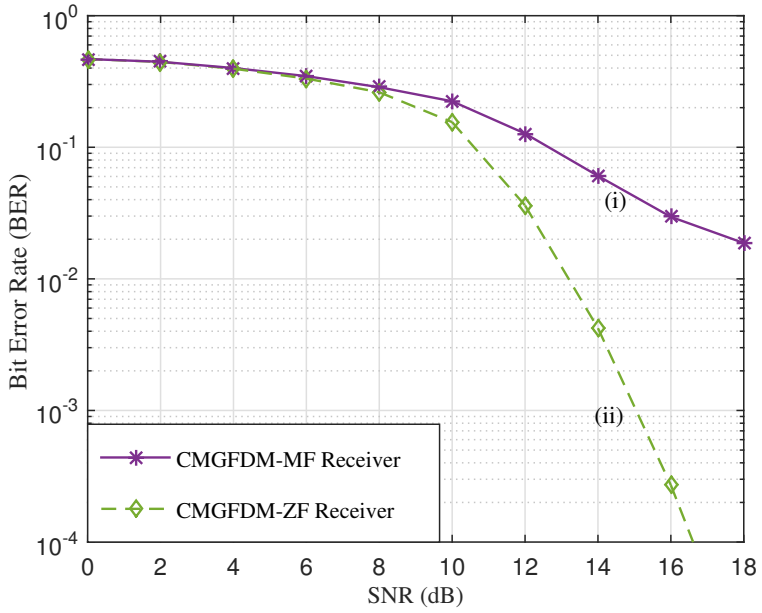

Figure 6.18: BER performance of CMGFDM with ZF and MF Receivers for N=32, M=2, 16-QAM

GFDM system for any roll-off factors which is due to using orthogonal filters with DPSSs in the MGFDM system. Also note that, as we increase the roll-off factor from 0.5 to 0.9 the PAPR of conventional GFDM is considerably increased. For example, a CCDF

of 10^{-3} is achieved at a PAPR of 10.58, 10.84, 11.17 and 11.4 respectively for MGFDM, GFDM ($\alpha = 0.5$), CMGFDM and GFDM with $\alpha = 0.9$.

The BER performance of CMGFDM with ZF and MF receivers is depicted in Figure 6.18 under AWGN channel. At low SNRs both ZF and MF receivers are achieving the same error rates while at the higher ones, the error rate observed for MF is considerably increased as compared to the ZF receiver. A huge difference between the BER curves can be observed. For example at an SNR of $14dB$ an error rate of 0.006 and 0.05 is achieved and is shown in Figure 6.18.

6.5 Chapter Summary

These chapter presents channel estimation techniques, namely LS (with linear and spline interpolation) and MMSE with and without the DFT method. The channel estimation at the pilot tones and the interpolation of the channel at remaining points are presented. From the simulation results, among the investigated methods when compared to the LS estimator, the performance of the MMSE estimator, is observed to provide a better estimate of the channel response in both cases of with and without DFT. There is an additional computational cost that has to be paid in using DFT based channel estimation. Moreover as we increase the number of data sample points,the complexity of MMSE increases exponentially. Also, the overall efficiency of the system may be reduced due to the addition of the overhead pilot symbols to that of data symbols. Therefore a trade-off exits between the better channel estimation system performance and additional complexity of the overall system.

At last, a novel convolution coded MGFDM system is proposed. Simulation results suggest that the proposed CMGFDM BER performance is almost similar to that of the coded OFDM scheme in an AWGN channel. Both exhibit an increased robustness to noise interference compared to uncoded MGFDM and GFDM systems, thereby demonstrating the advantage of the proposed system. The receiver structure is also seen to play a key role. CMGFDM was tested with both the ZF and MF receivers. At low SNRs the error behavior was similar while at higher SNRs the difference was dramatic, with ZF strongly outperforming MF. Besides BER performance comparison, a comparative analysis of

PAPR of the proposed system to that of MGFDM and conventional GFDM was also investigated. In this case uncoded MGFDM displayed better performance that the coded version, probably due to the effect of adding redundant bits for data encoding. This indicates that PAPR performance still remains an issue even with convolutional coding and requires further investigation. Although the performance of CMGFDM is comparable to Coded OFDM, the advantage of lower OOB radiation in CMGFDM is to be noted. Hence for future 5G systems coded MGFDM can be used effectively in applications such as machine to machine communication.

Chapter 7

Conclusions and Future Scope

7.1 Conclusions

This thesis thoroughly investigated, GFDM, one of the leading physical layer scheme designed for 5G systems, using various performance metrics. After brief introduction to the broad area of research theme, the current state of art discussing the recent advancements in the multicarrier arena are presented. Immediately discussions on block diagram of GFDM transceiver structure, its principle, led the foundation to the topic of interest. The first claim is about deriving analytical expressions of GFDM and its variant (GFDM/OQAM), considering different fading environments namely Rayleigh, Nakagami-m, Nakagami-q, Rician-K and Weibull-v channels. The SER performance imposing strong fading conditions by varying the fading parameters of above channels are well examined. The effect of the RRC pulse shaping roll-off factor (α) and the trade off to the OOB radiation is discussed and therefore the designer has to choose an appropriate pulse shaping parameter, α.

Next approach of the thesis deals in proposing prolate spheroidal windows for pulse shaping, as multi-tapers has better OOB emission compared to the RRC filters which are generally used for pulse shaping. In addition, the effect of NEF which was induced from the roll-off factor α, is no longer relevant with the use of the orthogonal tapers and reduced to 1 for MGFDM system. A comparative analysis between OFDM, conventional GFDM and MGFDM under similar conditions are provided and results conclude that the benefit of employing tapers as prototype filter. This thesis also taken the interest

of applying walsh hadamard transform as a precoding technique to the standard PAPR reduction methods and shown the capability of diminishing the PAPR. Furthermore, the exchange of fourier transforms with wavelets follows the trend of improving the PAPR along with the spectral efficacy.

Besides, it appeared that Alamouti space time diversity is still an essential scheme for a reliable communication establishment. The theoretical expressions for the precoded OSTBC method for MGFDM and its comparison to STBC for different multicarrier techniques are presented and concludes the dominance of the precoded OSTBC over the others. Results suggests that an additional $2dB$ required for STBC-MGFDM compared to the precoded OSTBC-MGFDM. Further investigation continued to show the role of precoded OSTBC of MGFDM compared to precoded OSTBC of GFDM systems. Results demonstrates that an SER of 10^{-3} is achieved at an SNR of approximately $12dB$ for the precoded OSTBC-MGFDM system and $17dB$ in the case of the precoded OSTBC-GFDM system.

Afterwards the application of OQAM to a conventional GFDM system exploiting the near orthogonality concept of OQAM provides a GFDM system with more robustness in a fading environment were investigated. Analytical expressions of GFDM/OQAM performance under different fading channels are derived. The evaluation results show that there is a good match between the simulated results and the derived expressions. Numerical results, in terms of SER, show a performance improvement compared to conventional GFDM. In summary, the investigations provide us with an important understanding of the behaviour of OQAM, as applied to non-orthogonal conventional GFDM systems.

Last part this work covers the training based channel estimation techniques for MGFDM system with and without DFT. The performance evaluation is carried out using LS (linear & cubic spline) and MMSE channel estimation methods. A comparison of the obtained channel estimates to that of the true channel is exhibited. A DFT based CE method employing LS and MMSE is also studied. In addition, MSE of the proposed three techniques with and without the use of DFT based channel estimation is postured. MMSE results in a better performance when compared to LS approach in both scenarios i.e, with and without DFT estimation. In conclusion DFT based CE methods provide better estimates of the channel but with an additional computational cost. Finally, a

comparative analysis of coded MGFDM, coded OFDM and uncoded GFDM system is established using BER and PAPR as performance metrics. Coded MGFDM system using ZF outperforms uncoded MGFDM interms of SER at the cost of adding redundant bits. A good comparison among coded MGFDM, coded OFDM, uncoded MGFDM and GFDM is provided. Results suggest that coded MGFDM and coded OFDM have similar performance.

The overall conclusion of the thesis is, the pleasing advantages of GFDM and the modifications mentioned makes it a potential 5G candidate waveform for future wireless applications.

7.2 Future Scope

In this thesis several aspects, facts and issues related to the novel multicarrier technique GFDM are well investigated. The suggestions/opportunities for continuing research studies are mentioned below:

- The analysis carried out in this thesis assumed perfect channel estimation and synchronization in some cases which may not be possible in practice. So, the hardware implementation of GFDM over real time environment including the channel estimation, offset errors and synchronization methods is a point of interest.

- The short burst transmission which is possible with GFDM is a good sign for IoT applications but the complex receiver structure of GFDM is an concerning issue and it would be interesting to design a simpler receiver.

- An investigation on performance of GFDM in various fading channels are provided in this thesis with the support of analytical expressions. Proving the effect of the log-normal shadowing mathematically with suitable parameter analysis could be a reasonable issue to be addressed. Meanwhile, handling interference and proposing methods for interference cancellation is another topic of interest worthy exploring.

- Another valuable research area that could be interesting is to propose different methodologies for allocating resources smartly to huge number of users within a

GFDM block so as to minimize multiuser interferences of a network.

- Choosing variable block size structure optimally suitable for adverse channel conditions and exploring optimization methods for power allocations can be developed.
- The performance of GFDM can be improved by employing various diversity concepts and because of its ease in MIMO implementation compared to other 5G physical layer candidates.
- Finally a deeper analysis of different precoding MIMO techniques with different coding structures (Turbo, Low-Density Parity-Check (LDPC) and Polar codes) will fall into the interesting axis.

With this future scope and the progress of GFDM in this direction would actually reveal whether GFDM is a better 5G candidate to serve the next generation needs with 'Worldwide Wireless Web (WWWW)' or else *"Work Wherever With Web"*.

Publications

List of International Journals:

1. Shravan Kumar Bandari, V. V. Mani, and A. Drosopoulos, "Performance analysis of GFDM in various fading channels." COMPEL: The International Journal for Computation and Mathematics in Electrical and Electronic Engineering, Volume 35, Issue 1, pages 225-244, 2016.
   https://doi.org/10.1108/COMPEL-06-2015-0215. (**SCI**)

2. Shravan Kumar Bandari, V. V. Mani, and A. Drosopoulos, " PAPR analysis of wavelet based multitaper GFDM system", AEU - International Journal of Electronics and Communications, Volume 76, Pages 166-174, ISSN 1434-8411, June, 2017.
   https://doi.org/10.1016/j.aeue.2017.04.009. (**SCI**)

3. Shravan Kumar Bandari, V. V. Mani, and A. Drosopoulos," Training Based Channel Estimation for Multi-Taper GFDM System", Mobile Information Systems, Hindawi Publications, Article ID 4747256, October, 2017.
   https://www.hindawi.com/journals/misy/2017/4747256/ **(SCI)**

4. Shravan Kumar Bandari, V. V. Mani, and A. Drosopoulos, " GFDM/OQAM performance analysis under Nakagami fading channels", Physical Communication, Elsevier, Volume 26, Pages 162-169, ISSN 1874-4907, February 2018.
   https://doi.org/10.1016/j.phycom.2017.12.008. **(SCI)**

5. Shravan Kumar Bandari, V. V. Mani, and A. Drosopoulos, " Novel hybrid PAPR reduction schemes for the MGFDM system", Physical Communications (Special Issue on physical layer communications in 5G-II), Elsevier, Volume 31, Pages 69-78, ISSN 1874-4907, October 2018.
   https://doi.org/10.1016/j.phycom.2018.09.009. **(SCI)**

6. Shravan Kumar Bandari, V. V. Mani, and A. Drosopoulos, " Robust Precoded OSTBC for GFDM Systems." Elsevier,Procedia Computer Science 93, pages 176-182, 2016. http://www.sciencedirect.com/science/article/pii/S1877050916314387. **(Scopus)**

List of International Conferences:

---

1. Shravan Kumar Bandari, V. V. Mani, and A. Drosopoulos, "Exact SER Expressions of GFDM in Nakagami-m and Rician fading channels," Proceedings of 21th European Wireless Conference, pp. 1-6, Budapest, Hungary, 2015.
   http://ieeexplore.ieee.org/document/7147708/

2. Shravan Kumar Bandari, V. V. Mani, and A. Drosopoulos, "Multi-taper implementation of GFDM," IEEE Wireless Communications and Networking Conference (WCNC), pp. 1-5, Doha, Qatar, 2016.
   http://ieeexplore.ieee.org/document/7564952/

3. Shravan Kumar Bandari, V. V. Mani, and A. Drosopoulos, "OQAM implementation of GFDM," 23rd International Conference on Telecommunications (ICT), pp. 1-5, Thessaloniki, Greece, 2016.
   http://ieeexplore.ieee.org/document/7500463/

4. Shravan Kumar Bandari, V. V. Mani, and A. Drosopoulos, "GFDM/OQAM implementation under Rician fading channel," 2016 International Conference on Advances in Computing, Communications and Informatics (ICACCI), pp. 256-260, Jaipur, India, 2016.
   http://ieeexplore.ieee.org/document/7732056/

5. Shravan Kumar Bandari, V. V. Mani, and A. Drosopoulos, "Convolutional codes for MGFDM system,"IEEE International Conference on Information and Communication Technology Convergence (ICTC), pp. 545-550, Jeju Island, South Korea, October 2017.
   http://ieeexplore.ieee.org/document/8191037/

Appendix A

Alternate Proof

In this appendix, we will provide another method for solving integral (5.37). We first need to solve the following expression using the Mellin transform. This will also be useful in more general cases.

$$I = \int_0^\infty x^{p-1} e^{-zx^2 - \alpha x^r} dx \tag{A.1}$$

The Mellin transform of a function $f(x)$ is defined as, $\varphi(s) = \int_0^\infty x^{s-1} f(x) dx$ and its corresponding inverse Mellin transform is given by $f(x) = \frac{1}{2\pi i} \int_{c-i\infty}^{c+i\infty} x^{-s} \varphi(s) dx$

The Mellin transform of the function $e^{-\alpha x^r}$ is given by [[135],3.326],

$$\varphi(s) = \int_0^\infty x^{s-1} e^{-\alpha x^r} dx = \frac{1}{r} \alpha^{-\frac{s}{r}} \Gamma(\frac{s}{r}) \tag{A.2}$$

The inverse Mellin transform of the above function can be expressed as,

$$e^{-\alpha x^r} = \frac{1}{2\pi i} \int_{c-i\infty}^{c+i\infty} x^{-s} \varphi(s) ds = \frac{1}{2\pi i} \int_{c-i\infty}^{c+i\infty} x^{-rs} \alpha^{-s} \Gamma(s) ds \tag{A.3}$$

Substituting the above equation in (A.1) followed by some mathematical steps, the following expression can be obtained,

$$\begin{aligned} I &= \frac{1}{2\pi i} \int_{c-i\infty}^{c+i\infty} \alpha^{-s} \Gamma(s) \left[\int_0^\infty x^{p-rs-1} e^{-zx^2} dx \right] ds \\ &= \frac{1}{2\pi i} \int_{c-i\infty}^{c+i\infty} \alpha^{-s} \Gamma(s) \Gamma\left(\frac{p}{2} - \frac{r}{2}.s\right) \frac{z^{rs-p}}{2} ds \end{aligned} \tag{A.4}$$

By using [[135],8.335], we can write

$$\Gamma\left(\frac{p}{2}-\frac{r}{2}.s\right)=(2\pi)^{\frac{1-\frac{r}{2}}{2}}\left(\frac{r}{2}\right)^{\frac{p-rs}{2}-\frac{1}{2}}\prod_{k=1}^{r/2}\Gamma\left[\frac{\frac{p}{2}+k-1}{r/2}-s\right]$$

Substituting this equation in (A.4) and using [[135],9.301] the following final expression can be obtained for (A.1)

$$I=\frac{(2\pi)^{\frac{1-\frac{r}{2}}{2}}\left(\frac{r}{2}\right)^{\frac{p-1}{2}}}{2}z^{-p}G_{1,r/2}^{r/2,1}\left[\frac{z^r}{\alpha(r/2)^{r/2}}\;\middle|\;\begin{matrix}1\\ \frac{p/2}{r/2},\frac{(p/2)+1}{r/2},...,\frac{(p/2)+(r/2-1)}{r/2}\end{matrix}\right] \tag{A.5}$$

where G(.) is the Meijer's G function [135] and $\Delta(l_1,l_2)=\frac{l_2}{l_1},\frac{l_2+1}{l_1},...,\frac{l_2+l_1-1}{l_1}$. Now, coming back to integral (5.37), substitute $\sqrt{\gamma}=y$. This will yield the following expression,

$$I_3(\bar{\gamma}_n)=\frac{2}{\Gamma(m)}\int_0^\infty y^{2m-1}\exp\left(-\frac{my^2}{\bar{\gamma}_n}\right)\mathrm{erfc}(y)dy \tag{A.6}$$

Let $u_1=\mathrm{erfc}(y)$ and $dv_1=y^{2m-1}e^{\frac{-my^2}{\bar{\gamma}_n}}dy$ and using the by parts procedure $\int_a^b u_1dv_1=[u_1v_1]_a^b-\int_a^b v_1du_1$, the following equations can be obtained,

$$I_3(\bar{\gamma}_n)=\left(\frac{\bar{\gamma}_n}{m}\right)^m-\frac{2}{\sqrt{\pi}}\sum_{j=0}^{m-1}\frac{\bar{\gamma}_n^{m-j}}{j!m^{m-j}}\int_0^\infty y^{2j}e^{-y^2-\frac{m}{\bar{\gamma}_n}y^2}dy \tag{A.7}$$

Lastly, using the integral solution of (A.1) in the above equation, the final expression for $I_3(\bar{\gamma}_n)$ can be found as,

$$I_3(\bar{\gamma}_n)=\left(\frac{\bar{\gamma}_n}{m}\right)^m-\frac{1}{\sqrt{\pi}}\sum_{j=0}^{m-1}\frac{\bar{\gamma}_n^{m-j}}{j!m^{m-j}}G_{1,1}^{1,1}\left[\frac{\bar{\gamma}_n}{m}\;\middle|\;\begin{matrix}1\\ \frac{2j+1}{2}\end{matrix}\right] \tag{A.8}$$

For Rayleigh fading channel, $m=1$ the above equation matches with the one derived in equation (5.37).

Appendix B

Noise Enhancement Factor (NEF) Derivation

This appendix deals with the derivation of NEF [43]. In order to do so, first let us consider the received signal which is having the following representation,

$$\mathbf{Z} = \mathbf{Hx} + \mathbf{w} \tag{B.1}$$

where the assumptions on $\mathbf{H}$ and $\mathbf{w}$ of B.1 are as mentioned in Chapter 3. The estimated data symbols under ZF can be given as,

$$\begin{aligned} \hat{\mathbf{d}} &= \mathbf{B_{ZF}Z} = \mathbf{B_{ZF}}\left[\mathbf{Hx} + \mathbf{w}\right] \\ &= \mathbf{B_{ZF}Hx} + \mathbf{B_{ZF}w} \end{aligned} \tag{B.2}$$

In order to obtain the NEF, we have to calculate the variance of the estimated data vector $\hat{\mathbf{d}}$. Accordingly, upon applying the expectation operator $\mathbb{E}$,

$$\begin{aligned} \mathbb{E}\left\{\hat{\mathbf{d}}\hat{\mathbf{d}}^H\right\} =& \mathbb{E}\left\{\left[\mathbf{B_{ZF}Hx} + \mathbf{B_{ZF}w}\right]\left[\mathbf{B_{ZF}Hx} + \mathbf{B_{ZF}w}\right]^H\right\} \\ =& \mathbb{E}\left\{\left[\mathbf{B_{ZF}Hx} + \mathbf{B_{ZF}w}\right]\left[\mathbf{x}^H\mathbf{H}^H{\mathbf{B_{ZF}}}^H + \mathbf{w}^H{\mathbf{B_{ZF}}}^H\right]\right\} \end{aligned} \tag{B.3}$$

$$\begin{aligned} \mathbb{E}\left\{\hat{\mathbf{d}}\hat{\mathbf{d}}^H\right\} =& \mathbb{E}\left\{\mathbf{B_{ZF}Hxx}^H\mathbf{H}^H{\mathbf{B_{ZF}}}^H\right\} + \mathbb{E}\left\{\mathbf{B_{ZF}Hxw}^H{\mathbf{B_{ZF}}}^H\right\} \\ &+ \mathbb{E}\left\{\mathbf{B_{ZF}wx}^H\mathbf{H}^H{\mathbf{B_{ZF}}}^H\right\} + \mathbb{E}\left\{\mathbf{B_{ZF}ww}^H{\mathbf{B_{ZF}}}^H\right\} \end{aligned} \tag{B.4}$$

$$\mathbb{E}\left\{\hat{\mathbf{d}}\hat{\mathbf{d}}^H\right\} = \mathbb{E}\left\{\mathbf{B_{ZF}Hxx}^H\mathbf{H}^H{\mathbf{B_{ZF}}}^H\right\} + \mathbb{E}\left\{\mathbf{B_{ZF}ww}^H{\mathbf{B_{ZF}}}^H\right\} \tag{B.5}$$

From equation (B.5), the first term constitutes the signal power and the second term is the post processed noise power.

$$\begin{aligned} \mathbb{E}\left\{\mathbf{B_{ZF}ww}^H{\mathbf{B_{ZF}}}^H\right\} =& \mathbf{B_{ZF}}{\mathbf{B_{ZF}}}^H\mathbb{E}\left\{\mathbf{ww}^H\right\} \\ =& \mathbf{B_{ZF}}{\mathbf{B_{ZF}}}^H\sigma_w^2 = \xi\sigma_w^2 \end{aligned} \tag{B.6}$$

where σ_w^2 is the gaussian noise power and ξ is the additional multiplier that enhances σ_w^2, which is termed as Noise Enhancement Factor under ZF receiver. Considering for the i^{th} subcarrier, ξ can be expressed as,

$$\xi = \sum_{n=0}^{NM-1} \left| [\mathbf{B_{ZF}}]_{i,n} \right|^2 \tag{B.7}$$

The value of ξ is equal for every subcarrier.

B.0.1 Under MGFDM

Since we are using different multi-tapers on each subcarrier which are orthogonal, the ξ value that is equal for all subcarriers in GFDM doesn't hold good in this situation. Hence among the different ξ's that we obtained, the best performance can be attained for the value of ξ which maximizes the SNR and can be given as,

$$\xi = min \left\{ \sum_{n=0}^{NM-1} \left| [\mathbf{B_{ZF}}]_{i,n} \right|^2 \right\} \tag{B.8}$$

Appendix C

Meijer's G Function

Meijer G function was introduced by Cornelis Simon Meijer as a general function including most of the functions like exponential, hypergeometric, complementary error functions etc., as special cases. By definition Meijer'G function is given by,

$$G_{p,q}^{m,n}\left[x\left|\begin{matrix}a_1,\cdots,a_p\\ b_1,\cdots,b_q\end{matrix}\right.\right]=\frac{1}{2\pi i}\int\frac{\prod_{j=1}^{m}\Gamma\left(b_j-s\right)\prod_{j=1}^{n}\Gamma\left(1-a_j+s\right)}{\prod_{j=m+1}^{q}\Gamma\left(1-b_j+s\right)\prod_{j=n+1}^{p}\Gamma\left(a_j-s\right)}x^s ds \tag{C.1}$$

where $[0\leq m\leq q, 0\leq n\leq p]$. More details about the properties of Meijer's G function and applications of such functions can be found in [185,186]. Some of the useful relations which are required to solve the integrals shown in Chapter 3 can be given as [136],

$$e^{-g(x)}=G_{01}^{10}\left(g(x)\left|\begin{matrix}-\\ 0\end{matrix}\right.\right) \tag{C.2}$$

$$\operatorname{erfc}(x)=1-\frac{1}{\sqrt{\pi}}G_{1,2}^{1,1}\left(x^2\left|\begin{matrix}1\\ 1/2,0\end{matrix}\right.\right)=\frac{1}{\sqrt{\pi}}G_{1,2}^{2,0}\left(x^2\left|\begin{matrix}1\\ 0,1/2\end{matrix}\right.\right) \tag{C.3}$$

Appendix D

SER Expressions

D.1 SER Performance of P-QAM in AWGN channel

Let the received QAM symbol be given as [1],

$$y = k\sqrt{E_s}s + n \tag{D.1}$$

where y is the received symbol, E_s is the symbol energy, $k = \sqrt{\frac{3}{2(P-1)}}$ is the normalization factor, s is transmitted symbol,P is the constellation order and n is the receiver noise which is considered to be complex Gaussian with mean zero and variance $\frac{N_0}{2}$. The total symbol error probability is defined as,

$$p_e^{PQAM} = \frac{N_{inside}\overbrace{p\left(e/inside\right)}^{case(i)} + N_{corner}\overbrace{p\left(e/corner\right)}^{case(ii)} + N_{ninc}\overbrace{p\left(e/ninc\right)}^{case(iii)}}{P} \tag{D.2}$$

where N_{inside} represents the number of signal points inside the constellation diagram, N_{corner} represents the number of signal points in the corners of the constellation diagram and N_{ninc} represents the number of signal points neither at the inside nor at the corner (ninc). $p\left(e/inside\right)$, $p\left(e/corner\right)$, $p\left(e/ninc\right)$ are the error probability of QAM symbol inside, corner and neither inside nor corner of the P-QAM constellation diagram (Figure D.1).

***case(i)*:** First let us consider the symbol $\{+k\sqrt{E_s}, +k\sqrt{E_s}\}$ (red colour) inside the constellation diagram. The corresponding conditional PDF of y is given as,

$$f\left(y/inside\right) = \frac{1}{\sqrt{\pi N_0}} \exp\left(-\frac{\left(y - k\sqrt{E_s}\right)^2}{N_0}\right) \tag{D.3}$$

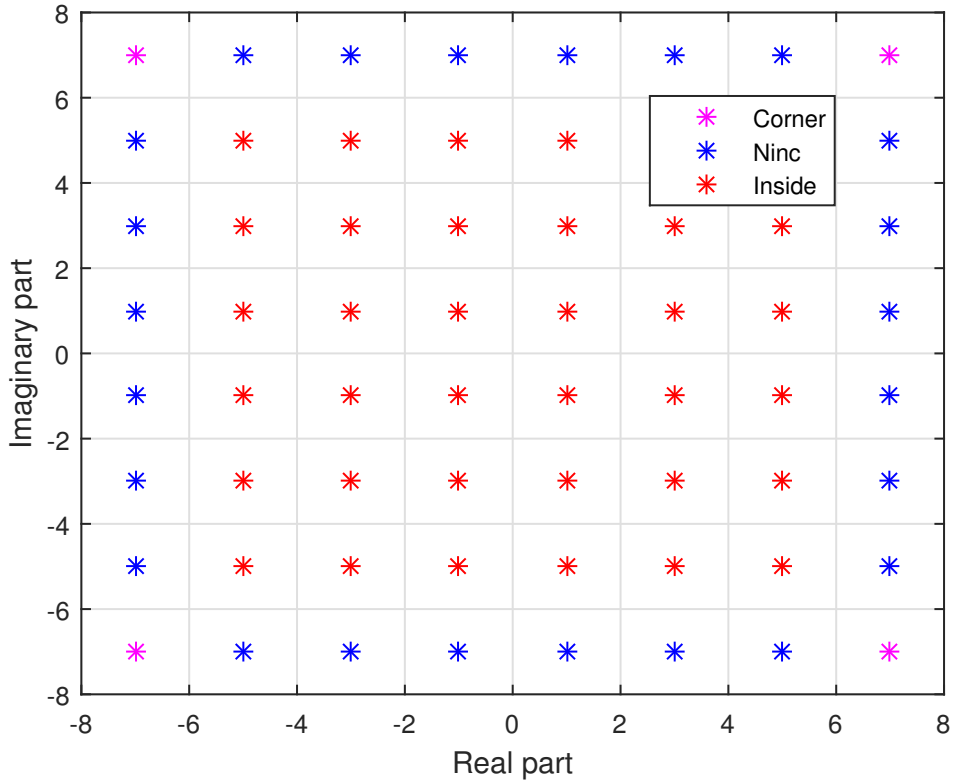

Figure D.1: 64-QAM constellation.

The probability of correct demodulation of signal point ($I = +1, Q = +1$ for 64-QAM) inside the P-QAM constellation is defined as,

$$p\left(y/inside\right) = p\left(\Re\{y\} > 0, \Re y \leq 2k\sqrt{E_s}/ + 1\right) p\left(\Im\{y\} > 0, \Im\{y\} \leq 2k\sqrt{E_s}/ + 1\right) \tag{D.4}$$

The probability of correct demodulation of real component is,

$$p\left(\Re\{y\} > 0, \Re\{y\} \leq 2k\sqrt{E_s}/ + 1\right) =$$
$$1 - \left[\frac{1}{\sqrt{\pi N_0}} \int_{-\infty}^{0} \exp\left(-\frac{\left(y - k\sqrt{E_s}\right)^2}{N_0}\right) dy + \frac{1}{\sqrt{\pi N_0}} \int_{2k\sqrt{E_s}}^{\infty} \exp\left(-\frac{\left(y - k\sqrt{E_s}\right)^2}{N_0}\right) dy\right] \tag{D.5}$$

making the change of integration variable, namely $\frac{y-k\sqrt{E_s}}{N_0} = t$

$$\begin{aligned} p\left(\Re\{y\} > 0, \Re\{y\} \leq 2k\sqrt{E_s}/ + 1\right) =& 1 - \frac{1}{\sqrt{\pi N_0}} \left[\int_{-\infty}^{\frac{-k\sqrt{E_s}}{\sqrt{N_0}}} \exp\left(-t^2\right) \sqrt{N_0} dt \right. \\ & \left. + \int_{\frac{k\sqrt{E_s}}{\sqrt{N_0}}}^{\infty} \exp\left(-t^2\right) \sqrt{N_0} dt \right] \\ =& 1 - \frac{2}{\sqrt{\pi}} \int_{\frac{k\sqrt{E_s}}{\sqrt{N_0}}}^{\infty} \exp\left(-t^2\right) dt \\ =& 1 - \text{erfc}\left(k\sqrt{\frac{E_s}{N_0}}\right) \end{aligned} \tag{D.6}$$

Similarly, probability of correct demodulation of imaginary component is

$$p\left(\Im\{y\} > 0, \Im\{y\} \leq 2k\sqrt{E_s}/ + 1\right) = 1 - \text{erfc}\left(k\sqrt{\frac{E_s}{N_0}}\right) \tag{D.7}$$

letting (D.6) and (D.7) into (D.4) yields

$$p\left(y/inside\right) = \left[1 - erfc\left(k\sqrt{\frac{E_s}{N_0}}\right)\right]^2 \tag{D.8}$$

The probability of the symbol decoded being in error is,

$$\begin{aligned} p\left(e/inside\right) =& 1 - p\left(y/inside\right) \\ =& 1 - \left[1 - \text{erfc}\left(k\sqrt{\frac{E_s}{N_0}}\right)\right]^2 \\ =& 2\text{erfc}\left(k\sqrt{\frac{E_s}{N_0}}\right) - \text{erfc}^2\left(k\sqrt{\frac{E_s}{N_0}}\right) \end{aligned} \tag{D.9}$$

***case(ii)*:** The probability of correct demodulation of symbol (I = +7, Q = +7 for 64-QAM, magenta colour) in the corner of the P-QAM constellation diagram is defined as

$$p\left(y/corner\right) = p\left(\Re\left\{y\right\} \geq 6k\sqrt{E_s}, \Re\left\{y\right\} \leq \infty/ + 7\right) p\left(\Im\left\{y\right\} \geq 6k\sqrt{E_s}, \Im\left\{y\right\} \leq \infty/ + 7\right) \tag{D.10}$$

after substituting the conditional PDF of In-phase and Quadrature components, respectively, leads

$$\begin{aligned} p\left(y/corner\right) = & \left(\frac{1}{\sqrt{\pi N_0}} \int\limits_{6k\sqrt{E_s}}^{\infty} \exp\left(\frac{-\left(y-7k\sqrt{E_s}\right)^2}{N_0} \right) dy \right) \\ & \left(\frac{1}{\sqrt{\pi N_0}} \int\limits_{6k\sqrt{E_s}}^{\infty} \exp\left(\frac{-\left(y-7k\sqrt{E_s}\right)^2}{N_0} \right) dy \right) \\ = & \left[1 - \frac{1}{2}\mathrm{erfc}\left(k\sqrt{\frac{E_s}{N_0}} \right) \right]^2 \end{aligned} \tag{D.11}$$

probability of error of detecting the corner symbol

$$\begin{aligned} p\left(e/corner\right) = & 1 - p\left(y/corner\right) \\ = & 1 - \left[1 - \frac{1}{2}\mathrm{erfc}\left(k\sqrt{\frac{E_s}{N_0}} \right) \right]^2 \\ = & \mathrm{erfc}\left(k\sqrt{\frac{E_s}{N_0}} \right) - \frac{1}{4}\mathrm{erfc}^2\left(k\sqrt{\frac{E_s}{N_0}} \right) \end{aligned} \tag{D.12}$$

***case(iii)*:** Symbol ($I = +7, Q = +1$ for 64-QAM, blue colour) at neither inside nor corner of the P-QAM constellation can be defined as,

$$p\left(y/ninc\right) = p\left(\Re\left\{y\right\} \geq 6k\sqrt{E_s}, \Re\left\{y\right\} \leq \infty/+7\right) p\left(\Im\left\{y\right\} \geq 0, \Im\left\{y\right\} \leq 2k\sqrt{E_s}/+1\right) \tag{D.13}$$

after substituting the PDF of correct demodulation of real and imaginary components, respectively, yields

$$\begin{aligned} p\left(y/ninc\right) = & \left(\frac{1}{\sqrt{\pi N_0}} \int\limits_{6k\sqrt{E_s}}^{\infty} \exp\left(-\frac{\left(y-7k\sqrt{E_s}\right)^2}{N_0} \right) dy \right) \\ & \left(1 - \left[\frac{1}{\sqrt{\pi N_0}} \int\limits_{-\infty}^{0} \exp\left(\frac{-\left(y-k\sqrt{E_s}\right)^2}{N_0} \right) dy \right. \right. \\ & \left. \left. + \frac{1}{\sqrt{\pi N_0}} \int\limits_{2k\sqrt{E_s}}^{\infty} \exp\left(\frac{-\left(y-k\sqrt{E_s}\right)^2}{N_0} \right) dy \right] \right) \\ = & \left(1 - \frac{1}{2}\mathrm{erfc}\left(k\sqrt{\frac{E_s}{N_0}} \right) \right) \left(1 - \mathrm{erfc}\left(k\sqrt{\frac{E_s}{N_0}} \right) \right) \\ = & 1 - \frac{3}{2}\mathrm{erfc}\left(k\sqrt{\frac{E_s}{N_0}} \right) + \frac{1}{2}\mathrm{erfc}^2\left(k\sqrt{\frac{E_s}{N_0}} \right) \end{aligned} \tag{D.14}$$

Probability of symbol decoded being error is

$$\begin{aligned} p\left(e/ninc\right) =& 1 - p\left(y/ninc\right) \\ =& \frac{3}{2}\text{erfc}\left(k\sqrt{\frac{E_s}{N_0}}\right) - \frac{1}{2}\text{erfc}^2\left(k\sqrt{\frac{E_s}{N_0}}\right) \end{aligned} \tag{D.15}$$

Substituting (D.9), (D.12) and (D.15) into (D.2) and simplifying results leads

$$\begin{aligned} p_e^{PQAM} = & \frac{\left(\sqrt{P}-2\right)\left(\sqrt{P}-2\right)}{P}\left[2\text{erfc}\left(k\sqrt{\frac{E_s}{N_0}}\right) - \text{erfc}^2\left(k\sqrt{\frac{E_s}{N_0}}\right)\right] \\ & + \frac{4}{P}\left[\text{erfc}\left(k\sqrt{\frac{E_s}{N_0}}\right) - \frac{1}{4}\text{erfc}^2\left(k\sqrt{\frac{E_s}{N_0}}\right)\right] \\ & + \frac{4\left(\sqrt{P}-2\right)}{P}\left[\frac{3}{2}\text{erfc}\left(k\sqrt{\frac{E_s}{N_0}}\right) - \frac{1}{2}\text{erfc}^2\left(k\sqrt{\frac{E_s}{N_0}}\right)\right] \end{aligned} \tag{D.16}$$

After simplification, we arrived to

$$p_e^{PQAM} = 2\left(\frac{\sqrt{P}-1}{\sqrt{P}}\right)\text{erfc}\left(k\sqrt{\frac{E_s}{N_0}}\right) - \left(\frac{\sqrt{M}-1}{\sqrt{M}}\right)^2\text{erfc}^2\left(k\sqrt{\frac{E_s}{N_0}}\right) \tag{D.17}$$

$$p_e^{PQAM} = 2\left(\frac{\sqrt{P}-1}{\sqrt{P}}\right)\text{erfc}\left(\sqrt{\gamma}\right) - \left(\frac{\sqrt{M}-1}{\sqrt{M}}\right)^2\text{erfc}^2\left(\sqrt{\gamma}\right) \tag{D.18}$$

where $\gamma = \frac{3}{2(2^\mu-1)}\frac{E_s}{N_0}$

D.2 SER expression under AWGN channel for OFDM

The SER for OFDM under AWGN channel can be given as [96, 187],

$$p_e^{OFDM} = 2\left(\frac{\sqrt{P}-1}{\sqrt{P}}\right)\text{erfc}\left(\sqrt{\gamma}\right) - \left(\frac{\sqrt{P}-1}{\sqrt{P}}\right)^2\text{erfc}^2\left(\sqrt{\gamma}\right) \tag{D.19}$$

where $\gamma = \frac{3}{2(2^\mu-1)}\frac{N}{N+N_{CP}}\frac{E_s}{N_0}$

D.3 SER expression under AWGN channel for GFDM

In GFDM, the total number of symbols is NM and the NEF (ξ) are the two factors that adjusts the equivalent SNR at the receiver side. Hence the SER for GFDM under

AWGN channel, ZF receiver, can be given by [43],

$$p_e^{GFDM} = 2\left(\frac{\sqrt{P}-1}{\sqrt{P}}\right)\operatorname{erfc}\left(\sqrt{\gamma}\right) - \left(\frac{\sqrt{P}-1}{\sqrt{P}}\right)^2 \operatorname{erfc}^2\left(\sqrt{\gamma}\right) \tag{D.20}$$

where

$$\gamma = \frac{3R_T}{2(2^\mu - 1)}\frac{E_s}{\xi N_0} \tag{D.21}$$

and

$$R_T = \frac{NM}{NM + N_{CP} + N_{CS}} \tag{D.22}$$

μ is the number of bits per QAM symbol, $P = 2^\mu$, N_{CP} and N_{CS} are the length of the CP and CS respectively, N and M denote the number of subcarriers and subsymbols respectively, E_s is the average energy per symbol and N_0 is the noise power density.

Appendix E

Toeplitz System

This appendix proves the Toeplitz nature of the system given by the following equation,

$$\sum_{m=0}^{Q-1} \frac{\sin 2\pi W(n-m)}{\pi(n-m)} v_m^{(l)}(Q,W) = \lambda_l(Q,W) v_n^{(l)}(Q,W) \tag{E.1}$$

A Toeplitz matrix is a matrix whose diagonal elements having constant entries and each descending diagonal from left to right is a constant. As an example, a matrix of the form $\mathbf{T}$ is said to be a Toeplitz if it has the following structure,

$$\mathbf{T} = \begin{bmatrix} t_0 & t_{-1} & t_{-2} & \cdots & t_{-(n-1)} \\ t_1 & t_0 & t_{-1} & \ddots & \vdots \\ t_2 & t_1 & t_0 & \ddots & t_{-2} \\ \vdots & \ddots & \ddots & \ddots & t_{-1} \\ t_{n-1} & \cdots & t_2 & t_1 & t_0 \end{bmatrix} \tag{E.2}$$

By expanding equation (E.1),

$$n=0 \qquad \frac{\sin 2\pi W(0-0)}{\pi(0-0)} v_0^{(l)} + \frac{\sin 2\pi W(0-1)}{\pi(0-1)} v_1^{(l)} + \cdots + \frac{\sin 2\pi W(0-N+1)}{\pi(0-Q+1)} v_{Q-1}^{(l)} = \lambda_l v_0^{(l)}$$

$$n=1 \qquad \frac{\sin 2\pi W(1-0)}{\pi(1-0)} v_0^{(l)} + \frac{\sin 2\pi W(1-1)}{\pi(1-1)} v_1^{(l)} + \cdots + \frac{\sin 2\pi W(1-Q+1)}{\pi(1-Q+1)} v_{Q-1}^{(l)} = \lambda_l v_1^{(l)}$$

$$n=2 \qquad \frac{\sin 2\pi W(2-0)}{\pi(2-0)} v_0^{(l)} + \frac{\sin 2\pi W(2-1)}{\pi(2-1)} v_1^{(l)} + \cdots + \frac{\sin 2\pi W(2-Q+1)}{\pi(2-Q+1)} v_{Q-1}^{(l)} = \lambda_l v_2^{(l)}$$

$$\vdots$$

$$n=Q-1 \qquad \frac{\sin 2\pi W(Q-1-0)}{\pi(Q-1-0)} v_0^{(l)} + \cdots + \frac{\sin 2\pi W(Q-1-Q+1)}{\pi(Q-1-Q+1)} v_{Q-1}^{(l)} = \lambda_l v_{Q-1}^{(l)}$$

and given that

$$\lim_{x\to 0}\frac{\sin 2Wx}{x} = 2W$$

In matrix form, equation (E.1) can be written as [103],

$$\mathbf{T}(Q,W)\mathbf{v}_{(l)}(Q,W) = \lambda_l(Q,W)\mathbf{v}_{(l)}(Q,W) \tag{E.3}$$

where

$$T\left(Q,W\right) = \begin{cases} \frac{sin[2\pi W(m-n)]}{\pi[m-n]} & ;for\ m,n = 0,1,2,\cdots Q-1 \quad m \neq n \\ 2W & ;for\ m = n \end{cases} \tag{E.4}$$

Now let us prove that $T\left(Q,W\right)$ is a Toeplitz matrix. For simplicity, let us begin with $Q = 4$ i.e., $m,n = 0,1,2,3$. Following the definition of $T\left(Q,W\right)$ as in equation (E.4), one can easily write the matrix expansion as,

$$T\left(Q,W\right) = \begin{bmatrix} 2W & \frac{sin[2\pi W]}{\pi} & \frac{sin[4\pi W]}{2\pi} & \frac{sin[6\pi W]}{3\pi} \\ \frac{sin[2\pi W]}{\pi} & 2W & \frac{sin[2\pi W]}{\pi} & \frac{sin[4\pi W]}{2\pi} \\ \frac{sin[4\pi W]}{2\pi} & \frac{sin[2\pi W]}{\pi} & 2W & \frac{sin[2\pi W]}{\pi} \\ \frac{sin[6\pi W]}{3\pi} & \frac{sin[4\pi W]}{2\pi} & \frac{sin[2\pi W]}{\pi} & 2W \end{bmatrix} \tag{E.5}$$

By definition a Toeplitz system is a linear system where the system matrix has each descending diagonal from left to right constant. Observing equation (E.5), $T\left(Q,W\right)$ expressed in equation (E.3) is a Toeplitz system. One can also add that the system is seen to be symmetric since $sin[x]$ is an odd function. Matlab takes care of all the above giving the correct eigenvalues/eigenvectors. Further reading on Toeplitz system can be found in [188, 189] and the references therein.

Bibliography

[1] J. Proakis, *Digital Communications*. McGraw-Hill, 1995.

[2] J. T. J. Penttinen, *3GPP Mobile Communications: GSM*. John Wiley & Sons, Ltd, 2015.

[3] M. Sauter, *Global System for Mobile Communications (GSM)*. John Wiley & Sons, Ltd, 2014.

[4] J. Eberspcher, H.-J. Vgel, C. Bettstetter, and C. Hartmann, *Improved Data Services in GSM: GPRS, HSCSD and EDGE*. John Wiley & Sons, Ltd, 2008.

[5] J. Romero, J. Martinez, S. Nikkarinen, and M. Moisio, *GPRS and EGPRS Performance*. John Wiley & Sons, Ltd, 2004.

[6] J. Melero, A. Toskala, P. Hakalin, and A. Tolli, *IMT-2000 3G Radio Access Technologies*. John Wiley & Sons, Ltd, 2004.

[7] T. Chapman, E. Larsson, P. von Wrycza, E. Dahlman, S. Parkvall, and J. Skld, "Chapter 7 - introduction to HSPA," in *HSPA Evolution*. Oxford: Academic Press, pp. 105–114, 2015.

[8] K. P. Murray and S. Patil, *HSDPA*. John Wiley & Sons, Ltd, 2006.

[9] E. Dahlman, S. Parkvall, J. Skld, and P. Beming, "12 - HSPA evolution," in *3G Evolution*. Oxford: Academic Press, pp. 251–274, 2007.

[10] H. Holma, J. Kallio, M. Kuusela, P. Lundn, E. Malkamki, J. Ojala, and H. Wang, *Voice over IP (VoIP)*. John Wiley & Sons, Ltd, 2011.

[11] E. Dahlman, S. Parkvall, and J. Skold, *4G:LTE/LTE-advanced for mobile broadband*. Academic press, 2013.

[12] D. Astély, E. Dahlman, A. Furuskär, Y. Jading, M. Lindström, and S. Parkvall, "LTE: the evolution of mobile broadband," *IEEE Communications magazine*, vol. 47, no. 4, 2009.

[13] A. Ghosh, R. Ratasuk, B. Mondal, N. Mangalvedhe, and T. Thomas, "LTE-advanced: next-generation wireless broadband technology," *IEEE wireless communications*, vol. 17, no. 3, 2010.

[14] A. Toskala, *LTE and LTE Advanced in Releases 8-11.* John Wiley & Sons Ltd, 2015.

[15] D. Tse and P. Viswanath, *Fundamentals of wireless communication.* Cambridge university press, 2005.

[16] 3GPP, "TS36.211: Evolved Universal Terrestrial Radio Access (E-UTRA); Physical Channels and Modulation (Release 10), V10.7.0," Tech. Rep., February, 2013.

[17] ——, "TS36.212: Evolved Universal Terrestrial Radio Access (E-UTRA); Multiplexing and channel coding (Release 10), V10.8.0," Tech. Rep., June, 2013.

[18] ——, "TS36.213: Evolved Universal Terrestrial Radio Access (E-UTRA); Physical layer procedures (Release 10), V10.12.0,," Tech. Rep., March, 2014.

[19] A. Benjebbour, K. Saito, A. Li, Y. Kishiyama, and T. Nakamura, *Non-Orthogonal Multiple Access (NOMA): Concept and Design.* John Wiley & Sons, Ltd.

[20] A. Mokdad, P. Azmi, and N. Mokari, "Radio resource allocation for heterogeneous traffic in gfdm-noma heterogeneous cellular networks," *IET Communications*, vol. 10, no. 12, pp. 1444–1455, 2016.

[21] Cisco, "Visual Networking Index: Global Mobile Data Traffic Forecast Update," *White Paper*, February 2015.

[22] A. Osseiran, F. Boccardi, V. Braun, K. Kusume, P. Marsch, M. Maternia, O. Queseth, M. Schellmann, H. Schotten, H. Taoka *et al.*, "Scenarios for 5G mobile and wireless communications: the vision of the METIS project," *IEEE Communications Magazine*, vol. 52, no. 5, pp. 26–35, 2014.

[23] A. Maaref, J. Ma, M. Salem, H. Baligh, and K. Zarin, "Device-centric radio access virtualization for 5G networks," in *IEEE Globecom Workshops (GC Wkshps)*, pp. 887–893, 2014.

[24] T. S. Rappaport, Y. Xing, G. R. MacCartney, A. F. Molisch, E. Mellios, and J. Zhang, "Overview of millimeter wave communications for fifth-generation (5g) wireless networks-with a focus on propagation models," *IEEE Transactions on Antennas and Propagation*, 2017.

[25] J. G. Andrews, T. Bai, M. N. Kulkarni, A. Alkhateeb, A. K. Gupta, and R. W. Heath, "Modeling and Analyzing Millimeter Wave Cellular systems," *IEEE Transactions on Communications*, vol. 65, no. 1, pp. 403–430, Jan 2017.

[26] Y. Niu, Y. Li, D. Jin, L. Su, and A. V. Vasilakos, "A survey of millimeter wave communications (mmwave) for 5G: opportunities and challenges," *Wireless Networks*, vol. 21, no. 8, pp. 2657–2676, Nov 2015.

[27] L. Lu, G. Y. Li, A. L. Swindlehurst, A. Ashikhmin, and R. Zhang, "An overview of massive MIMO: Benefits and challenges," *IEEE journal of selected topics in signal processing*, vol. 8, no. 5, pp. 742–758, 2014.

[28] F. Boccardi, R. W. Heath, A. Lozano, T. L. Marzetta, and P. Popovski, "Five disruptive technology directions for 5G," *IEEE Communications Magazine*, vol. 52, no. 2, pp. 74–80, 2014.

[29] T. E. Bogale and L. B. Le, "Massive MIMO and mmwave for 5G wireless Hetnet: Potential benefits and challenges," *IEEE Vehicular Technology Magazine*, vol. 11, no. 1, pp. 64–75, 2016.

[30] Y. Mehmood, N. Haider, M. Imran, A. Timm-Giel, and M. Guizani, "M2M communications in 5G: State-of-the-art architecture, recent advances, and research challenges," *IEEE Communications Magazine*, vol. 55, no. 9, pp. 194–201, 2017.

[31] Z. Dawy, W. Saad, A. Ghosh, J. G. Andrews, and E. Yaacoub, "Toward massive machine type cellular communications," *IEEE Wireless Communications*, vol. 24, no. 1, pp. 120–128, 2017.

[32] M. Agiwal, A. Roy, and N. Saxena, "Next generation 5G wireless networks: A comprehensive survey," *IEEE Communications Surveys & Tutorials*, vol. 18, no. 3, pp. 1617–1655, 2016.

[33] B. Farhang-Boroujeny, "OFDM versus filter bank multicarrier," *IEEE Signal Processing Magazine*, vol. 28, no. 3, pp. 92–112, 2011.

[34] "PHYDYAS project FBMC primer," http://www.ict-phydyas.org/teamspace/internal-folder/ FBMC-Primer_06-2010.pdf.

[35] *FP7 PHYDYAS Project*, http://www.ict-phydyas.org.

[36] *FP7 EMPhAtiC Project*, http://www.ict-emphatic.eu/.

[37] M. Payaro, A. Pascual-Iserte, and M. Najar, "Performance comparison between FBMC and OFDM in MIMO systems under channel uncertainty," in *European Wireless Conference (EW)*, pp. 1023–1030, April, 2010.

[38] V. Vakilian, T. Wild, F. Schaich, S. Ten Brink, and J. Frigon, "Universal-filtered multi-carrier technique for wireless systems beyond LTE," in *IEEE Globecom Workshops (GC Wkshps)*, pp. 223–228, Dec, 2013.

[39] T. Wild, F. Schaich, and Y. Chen, "5G air interface design based on Universal Filtered UF-OFDM," in *19th International Conference on Digital Signal Processing (DSP)*, pp. 699–704, Aug, 2014.

[40] M. Kasparick, G. Wunder, G. Wunder, P. Jung, P. Jung, and D. Maryopi, "Bi-orthogonal waveforms for 5G random access with short message support," in *Proceedings of 20th European Wireless Conference*, pp. 1–6, May, 2014.

[41] P. Banelli, S. Buzzi, G. Colavolpe, A. Modenini, F. Rusek, and A. Ugolini, "Modulation formats and waveforms for 5G networks: Who will be the heir of OFDM?: An overview of alternative modulation schemes for improved spectral efficiency," *IEEE Signal Processing Magazine*, vol. 31, no. 6, pp. 80–93, Nov 2014.

[42] F. Schaich, T. Wild, and Y. Chen, "Waveform contenders for 5G - Suitability for short packet and low latency transmissions," in *79th IEEE Vehicular Technology Conference (VTC Spring)*, pp. 1–5, May, 2014.

[43] N. Michailow, M. Matthe, I. Gaspar, A. Caldevilla, L. Mendes, A. Festag, and G. Fettweis, "Generalized Frequency Division Multiplexing for 5th generation cellular networks," *IEEE Transactions on Communications*, vol. 62, no. 9, pp. 3045–3061, Sept 2014.

[44] G. Fettweis, M. Krondorf, and S. Bittner, "GFDM - Generalized Frequency Division Multiplexing," in *IEEE 69th Vehicular Technology Conference*, pp. 1–4, April, 2009.

[45] N. Michailow and G. Fettweis, "Low peak-to-average power ratio for next generation cellular systems with generalized frequency division multiplexing," in *International Symposium on Intelligent Signal Processing and Communications Systems (ISPACS)*, pp. 651–655, Nov, 2013.

[46] *FP7 METIS 2020 Project*, https://www.metis2020.com.

[47] *FP7 5GNOW Project*, http://www.5gnow.eu/.

[48] *FP7 PHYLAWS Project*, http://www.phylaws-ict.org.

[49] *FP7 COMBO Project*, http://www.ict-combo.eu.

[50] T. S. Rappaport, S. Sun, R. Mayzus, H. Zhao, Y. Azar, K. Wang, G. N. Wong, J. K. Schulz, M. Samimi, and F. Gutierrez, "Millimeter wave mobile communications for 5G cellular: It will work!" *IEEE access*, vol. 1, pp. 335–349, 2013.

[51] J. Lee, Y. Song, E. Choi, and J. Park, "mmwave cellular mobile communication for giga korea 5G project," in *21st Asia-Pacific Conference on Communications (APCC)*. IEEE, pp. 179–183, 2015.

[52] J. Bae, Y. S. Choi, J. S. Kim, and M. Y. Chung, "Architecture and performance evaluation of mmwave based 5G mobile communication system," in *International Conference on Information and Communication Technology Convergence (ICTC)*. IEEE, pp. 847–851, 2014.

[53] *5G Innovation Center*, https://www.surrey.ac.uk/5gic.

[54] S. K. Bandari, A. Drosopoulos, and V. Mani, "Exact ser expressions of GFDM in nakagami-m and rician fading channels," in *Proceedings of 21th European Wireless Conference*. VDE, pp. 1–6, 2015.

[55] S. K. Bandari, V. Mani, and A. Drosopoulos, "Performance analysis of GFDM in various fading channels," *COMPEL - The international journal for computation and mathematics in electrical and electronic engineering*, vol. 35, no. 1, pp. 225–244, 2016.

[56] S. K. Bandari, V. V. Mani, and A. Drosopoulos, "Multi-taper implementation of GFDM," in *Wireless Communications and Networking Conference (WCNC), 2016 IEEE*. IEEE, pp. 1–5, 2016.

[57] S. Nobilet, J.-F. Hélard, and D. Mottier, "Spreading sequences for uplink and downlink MC-CDMA systems: PAPR and MAI minimization," *European Transactions on Telecommunications*, vol. 13, no. 5, pp. 465–474, 2002.

[58] S. K. Bandari, V. M. Vakamulla, and A. Drosopoulos, "PAPR analysis of wavelet based multitaper GFDM system," *AEU - International Journal of Electronics and Communications*, vol. 76, pp. 166 – 174, 2017.

[59] S. K. Bandari, V. Mani, and A. Drosopoulos, "Robust precoded OSTBC for GFDM systems," *Procedia Computer Science, Elsevier*, vol. 93, pp. 176–182, 2016.

[60] S. K. Bandari, V. V. Mani, and A. Drosopoulos, "OQAM implementation of GFDM," in *23rd International Conference on Telecommunications (ICT)*, pp. 1–5, May, 2016.

[61] S. K. Bandari, V. Mani, and A. Drosopoulos, "GFDM/OQAM implementation under rician fading channel," in *IEEE International Conference on Advances in Computing, Communications and Informatics (ICACCI)*, pp. 256–260, 2016.

[62] S. K. Bandari, V. V. Mani, and A. Drosopoulos, "GFDM/OQAM performance analysis under nakagami fading channels," *Physical Communication, Elsevier*, 2017.

[63] S. K. Bandari, V. M. Vakamulla, and A. Drosopoulos, "Training based channel estimation for multitaper GFDM system," *Mobile Information Systems*, 2017.

[64] S. K. Bandari, V. V. Mani, and A. Drosopoulos, "Convolutional codes for MGFDM system," in *International Conference on Information and Communication Technology Convergence (ICTC)*, pp. 545–550, Oct, 2017.

[65] H. Sari, G. Karam, and I. Jeanclaud, "Frequency-domain equalization of mobile radio and terrestrial broadcast channels," in *IEEE GLOBECOM Communications: The Global Bridge*, vol. 1, pp. 1–5, Nov, 1994.

[66] A. Peled and A. Ruiz, "Frequency domain data transmission using reduced computational complexity algorithms," in *IEEE International Conference on Acoustics, Speech, and Signal Processing*, vol. 5, pp. 964–967, April, 1980.

[67] T. Pollet, M. V. Bladel, and M. Moeneclaey, "BERsensitivity of OFDM systems to carrier frequency offset and wiener phase noise," *IEEE Transactions on Communications*, vol. 43, no. 2/3/4, pp. 191–193, Feb 1995.

[68] G. Carron, R. Ness, L. Deneire, L. V. der Perre, and M. Engels, "Comparison of two modulation techniques using frequency domain processing for in-house networks," *IEEE Transactions on Consumer Electronics*, vol. 47, no. 1, pp. 63–72, Feb 2001.

[69] J. Bingham, "Multicarrier modulation for data transmission: an idea whose time has come," *IEEE Communications Magazine*, vol. 28, no. 5, pp. 5–14, May 1990.

[70] R. W. Chang, "Synthesis of band-limited orthogonal signals for multichannel data transmission," *The Bell System Technical Journal*, vol. 45, no. 10, pp. 1775–1796, Dec 1966.

[71] B. Saltzberg, "Performance of an Efficient Parallel Data Transmission System," *IEEE Transactions on Communication Technology*, vol. 15, no. 6, pp. 805–811, December 1967.

[72] R. Chang and R. Gibby, "A Theoretical Study of Performance of an Orthogonal Multiplexing Data Transmission Scheme," *IEEE Transactions on Communication Technology*, vol. 16, no. 4, pp. 529–540, August 1968.

[73] S. Weinstein and P. Ebert, "Data Transmission by Frequency-Division Multiplexing Using the Discrete Fourier Transform," *IEEE Transactions on Communication Technology*, vol. 19, no. 5, pp. 628–634, October 1971.

[74] B. Hirosaki, "An Orthogonally Multiplexed QAM system using the Discrete Fourier Transform," *IEEE Transactions on Communications*, vol. 29, no. 7, pp. 982–989, July 1981.

[75] M. Ghosh, "Analysis of the effect of impulse noise on multicarrier and single carrier QAM systems," *IEEE Transactions on Communications*, vol. 44, no. 2, pp. 145–147, Feb 1996.

[76] A. R. Bahai and B. R. Saltzberg, *Multi-CarrierDigital Communications: Theory and Applications of OFDM.* Plenum Publishing Co., 1999.

[77] T. Hwang, C. Yang, G. Wu, S. Li, and G. Y. Li, "OFDM and Its Wireless Applications: A Survey," *IEEE Transactions on Vehicular Technology*, vol. 58, no. 4, pp. 1673–1694, May 2009.

[78] M. Park, H. Jun, J. Cho, N. Cho, D. Hong, and C. Kang, "PAPR reduction in OFDM transmission using Hadamard transform," in *IEEE International Conference on Communications*, vol. 1, pp. 430–433, 2000.

[79] X. C. Wu, J. X. Wang, and Z. GangMao, "A novel PTS architecture for PAPR reduction of OFDM signals," in *11th IEEE Singapore International Conference on Communication Systems*, pp. 1055–1060, Nov, 2008.

[80] K. Yang and S. Chang, "Peak-to-average power control in OFDM using standard arrays of linear block codes," *IEEE Communications Letters*, vol. 7, no. 4, pp. 174–176, April 2003.

[81] E. Lizarraga, A. Dowhuszko, and V. Sauchelli, "Improving out-of-band power emissions in OFDM systems using double-length symbols," *IEEE Latin America Transactions (Revista IEEE America Latina)*, vol. 10, no. 3, pp. 1710–1718, April 2012.

[82] Y. Zhao and S. Haggman, "Intercarrier interference self-cancellation scheme for OFDM mobile communication systems," *IEEE Transactions on Communications*, vol. 49, no. 7, pp. 1185–1191, Jul 2001.

[83] F. Rezaei, M. Hempel, and H. Sharif, "LTE PHY performance analysis under 3GPP standards parameters," in *IEEE 16th International Workshop on Computer Aided Modeling and Design of Communication Links and Networks (CAMAD)*, pp. 102–106, June, 2011.

[84] B. Muquet, Z. Wang, G. Giannakis, M. de Courville, and P. Duhamel, "Cyclic prefixing or zero padding for wireless multicarrier transmissions?" *IEEE Transactions on Communications*, vol. 50, no. 12, pp. 2136–2148, Dec 2002.

[85] G. Fettweis, "The tactile internet: Applications and challenges," *IEEE Vehicular Technology Magazine*, vol. 9, no. 1, pp. 64–70, March 2014.

[86] T. M. Schmidl and D. C. Cox, "Robust frequency and timing synchronization for OFDM," *IEEE transactions on communications*, vol. 45, no. 12, pp. 1613–1621, 1997.

[87] N. Michailow, M. Lentmaier, P. Rost, and G. Fettweis, "Integration of a GFDM secondary system in an OFDM primary system," in *Future Network Mobile Summit (FutureNetw)*, pp. 1–8, June, 2011.

[88] R. Datta, N. Michailow, M. Lentmaier, and G. Fettweis, "GFDM Interference Cancellation for Flexible Cognitive Radio Phy Design," in *IEEE Vehicular Technology Conference (VTC Fall)*, pp. 1–5, Sept, 2012.

[89] D. Panaitopol, R. Datta, and G. Fettweis, "Cyclostationary detection of cognitive radio systems using GFDM modulation," in *IEEE Wireless Communications and Networking Conference (WCNC)*, 2012, pp. 930–934, April, 2012.

[90] P. Wei, X. G. Xia, Y. Xiao, and S. Li, "Fast dgt-based receivers for gfdm in broadband channels," *IEEE Transactions on Communications*, vol. 64, no. 10, pp. 4331–4345, Oct 2016.

[91] B. Lim and Y. C. Ko, "Sir analysis of ofdm and gfdm waveforms with timing offset, cfo, and phase noise," *IEEE Transactions on Wireless Communications*, vol. 16, no. 10, pp. 6979–6990, Oct 2017.

[92] S. S. Das and S. Tiwari, "Discrete fourier transform spreading-based generalised frequency division multiplexing," *Electronics Letters*, vol. 51, no. 10, pp. 789–791, 2015.

[93] S. Tiwari, S. S. Das, and K. K. Bandyopadhyay, "Precoded generalised frequency division multiplexing system to combat inter-carrier interference: performance analysis," *IET Communications*, vol. 9, no. 15, pp. 1829–1841, 2015.

[94] S. Tiwari and S. S. Das, "Low-complexity joint-mmse gfdm receiver," *IEEE Transactions on Communications*, vol. 66, no. 4, pp. 1661–1674, April 2018.

[95] N. Michailow, S. Krone, M. Lentmaier, and G. Fettweis, "Bit error rate performance of Generalized Frequency Division Multiplexing," in *IEEE Vehicular Technology Conference (VTC Fall)*, pp. 1–5, Sept, 2012.

[96] M. K. Simon and M.-S. Alouini, *Digital communication over fading channels*. John Wiley & Sons, Vol. 95, 2005.

[97] S. Mukherjee, S. S. Das, A. Chatterjee, and S. Chatterjee, "Analytical calculation of rician k-factor for indoor wireless channel models," *IEEE Access*, vol. 5, pp. 19 194–19 212, 2017.

[98] M. NAKAGAMI, "The m-distributiona general formula of intensity distribution of rapid fading," in *Statistical Methods in Radio Wave Propagation*, W. HOFFMAN, Ed. Pergamon, 1960, pp. 3 – 36.

[99] R. S. Hoyt, "Probability functions for the modulus and angle of the normal complex variate," *The Bell System Technical Journal*, vol. 26, no. 2, pp. 318–359, April 1947.

[100] B. Chytil, "The distribution of amplitude scintillation and the conversion of scintillation indices," *Journal of Atmospheric and Terrestrial Physics*, vol. 29, no. 9, pp. 1175 – 1177, 1967.

[101] S. C. Schwartz and Y. S. Yeh, "On the distribution function and moments of power sums with log-normal components," *The Bell System Technical Journal*, vol. 61, no. 7, pp. 1441–1462, Sept 1982.

[102] H. Hashemi, "The indoor radio propagation channel," *Proceedings of the IEEE*, vol. 81, no. 7, pp. 943–968, July 1993.

[103] D. Slepian, "Prolate spheroidal wave functions, fourier analysis, and uncertaintyv: The discrete case," *Bell System Technical Journal*, vol. 57, no. 5, pp. 1371–1430, 1978.

[104] D. J. Thomson, "Spectrum estimation and harmonic analysis," *Proceedings of The IEEE*, vol. 70, pp. 1055–1096, 1982.

[105] N. Michailow and G. Fettweis, "Low peak-to-average power ratio for next generation cellular systems with generalized frequency division multiplexing," in *International Symposium on Intelligent Signal Processing and Communication Systems*, pp. 651–655, Nov, 2013.

[106] B. Robert, F. Robert, and B. Johannes, "Reducing the peak-to-average power ratio of multicarrier modulation by selected mapping," *Electronics letter*, vol. 32, pp. 2056–2057, 1996.

[107] S. H. Muller and J. B. Huber, "OFDM with reduced peak-to-average power ratio by optimum combination of partial transmit sequences," *Electronics Letters*, vol. 33, no. 5, pp. 368–369, Feb 1997.

[108] I. Baig and V. Jeoti, "PAPR reduction in OFDM systems: Zadoff-chu matrix transform based pre/post-coding techniques," in *Second International Conference on Computational Intelligence, Communication Systems and Networks (CICSyN)*. IEEE, pp. 373–377, 2010.

[109] M. K. Gupta and S. Tiwari, "Performance evaluation of conventional and wavelet based OFDM system," *AEU-International Journal of Electronics and Communications*, vol. 67, no. 4, pp. 348–354, 2013.

[110] K. Abdullah and Z. M. Hussain, "Performance of fourier-based and wavelet-based OFDM for DVB-T systems," in *Australasian Telecommunication Networks and Applications Conference (ATNAC)*. IEEE, pp. 475–479, Dec, 2007.

[111] S. M. Alamouti, "A simple transmit diversity technique for wireless communications," *IEEE Journal on Selected Areas in Communications*, vol. 16, no. 8, pp. 1451–1458, 1998.

[112] V. Tarokh, H. Jafarkhani, and A. R. Calderbank, "Space-time block codes from orthogonal designs," *IEEE Transactions on Information Theory*, vol. 45, no. 5, pp. 1456–1467, 1999.

[113] G. Jöngren, M. Skoglund, and B. Ottersten, "Combining beamforming and orthogonal space-time block coding," *IEEE Transactions on Information Theory*, vol. 48, no. 3, pp. 611–627, 2002.

[114] G. Jöngren and M. Skoglund, "Improving orthogonal space-time block codes by utilizing quantized feedback information," in *IEEE International Symposium on Information Theory (ISIT)*. IEEE, pp. 220, June, 2001.

[115] H. Wang, Y. Li, X.-G. Xia, and S. Liu, "Unitary and non-unitary precoders for a limited feedback precoded OSTBC system," *IEEE Transactions on Vehicular Technology*, vol. 62, no. 4, pp. 1646–1654, 2013.

[116] A. Hjørungnes and D. Gesbert, "Precoded orthogonal space–time block codes over correlated ricean MIMO channels," *IEEE Transactions on Signal Processing*, vol. 55, no. 2, pp. 779–783, 2007.

[117] M. Matthé, L. L. Mendes, and G. Fettweis, "Space-time coding for generalized frequency division multiplexing," in *Proceedings of 20th European Wireless Conference*. VDE, pp. 1–5, May, 2014.

[118] P. Siohan, C. Siclet, and N. Lacaille, "Analysis and design of OFDM/OQAM systems based on filterbank theory," *IEEE Transactions on Signal Processing*, vol. 50, no. 5, pp. 1170–1183, 2002.

[119] D. Katselis, E. Kofidis, and S. Theodoridis, "On OFDM/OQAM receivers," in *Proceedings of the 20th European Signal Processing Conference (EUSIPCO)*, pp. 2566–2570, Aug, 2012.

[120] H. Lei, C. Gao, I. S. Ansari, Y. Guo, Y. Zou, G. Pan, and K. A. Qaraqe, "Secrecy Outage Performance of Transmit Antenna Selection for MIMO Underlay Cognitive Radio Systems Over Nakagami- m Channels," IEEE Transactions on Vehicular Technology, vol. 66, no. 3, pp. 2237–2250, March 2017.

[121] A. Mehrnia and H. Hashemi, "Mobile satellite propagation channel. part ii-a new model and its performance," in *Gateway to 21st Century Communications Village. VTC 1999-Fall. IEEE VTS 50th Vehicular Technology Conference (Cat. No.99CH36324)*, vol. 5, pp. 2780–2784, Sept, 1999.

[122] R. M. Radaydeh, "Average Error performance of M-ary Modulation Schemes in Nakagami-q (Hoyt) Fading Channels," *IEEE Communications Letters*, vol. 11, no. 3, pp. 255–257, March 2007.

[123] K. T. Hemachandra and N. C. Beaulieu, "Simple Expressions for the SER of Dual MRC in Correlated Nakagami-q (Hoyt) fading," *IEEE Communications Letters*, vol. 14, no. 8, pp. 743–745, August 2010.

[124] N. Hajri, N. Youssef, and M. Patzold, "Performance analysis of binary dpsk modulation schemes over hoyt fading channels," in *6th International Symposium on Wireless Communication Systems*, pp. 609–613, Sept, 2009.

[125] J.-J. Van de Beek, O. Edfors, M. Sandell, S. K. Wilson, and P. O. Borjesson, "On channel estimation in OFDM systems," in *IEEE 45th Vehicular Technology Conference*, vol. 2, pp. 815–819, 1995.

[126] F. Tufvesson and T. Maseng, "Pilot assisted channel estimation for OFDM in mobile cellular systems," in *IEEE 47th Vehicular Technology Conference*, vol. 3, pp. 1639–1643, 1997.

[127] U. Vilaipornsawai and M. Jia, "Scattered-pilot channel estimation for GFDM," in *IEEE Wireless Communications and Networking Conference (WCNC)*, pp. 1053–1058, 2014.

[128] L. Chang, G. Y. Li, J. Li, and R. Li, "Blind parameter estimation of GFDM signals over frequency-selective fading channels," *IEEE Transactions on Communications*, vol. 64, no. 3, pp. 1120–1131, 2016.

[129] P. Shelswell, "The COFDM modulation system: the heart of digital audio broadcasting," *Electronics Communication Engineering Journal*, vol. 7, no. 3, pp. 127–136, Jun 1995.

[130] M. Matthé, N. Michailow, I. Gaspar, and G. Fettweis, "Influence of pulse shaping on bit error rate performance and out of band radiation of generalized frequency division multiplexing," in *IEEE International Conference on Communications Workshops (ICC)*, pp. 43–48, June, 2014.

[131] N. Michailow, M. Lentmaier, P. Rost, and G. Fettweis, "Integration of a GFDM secondary system in an OFDM primary system," in *Future Network Mobile Summit (FutureNetw)*, pp. 1–8, June, 2011.

[132] I. S. Gaspar, L. L. Mendes, N. Michailow, and G. Fettweis, "A synchronization technique for generalized frequency division multiplexing," *EURASIP Journal on Advances in Signal Processing*, vol. 2014, no. 1, p. 67, May 2014.

[133] S. Tiwari, S. S. Das, and K. K. Bandyopadhyay, "Precoded generalised frequency division multiplexing system to combat inter-carrier interference: performance analysis," *IET Communications*, vol. 9, no. 15, pp. 1829–1841, 2015.

[134] A. Farhang, N. Marchetti, and L. E. Doyle, "Low-complexity modem design for GFDM," *IEEE Transactions on Signal Processing*, vol. 64, no. 6, pp. 1507–1518, March 2016.

[135] I. Gradshteyn and I. Ryzhik, "Table of integrals," *Series, and Products, Seventh edition*, vol. 885, Feb 2007.

[136] V. S. Adamchik and O. I. Marichev, "The algorithm for calculating integrals of hypergeometric type functions and its realization in reduce system," in *Proceedings of the International Symposium on Symbolic and Algebraic Computation.* New York, NY, USA: ACM, pp. 212–224, 1990.

[137] M. Abramowitz, I. A. Stegun *et al.*, "Handbook of mathematical functions," *Applied mathematics series*, vol. 55, p. 62, 1966.

[138] S. Nallagonda, S. K. Bandari, S. Dhar Roy, and S. Kundu, "On performance of weighted fusion based spectrum sensing in fading channels," *Journal of Computational Engineering*, 2013.

[139] N. Sagias, G. Karagiannidis, D. Zogas, P. Mathiopoulos, and G. Tombras, "Performance analysis of dual selection diversity in correlated weibull fading channels," *IEEE Transactions on Communications*, vol. 52, no. 7, pp. 1063–1067, July 2004.

[140] V. Erceg, L. Greenstein, S. Tjandra, S. Parkoff, A. Gupta, B. Kulic, A. Julius, and R. Bianchi, "An empirically based path loss model for wireless channels in suburban environments," *IEEE Journal on Selected Areas in Communications*, vol. 17, no. 7, pp. 1205–1211, Jul 1999.

[141] R. Hekmat and P. V. Mieghem, "Connectivity in wireless adhoc networks with a lognormal radio model," *Mobile Networks and Applications*, pp. 351–360, 2006.

[142] H. Breiling, S. H. Muller-Weinfurtner, and J. B. Huber, "Slm peak-power reduction without explicit side information," *IEEE Communications Letters*, vol. 5, no. 6, pp. 239–241, June 2001.

[143] N. Ohkubo and T. Ohtsuki, "A peak to average power ratio reduction of multicarrier CDMA using selected mapping," in *Proceedings of IEEE 56th Vehicular Technology Conference (VTC-Fall)*, vol. 4, pp. 2086–2090, 2002.

[144] N. Ahmed and K. R. Rao, *Orthogonal transforms for digital signal processing*. Springer Science & Business Media, 2012.

[145] S. D. Sandberg and M. A. Tzannes, "Overlapped discrete multitone modulation for high speed copper wire communications," *IEEE Journal on selected areas in communications*, vol. 13, no. 9, pp. 1571–1585, 1995.

[146] D. Slepian, "Some asymptotic expansions for prolate spheroidal wave functions," 1965.

[147] S. David, "A numerical method for determining the eigenvalues and eigenfunctions of analytic kernels," *SIAM Journal on Numerical Analysis*, vol. 5, no. 3, pp. 586–600, 1968.

[148] D. S. Sonnenblick *et al.*, "Eigenvalues associated with prolate spheroidal wave functions of zero order," *Bell System Technical Journal*, vol. 44, no. 8, pp. 1745–1759, 1965.

[149] D. Percival and A. Walden, *Spectral Analysis for Physical Applications*. Cambridge University Press, 1993.

[150] A. Sahin, I. Guvenc, and H. Arslan, "A survey on multicarrier communications: Prototype filters, lattice structures, and implementation aspects," *IEEE Communications Surveys Tutorials*, vol. 16, no. 3, pp. 1312–1338, 2014.

[151] G. Nigam, R. Singh, and A. Chaturvedi, "Finite duration root Nyquist pulses with maximum in-band fractional energy," *IEEE Communications Letters*, vol. 14, no. 9, pp. 797–799, 2010.

[152] H. Lin and P. Siohan, "Multi-carrier modulation analysis and WCP-COQAM proposal," *EURASIP Journal on Advances in Signal Processing*, vol. 79, no. 1, pp. 1–19, 2014.

[153] J. Klapper, "Discrete fourier analysis and wavelets," *Journal of Applied Statistics*, vol. 37, no. 10, pp. 1783–1784, 2010.

[154] B. Vidakovic, *Statistical modeling by wavelets*. John Wiley & Sons, 2009, vol. 503.

[155] A. H. Kattoush, "A novel radon-wavelet based OFDM system design and performance under different channel conditions." *Int. Arab J. Inf. Technol.*, vol. 7, no. 4, pp. 419–427, 2010.

[156] I. Daubechies, *Ten Lectures on Wavelets*. Society for Industrial and Applied Mathematics, vol. 61, 1992.

[157] C. S. Burrus, R. A. Gopinath, and H. Guo, "Introduction to wavelets and wavelet transforms: a primer," 1997.

[158] M. Failli, *Digital Land Mobile Radio Communications. COST 207*. EC, 1989.

[159] J. Mietzner, R. Schober, L. Lampe, W. H. Gerstacker, and P. A. Hoeher, "Multiple-antenna techniques for wireless communications - a comprehensive literature survey," *IEEE Communications Surveys Tutorials*, vol. 11, no. 2, pp. 87–105, Second 2009.

[160] M. Matthe, L. L. Mendes, I. Gaspar, N. Michailow, D. Zhang, and G. Fettweis, "Multi-user time-reversal stc-gfdma for future wireless networks," *EURASIP Journal on Wireless Communications and Networking*, vol. 2015, no. 1, p. 132, May 9.

[161] M. Matth, L. L. Mendes, N. Michailow, D. Zhang, and G. Fettweis, "Widely linear estimation for space-time-coded gfdm in low-latency applications," *IEEE Transactions on Communications*, vol. 63, no. 11, pp. 4501–4509, Nov 2015.

[162] M. Danneberg, N. Michailow, I. Gaspar, M. Matth, D. Zhang, L. L. Mendes, and G. Fettweis, "Implementation of a 2 by 2 mimo-gfdm transceiver for robust 5g

networks," in *2015 International Symposium on Wireless Communication Systems (ISWCS)*, Aug 2015, pp. 236–240.

[163] M. Matth, D. Zhang, and G. Fettweis, "Sphere-decoding aided sic for mimo-gfdm: Coded performance analysis," in *2016 International Symposium on Wireless Communication Systems (ISWCS)*, Sept 2016, pp. 165–169.

[164] G. Al-Juboori, A. Doufexi, and A. R. Nix, "System level 5g evaluation of mimo-gfdm in an lte-a platform," in *2017 24th International Conference on Telecommunications (ICT)*, May 2017, pp. 1–5.

[165] H. G. Feichtinger and T. Strohmer, *Gabor analysis and algorithms: Theory and applications*. Springer Science & Business Media, 2012.

[166] H. Bolcskei, P. Duhamel, and R. Hleiss, "Design of pulse shaping ofdm/oqam systems for high data-rate transmission over wireless channels," in *1999 IEEE International Conference on Communications (Cat. No. 99CH36311)*, vol. 1, 1999, pp. 559–564 vol.1.

[167] D. J. Love and R. W. Heath Jr, "Limited feedback unitary precoding for orthogonal space-time block codes," *IEEE Transactions on Signal Processing*, vol. 53, no. 1, pp. 64–73, 2005.

[168] G. Jongren and M. Skoglund, "Utilizing quantized feedback information in orthogonal space-time block coding," in *Global Telecommunications Conference, 2000. GLOBECOM '00. IEEE*, vol. 2, 2000, pp. 995–999 vol.2.

[169] V. Tarokh, H. Jafarkhani, and A. R. Calderbank, "Space-time block coding for wireless communications: performance results," *IEEE Journal on Selected Areas in Communications*, vol. 17, no. 3, pp. 451–460, Mar 1999.

[170] E. G. Larsson, G. Ganesan, P. Stoica, and W.-H. Wong, "On the performance of orthogonal space-time block coding with quantized feedback," *IEEE Communications Letters*, vol. 6, no. 11, pp. 487–489, Nov 2002.

[171] B. M. Hochwald, T. L. Marzetta, T. J. Richardson, W. Sweldens, and R. Urbanke, "Systematic design of unitary space-time constellations," *IEEE Transactions on Information Theory*, vol. 46, no. 6, pp. 1962–1973, Sep 2000.

[172] T. Strohmer and R. W. Heath, "Grassmannian frames with applications to coding and communication," *Applied and Computational Harmonic Analysis*, vol. 14, no. 3, pp. 257 – 275, 2003.

[173] S. Ehsanfar, M. Matthe, D. Zhang, and G. Fettweis, "A study of pilot-aided channel estimation in mimo-gfdm systems," in *20th International ITG Workshop on Smart Antennas*, March 2016, pp. 1–8.

[174] U. Vilaipornsawai and M. Jia, "Scattered-pilot channel estimation for gfdm," in *IEEE Wireless Communications and Networking Conference (WCNC)*, April 2014, pp. 1053–1058.

[175] M.-H. Hsieh and C.-H. Wei, "Channel estimation for OFDM systems based on comb-type pilot arrangement in frequency selective fading channels," *IEEE Transactions on Consumer Electronics*, vol. 44, no. 1, pp. 217–225, 1998.

[176] O. Edfors, M. Sandell, J. J. van de Beek, S. K. Wilson, and P. O. Borjesson, "Ofdm channel estimation by singular value decomposition," in *Proceedings of Vehicular Technology Conference - VTC*, vol. 2, Apr 1996, pp. 923–927 vol.2.

[177] O. Edfors, M. Sandell, J.-J. Van De Beek, S. K. Wilson, and P. O. Börjesson, "Analysis of DFT-based channel estimators for OFDM," *Wireless Personal Communications*, vol. 12, no. 1, pp. 55–70, 2000.

[178] M. F.-G. García, J. M. Paez-Borrallo, and S. Zazo, "DFT-based channel estimation in 2d-pilot-symbol-aided OFDM wireless systems," in *IEEE 53rd Vehicular Technology Conference*, vol. 2, pp. 810–814, 2001.

[179] Y. Shen and E. Martinez, "Channel estimation in OFDM systems," 2006.

[180] A. Viterbi, "Error bounds for convolutional codes and an asymptotically optimum decoding algorithm," *IEEE transactions on Information Theory*, vol. 13, no. 2, pp. 260–269, 1967.

[181] K. Moon Todd, "Error correction coding: mathematical methods and algorithms," Tech. Rep., 2005.

[182] A. Technlogies, *Advanced design system LTE channel model - R4-070872 3GPP TR 36.803 v0.3.0*, 2008.

[183] I.-R. Recommendation, "Guidelines for evaluation of radio transmission technologies for imt-2000," *Rec. ITU-R M. 1225*, 1997.

[184] R. Jain, "Channel models: A tutorial," in *WiMAX forum AATG*, 2007, pp. 1–6.

[185] R. Beals and J. Szmigielski, "Meijer g-functions: a gentle introduction," *Notices of the AMS*, vol. 60, no. 7, pp. 866–872, 2013.

[186] E. E. Fichard and V. Franco, "Differential properties of meijer's g-function," *Journal of Physics A: Mathematical and General*, vol. 13, no. 7, p. 2331, 1980.

[187] S. Bernard, "Digital communications fundamentals and applications," *Prentice Hall, USA*, 2001.

[188] R. M. Gray, "Toeplitz and circulant matrices: A review." STANFORD UNIV CALIF STANFORD ELECTRONICS LABS, Tech. Rep., 1971.

[189] R. E. Blahut, *Algebraic methods for signal processing and communications coding*. Springer Science & Business Media, 2012.